Ultrafast mid-infrared pulse generation in chalcogenide glass

Md Imtiaz Alamgir

Department of Electrical & Computer Engineering

McGill University

Montreal, Canada

April 2022

A thesis submitted to McGill University in partial fulfillment of the requirements of the degree of Doctor of Philosophy

Abstract

The presence of vibrational and rotational transition lines in the mid-infrared (MIR) (2-10 μm) spectral range has stimulated numerous applications in the fields of spectroscopy, sensing and medicine. These emerging applications have intensified the research effort for the growth and development of novel optical light sources. Nonlinear effects in glass fibers are being extensively studied to generate ultrafast pulses at this wavelength range. Highly nonlinear silica fiber has shown record performance in the telecommunication wavelength band, however the strong material absorption of silica glass at wavelengths >2 μm limits its applicability in MIR. Recently, due to the extended MIR transmission (>12 μm wavelength) and ultra-high nonlinear gain, chalcogenide (ChG) fibers have attracted a great deal of attention and being widely investigated as an efficient solution towards this end. ChG microwires, in addition, enable engineerable chromatic dispersion, thereby allowing easy access to different nonlinear processes for pulse generation.

This dissertation explores the potential of ChG microwires for generation of ultrafast pulses at MIR wavelengths. Several different all-fiber optical sources are developed as a result of the nonlinear processes implemented to reach these wavelengths. This includes the design and development of parametric oscillators and mode-locked lasers, four-wave mixing wavelength converters, Raman soliton generation systems and supercontinuum lasers. The demonstrated sources generate pulses of wide range of temporal duration and power level, while covering a wavelength range of 1.9 μm to 3.0 μm with broadband and/or selective wavelength tunability. The numerical investigation of the underlying nonlinear process are also performed to confirm and predict the experimental behavior. Owing to their compactness, hand-portability, low power consumption and broad operation window, these novel optical sources are expected find wide range of applications in MIR spectroscopy and sensing.

Résumé

La présence de lignes de transition vibrationnelles et rotationnelles dans la gamme spectrale de l'infrarouge moyen (MIR) (2-10 μm) a stimulé de nombreuses applications dans les domaines de la spectroscopie, de la détection et de la médecine. Ces applications émergentes ont intensifié les efforts de recherche pour la croissance et le développement de nouvelles sources lumineuses optiques. Les effets non linéaires dans les fibres de verre sont largement étudiés pour générer des impulsions ultrarapides dans cette gamme de longueurs d'onde. Les fibres de silice hautement non linéaires ont montré des performances record dans la bande de longueur d'onde des télécommunications, cependant la forte absorption matérielle du verre de silice à des longueurs d'onde > 2 μm limite son applicabilité dans le MIR. Récemment, en raison de la transmission MIR étendue (longueur d'onde >12 μm) et du gain non linéaire ultra-élevé, les fibres de chalcogénure (ChG) ont attiré beaucoup d'attention et ont été largement étudiées comme une solution efficace à cette fin. Les microfils ChG, en outre, permettent une dispersion chromatique machinable, permettant ainsi un accès facile à différents processus non linéaires pour la génération d'impulsions.

Cette thèse explore le potentiel des microfils ChG pour la génération d'impulsions ultrarapides aux longueurs d'onde MIR. Plusieurs sources optiques toutes fibres différentes sont développées à la suite des processus non linéaires mis en œuvre pour atteindre ces longueurs d'onde. Cela comprend la conception et le développement d'oscillateurs paramétriques et de lasers à mode verrouillé, de convertisseurs de longueur d'onde de mélange à quatre ondes, de systèmes de génération de solitons Raman et de lasers supercontinuum. Les sources démontrées génèrent des impulsions d'une large plage de durée temporelle et de niveau de puissance, tout en couvrant une plage de longueurs d'onde de 1,9 μm à 3,0 μm avec une accordabilité à large bande et/ou sélective en longueur d'onde. L'étude numérique du processus non linéaire sous-jacent est également effectuée pour confirmer et prédire le comportement expérimental. En raison de leur compacité, de leur portabilité, de leur faible consommation d'énergie et de leur large fenêtre de fonctionnement, ces nouvelles sources optiques devraient trouver une large gamme d'applications dans la spectroscopie et la détection MIR.

To Aytija

Acknowledgements

My deepest gratitude goes to the *Almighty Allah (SWT)*, the Most Gracious, and the Most Merciful, for providing me the opportunity and granting me the capacity and patience to pursue my graduate studies.

I believe words would never be enough for be to express my gratitude to my thesis advisor *Prof. Martin Rochette*. I am greatly indebted to him for recruiting me as a graduate student and providing the opportunity to conduct research in the fascinating field of nonlinear photonics. His extensive supervision, endless guidance and constant support throughout the duration of my PhD research has greatly encouraged me and allowed me to achieve significant scientific results. The large degree of freedom I received from him in pursuing different ideas were crucial for developing my research skills. His meticulous review of my manuscripts and presentation slides have been tremendously beneficial in sharpening my academic writing and presentation skills. I feel truly blessed to have such experienced, skilled and friendly supervisor and mentor.

Many thanks go to the professors in my supervisory committee, *Prof. Andrew Kirk and Prof. Odile Liboiron-Ladouceur* for their valuable comments and suggestions throughout my qualifying exam, research proposal and seminar.

I would like to express my sincere appreciations to my colleagues from whom I had many opportunities to learn. I am thankful to *Lizhu Li* for introducing me to the lab facilities and training me in the hybrid fiber drawing and chalcogenide microwire fabrication process in the beginning of my PhD. Even deeper gratitude goes to *Nurmemet Abdukerim* for being my lab mentor and training me in developing different fiber and laser systems. We had aspiring discussions in the widespread topics of nonlinear optics that had helped me in great extent in finding new ideas and shaping my research. I am also thankful to *Moshen Rezaei* for his extended collaboration and keeping our parametric oscillator project active with his immense patience regarding coupler fabrication process. I thank *Md Hosne Mobarok Shamim* for many insightful discussions and his continuous assistance with simulations in the supercontinuum generation and soliton-self frequency shift project. I am in great debt to *François Saint-Hilaire* for his assistance in simulating pulse propagation equation and for sharing his matlab codes that has benefited me almost throughout my entire PhD. I am grateful to *Kaixuan Zhang* for his collaboration and sharing his knowledge regarding fiber optics filters and fiber lasers. A big

thanks goes to *Don Pavlasek* in the mechanical workshop who designed the microwire transportation systems that made my last project possible. Special thanks go to *Fatma Oudjedi* for the translation of the thesis abstract to French. Thanks goes to all my present colleagues *Robi Kormoker*, *Weixuan Lin*, and *Arslan Anjum* for many delightful discussions, occasionally related to optics. I thank my former colleagues including *Cameron Berge*, *Nazmul Islam,* and *Wasim Firdaus* for their wonderful friendship. I will always remember the basketball games, the long walks and the pizza hours that we enjoyed together. I am thankful to other members of the photonic system group, especially *Samiul Alam* for sharing different fiber optic components and equipment. I also thank all those people with whom I shared the office facility and all the students and postdoc fellows in the photonics system group, whom I interacted with during my graduate studies.

I am grateful to the Natural Sciences and Engineering Research Council of Canada for financial support in the research, and to CorActive High-Tech and Le Verre Fluoré for providing the chalcogenide and ZBLAN fiber used in my experiments. I would also like to thank the external chalcogenide fiber partners *Wagner Correr*, *Mohammed El Amraoui* and *Younès Messaddeq* from Laval University for their collaboration in providing the chalcogenide fibers.

I am forever indebt to my parents, *Alamgir Chowdhury* and *Nasima Alamgir* for their unconditional trust, unparalleled love, and endless patience. They have always been my guiding light, giving me strength and selflessly encouraging me to explore new directions. I am endlessly thankful to my brother *Istiak Alamgir* and my sister-in-law *Shamima Akhi* for their constant support and for being beside our parents when I was abroad.

Above all, I would like to thank my wife *Nafila Farheen*, who with her immense patience, has always stood by me through all the restless weekends, the late nights and the early mornings. Her enduring love and constant encouragement have supported me massively throughout this entire journey.

Contents

List of figures

List of tables

List of Acronyms

CW	continuous-wave
OPO	optical parametric oscillator
FWHM	full-width at half-maximum
FWM	four-wave mixing
GVD	group velocity dispersion
MIR	mid-infrared
NLSE	nonlinear Schrödinger equation
GNLSE	generalized nonlinear Schrödinger equation
PMMA	poly-methyl methacrylate
SMF	single mode fiber
SPM	self-phase modulation
XPM	cross-phase modulation
TPA	two-photon absorption
ZDW	zero-dispersion wavelength
ChG	chalcogenide
SSFS	soliton self-frequency shift
NPR	nonlinear polarization rotation
DW	dispersive waves
EM	electromagnetic
TDFL	thulium-doped fiber laser
CNT	carbon nanotube

SSFM	split-step Fourier method
MI	modulation instability
CE	conversion efficiency
ZDD	zero-dispersion diameter
TDFA	thulium doped fiber amplifier
TBPF	tunable band pass filter
PC	polarization controller
WDM	wavelength division multiplexer
OSA	optical spectrum analyzer
MLFL	mode-locked fiber laser
SM	single mode
HLNF	highly nonlinear fiber
EDFA	erbium-doped fiber amplifier
LPF	long-pass filter
TDL	tunable delay line
VOA	variable optical attenuator
MOF	microstructure optical fiber
CD	constant-dispersion
DV	dispersion-varying
QML	Q-switched mode-locking
CWML	continuous wave mode-locking
TDF	thulium doped fiber

1 Introduction

In 17th century, Isaac Newton published the findings of his famous dispersion experiment in the *Transactions of the Royal Society*, which concluded that the light perceived by human eye could be decomposed into different colors. Later on in 1800, William Herschel studied the temperature induced by the different colors of light and established the presence of "calorific rays" beyond the red part of the spectrum, what would later be known as the "infrared" radiation. Since its discovery, the infrared spectral region has found its way in numerous research fields, for example in infrared astronomy where, scientists analyze the emitted radiation to find composition, temperature of celestial objects as well as the expansion of the galaxies [1], [2]. Later on, infrared imaging was used in meteorology and climatology to determine cloud heights, locating ocean surface features and finding long-term change in earth's climate [3], [4].

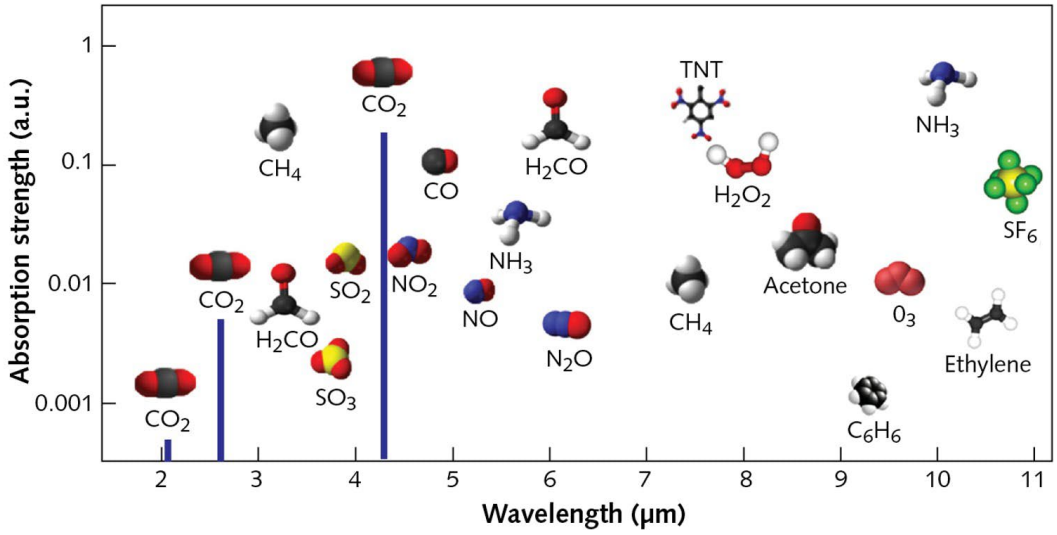

Figure 1.1 Absorption lines of different molecules within the spectral range of 2-11 μm wavelength (reproduced from [5]).

Over the last few decades, the spectral range within the infrared region, known as the mid-infrared (MIR) (2 μm to 20 μm) has attracted a great deal of attention due to its growing number of applications [6]. The MIR is recognized as the molecular fingerprint region since many fundamental molecules of gases, liquids and solids exhibit rotational and vibrational transitional

lines within this wavelength range. Fig. 1.1 shows the absorption wavelengths of different molecular compounds in MIR. Such potential indicates that a vast number of applications would directly benefit from the development MIR optical sources. For example, in atmospheric and pollution control applications, the detection of compounds such as CO_2 and CO would allow the monitoring of urban and industrial emission [7]–[9]. The potent green house gasses including CH_4 and C_2H_4 can also be detected using MIR lasers for the purpose of global warming [10], [11] and volcanic activity studies [12]. Apart from the scientific motivation, recently, the regulatory bodies around the world are also placing strong consideration in monitoring these compounds prior to and during oil and gas drilling activities. Advanced MIR spectroscopy system can detect the concentration of these compounds with a sensitivity as high as parts per billion, which is more sensitive than its natural background concertation. For security applications, detection of nitrogen based gases have utmost importance as they are found in mostly in the explosive materials [13]. In the food industry, MIR spectroscopy enables faster, highly sensitive and flexible analysis of grains, soils and diary products. This includes the concentration analysis of protein and glucose for food quality control [14], detecting mycotoxins in food and feed chain [15], identification of foodborne pathogen [16], and detection of melamine and acetone in cow milk [17], [18], to mention a few. In medicine, MIR spectroscopy represents a powerful tool for non-invasive medical diagnosis and early detection of diseases using technique such as breath analysis [19]. Human body produces different organic compound that are link to certain metabolic processes and can be directly related to specific pathological conditions. For example, presence of acetone in breath can be associated with diabetics [20] while nitric oxide is linked to lung diseases [21]. In the similar fields, MIR spectroscopy can also be used to determine the chemical structure of different biological tissues [22].

Such vast number of applications have intensified the research effort for the growth and development of numerous MIR sources. Solid-state mode-locked lasers such as Cr^{2+} or Fe^{2+} doped ZnS/$ZnSe$ lasers generate pulses within the wavelength range of 1.8-3.4 μm [23], [24] and 3.4-5.2 μm [25], respectively. Optical parametric oscillators (OPO) and intrapulse difference frequency generators based on periodically poled $LiNbO_3$ [26], orientation patterned $GaAs$ [27] and $CdSiP_2$ [28], are also known for generating MIR pulses of large tunability and high pulse quality. Although such high energy pulses find use in certain fields including strong-field physics and high-harmonic generation [29], these systems are generally bulky complex

optical systems that require precision alignment, expensive high maintenance pump lasers and lack field level deployability.

In contrast, optical sources developed in all-fiber architecture provide the advantages of compactness, mechanical stability, reliability of operation, high beam quality, and easy integration with external fiber systems. Since the development of low loss silica fiber in 1970s, rare earth doped silica lasers and amplifiers has shown particular success in a few specific regions of the near-infrared spectral window. To develop sources that operates beyond the restriction of these dopant emission bands, an often applied strategy is to utilize the nonlinear effects. Nonlinearity in silica fiber has been meticulously investigated in several novel fiber geometries, including microstructured optical fiber [30], photonic crystal fiber [31] and tapered optical fiber [32]. However, due to strong absorption losses in the wavelength region beyond 2 μm, the applicability of silica fibers as a nonlinear media in MIR remain limited.

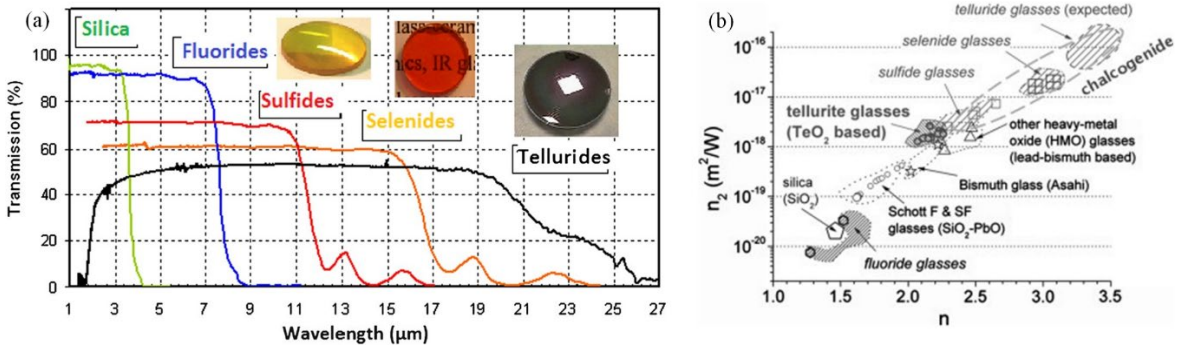

Figure 1.2: Transmission windows of silica, fluoride and chalcogenide glasses (reproduced from [33]). (b) Relation between the refractive index n and nonlinear refractive index n_2 for various types of glass (reproduced from [34]).

Therefore, as an alternative to silica fiber, different non-silica glass fibers with extended MIR transmission are being considered as an attractive candidate. Fig. 1.2 (a) and (b) shows the transmission spectrum and the nonlinear refractive index of different soft glass fibers. Fluoride fibers has a transparency window up to a wavelength of 6 μm, with nonlinear properties similar to that of silica fiber. On the other hand, ChG (As_2Se_3 and As_2S_3) fibers possess a nonlinear refractive index that is factor of 200 to 1000 more higher than silica, depending on the content of sulfur (*S*) or selenium (*Se*) [35], [36]. ChG glasses also shows negligible two-photon absorption and free carrier absorption in the MIR wavelength [37], [38]. Furthermore, tapering the ChG fiber down into a microwire provides strong light confinement and an increase in the

nonlinear waveguide parameter by more than 5 orders of magnitude, in comparison with the silica fiber [39]. It also allows to engineer and shift the zero-dispersion wavelength (ZDW) to align with the wavelengths of the commercially available compact fiber lasers, thereby providing an easy access to different nonlinear processes that can be used to develop optical sources in the MIR.

The objective of this dissertation is to investigate the nonlinear effects in ChG microwires and explore their potentials in developing all-fiber optical sources operating at MIR wavelengths. These nonlinear systems would be compact, hand portable, require low power consumption, and enable the generation of ultrafast (picosecond to femtosecond) pulses of broad range of power levels (μW to mW). The demonstrated sources are expected to find numerous applications in MIR sensing and spectroscopy [40]–[43].

1.1 Main contributions and thesis outline

In this thesis, a number of nonlinear effects in ChG microwires including parametric effect, supercontinuum (SC) generation, soliton self-frequency shift (SSFS) and nonlinear polarization rotation (NPR) are exploited to generate a broad range of MIR pulses of different duration, wavelength, spectral coverage and selectivity. After providing a general overview of the linear and nonlinear light-matter interaction in ChG optical fibers in chapter 2, the major contributions of this dissertation are presented in the following chapters.

In chapter 3, a novel all-fiber wavelength converter fabrication technique is presented that allows the *in situ* optimization of far-detuned parametric gain and sideband offset. The parametric gain of A_2Se_3 microwires are finely tuned from the successive adjustments of microwire diameter along with real-time monitoring. Wavelength conversion is achieved from a pump at a wavelength of 1.938 μm to any far-detuned idler within the spectral range of 2.347 - 2.481 μm, resulting into a detuning of 27.0 - 33.9 THz with a wavelength offset precision within 3.1 THz.

In chapter 4, an all-fiber C-band to MIR nonlinear wavelength conversion systems is demonstrated. The system generates picosecond pulses within the wavelength range of 2.30-2.64 μm, as a result of the synchronization among the effect of self-phase modulation (SPM), Raman-induced SSFS and far-detuned four-wave mixing (FWM) in silica and ChG fiber. A total spectral shift excess of 80 THz is obtained with a conversion efficiency as high as -3 dB .

In chapter 5, the development of a highly efficient tunable soliton source based on SSFS in As_2S_3 microstructured fiber microwire is presented. The demonstrated system is exceptionally simple and fully fiberized. It generates continuously tunable Raman solitons over a broad spectral range of 2.047-2.667 μm, by consuming no more than 87 pJ per pulse. The generated pulses are as short as 62 fs and shows a maximum power conversion efficiency of 43%.

In Chapter 6, a novel SC efficiency enhancement method is demonstrated by using dispersion-varying As_2S_3 suspended core microwire structure. The specially designed dispersion profile of the microwire results in an enhanced energy transfer to the dispersive waves (DW) in the shorter wavelength edge, as well as an increased SSFS towards the longer wavelength edge of the SC. The generated SC spans within the spectral range of 1.2-2.98 μm with an out-of-pump SC power enhancement of 4.5 dB towards shorter wavelength and a bandwidth extension of 262 nm, compared to the SC generated with the tradition dispersion profile.

In chapter 7, a mode-locking technique based on NPR in As_2S_3 microwire is presented. The high nonlinearity of the microwire leads to a combined reduction in mode-locking threshold power and cavity length compared to any all-silica NPR based mode-locked lasers. In the continuous wave mode-locking regime, the laser generates stable, tunable solitons pulses. In the Q-switched mode-locked regime, it allows single and multiwavelength pulses, tunable central wavelength and tunable multiwavelength separation.

In chapter 8, the development of a MIR optical parametric oscillator (OPO) is shown that is designed entirely out of soft-glass fiber cavity. This novel cavity design consists of an As_2Se_3 low loss single-mode fiber coupler, an As_2Se_3 highly nonlinear and dispersion engineered microwire gain medium and commercially available ZBLAN delay fiber. The OPO generates both Raman assisted and pure parametric gain and oscillates with tunable Stokes emission lines within 2.023-2.048 μm and 2.088-2.139 μm wavelength, respectively.

Finally, chapter 9 concludes the thesis by presenting a short summary and the future scopes of MIR pulse generation in ChG microwires.

1.2 List of publications

Below is the full list of journal publications and conference proceedings produced during the course of this doctoral work.

1.2.1 Journal publications

1. ***I. Alamgir***, M. Rezaei and M. Rochette, "Fiber optical parametric oscillator made of soft-glass", under review in Optics Letters (2022).

Contribution: *I. Alamgir* fabricated the microwire device, conducted the experiment, performed the numerical simulation and the data analysis. *M. Rezaei* fabricated the coupler. *I. Alamgir* and *M. Rochette* prepared the manuscript. *M. Rochette* conceived the concept and supervised the project.

2. ***I. Alamgir***, M. Shamim, W. Correr, Y. Messaddeq and M. Rochette, "Supercontinuum generation in a dispersion-varying chalcogenide fiber" to be submitted in Applied physics letters (2022).

Contribution: *I. Alamgir* conceived the concept, fabricated the microwire device, conducted the experiment, performed the numerical simulation and the data analysis. *M. Shamim* contributed to the numerical simulation. *W. Correr* and *Y. Messaddeq* fabricated the ChG fiber. *I. Alamgir* and *M. Rochette* prepared the manuscript. *M. Rochette* supervised the project.

3. ***I. Alamgir*** and M. Rochette, "Thulium-doped fiber laser mode-locked by nonlinear polarization rotation in a chalcogenide taper" accepted in Optics Express (2022).

Contributions: *I. Alamgir* conceived the concept, fabricated the microwire device, conducted the experiment and performed the data analysis. *I. Alamgir* and *M. Rochette* prepared the manuscript. *M. Rochette* supervised the project.

4. ***I. Alamgir***, M. Shamim, W. Correr, Y. Messaddeq, and M. Rochette "Mid-infrared soliton self-frequency shift in chalcogenide glass," Optics Letters 46(21), 5513-5516 (2021).

Contribution: *I. Alamgir* conceived the concept, fabricated the microwire device, conducted the experiment, performed the numerical simulation and the data analysis. *M. Shamim* contributed to the experimental design and the numerical simulation. *W. Correr* and *Y. Messaddeq*

fabricated the ChG fiber. *I. Alamgir* and *M. Rochette* prepared the manuscript. *M. Rochette* supervised the project.

5. ***I. Alamgir***, F. St-Hilaire and M. Rochette, "All-fiber nonlinear optical wavelength conversion system from the C-band to the mid-infrared," Optics Letters 45(4), 857-860 (2020).

Contributions: *I. Alamgir* conceived the concept, fabricated the microwire device, conducted the experiment, performed the numerical simulation and the data analysis. *F. St-Hilaire* developed the simulator. *I. Alamgir* and *M. Rochette* prepared the manuscript. *M. Rochette* supervised the project.

6. ***I. Alamgir***, N. Abdukerim and M. Rochette, "In situ fabrication of far-detuned optical fiber wavelength converters", Optics Letters 44 (18), 4467-4470 (2019).

Contributions: *I. Alamgir* conceived the concept, fabricated the microwire device, conducted the experiment, performed the numerical simulation and the data analysis. *N. Abdukerim* contributed to the experimental design. *I. Alamgir* and *M. Rochette* prepared the manuscript. *M. Rochette* supervised the project.

7. M. Shamim, ***I. Alamgir***, and M. Rochette, "High-efficiency, nano-joule level wavelength conversion from soliton self-frequency shift in a passive silica fiber at 2 μm", under review in Photonic Technology Letters (2022).

Contributions: *M. Shamim* conceived the concept, conducted the experiment, performed the numerical simulation and the data analysis. *I. Alamgir* contributed to the experimental design and the data analysis. *M. Shamim* and *M. Rochette* prepared the manuscript. *M. Rochette* supervised the project.

8. K. Zhang, ***I. Alamgir*** and M. Rochette, "Mid-infrared Compatible Tunable Bandpass Filter Based on Multimode Interference in Chalcogenide Fiber," Journal of Lightwave Technology 38(4), 857-863 (2020).

Contributions: *K. Zhang* conceived the concept, conducted the experiment, performed the numerical simulation and the data analysis. *I. Alamgir* designed and fabricated the fiber and contributed to the experimental design and the data analysis. *K. Zhang* and *M. Rochette* prepared the manuscript. *M. Rochette* supervised the project.

9. N. Abdukerim, ***I. Alamgir***, and M. Rochette, "Pulse characterization by cross-phase modulation in chalcogenide glass," Optics Letters 43(19), 4771 4774 (2018).

Contributions: *N. Abdukerim* conceived the concept, conducted the experiment, performed the numerical simulation and the data analysis. *I. Alamgir* designed and fabricated the microwire and contributed to the experimental design. *N. Abdukerim* and *M. Rochette* prepared the manuscript. *M. Rochette* supervised the project.

10. N. Abdukerim, ***I. Alamgir***, and M. Rochette, "All-fiber frequency-resolved optical gating pulse characterization from chalcogenide glass," Optics Letters 43(14), 3228–3231 (2018).

Contributions: *N. Abdukerim* conceived the concept, conducted the experiment, performed the numerical simulation and the data analysis. *I. Alamgir* designed and fabricated the microwire. *N. Abdukerim* and *M. Rochette* prepared the manuscript. *M. Rochette* supervised the project.

11. D. Hudson, S. Antipov, L. Li, ***I. Alamgir***, T. Hu, M. El Amraoui, Y. Messaddeq, M. Rochette, S. D. Jackson, and A. Fuerbach, "Toward all-fiber supercontinuum spanning the mid-infrared," Optica, 4 (10), 1163 (2017).

Contributions: *I. Alamgir* contributed to the design and fabrication of the microwire device.

1.2.2 Conference proceedings

1. ***I. Alamgir***, M. Rezaei and M. Rochette, "Optical parametric oscillation from soft-glass fiber cavity", accepted in *CLEO Conference,* San Jose, California, May 2022.

2. ***I. Alamgir*** and M. Rochette, "Q-switched mode-locking by NPR in As_2S_3 tapers", accepted in *CLEO Conference*, San Jose, California, May 2022.

3. ***I. Alamgir***, M. H. M. Shamim, W. Correr, Y. Messaddeq and M. Rochette, "Supercontinuum enhancement in dispersion-varying chalcogenide taper" at the *Photonics North Conference*, CMC- 1 (virtual), June 2021.

4. ***I. Alamgir*** and M. Rochette, "2 μm mode-locked fiber laser enabled by NPR in a chalcogenide taper", at the *CLEO/Europe EQEC Conference,* CJ-2.5 (virtual), June 2021.

5. ***I. Alamgir***, M. H. M. Shamim, W. Correr, Y. Messaddeq and M. Rochette, "Mid-infrared soliton self-frequency shift using ultra-low pump pulse energy", at the *CLEO/Europe EQEC Conference,* CD-2.5 (virtual), June 2021.

6. ***I. Alamgir***, M. H. M. Shamim, W. Correr, Y. Messaddeq and M. Rochette, "Enhanced supercontinuum from a dispersion-varying fiber" at the *CLEO Conference*, JTu3A.93 (virtual), May 2021.

7. ***I. Alamgir***, M. H. M. Shamim, W. Correr, Y. Messaddeq and M. Rochette, "Raman soliton generation using ultra-low pump pulse energy", at the *CLEO Conference*, STh5A.6 (virtual) May 2021.

8. ***I. Alamgir***, H. Mobarok Shamim, W. Correr, Y. Messaddeq, and M. Rochette, "Glissement de fréquence de solitons dans l'infrarouge moyen à partir d'impulsions de faible énergie," at *Optique Dijon*, O8-B:1 (virtual), Dijon, France, July 2021.

9. ***I. Alamgir***, M. Rezaei and M. Rochette "Optical Parametric Oscillator based on All-Chalcogenide Fiber Components," at the *Advanced Photonics Congress*, NpM3E.4 (virtual) July 2020.

10. ***I. Alamgir***, M. Shamim, M. El. Amraoui, Y. Messaddeq, M. Rochette "Supercontinuum Generation in Suspended Core As2S3 Tapered Fiber" at the *IEEE Photonics Conference*, WE2.3 (virtual), September 2020.

11. ***I. Alamgir***, F. St-Hilaire and M. Rochette "Nonlinear Optical Wavelength Conversion System from the C-Band to the Mid-Infrared," at the *CLEO Conference*, JTu2F.25 (virtual) May 2020.

12. ***I. Alamgir***, N. Abdukerim and M. Rochette "In Situ Fabrication of Far-Detuned Mid-Infrared Optical Fiber Wavelength Converters," at the *CLEO/Europe EQEC Conference*, CD-P.37, June 2019.

13. ***I. Alamgir***, N. Abdukerim and M. Rochette "Far-Detuned parametric gain optimization in Wavelength Converters," *at the IEEE Photonics Conference*, Reston, Virginia, September 2018.

14. ***I. Alamgir***, N. Abdukerim, and M. Rochette "In Situ Fabrication of Far-Detuned Wavelength Converters," at the *21st International Symposium on Non-Oxide and New Optical Glasses*, P-34, Québec city, Québec, June 2018.

15. M. Shamim, ***I. Alamgir,*** Wagner Correr, Y. Messaddeq, M. Rochette, "Mid-infrared soliton self-frequency shift in a cascade of silica, fluoride, and chalcogenide fibers", submitted at *Advanced Photonics Congress*, July 2022.

16. M. Shamim, ***I. Alamgir*** and M. Rochette, "High efficiency mid-infrared soliton self-frequency shift in a fluoride fiber" accepted in *CLEO Conference*, San Jose, California, May 2022.

17. M. Shamim, ***I. Alamgir***, and M. Rochette, "High Efficiency Raman Soliton Generation in Passive Silica Fiber," at the *CLEO/Europe EQEC*, CD-2.3 (virtual), June 2021.

18. M. Shamim, ***I. Alamgir*** and M. Rochette, "Soliton self-frequency shift in a passive silica fiber with conversion efficiency of 84.6%," at the *CLEO Conference*, STh5A.2 (virtual) May 2021.

19. M. Shamim, ***I. Alamgir***, and M. Rochette, "Efficient Supercontinuum Generation in As2S3 Tapered Fiber Pumped by Soliton-Self Frequency Shifted Source," at the *Advanced Photonics Congress*, ITh1A.5 (virtual) conference, July 2020.

20. M. Shamim, ***I. Alamgir*** and M. Rochette, "All-Fiber Wavelength Conversion from Low Power Pumping," at the *Photonics North Conference*, NL-3-26-1 (virtual), May 2020.

21. K. Zhang, ***I. Alamgir***, Y. A. Peter, and M. Rochette "Multimode interference tunable filter in chalcogenide fiber," at the *IEEE Photonics Conference*, MF4.2, San Antonio, Texas, September 2019.

22. N. Abdukerim, ***I. Alamgir*** and M. Rochette "Frequency-Resolved Optical Gating Pulse Characterization with Chalcogenide Microwires," at the *Advanced Photonics Congress*, NpM4I, Zurich, Switzerland, July 2018.

23. A. Fuerbach, D. Hudson, S. Jackson, S. Antipov, R. Woodward, L. Li, ***I. Alamgir***, M. El Amraoui, Y. Messaddeq, and M. Rochette "Mid-IR Supercontinuum Generation," at the *Advanced Photonics Congress*, SoTh3H, Zurich, Switzerland, July 2018.

24. D. D. Hudson, S. Antipov, L. Li, ***I. Alamgir***, M. El Amraoui, Y. Messaddeq, M. Rochette, S. D. Jackson, and A. Fuerbach "Octave-spanning supercontinuum in the mid-IR with a 3 μm ultrafast fiber laser," at the *Nonlinear Optics: Materials, Fundamentals and Applications*, NTu3A.3, Waikoloa, Hawaii, July 2017.

2 Light-matter interaction in Chalcogenide fiber

This chapter provides an overview of the physics of light-matter interaction in ChG optical fibers. First, the linear and nonlinear responses of the material to an external optical field are introduced. Once these properties have been established, the GNLSE that governs the light propagation in optical fibers is discussed. Finally, the nonlinear phenomenon that are relevant to the ultrafast pulse generation in ChG fibers are explained and placed in the context of GNLSE. In general, if not otherwise indicated this chapter is based on reference [44], [45], where a more detailed derivation of the equations for nonlinear fiber optics can be found.

2.1 Linear properties

2.1.1 Optical attenuation

Light propagating in the optical fibers are attenuated by a number of effects, with material absorption and Rayleigh scattering being the dominant factor. The material absorption includes the electronic absorption at shorter wavelength, vibrational or multiphonon absorption at longer wavelengths and the impurity absorption in between. The electronic absorption arises from the amorphous semiconductor nature of the ChG glass, where an incident photon with energy exceeding the characteristic bandgap is absorbed, creating an electron-hole pair in the process. This absorption governs the shorter wavelength limit of the transmission window and it has a gradual wavelength dependence known as the Urbach tail, resulting from the deviation of the crystalline order of the material in the macroscopic scale [46]. The longer wavelength transmission edge, on the other hand, depends on the vibrational transitions of the atomic network which is determined by the atomic mass and the bond strength. ChG is glasses are generally characterized by larger atoms and weaker bonds that results in lower vibrational frequencies and shifts the fundamental infrared cut off to longer wavelengths [47]. In between the shorter and longer wavelength edge, the optical transmission is affected by the extrinsic absorption losses from the material impurity. The most common impurities contained in the ChGs during the purification process are hydrogen, oxygen and water, which form R-O and R-

H bonds (where R is the chalcogen and 4B and 5B elements) in the glass matrix. Such impurity related losses can be significantly reduced by the purification of precursor during glass fabrication [48]. Recently, high purity ChG glass optical fibers with losses as low as 0.012 dB/m and 0.06 dB/m has been demonstrated for As-S and As-S-Se fibers, respectively [49] .

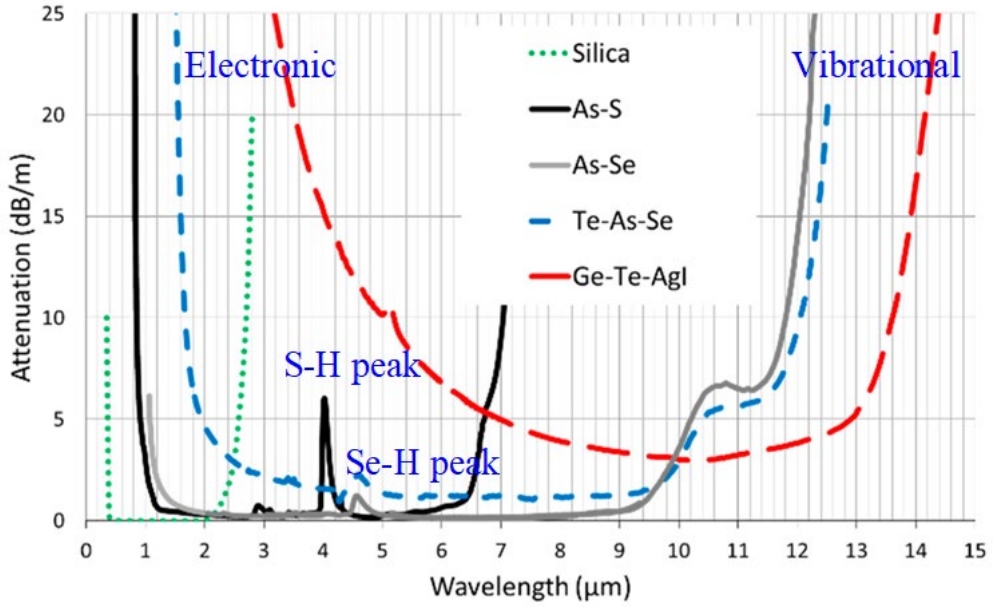

Figure 2.1: MIR transmission spectrum of ChG optical fibers in comparison to silica. (Modified from [50])

Another primary source of attenuation in the optical fiber is related to the Rayleigh scattering mechanism that occurs due to material inhomogeneity. During the fiber manufacturing process, the density fluctuations are frozen into the fused glass, which results in a local fluctuation in refractive index and scatter light in all direction. This process is known as a quasi-elastic scattering event as it induces no frequency shift [51]. The Rayleigh scattering loss is more dominant at short wavelengths due to its λ^{-4} dependence. Since this loss is intrinsic to the fiber, its sets the ultimate limit on the fiber losses. Theoretical prediction indicate a minimum loss of 0.1-0.01 dB/km can be obtained for ChG fibers [52]. Fig. 2.1 shows the experimental transmission data for ChG fibers with various chalcogen elements. It is observed that As_2S_3 fiber can transmit light from 1 to 6.5 µm [49], As_2Se_3 fiber from 1.4 to 10 µm [53] and Te-based fibers are transparent up to 15 µm wavelength. The absorption peak at the wavelength of 4.1 µm and 4.56 µm for As_2S_3 and As_2Se_3 corresponds to the vibrational resonance of S- H and Se-H impurity, respectively.

2.1.2 Chromatic dispersion

Chromatic dispersion of an optical fiber is characterized by the wavelength dependent effective index of the guided mode and determined by both material and waveguide contributions. The material dispersion is the wavelength dependence of the refractive index $n(\lambda)$, which originates from the characteristic resonances, due to the mutual relation between refractive index and absorption coefficient through Kramers-Kronig relations [54]. Far from the material resonances, the refractive index is well approximated by the Sellmeier equation.

$$n^2(\omega) = 1 + \sum_{j=1}^{m} \frac{B_j \omega_j^2}{\omega_j^2 - \omega^2} \tag{2.1}$$

where, ω_j is the resonance frequency and B_j is the strength of the j_{th} resonance, For bulk As_2Se_3 glasses, these parameters are found to be B_1=0.2274, B_2= 6.74238, λ_1=508.05159 µm, λ_2=0.10545 µm, where $\lambda_j = 2\pi c/\omega_j$ [55]. Equation 2.1 remains valid for wavelengths far from the resonances, which is approximately between 1-12 µm. Fig. 2.2 shows the wavelength dependent refractive index for As_2Se_3.

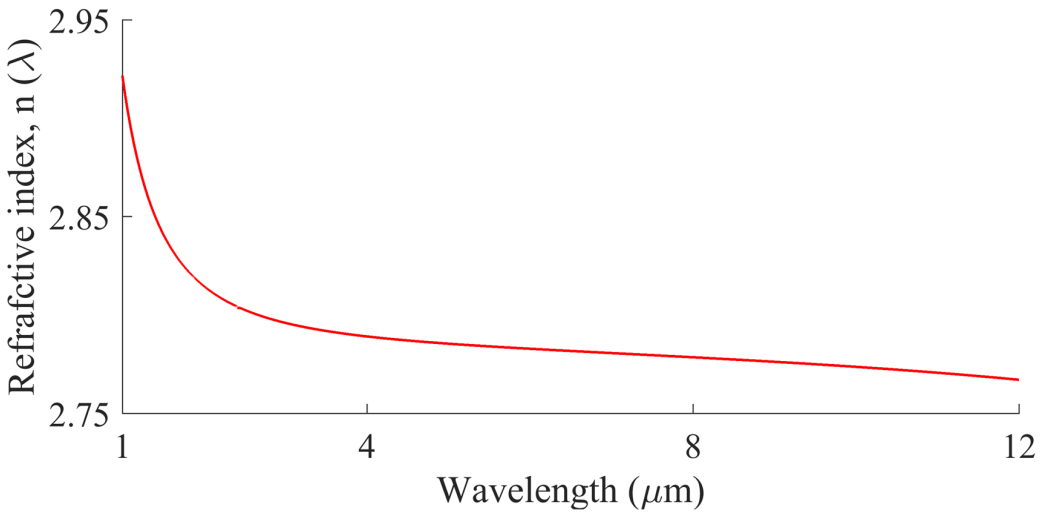

Figure 2.2. The linear refractive index of As_2Se_3 as a function of wavelength, calculated from eq. 2.1.

Chromatic dispersion is mathematically expressed by expanding the mode-propagation constant β in the Taylor series about the center frequency ω_0,

$$\beta(\omega) = n(\omega)\frac{\omega}{c} = \beta_0 + \beta_1(\omega - \omega_0) + \frac{1}{2}\beta_2(\omega - \omega_0)^2 + \cdots \tag{2.2}$$

where,

$$\beta_m = \left(\frac{d^m \beta}{d\omega^m}\right)_{\omega=\omega_0} \tag{2.3}$$

β_1 and β_2 are related to the refractive index through the following relation

$$\beta_1 = \frac{1}{v_g} = \frac{n_g}{c} = \frac{1}{c}\left(n + \omega \frac{dn}{d\omega}\right) \tag{2.4}$$

$$\beta_2 = \frac{1}{c}\left(2\frac{dn}{d\omega} + \omega \frac{d^2 n}{d\omega^2}\right) \tag{2.5}$$

where, v_g is the group velocity, which is responsible for the temporal delay of the optical pulse as a whole. β_2 represents the GVD, which accounts for the variable propagation speeds for the different frequency components associated with the pulse and is responsible for temporal pulse broadening. Two important dispersion regimes depending on the GVD sign need to be distinguished. The normal dispersion regime ($\beta_2>0$) is characterized by an increase in the group velocity with wavelength, whereas the anomalous dispersion ($\beta_2<0$) is the other way around. The wavelength at which two dispersion regimes crosses and the sign is reversed for longer wavelengths is called the ZDW. Higher order dispersion parameters β_m becomes relevant near the ZDW. Due to the waveguiding effect in the fiber, there is a minor wavelength dependent reduction in the effective mode index from the material index $n(\omega)$ of the core. This waveguide contribution should be taken into accounted along with the material contribution to obtain the total dispersion of the fiber. Fig. 2.3 shows the calculated GVD of As_2Se_3 fiber of IRT-SE-6/170 model from Coractive HighTech [56].

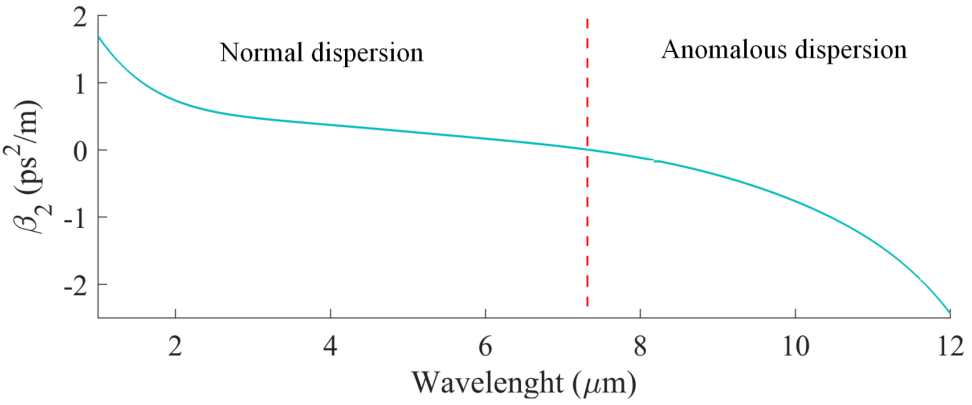

Figure 2.3 The GVD spectrum of As_2Se_3 fiber as function of wavelength. The vertical line located at 7.4 μm indicates the ZDW.

2.1.3 Chalcogenide microwire

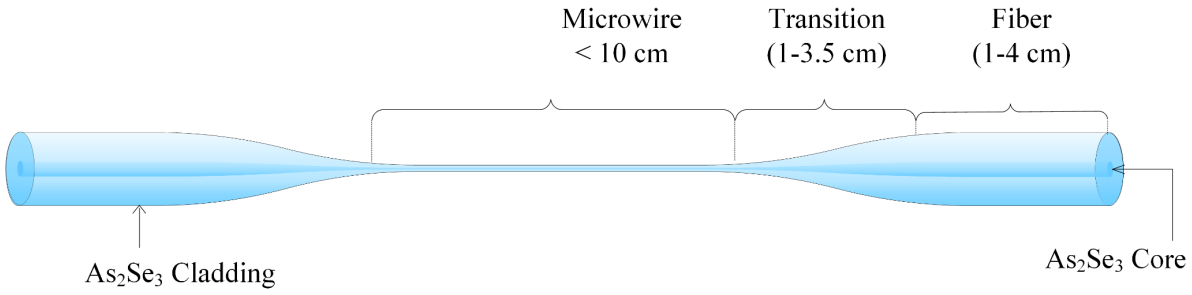

Figure 2.4 Schematics of a ChG microwire.

Microwires are fabricated using heat-brush tapering approach, where a segment of a fiber is heated and stretched to obtain a waveguide of subwavelength core diameter [57], [58]. Fig. 2.4 shows the schematics of such device, which consists of a microwire section where the nonlinear process occurs, two fiber sections for efficient coupling to input/output fiber, and two transition sections for adiabatic transition of fundamental mode from fiber to microwire section. First experimental demonstration of enhanced optical nonlinearity in microwire was shown with silica fibers in 1993 [59]. Since then, a number of experimental and numerical investigations of the nonlinear dynamics in the micowire structure have been reported. In 2007, E. Mägi *et al.* demonstrated the first ChG micowire, where a core diameter of 1.2 μm resulted in a nonlinear coefficient of 68 $W^{-1}m^{-1}$ [60]. When the ChG fibers are tapered to micron core diameter, the ChG cladding in the microwire section disappears and a strong confinement is developed between the ChG core and surrounding air, resulting in air-cladded microwires. In comparison

to ChG fibers, the total dispersion is more significantly affected by the waveguide dispersion in air-cladded ChG microwires. This waveguide dispersion can be precisely controlled to shift the ZDW of the microwire at wavelengths where compact pump fiber laser sources are available. Fig 2.5 shows the calculated GVD of As_2Se_3 microwire as a function of wavelength. For three different microwire core diameter, the ZDW is obtained at 1.55 µm, 1.9 µm and 2.8 µm wavelength, where *Er*- and *Tm*-doped silica fiber laser and *Er*-doped ZBLAN fiber laser are commercially available. Besides air-cladding, polymer-cladded microwires have been demonstrated as well. In addition to dispersion engineering, the polymer provides optical and mechanical protection, thus enabling robust handling capacity without damaging the device. So far, there has been multiple demonstration of polymer-cladded microwire including poly-methyl methacrylate (PMMA) [61][39], polycarbonate, Cyclo olefin polymer [62] and Cyclic transparent optical polymer [63]. However, due to presence of first order and second order vibrational wavelengths of C-H bonds, C=O bonds, C-C bonds and C-O bonds of the polymer, a severe impact on the MIR transparency of the waveguides are observed [64].

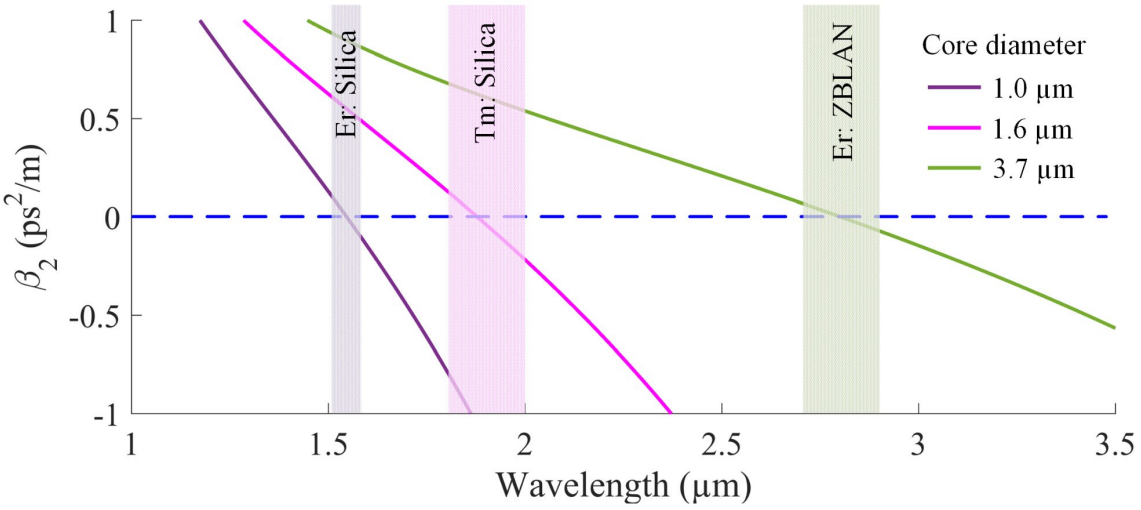

Figure 2.5 Calculated GVD of air-cladded As_2Se_3 as a function of wavelength. The dashed horizontal line indicates the zero dispersion.

2.2 Nonlinear properties

The polarization induced by the electric dipoles of the medium in response to an external EM field can be written as a Taylor series expression,

$$\boldsymbol{P} = \varepsilon_0(\chi^{(1)}.\boldsymbol{E} + \chi^{(2)}:\boldsymbol{EE} + \chi^{(3)}:\boldsymbol{EEE} + \cdots) = P_L + P_{NL} \quad (2.6)$$

where ε_0 is the vacuum electric permittivity, and $\chi^{(j)}$ is the j_{th} order susceptibility of the medium. $\chi^{(1)}$ represents the linear contribution to the polarization, effects of which are included as attenuation and dispersion in section 2.1. However, under the influence of intense EM field, the induced polarization shows nonlinear relationship with the applied field strength, as shown by equation 2.6. The origin of such nonlinear response is related to anharmonic motion of the bound electrons under the influence of the applied field. ChG glasses possess an inherent inversion symmetry that forces the second order and the subsequent even higher order susceptibilities to vanish, leaving the $\chi^{(3)}$ term as the most dominant nonlinear contribution to the polarization. As a result, the nonlinear effects in the ChG fibers only correspond to the $\chi^{(3)}$ processes that gives rise to nonlinear refraction and Raman scattering.

2.2.1 Nonlinear refraction

Nonlinear refraction, also known as Kerr effect is a process that refers to the intensity dependence of the refractive index. In its simplest form, the refractive index is expressed as,

$$n(\omega, I) = n_0(\omega) + n_2 I = n_0(\omega) + n_2|\boldsymbol{E}|^2 \quad (2.7)$$

where n_0 is the linear part given by equation 2.1, I is the optical intensity in the fiber associated with the EM field E. n_2 is known as the nonlinear index coefficient, which is experimentally measured using several approaches such as Z-scan, optical Kerr gating and Ellipse rotation and third-harmonic generation [65]. Theoretically, it is related to the real part of $\chi^{(3)}_{xxxx}$ by the following expression.

$$n_2 = \frac{3}{8n_0} Re(\chi^{(3)}_{xxxx}) \quad (2.8)$$

Although $\chi^{(3)}_{xxxx}$ is a fourth-rank tensor, only one its component contributes if EM field is considered to be linearly polarized. Qualitatively, it is understood as the response of the dielectric when an intense EM field perturb the electronic structure of the molecules and causes an intensity dependent change in the polarizability. Since the bound electron clouds can be distorted by the applied field within a few femtoseconds, this electronic response can be treated as an instantaneous effect for pump pulses of few hundred femtosecond duration or less. This

intensity dependence of the refractive index leads to numerous nonlinear effects, among which SPM and XPM are widely known and discussed in section 2.3.1.

The imaginary part of $\chi^{(3)}$ gives the intensity dependent nonlinear absorption coefficient, known as the two-photon absorption (TPA) and expressed as,

$$\alpha_2 = -\frac{3k_0}{4n_0} Im(\chi^{(3)}_{xxxx}) \tag{2.9}$$

The magnitude of n_2 and α_2 for *As-S-Se* systems have been experimentally determined by using spectrally resoled two beam coupling measurements [36]. Fig. 2.6 shows the corresponding results. n_2 values for As_2S_3 glasses are found to be ~220 times higher than silica glass at 1.55 μm wavelength and increases further with the *Se* substitution of *S*. For As_2Se_3 compositions, this vales reaches as high as ~ 930 times of fused silica. Such a high value of nonlinear index shows the potential for the development of small, compact and low power nonlinear devices out of ChG fibers.

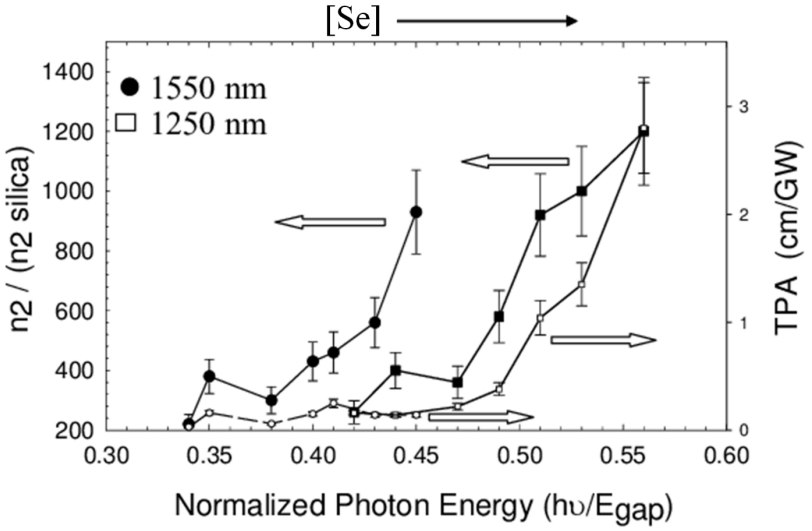

Figure 2.6: n_2 and α_2 coefficient of As-S-Se glass system (reproduced from [66])

2.2.2 Inelastic nonlinear scattering

The nonlinear effects governed by $\chi^{(3)}$ nonlinearity are elastic in nature since no energy exchange takes place between the propagating EM field and the dielectric medium. However, there exists another class of nonlinear effect, known as the inelastic scattering process where the EM field transfers part of its energy to the nonlinear medium. Raman scattering is such

inelastic scattering process known to be related to the vibrational excitation modes of the medium. In Raman scattering, the propagating pump photon creates a vibrational quanta known as the optical phonon, resulting in a loss of photon energy and corresponding Stokes shift. Similarly, anti-Stokes shift can also be obtained if a phonon of right energy and momentum is available in the medium. If no prior photons are present at the Stokes or anti-Stokes frequency, the scattering process is known as the spontaneous Raman scattering, whereas the presence of a seed will lead to a significant Raman amplification, known as the stimulated Raman scattering. Raman scattering can be understood through the nonlinear response function, defined as:

$$R(t) = (1 - f_R)\delta(t) + f_R h_R(t) \tag{2.10}$$

It comprises of two responses, 1) the electronic response, which is assumed to be instantaneous and hence described by the delta function, δ(t), and 2) the delayed Raman response $h_R(t)$, originating from photon-phonon interaction [67]. f_R represents the fractional contribution of the delayed Raman response and has value of 0.1 for As_2Se_3 material. $h_R(t)$ can be approximated by a simple damped oscillator model,

$$h_R(t) = \frac{\tau_1^2+\tau_2^2}{\tau_1\tau_2^2}\exp\left(-\frac{t}{\tau_2}\right)\sin\left(\frac{t}{\tau_1}\right) \tag{2.11}$$

with τ_1=23 fs is the inverse phonon frequency, and τ_2=195 fs is the phonon lifetime or the inverse bandwidth of the Raman gain spectrum for bulk As_2Se_3 [68]. The Raman gain is given by the imaginary part of the $h_R(t)$ in the frequency domain,

$$g_R(\omega) = \frac{2\omega_p}{c_0} n_2 f_R Im(H_R(\omega)) \tag{2.12}$$

Fig. 2.7 shows normalized Raman gain spectra of As_2S_3 and As_2Se_3 glasses compared with that of silica. The Raman shift of As_2Se_3 and As_2S_3 glasses are ~240 cm^{-1} and ~345 cm^{-1}, respectively which are smaller compared to Raman shift of silica glass (440 cm^{-1}). The difference occurs due to the presence of heavier atoms in the ChG glass. Additionally, the Raman linewidth are relatively narrower (~60 cm^{-1} and ~85 cm^{-1}) compared to the linewidth of silica (~250 cm^{-1}) [66]. Due to the relatively large n_2 compared to silica, the magnitude of the Raman gain are also ~900 and ~100 times higher for As_2Se_3 and As_2S_3 glass, respectively.

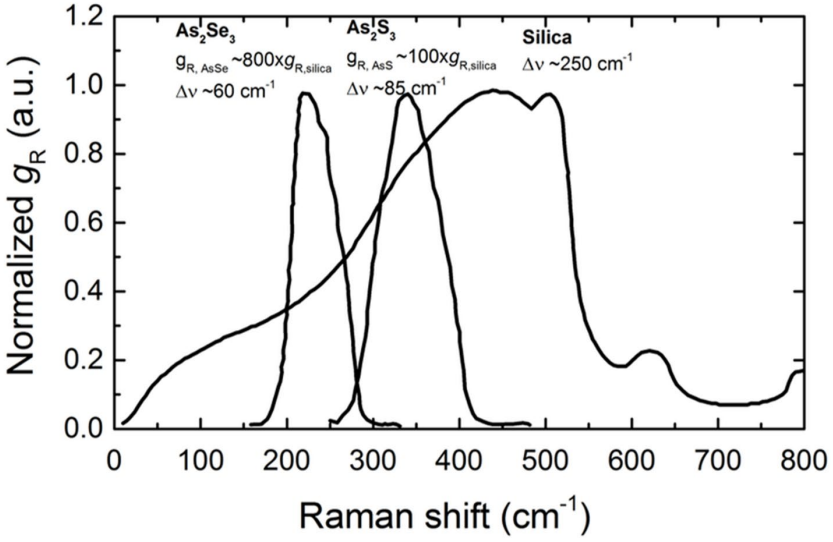

Figure 2.7. Raman gain spectra of silica and chalcogenide glasses (reproduced from [69]).

2.3 Nonlinear Schrödinger equation

Light propagation inside an optical fiber can be described by the wave equation derived from the Maxwell's equation,

$$\nabla^2 \boldsymbol{E} - \frac{1}{c^2}\frac{\partial^2 \boldsymbol{E}}{\partial t^2} = \mu_0 \frac{\partial^2 \boldsymbol{P}_L}{\partial t^2} + \mu_0 \frac{\partial^2 \boldsymbol{P}_{NL}}{\partial t^2} \tag{2.13}$$

Some simplifications are required in order to solve equation 2.13. First, P_{NL} is treated as a small perturbation compared to P_L. Additionally, the pulse is assumed to be quasi-monochromatic that maintains its polarization throughout the entire length of the propagation. In this slowly varying envelope approximation, the rapidly varying part is separated and the electric field is expressed as,

$$\boldsymbol{E}(\boldsymbol{r}, t) = \frac{1}{2}\hat{x}[E(\boldsymbol{r}, t)e^{-i\omega 0t} + c.c] \tag{2.14}$$

where, ω_0 is the center frequency of the pulse, and $\hat{x}$ is the polarization unit vector. Considerable simplification occurs if the nonlinear polarization, P_{NL} is assumed to be instantaneous. This assumption is valid when the propagating optical pulse is temporally wider than the time scale Raman response of the fiber. For ChG fiber Raman response occurs over a time scale of ~1 ps, whereas it is ~0.1 ps for fused silica [70]. Therefore slowly varying nonlinear polarization takes the following form,

$$P_{NL}(\boldsymbol{r},t) = \varepsilon_0 \frac{3}{4}\chi^{(3)}_{\chi\chi\chi\chi}|E(\boldsymbol{r},t)|^2 E(\boldsymbol{r},t) = \varepsilon_0 \varepsilon_{NL} E(\boldsymbol{r},t) \tag{2.15}$$

where, $\frac{3}{4}\chi^{(3)}_{\chi\chi\chi\chi}|E(\boldsymbol{r},t)|^2$ indicates the nonlinear contribution to the dielectric constant. It should be noted that in the derivation of P_{NL}, the term related to the third-harmonic generation is neglected since this process requires special phase matching in the optical fiber. To solve wave equation of the slowly varying amplitude *E(r,t)*, its Fourier transform is substituted in equation 2.13 and the corresponding Helmholtz equation 2.16 is derived. The dielectric constant is found to be related to the refractive index and the absorption coefficient as.

$$\nabla^2 \tilde{E} + \varepsilon(\omega) k_0^2 \tilde{E} = 0 \tag{2.16}$$

$$\varepsilon(\omega) = 1 + \tilde{\chi}^{(1)}(\omega) + \varepsilon_{NL} \tag{2.17}$$

The intensity dependent refractive index and absorption coefficient are introduced as

$$\tilde{n} = n + n_2|E|^2, \quad \tilde{\alpha} = \alpha + \alpha_2|E|^2 \tag{2.18}$$

where, n_2 and α_2 are defined by equation 2.8 and 2.9. From the wave equation in 2.16, the propagation equation for the slowly varying envelope is derived, known as nonlinear Schrödinger equation. In the following part, the derivation is briefly presented, but a more detailed explanation can found in the textbook of Agrawal [45]. The electric field in equation 2.14 can be represented with a separation ansatz, where *A(z,t)* is the slowly varying function, *F(x,y)* is the radial field distribution and β_0 is the propagation constant at the center frequency.

$$\boldsymbol{E}(\boldsymbol{r},t) = \frac{1}{2}\{F(x,y)A(z,t)\exp[i(\beta_0 z - \omega_0 t)] + c.c\}\hat{x} \tag{2.19}$$

Using this and equation 2.16, the following equations are derived under slowing varying envelope approximation,

$$\frac{\partial^2 F}{\partial x^2} + \frac{\partial^2 F}{\partial y^2} + \left[\varepsilon(\omega)k_0^2 - \tilde{\beta}^2\right]F = 0 \tag{2.20}$$

$$\frac{\partial \tilde{A}}{\partial z} - j\left(\tilde{\beta} - \beta_0\right)\tilde{A} = 0 \tag{2.21}$$

In the first order perturbation theory, *F(x,y)* remains unaffected, whereas the eigenvalue $\tilde{\beta}$ becomes modified by the nonlinearity to $\tilde{\beta}(\omega) = \beta(\omega) + \Delta\beta(\omega)$. Both $\beta(\omega)$ and $\Delta\beta(\omega)$ are

expanded in Taylor series about the central frequency, and coefficients up to second and zeroth order are considered, respectively. This results into a new pulse propagation equation, the nonlinear Schrödinger equation (NLSE) that governs both the linear and nonlinear propagation dynamics in an optical fiber, taking the following form,

$$\frac{\partial A}{\partial z} + \beta_1 \frac{\partial A}{\partial t} + i\frac{\beta_2}{2}\frac{\partial^2 A}{\partial t^2} + \frac{\alpha}{2}A = i\gamma(\omega_0)|A|^2 A \tag{2.22}$$

A new nonlinear parameter known as the waveguide nonlinearity is defined as

$$\gamma(\omega_0) = \frac{\omega_0 n_{2I}}{cA_{eff}} \tag{2.23}$$

where, A_{eff} is the effective area of the fundamental mode, expressed as

$$A_{eff} = \frac{(\iint_{-\infty}^{+\infty}|F(x,y)|^2 dxdy)^2}{\iint_{-\infty}^{+\infty}|F(x,y)|^4 dxdy} \tag{2.24}$$

The right side of the equation 2.23 indicate that a strong nonlinear contribution can be obtained either by material of large nonlinear refractive index, n_{2I} or by a small fiber geometry. Nonlinear refractive index n_{2I} and n_2 in eqn. 2.8 are connected as, $n_{2I} = 2n_2/\varepsilon_0 nc$. Dispersion effects are included by two dispersion coefficients β_1 and β_2 obtained from equation 2.3 and 2.4. The linear fiber losses accounted for by the absorption coefficient α, but the nonlinear losses are ignored.

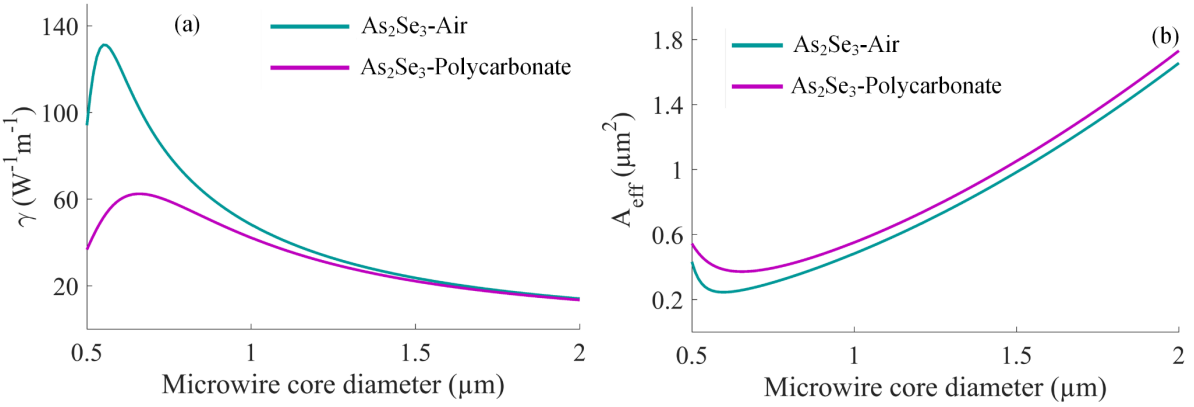

Figure 2.8. (a) Waveguide nonlinearity and (b) effective mode area of As_2Se_3 at 1.95 μm wavelength, calculated as a function of microwire diameters.

Fig. 2.8 shows the calculated values of γ and A_{eff} at a pump wavelength of 1.95 μm for both air and polycarbonate cladded As_2Se_3 microwire. Stronger confinement in the air cladding allows

twice as high nonlinearly in comparison to the polymer cladded microwire, whereas this nonlinearity becomes four orders of magnitude higher than that of silica fiber. As a result, ChG microwires generates nonlinear effects in a cm long propagation length at picojoule level pump energy, which allow the design of ultra-compact, low dimension and low power consuming nonlinear systems.

2.3.1 Self-phase and Cross-phase modulation

An optical pulse propagating in the nonlinear fiber experiences a self-induced phase shift due to the intensity dependent refractive index. This effect, known as the self-phase modulation (SPM) is responsible for the generation of new spectral component. A general description of SPM requires the numerical solution of the NLSE derived in equation 2.22. However, a simplistic analytical solution can be obtained by considering only the electronic contribution and neglecting the effects of both dispersion and absorption. The NLSE can be written as,

$$\frac{\partial A}{\partial z} = i\gamma|A|^2 A \tag{2.25}$$

The general solution is

$$A(z,T) = A(0,T)\exp\left(i\Phi_{NL}(z,T)\right) \tag{2.26}$$

With the intensity dependent phase shift Φ_{NL} defined as,

$$\Phi_{NL}(z,T) = |A(0,T)|^2 \frac{L_{eff}}{L_{NL}} \tag{2.27}$$

where, $L_{eff} = (1 - \exp(-\alpha L))/\alpha$ and $L_{NL} = 1/\gamma P_0$ are the effective and nonlinear length, respectively, P_0 being the peak power of the pulse. The time dependence of this phase shift leads to the instantaneous frequency shift of the pulse, which is understood as

$$\delta\omega(T) = -\frac{\partial \Phi_{NL}}{\partial T} \tag{2.28}$$

The time-dependent frequency chirp induces a red shift ($\delta\omega < 0$) near the leading edge of the pulse and a blue shift ($\delta\omega > 0$) near the trailing edge of the pulse. Fig. 2.9 shows the spectral evolution of an initial unchirped pulse that encounters spectral broadening as it propagates down the optical fiber.

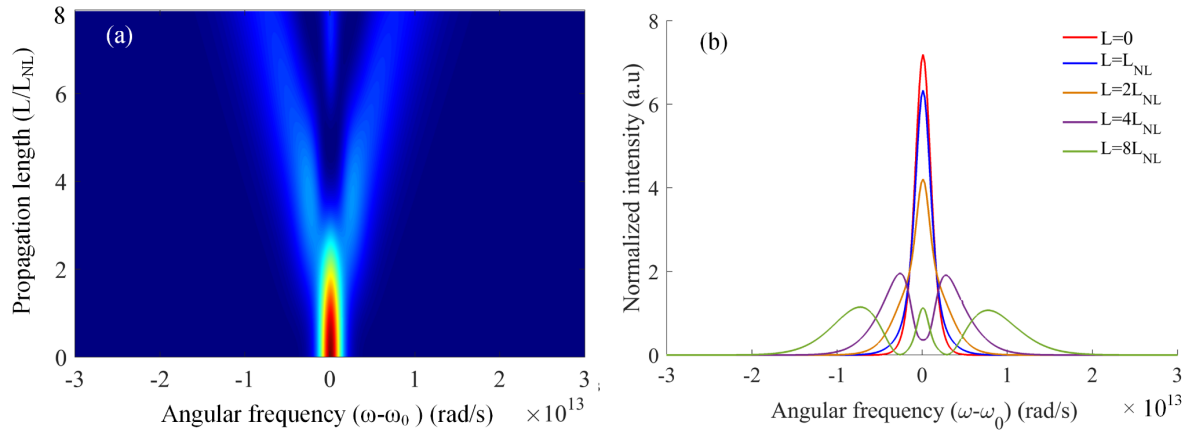

Figure 2.9. Illustration of (a) the spectral evolution and (b) the spectra of SPM induced broadening with increasing propagation length from z=0 to z=8L_{NL}.

Cross phase modulation (XPM) refers to the nonlinear phase shift that occurs due to the interaction of pulses that are overlapping in time. For two co-propagating optical field, the XPM is modeled by the coupled NLSE,

$$\frac{\partial A_1}{\partial z} + \beta_1 \frac{\partial A_1}{\partial t} + i\frac{\beta_{21}}{2}\frac{\partial^2 A_1}{\partial t^2} = i\gamma_1(|A_1|^2 + 2|A_2|^2)A_1 \tag{2.29}$$

$$\frac{\partial A_2}{\partial z} + \beta_1 \frac{\partial A_2}{\partial t} + i\frac{\beta_{22}}{2}\frac{\partial^2 A_2}{\partial t^2} = i\gamma_2(|A_2|^2 + 2|A_1|^2)A_2 \tag{2.30}$$

Equation 2.29 and 2.30 includes the effects of XPM, SPM, and GVD. Two optical fields of different wavelength propagate with unequal group velocity and lead to pulse separation in time, thus limiting the effect of XPM. This effect, known as the walk-off is described by the walk-off length and defined in the following manner for an optical pulse of width T_0,

$$L_W = T_0/|d_{12}| = T_0/|1/v_{g1} - 1/v_{g2}| \tag{2.31}$$

2.3.2 Generalized nonlinear Schrödinger equation

The NLSE derived in the previous section only takes into account the effects of SPM and XPM through the instantaneous electronic contributions. There are additional nonlinear effects related to the delayed nuclear contributions that can superimpose and modify behavior of SPM induced spectral broadening. Such contribution becomes significant for highly nonlinear fibers pumped with ultrashort pulses in the sub-picosecond regime, thereby requires the modification of pulse propagation equation 2.22.

Taking into account the retarded effects through the nonlinear response function introduced in section 2.2.2, the nonlinear polarization takes the form,

$$P_{NL}(\boldsymbol{r},t) = \frac{3\varepsilon_0}{4}\chi^{(3)}_{xxxx}E(\boldsymbol{r},t)\int_0^\infty R(t')\,|E(r,t-t')|^2dt' \tag{2.32}$$

This equation illustrates the temporal dynamics of the intensity dependent polarization in the molecules, resulting from an intense optical pulse propagation in the fiber. Taking into account the frequency dependence of γ and α, as well as the higher-order terms of the propagation constant, the following generalized pulse propagation equation is obtained.

$$\begin{aligned}\frac{\partial A}{\partial z} + \frac{1}{2}\left(\alpha(\omega_0) + i\alpha_1\frac{\partial}{\partial t}\right)A - i\sum_{n=1}^{\infty}\frac{i^n\beta_n}{n!}\frac{\partial^n A}{\partial t^n} \\ = i(\gamma(\omega_0) + i\gamma_1\frac{\partial}{\partial t})(A(z,t)\int_0^\infty R(t')|A(z,t-t'|^2dt'))\end{aligned} \tag{2.33}$$

The equation is valid for pulses as short as a few optical cycles as long as enough higher-order dispersion terms are included. The frequency dependence of both n_{2I} and A_{eff} are included in $\gamma_1 = (\partial\gamma/\partial\omega)_{\omega=\omega_0}$ where the ratio γ_1/γ is expressed as follows,

$$\frac{\gamma_1(\omega_0)}{\gamma(\omega_0)} = \frac{1}{\omega_0} + \frac{1}{n_2}(\frac{dn_2}{d\omega})_{\omega=\omega_0} - \frac{1}{A_{eff}}(\frac{dA_{eff}}{d\omega})_{\omega=\omega_0} \tag{2.34}$$

The first term is the most dominant one and responsible for the intensity dependence of the group velocity, known as the self-steeping effect. The rest of the terms are only important when generating supercontinuum of ultra-broad spectral width.

2.3.3 Split-step Fourier method

The GNLSE is a partial differential equation that does not generally have analytical solution, rather it is solved numerically using split-step Fourier method (SSFM). The GNLSE can be rewritten in the following manner by considering a reference time frame that moves along with the pulse at a group velocity v_g, and obtained by the transformation, $T = t - z/v_g$,

$$\frac{\partial A}{\partial z} = (\widehat{D} + \widehat{N})A \tag{2.35}$$

where, $\widehat{D}$ is the dispersion operator that takes into account of the linear propagation characteristics, i.e. the dispersion and the losses, while $\widehat{N}$ is the nonlinear operator that governs the nonlinear effects during pulse propagation.

$$\widehat{D} = -\sum_{m=2}^{M} i^{m-1} \frac{\beta_m}{m!} \frac{\partial^m}{\partial T^m} - \frac{\alpha}{2} \tag{2.36}$$

$$\widehat{N} = i(\gamma(\omega_0) + i\gamma_1 \frac{\partial}{\partial T}) \int_0^{\infty} R(t')|A(z, T - t'|^2 dt'))$$

In SSFM, the total propagation length is divided into small segments *h* and in each segment an approximate solution of equation 2.35 is obtained by treating the dispersion and nonlinearity independently. In the first step, nonlinearity acts alone, and $\widehat{D}$ is set to zero whereas, in the second step $\widehat{N} = 0$ and dispersion acts alone. This process is schematized in fig. 2.10.

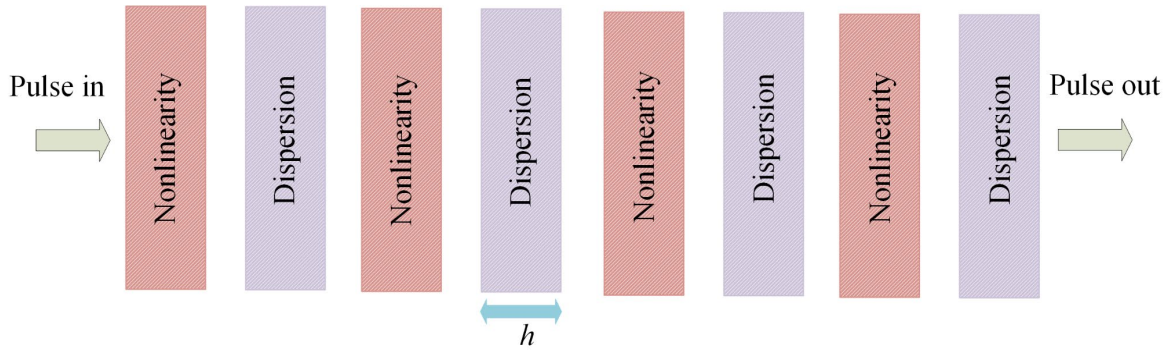

Figure 2.10. Schematics of SSFM.

2.4 Soliton and solitonic effects

When an optical pulse propagates in a fiber characterized by anomalous GVD, it experiences linear chirp from the GVD and nonlinear chirp from the effect of SPM that act together to yield a pulse of stable or periodically evolving temporal and spectral profile. Such nonlinear waves are know as the optical solitons. Solitary waves were first discovered in 1834 by S. Russell in the form of water waves and later on, the conceptual formation of solitons in optical fiber were presented in 1973 by A. Hasegawa *et al.* [71] and experimentally demonstrated by L. F. Mollenauer *et al.* in 1980 [72]. In the absence of strong perturbation effects, the GNLSE can be analytically solved using inverse scattering method, resulting in *sech* solution of the optical solitons. The condition of soliton formation in a optical fiber is related to both the fiber and

input pulse parameters through the relation of soliton number, $N^2 = L_D/L_{NL}$, where $L_D = T_0^2/|\beta_2|$ and $L_{NL} = 1/\gamma P_0$, are the characteristic dispersion and nonlinear lengths, respectively. T_0 and P_0 are the input pump pulse duration and peak power, respectively. The fundamental soliton is represented by $N=1$ and known to be exceptionally stable that maintains its spectral and temporal shape during the propagation in the fiber. For a soliton number between 0.5 to 1.5, the input pulse automatically adjusts its shape, disperse excessive energy and evolves into a fundamental soliton. The solutions that corresponds to $N \geq 2$ are known as the higher-order solitons. These solitons corresponds to a bound state superposition of N fundamental solitons that propagates together at equal group velocity. The duration and peak power of these fundamental solitons are expressed as,

$$P_k = \frac{(2N+1-2k)^2}{N^2} P_0$$
$$T_k = \frac{T_0}{2N+1-2k} \tag{2.37}$$

where, k varies from 1 to N. The higher-order solitons undergo periodic spectral and temporal evolution during its propagation in the fiber, as shown in fig 2.11.

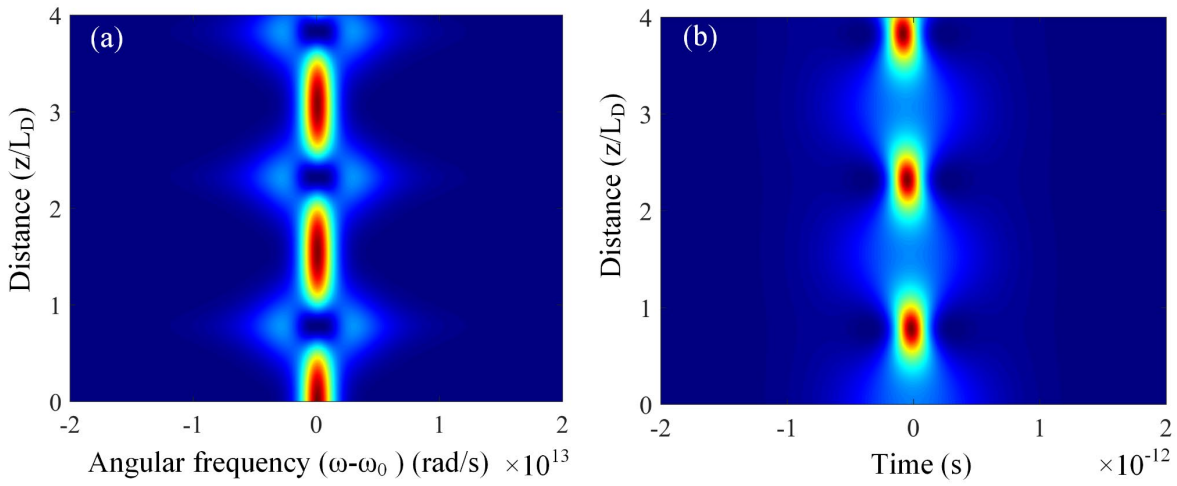

Figure 2.11. (a) Spectral and (b) temporal evolution of second-order soliton over four soliton periods.

However, in the femtosecond regime, due to the presence of asymmetric perturbations, including higher-order dispersion, self-steepening and Raman effect, the degeneracy of the soliton bound state is lifted. Therefore, the higher-order soliton deviates from its ideal periodic behavior, resulting into a pulse breakup to a series of low amplitude fundamental solitons. This phenomenon is known as the soliton fission process. The propagation distance at which fission

occurs correspond to the point where the evolving pulse reaches the maximum bandwidth. This length is know as the fission length and expressed as, $L_{fiss} \sim L_D/N$.

After fission the generated fundamental solitons can be as short as femtosecond. For solitons of such short duration, the spectral bandwidth is sufficiently broad for the high frequency components to amplify the low frequency components through Raman scattering. This intrapulse Raman scattering process continuously transfers energy from the blue to the red edge of the soliton, resulting into a spectral shift of the soliton towards the longer wavelength. This phenomenon is known as the SSFS. The first ejected soliton (k=1 in equation 2.37) in the fission process has the highest peak power and shortest pulse duration, thereby experiences the maximum red shift, whereas the spectral shift of the following solitons will slow down and form a spectral continuum. The spectral shift due to SSFS is has a linear relation with the propagation distance, expressed as the following,

$$\Omega(z) \propto -\frac{|\beta_2|}{T_0^4} z \tag{2.38}$$

This linear relationship remains valid only for the early stages of the soliton evolution. The saturation in the spectral shift occurs due to the continuous chirping and subsequent temporal broadening of the soliton, resulting from the effect of third-order dispersion. Fig 2.12 shows the spectral and temporal evolution of higher-order soliton as it undergoes soliton fission and the SSFS process. The shortest soliton created after the fission process separates from the main part of the pulse and continuously delayed as it propagates down the fiber. This declaration occurs due to the continuous frequency shift of the soliton toward longer wavelength, where the GVD increases.

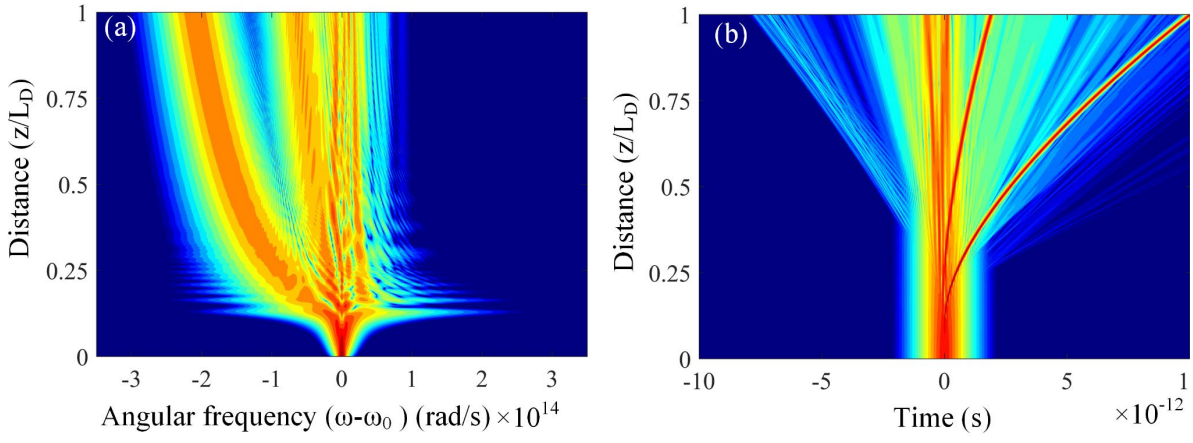

Figure 2.12. (a) Spectral and (b) temporal evolution showing soliton fission and SSFS process.

In the presence of higher-order dispersion, a soliton propagating close to ZDW can transfer a portion of its energy to normal GVD regime to generate dispersive wave (DW), also known as Cherenkov or nonsolitonic radiation. DW is emitted at frequency at which it is phase velocity matched with the soliton. This resonance frequency can be calculated by a simple phase-matching argument given as,

$$\frac{\beta_2\Omega^2}{2}+\frac{\beta_3\Omega^3}{6}+\frac{\beta_4\Omega^4}{24}=\delta\beta_1\Omega+\frac{\gamma P_0}{2} \tag{2.39}$$

where, $\delta\beta_1$ takes into account the change in the soliton's group velocity that might occur after fission, and P_0 is the power of the soliton after fission. The frequency shift between the soliton and the DW, $\Omega=\omega_s-\omega_{DW}$ can be approximated as, $\Omega=-\frac{3\beta_2}{\beta_3}+\frac{\gamma P_0\beta_3}{3\beta_2^2}$.

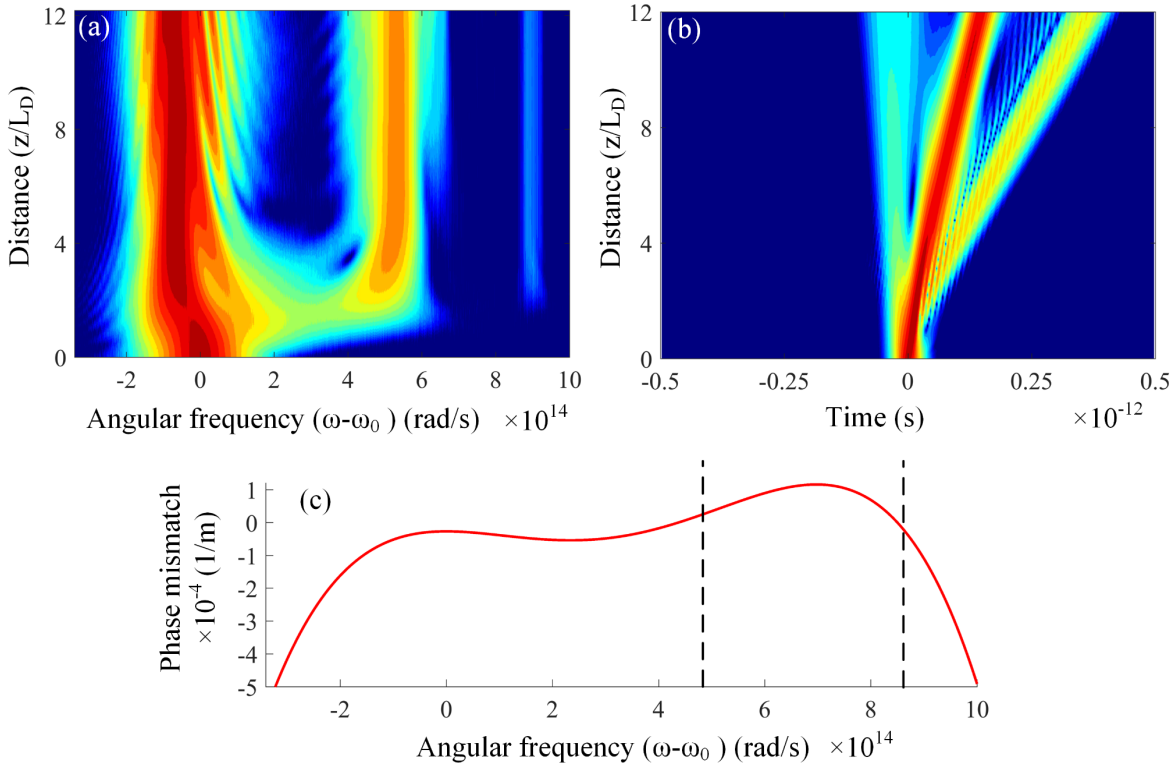

Figure 2.13 (a) Spectral and (b) temporal evolution of a propagating soliton generating DW. (c) The DW phase matching diagram, calculated from equation 2.39. The vertical lines indicate the DW generation frequencies i.e the frequencies at which the phase mismatch becomes zero.

Fig. 2.13 shows the DW generation process of a fundamental soliton. The soliton is propagating in a region of positive dispersion slope (β_3>0), which indicates a positive frequency shift of the DW. This means that the DW is generated in the normal GVD regime i.e the higher frequency side of the spectrum, as seen in fig. 2.13 (a). Fig. 2.13 (b) shows that immediately after

generation, the blue shifted DW rapidly separates from the pump and gradually slows down. This behavior occurs due to the large group velocity mismatch between both pulses.

2.5 Four-wave mixing

FWM is a third-order parametric process that involves the interaction among four optical waves of different frequencies. In the case of degenerate FWM, as illustrated in fig. 2.14, two pump photons at ω_p interacts in the nonlinear medium to create two new frequencies, signal (ω_s) and idler (ω_i) such that frequency detuning becomes, $\Omega_{FWM} = \omega_p - \omega_s = \omega_i - \omega_p$. The efficiency of this process depends on the phase-matching condition that requires the frequency and the wave vector matching between the interacting waves, given as,

$$\kappa = 2\gamma P_0 + \Delta\beta \tag{2.40}$$

where, $\Delta\beta$ is the phase mismatch between the pump and signal/idler wavelengths determined by the fiber waveguide dispersion,

$$\Delta\beta = \sum_{m=2}^{M} \frac{2\beta_m}{m!} \Omega_{FWM}^m \tag{2.41}$$

where, m=2, 4, 6….M. Under proper phase-matching condition, parametric gain is expressed as,

$$G = 1 + (\gamma P_0)^2 sinh^2(gL_{eff}) \tag{2.42}$$

with L_{eff} being the effective length of the nonlinear medium and g is the parametric gain coefficient expressed as, $g = \sqrt{(\gamma P_0)^2 - (\kappa/2)^2}$. Peak parametric gain occurs at the angular frequency at which, $\kappa = 0$. By Assuming an identical attenuation and nonlinear coefficient for the pump A_p , the signal A_s, and the idler A_i waves, the FWM process is governed by the coupled wave equations, derived from the NLSE

$$\begin{aligned} \frac{\partial A_p}{\partial z} &= i\gamma\left(|A_p|^2 + 2|A_s|^2 + 2|A_1|^2\right)A_p + 2i\gamma A_p^* A_s A_i \exp(i\Delta\beta z) - \frac{\alpha}{2}A_p \\ \frac{\partial A_s}{\partial z} &= i\gamma\left(2|A_p|^2 + |A_s|^2 + 2|A_1|^2\right)A_s + i\gamma A_p^2 A_i^* \exp(-i\Delta\beta z) - \frac{\alpha}{2}A_s \end{aligned} \tag{2.43}$$

$$\frac{\partial A_i}{\partial z} = i\gamma\left(2|A_p|^2 + 2|A_s|^2 + |A_1|^2\right)A_s + i\gamma A_p^2 A_s^* \exp(-i\Delta\beta z) - \frac{\alpha}{2}A_i$$

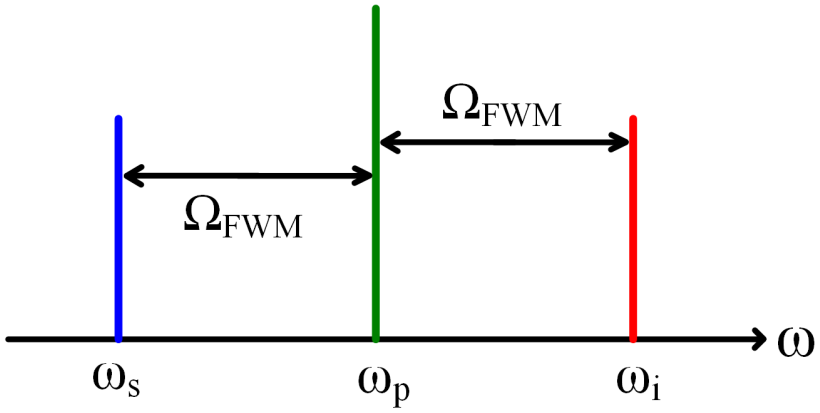

Figure 2.14. Illustration of FWM process where two pump photons at ω_p are annihilated to create a photon at the signal (ω_s) and a photon (ω_i) at the idler frequency.

2.6 Supercontinuum generation

SC generation is a spectral broadening process involving the interplay between dispersion and nonlinear effects that occur during the propagation of an optical pulse in a fiber. The nonlinear mechanisms that contribute to new frequency generation depend on both fiber and pump parameters, i.e. the pulse duration, peak power, fiber GVD and waveguide nonlinearity at the pump wavelength. In anomalous dispersion pumping regime, close to ZDW, soliton dynamics play a vital role in spectral broadening process. The produced spectrum is generally asymmetric towards longer wavelength with a performance depending predominantly on the pump pulse duration [73]. For femtosecond pulse, the pump power is typically high enough to be transformed into higher-order solitons. As it propagates down the fiber, it undergoes soliton evolution dynamics of spectral broadening and temporal compression, leading to pulse breakup though soliton fission, as described in section 2.4. For pulse duration in the range of few hundred femtosecond, the Raman effect acts as the dominant perturbation, whereas for ultrashort pulses of tens of femtosecond, third-order dispersion initiates soliton fission. The fundamental solitons created by this fission process shed radiation via the generation of dispersive waves in the normal dispersion region of the fiber, while experiencing continuous red shift towards longer wavelength due to SSFS. The temporal overlap between the Raman shifted solitons and the DWs interact through XPM and FWM that lead to further generation of

new frequency components [74], [75]. Since the soliton fission process is not noise driven, the generated SC generally has high shot-to-shot stability. Temporal coherence can be increased by pumping a relatively short highly nonlinear fiber with ultra-short pulses. In contrast, the temporal coherence can deteriorate when SC is generated by pumping with long pulses in tens of picosecond duration. The reason behind this is the initial spectral broadening mechanism. For long pulses, the fission length increases with propagation and therefore the effect of modulation instability (MI) dominates in the initial propagation phase. The MI leads to pulse breakup to multiple sub-pulses which then undergoes the SSFS and DW induced spectral broadening. Since MI is a noise seeded process, the SC shows low shot to shot stability. SCs generated in this process is useful for fluctuation insensitive applications e.g imaging, spectroscopy, sensing and breath analysis. The recent development in long pulse SC development has showed that the expensive femtosecond mode-locked lasers are no longer not required for ultra-broad, multi octave SC generation [76].

In the normal dispersion regime, femtosecond pump pulse produce spectral broadening that is mainly dominated by SPM, and results in a symmetric spectral properties. Whereas, for long pulse, spectral broadening develops from FWM and Raman scattering process. Deep inside the normal dispersion region, Raman scattering is more dominant since the FWM phase matching is only far-detuned. Closer to the ZDW, parametric sidebands move closer to the pump and become progressively dominant. During broadening, spectral components are also transferred towards the anomalous dispersion regime, where the soliton dynamics contributes further. For both cases, the propagating pulse experiences a normal dispersion induced temporal broadening and the conversion efficiency (CE) decreases accordingly. SC generated in this process possess high temporal coherence and shot to shot stability that find use in applications e.g frequency metrology [77].

3 *In situ* fabrication of far-detuned mid-infrared wavelength converters

This chapter describes an *in situ* approach for the fabrication of all-fiber wavelength converters with a wavelength offset that is both far-detuned and precisely engineered. The wavelength converters are fabricated using the parametric gain of A_2Se_3 microwires and finely tuned from successive adjustments of microwire diameter along with real-time monitoring. Wavelength conversion is achieved from a pump at a wavelength of 1.938 μm to any far-detuned MIR idler within the spectral range of 2.347 - 2.481 μm, resulting into a detuning of 27.0 - 33.9 THz with a wavelength offset precision within 3.1 THz. The results of this chapter has been published in [78]–[81].

3.1 Introduction

In recent years, all-fiber optical sources has become popular due to their in-built advantage of compactness, reliability and mechanical stability. Numerous fiber-based sources have been demonstrated so far, including optical parametric oscillators [82], rare-earth doped fiber lasers [83], [84], supercontinnum sources [85] and wavelength converters based on FWM [86]. As describe in section 2.5, in stimulated FWM process, an optical pump and a shorter wavelength probe signal, both are sent into a nonlinear medium. Two photons from the pump are converted into one photon that produces stimulated amplification at probe wavelength, and one idler photon that completes the energy conservation rule, emitted at a longer wavelength. Since the first demonstration of FWM in 1973 by Stolen *et al.* [87], this wavelength conversion technique has been investigated in different silica fiber profiles with the goal of maximizing both the conversion efficiency (CE) and the frequency detuning. This includes, for example, standard telecom fiber [88], tapered [89] and untapered [90] microstructure fiber and highly nonlinear fiber [91]. While the MIR wavelength is desirable for applications including sensing [7], spectroscopy [92], medical instrumentation [93] and free space communication [94]; the wavelength converters designed for these wavelengths are limited by the low nonlinearity and

large attenuation of silica glass. In all-silica configuration, the longest wavelength converted idler of 2.1 μm wavelength was realized in 350 m long highly nonlinear silica fiber at a average pump power as high as 2.6 W [95].

On the other hand, As_2Se_3 glasses are excellent candidates for the fabrication of MIR sources since their optical transmission spectrum extends to wavelengths up to 12 μm [33] and they possess exceptionally high nonlinear refractive indices (n_2), nearly three orders of magnitude beyond that of silica glass [35], [96]. The tapering of a ChG fiber down into a microwire provides strong light confinement and enhanced nonlinear optical effect [60]. It also allows for engineerable chromatic dispersion and thereby providing an easy access to FWM based wavelength conversion. There has been a number of demonstrations of FWM in ChG microwires [97]–[100], suspended core [101]–[104] and photonic crystal [105]–[107] fibers structures. Ahmad *et al.* demonstrated a FWM bandwidth of 190 nm and a CE of 21 dB in a polymer cladded As_2Se_3 microwire pumped at an anomalous dispersion wavelength of 1.55 μm [98]. Xing *et al.* showed wavelength conversion in $Ge_{10}As_{22}Se_{68}$ photonic crystal microwire, however achieved a relatively narrow bandwidth of 10 nm due to the high normal dispersion at the pump wavelength of 1.95 μm [107]. In contrast to these, the use of normal dispersion that is marginally close to the zero-dispersion leads to a parametric gain far-detuned from the pump wavelength [45]. Li *et al.* demonstrated far-detuned wavelength conversion from pumping at a wavelength of 1.94 μm in the normal dispersion regime of a 10 cm long As_2Se_3 microwire, leading to a frequency detuning up to 49.3 THz [99]. Godin *et al.* demonstrated far-detuned modulation instability from pumping at a wavelength of 2.6 μm in the normal dispersion regime of a 14 cm long As_2Se_3 microwire, leading to ~30 THz of frequency detuning [100]. Saini *et al.* generated a frequency detuning of 84 THz in a 3 cm long As_2S_3 microstructure fiber from a pump wavelength of 2 μm [101]. In FWM processes where the pump and wavelength converted idler are far-detuned by tens of THz, the exact phase matching wavelength is highly sensitive to material and waveguide chromatic dispersion, both data for which the typical precision is limited. Furthermore, during the microwire fabrication process using heat-brush technique, nanoscale fluctuation occurs in the core diameter along the propagation length of the micowire. Chow *et al.* measured a fluctuation of < 5 % from the designed core diameter core of 1.65 μm in a 13 cm long As_2Se_3 microwire using high-resolution distributed Brillouin sensing technique [108]. Such dispersion fluctuations are known to result in a randomly varying parametric gain profile due to the similar random variation in the phase-matching condition [109], [110]. N. Abdukerim numerically investigated the effect of such fluctuation in ChG microwires and

found that the far-detuned gain has a greater sensitivity to such fluctuations, in comparison to the parametric gain generated in the anomalous dispersion microwire [111] (detailed in appendix 10.2). As a result, one can hardly expect to successfully fabricate a far-detuned wavelength converter with predetermined frequency detuning, based solely on chromatic dispersion specifications from the microwire composition and geometry. As an element of solution from previous works, *in situ* tapering has been shown to enable the adjustment of spectral broadening in a SC generation process, thus allowing a fine adjustment of the optimal SC process in real time. [112], [113].

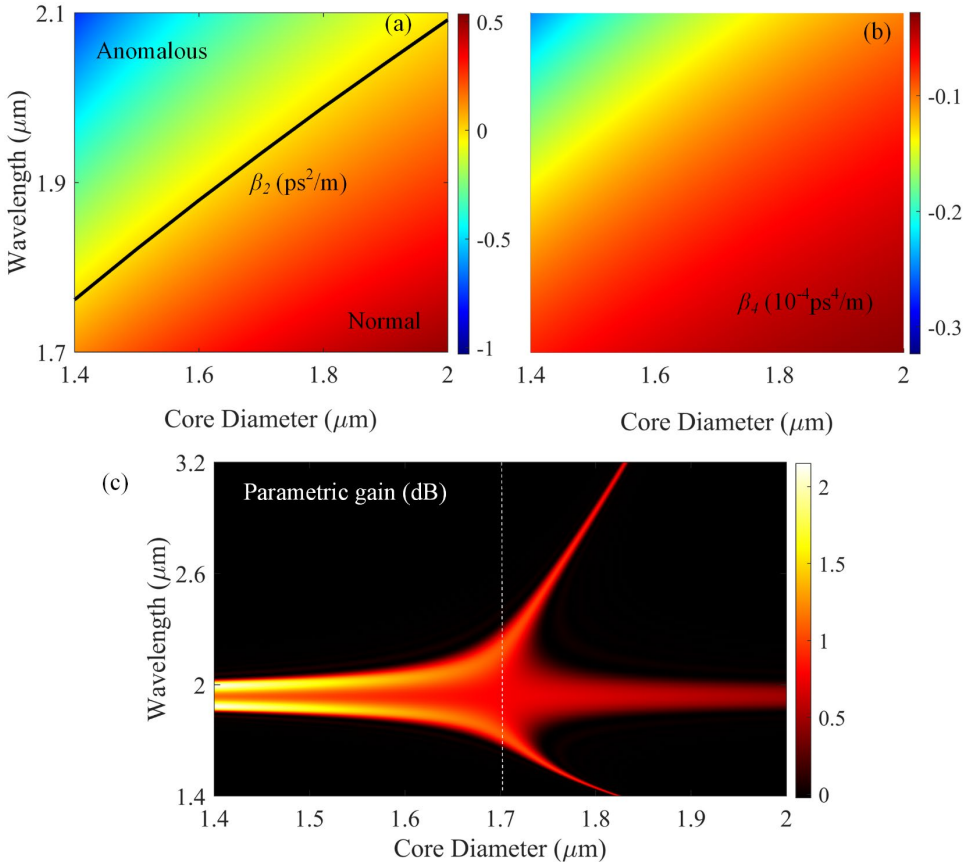

Figure 3.1. (a) β_2 of the As_2Se_3-Air microwire as a function of wavelength and core diameter. The zero dispersion line separates the anomalous and normal dispersion regions. (b) β_4 as a function of wavelength and core diameter. (c) Calculated parametric gain for a 1 cm long microwire as a function of core diameter. The pump power and wavelength is 2.5 W and 1.938 µm, respectively.

This chapter shows that the far-detuned wavelength conversion in a ChG microwire can be precisely attained by *in situ* monitoring of the wavelength converted output while tapering. This experimental result corresponds to the first *in situ* tracking of FWM in optical waveguides, thus enabling the fabrication of high precision, far-detuned wavelength converters.

3.2 Experimental results and discussion

The GVD parameter of the microwire can be engineered into zero, anomalous or normal dispersion at the pump wavelength by choosing an appropriate microwire section diameter. Figure 3.1 (a) and (b) show the calculated second and fourth order dispersion coefficients (β_2 and β_4), respectively, of an As_2Se_3 core surrounded by air for a range of microwire core diameters, determined by solving the characteristic equation of an infinite cladding cylindrical waveguide [114], considering the wavelength dependence of refractive index of As_2Se_3 obtained from the Sellmeier equation given in [55].

Parametric gain builds-up in the microwire section when pump and probe wavelengths satisfy the phase matching condition of degenerate FWM, given by $\Delta k = 2\gamma P_p + \beta_2 \Delta\omega^2 + \left(\frac{\beta_4}{12}\right)\Delta\omega^4$, where γ is the waveguide nonlinearity, P_p the pump peak power, and Δω the frequency detuning from the pump frequency, and β_n is the n-th order chromatic dispersion coefficient [45]. Fig. 3. 1 (c) shows the expected parametric gain for a 1 cm long As_2Se_3-Air microwire with a peak pump power of 2.5 W. Parametric gain was calculated by solving the coupled-wave equation provided by the NLSE for degenerate pump-probe FWM [45], [115] described in section 2.5. The dashed line indicates the zero-dispersion diameter (ZDD) of 1.708 μm. A widely spaced parametric gain is obtained for a core diameter above ZDD.

Figure 3.2 schematizes the experimental setup used to make *in situ* measurement of FWM. The pump is a mode-locked fiber laser emitting pulses with a full-width at half-maximum (FWHM) duration of 800 fs, a repetition rate of 30 MHz, and centered at a wavelength of 1.938 μm. To reduce the impact of group velocity walk-off in between pump, probe and idler pulses, the pump pulses are temporally broadened by passing through 100 m of SMF-28 fiber. The pulses are then amplified with a TDFA and filtered to eliminate the amplified spontaneous emission of the fiber amplifier with a 2 nm FWHM tunable band-pass filter. At this stage, the resulting pump pulses have a FWHM duration of 7 ps, measured from autocorrelation. A continuous wave (CW) laser provides the probe signal, wavelength tunable in the 1.590-1.650 μm range to ensure idler generation up to 2.5 μm. The measured probe signal linewidth is < 0.05 nm, smaller than the resolution bandwidth of the OSA. Polarization controllers ensure that the polarization state of the probe and pump signals are co-aligned. Pump and probe are coupled into the ChG fiber via a wavelength division multiplexer coupler. Output spectra are monitored using an

optical spectrum analyzer while the waveguide is tapered into a microwire. *In situ* monitoring consist of observing the gain spectrum that is far-detuned with respect to the pump wavelength, and eventually interrupting the tapering process when the gain spectrum reaches a target profile.

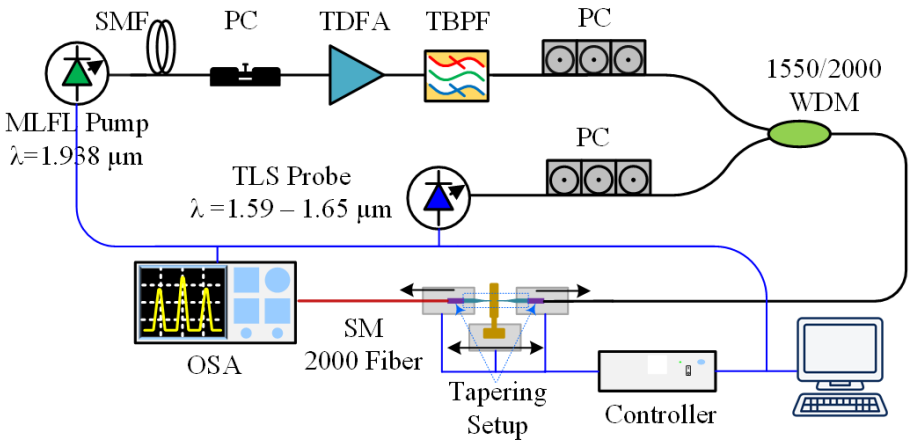

Figure 3.2. Schematics of the experimental setup. MLFL, mode-locked fiber laser; TLS, tunable laser source; SMF, single mode fiber; TDFA, thulium doped fiber amplifier; TBPF, tunable band pass filter; PC, polarization controller; WDM, wavelength division multiplexer; OSA, optical spectrum analyzer.

The ChG fiber used in this experiment is an As_2Se_3 ($n_{As_2Se_3}$=2.81) fiber with core/cladding diameter of 6 μm/167 μm and a numerical aperture of 0.2. The fiber is initially pre-tapered to a cladding diameter of 158 μm to match the mode field distribution of SMF-28 used for input coupling. The input facet of the ChG fiber is polished and coupled to SMF-28 fiber using UV epoxy. The output side is coupled to a 30 cm long SM2000 fiber to minimize the propagation loss at wavelengths > 2.1 μm. The total insertion loss of the SMF-28- ChG fiber-SM2000 assembly at a wavelength of 1.938 μm is 2.2 dB. From this loss, 0.5 dB per interface is due to Fresnel reflection at the ChG-silica interfaces, 0.04 dB/cm of propagation loss in the ChG fiber, and the rest is attributed to misalignment losses, surface roughness, and mode-mismatch of the fibers. The mode mismatch loss is also higher on the output side by 0.5 dB compared to the input side because of the use of SM2000 at that interface.

The initial length of fiber before tapering is 4 cm, of which the 1 cm central portion is subsequently tapered into a microwire of uniform diameter. Tapering is achieved over multiple sweeps of a heating element using a heat brush tapering approach [116]. For each tapering sweep, a translation stage moves a heater while two other stages pull the fiber in opposite

directions. The tapering resolution (Δd_0), defined as the diameter decrease in one single sweep, is determined by the pulling velocity of the drawing stages. In this investigation, both stages move at a constant velocity of 0.5 μm/s, providing a tapering resolution of 8 nm, calculated by the generalized heat brush model. The tapering temperature is maintained at 173±0.1° C during the tapering process. After one complete sweep, the microwire diameter has decreased uniformly and the heater is moved away to the fiber section of the microtaper for optical characterization. At this time, the pump laser is turned on and the probe laser is wavelength tuned. An idler spectrum results from FWM for every wavelength of the probe. In this way, a collection of idler spectra is recorded on the OSA, corresponding to a collection of probe wavelength. Since the probe wavelength is tuned from 1.650 μm to 1.590 μm, the FWM with a pump at a wavelength of 1.938 μm leads to an observable gain spectrum for idler wavelengths comprised in the range of 2.347 μm to 2.481 μm. The average pump power coupled into the microwire section is 0.6 mW, which corresponds to peak power of 2.5 W. The probe power into the microwire section is held constant at 0.97 mW.

In the initial stages of tapering, the microwire has significantly large normal dispersion that prevents the observation of any FWM gain triggered by the pump and probe in the idler observation window of 2.34 - 2.49 μm. As the tapering proceeds, the microwire diameter decreases and eventually provides enough waveguide dispersion to balance material dispersion. Phase matching becomes increasingly satisfied when reaching a diameter ~60 nm above the ZDD. At this point, a tapering loss of 1.5 dB is measured at the pump wavelength and the microwire has transition and microwire sections length of 4.2 cm and 1.0 cm, respectively. This length ensures that the microwire will preserve a uniform diameter without significant fluctuation. The optical mode inside the microwire is tightly guided due to the large refractive index contrast between As_2Se_3 core and air. The microwire has a high waveguide nonlinearity of ~ 17 $W^{-1}m^{-1}$ due to the strong optical confinement and the high nonlinear refractive index of As_2Se_3 ($n_2 = 7.6 \times 10^{-18}$ m^2/W) [117]. Tapering is pursued in this way with sequentially performing heat-brush sweeps followed by characterization steps.

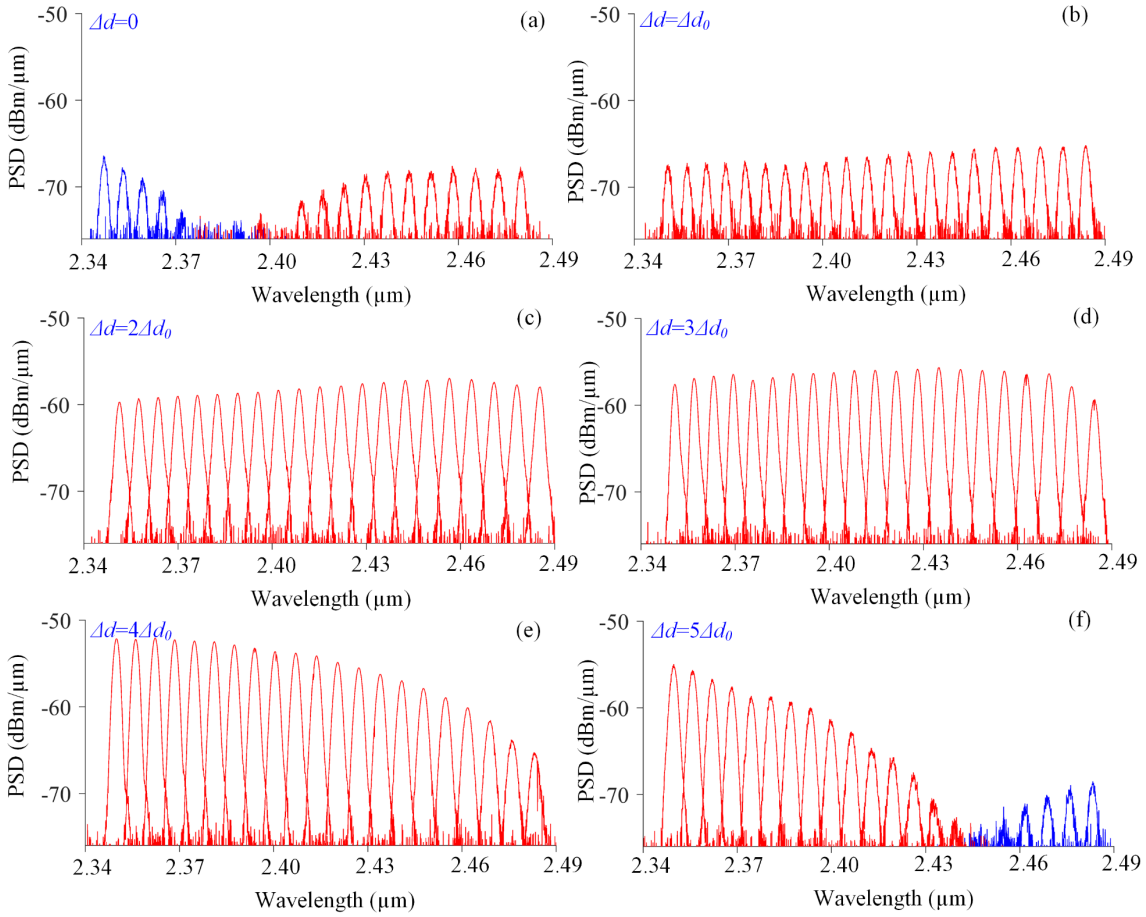

Figure 3.3. (a)-(f) Measured idler spectra at different times of the tapering process as the microwire GVD changes from normal to zero. Red and blue represent the main gain spectrum and the first side lobe respectively. Each spectrum spans over a wavelength range of 2.34 μm to 2.49 μm.

Fig. 3.3 and 3.4 show the recorded idler spectra for an OSA with a dynamic range of > 55 dB and a resolution bandwidth of 2 nm. Δd is defined as $\Delta d = k\Delta d_0$, where k is the number of complete heater sweeps. Initially ($\Delta d = 0$), due to the slight normal dispersion of the microwire, a minimum of the gain spectrum appears at 2.390 μm as seen in fig 3.3 (a). As the tapering proceeds, the microwire diameter decreases by steps of Δd_0 =8 nm for each tapering sweep and the phase matching condition is satisfied at wavelengths increasingly closer to the pump wavelength. As a result, minima and maxima of the gain spectrum gradually shift towards shorter wavelengths (fig. 3.3 (b)-(f)). The far detuned wavelength conversion confirms that the GVD of the microwire is positive and almost near to zero dispersion. The idlers have a FWHM spectral width of 2 nm with a maximum observable frequency detuning of 33.9 THz and an average wavelength offset precision of 3.1 THz in each tapering sweep. Since the length of the microwire is 1 cm, the generated gain spectrum is relatively broad. Further decrease in core

diameter causes the gain spectrum to disappear from the observation window and the first, second and third side lobes to shift towards shorter wavelengths, as observed in figure 3.4 (a)-(e). The idler power can be continuously monitored in this procedure and an optimized power can be used as a criterion to stop the tapering process.

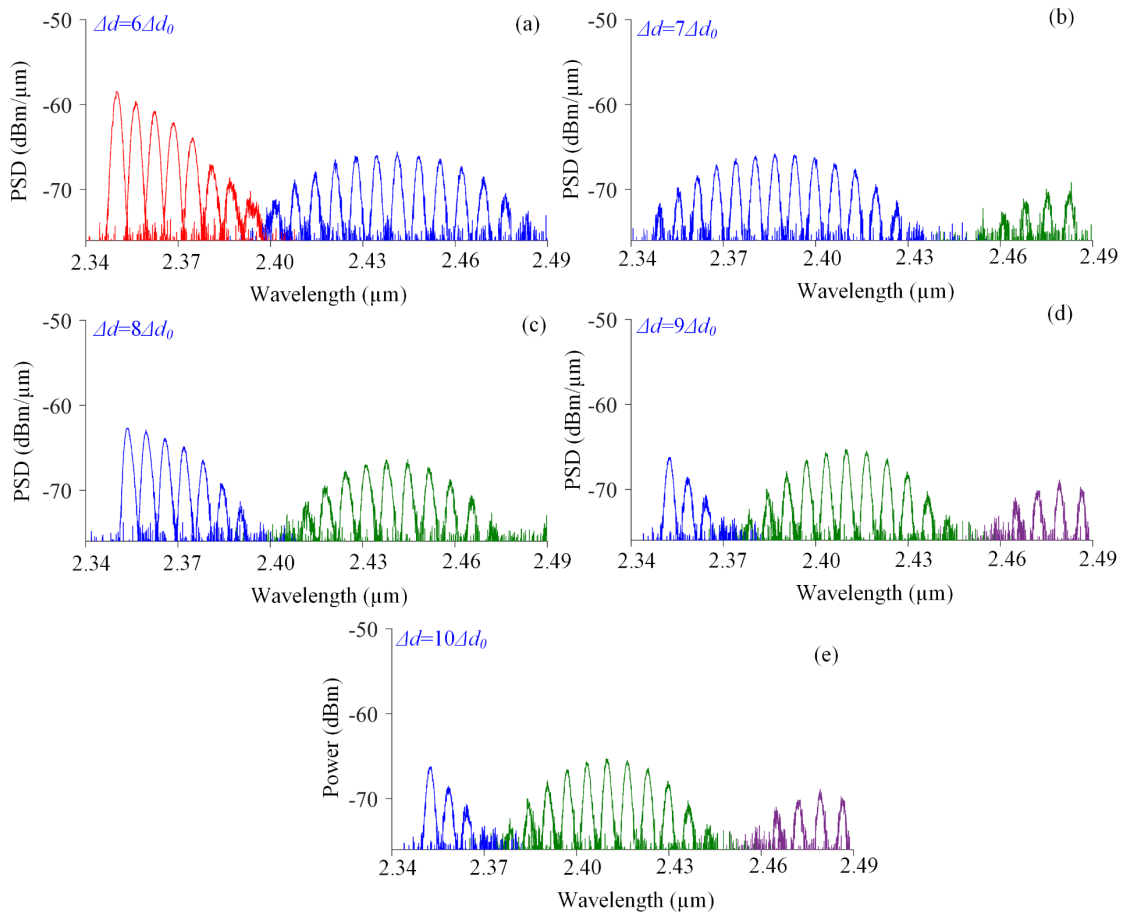

Figure 3.4. (a)-(e) Measured idler spectra at different times of the tapering process as the microwire GVD changes from zero to anomalous. Green and purple represent the second and third side lobe respectively.

The CE, defined as the output idler power over the input probe power, is calculated for each tapering steps. The coupled wave equations described in section 2.5 are used to fit CE data to retrieve the actual microwire parameters. Idler peak power is used to perform the CE measurement, calculated from idler average power and the duty cycle of the pump laser. The calculated walk-off length in between the pump at a wavelength of 1.938 μm and the idler at 2.481 μm is 7.3 cm and the dispersion length is 350 cm for a pulse duration of 7 ps, considerably longer than the physical length of the microwire of 1 cm. It is thus expected that

walk-off is not involved in the wavelength conversion process. The fiber and transition sections of the microtaper have no contribution to the far-detuned parametric gain since the phase matching is only satisfied in the microwire section. Figure 3.5 (a) shows the retrieved GVD as the microwire core diameter decreases, along with a quadratic fit. Throughout the tapering process, the microwire experiences a gradual transition from normal dispersion of 0.0453 ps^2/m to anomalous dispersion of -0.0258 ps^2/m. The average change in GVD in each tapering step is thus ~0.0071 ps^2/m. Such a resolution allows a substantial control over the far detuned parametric gain spectrum in terms of its central wavelength profile. In figure 3.5 (b), CE is plotted as a function of idler wavelength for two successive tapering periods. The value of CE is limited in the lower limit by the detected idler power, hence the level sensitivity of the OSA. The maximum error for the CE is ±0.5 dB, calculated by considering the background noise on the OSA measurements and amplitude jitter of the probe laser. An excellent agreement is found between the experimental results and simulation. The sensitivity of the gain spectrum on the GVD is clearly observed. For instance, the CE of the idler generated at 2.348 µm due the probe at 1.650 µm decreases from a maximum value of -13.8 dB to -16.1 dB as the GVD decreases by only 0.009 ps^2/m. This further corroborates the potential of this approach for the fabrication of highly precise wavelength converters.

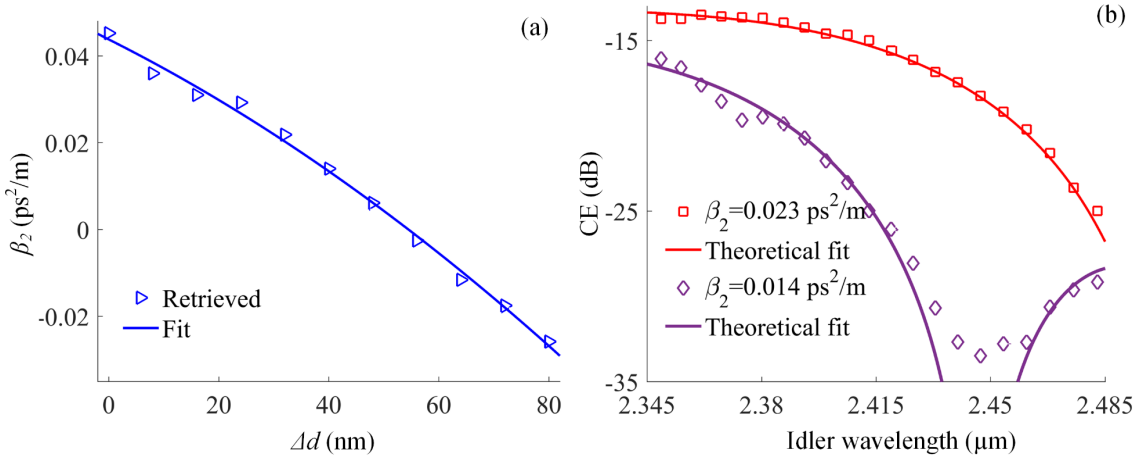

Figure 3.5. (a) Retrieved GVD plotted against Δd. (b) CE versus idler wavelength for two different tapering periods.

To understand the impact of microwire temperature on the gain spectrum, the experiment is also performed as the heater moves along the length of the microwire at tapering temperature, but without moving the drawing stages. Only a certain portion of the microwire section remains

at the tapering temperature at a time, determined by the heater dimension. Fig. 3.6 depicts the measured CE for the static and moving heater for β_2=0.0016 ps^2/m, close to the zero dispersion of the microwire. It is observed that the parametric gain spectrum remains identical with no significant shift in the CE's dip position. This behavior is expected due to the negligible dependence of the As_2Se_3 glass refractive index on temperature. The temperature coefficient of refractive index *dn/dT* of As_2Se_3 glass is estimated from the following equation [118].

$$\frac{dn}{dT} = \frac{n^2 - 1}{2n}\left[2.63 * 10^{-5} + \frac{2.93 * 10^{-5}}{\lambda^2 - 3.15 * 10^{-1}}\right]$$

For the probe, pump and idler wavelength of 1.6 µm, 2 µm and 2.4 µm respectively, the calculated values *dn/dT* are 47.2, 41.7 and 38.8 in ppm/K. The parametric gain however, mainly depends on the chromatic dispersion at the pump wavelength. Therefore, an increase in temperature of 148 °C above the room temperature increases the refractive index at 2 µm wavelength by 0.61 %. Such increase results in a decrease of the ZDD by ~3 nm from 1.708 µm, the ZDD at room temperature. Consequently, the parametric gain spectrum is negligibly affected for a heat zone length of ~3 mm.

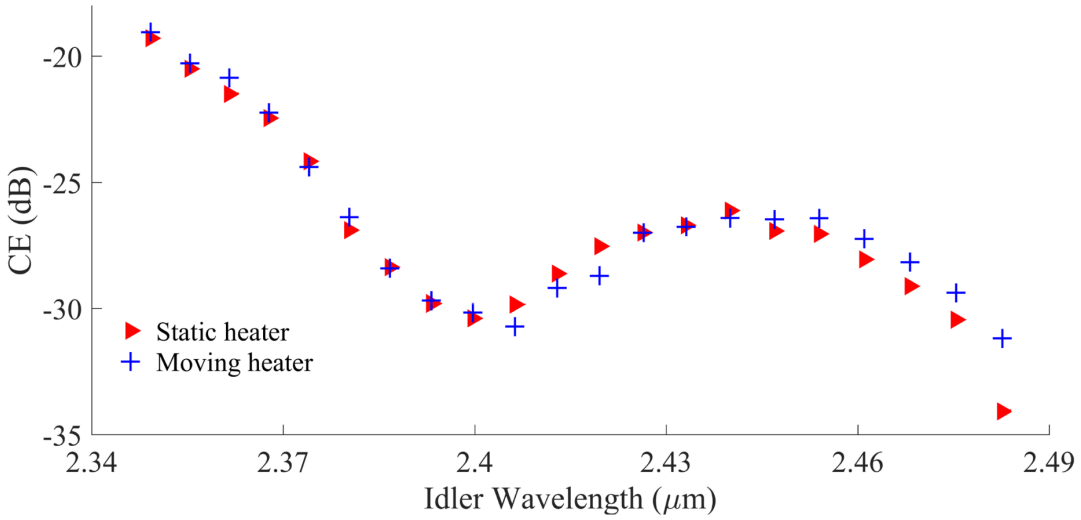

Figure 3.6. CE versus idler wavelength for static and moving heater when GVD is 0.0016 ps^2/m.

The performance of the wavelength converter is also characterized as a function of pump power. Fig. 3.7 (a) shows the CE of the FWM process as a function of peak pump power for a GVD of 0.014 ps^2/m. The probe wavelength is fixed at 1.65 µm and the power is maintained at - 0.13 dBm. The CE follows a quadratic behavior as predicted by theory [98][119]. The

maximum CE obtained is -15.2 dB for a peak pump power of 34.3 dBm, which corresponds to a peak intensity of 230 MW/cm^2. No sign of saturation is observed due to multiphoton absorption or structural damage in the microwire. This indicates that the idler CE could be increased further by increasing the pump power. The idler peak power is also measured as a function of probe power. The probe wavelength is 1.65 μm and the pump power is 33.2 dBm. The linear increase (slope= 1.05) in the idler power with increasing probe further corroborates with the theory.

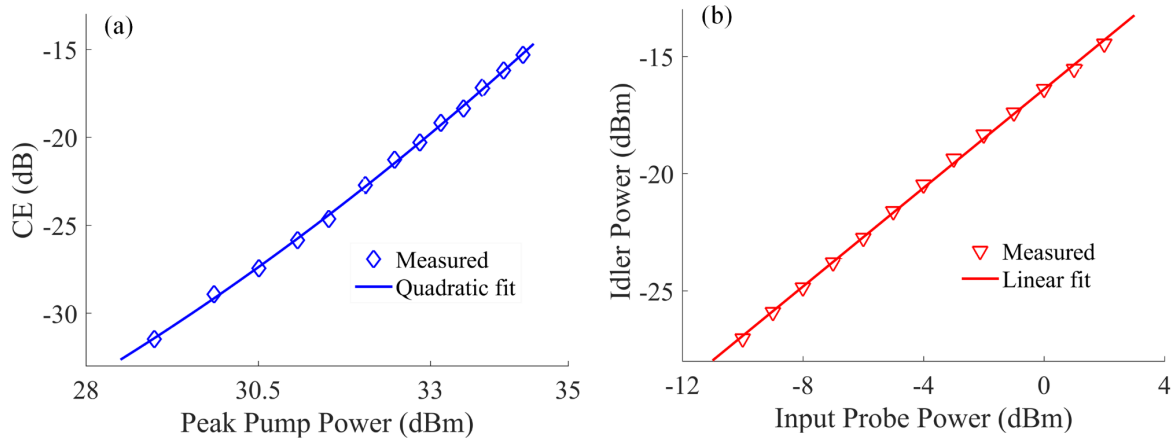

Figure 3.7. (a) The output idler CE as a function of peak pump power for a fixed probe wavelength of 1.65 μm and power of -0.13 dBm. (b) The input probe power versus the output idler peak power at a fixed pump power of 33.2 dBm and probe wavelength of 1.65 μm.

3.3 Summary

In summary, an *in situ* approach for the fabrication of finely tuned and far-detuned wavelength converters has been demonstrated. Parametric conversion was performed while tapering an As_2Se_3 microwire, allowing to obtain an optimum parametric gain at a predefined wavelength. The idlers were generated from 2.347 μm to 2.481 μm in a 1 cm long microwire. A wavelength offset precision of 3.1 THz was obtained. This demonstrates the excellent potential of this *in situ* method for the fabrication of high precision far-detuned wavelength converters.

4 All-fiber nonlinear optical wavelength conversion system from the C-band to the MIR

This chapter describes an all-fiber wavelength conversion system from the C-band to the wavelength range of 2.30-2.64 μm of the MIR. A series of nonlinear processes are used to perform this spectral shift in excess of 80 THz: From optical pulses in the C-band, SPM spectral broadening and offset filtering generate probe pulses in the C and L-band. In parallel to this, Raman-induced SSFS converts pulses from the C-band into pump pulses in the 2 μm wavelength band. The resulting synchronized probe and pump pulses interact via degenerate FWM to produce wavelength-converted idler pulses in the MIR. Silica fiber is used for nonlinear processes at wavelengths < 2 μm whereas ChG glass is used for nonlinear processes at wavelengths ≥ 2 μm. The results of this chapter has been published in [120], [121].

4.1 Introduction

ChG microwires, as highlighted in section 2.1, make excellent candidate for MIR sources due to their extended optical transmission, enhanced optical nonlinearity and engineerable chromatic dispersion. There has been a few demonstration of such microwire based MIR sources that includes supercontinuum sources [122], Raman lasers [123] and parametric wavelength converters [101]. Among these, far-detuned parametric FWM is an interesting approach for MIR light generation thanks to its precise and controlled frequency conversion in specific spectral regions, as shown is chapter 3. One clear distinction of FWM over supercontinuum generation is that wavelength conversion via FWM is performed toward a narrow, specific set of wavelengths, thus providing advantages in terms of power spectral density and power conversion efficiency. Using an As_2Se_3 microwire, Godin *et al.* demonstrated modulation instability in normal dispersion and frequency detuning of 30 THz by pumping at

a wavelength of 2.60 µm [100]. Li *et al.* developed ChG microwires to demonstrate frequency conversion up to 49.3 THz from a pump wavelength of 1.938 µm [99].

In general, wavelength conversion from the C-band is desirable because of the technological maturity, compactness, robustness, and low-cost of erbium-doped fiber lasers. However, wavelength conversion from the C-band to the MIR should also be performed by avoiding two-photon absorption (TPA) in As_2Se_3 glass and ensure a good power conversion efficiency [38]. Wavelength conversion from the C-band to the MIR has been demonstrated using silicon waveguides [124], [125]. In one report, pump and probe intermediate signals in the thulium band were generated from C and O-band lasers, leading to tunable wavelength conversion from 2.056 to 2.152 µm [124]. In a second report, discrete wavelength tunability in the range of 2.60-3.60 µm was performed by permutation of distinct engineered planar waveguides, leading to a frequency conversion up to 100 THz in a hybrid fiber/free space system [125].

In this chapter, an all-fiber wavelength conversion system is reported that leads to the generation of MIR light tunable in the wavelength range of 2.300 µm to 2.640 µm by using only one laser from the C-band. Within the wavelength conversion system, a pump that is tunable in the wavelength range of 1.840-1.950 µm and a probe that is tunable in the wavelength range of 1.550-1.660 µm are generated from a common erbium-doped fiber laser. The pump arises from Raman-induced SSFS whereas the probe signal arises from SPM and offset filtering. The synchronized pump and probe are then combined in a ChG microwire to generate a wavelength-converted signal from degenerate FWM, tunable in the spectral range of 2.300-2.640 µm. The resulting spectral shift totalizes 80 THz while avoiding the effects of TPA in ChG glass. To the best of our knowledge, this experimental result corresponds to the first fiber-based C-band to MIR wavelength conversion. This is a major step towards the development of compact MIR optical sources generated from widespread pump lasers of the C-band.

4.2 Experimental setup

Figure 4.1 schematizes the wavelength conversion system. Seed pulses with a duration of 550 fs are launched from a mode locked erbium-doped fiber laser at a repetition rate of 20 MHz. The central wavelength and the average power of the laser are 1.550 µm and 3.7 mW, respectively. Pulses are split into two branches of a 90/10 fiber coupler. One branch serves for pump

generation (lower branch, 90 %), whereas the other branch serves for probe signal generation (upper branch, 10).

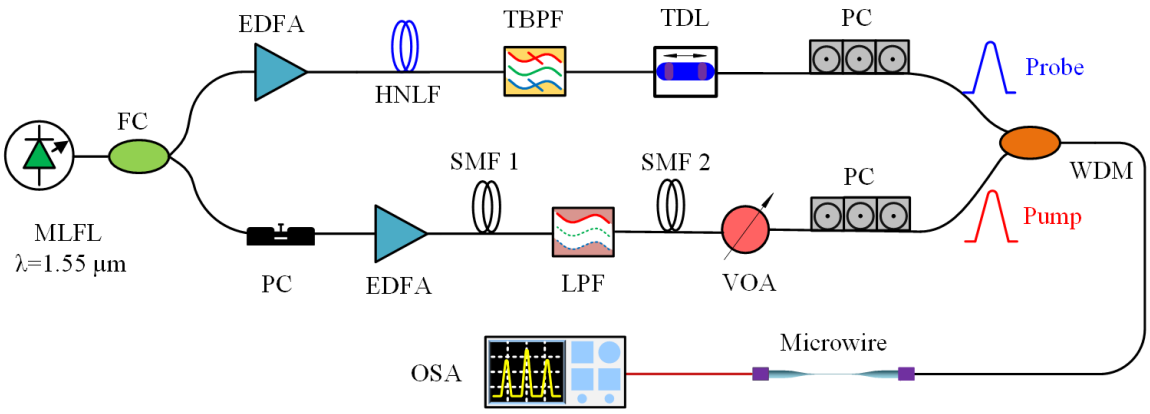

Figure 4.1 Schematics of the experimental setup. MLFL, mode-locked fiber laser; FC, fiber coupler; HLNF, highly nonlinear fiber; TBPF, tunable band-pass filter; EDFA, erbium-doped fiber amplifier; SMF, single-mode fiber; LPF, long-pass filter; TDL, tunable delay line; VOA, variable optical attenuator; PC, polarization controller; WDM, wavelength division multiplexer; OSA, optical spectrum analyzer.

4.2.1 Pump pulse generation by SSFS

In the pump (lower) branch, seed pulses are amplified with an erbium-doped fiber amplifier (EDFA) with a residual normal dispersion of 35 fs/nm. After amplification, Raman-induced SSFS occurs in a 30 m long SMF fiber (SMF 1). The wavelength of the frequency-shifted solitons is tuned by adjustment of the EDFA gain as shown in fig 4.2 (a). The resulting pump pulses are tunable within the wavelength range of 1.840-1.950 µm, with a FWHM pulse duration of 375 fs at 1.950 µm at a pump power of 89 mW. The amplitude and the wavelength jitter of the fundamental soliton is ±1.2 dB and ±2 nm, respectively. The fundamental soliton contains 52% of the total amplified power. A long pass filter (LPF) with a cut-off wavelength of 1.840 µm is used to separate the shifted soliton from the residual seed. The measured autocorrelation trace of the filtered pump pulse is shown in figure 4.2 (b). To reduce the impact of group velocity walk-off in between pump, probe and the generated idler pulses in the upcoming FWM experiment, the filtered soliton is temporally broadened by passing through 6 m of standard G.625 fiber (SMF 2), resulting in a final FWHM pulse duration of 1.2 ps. A variable optical attenuator (VOA) is inserted to control the pulse energy delivered to the

microwire. The wavelength conversion of the pump from 1.550 µm to 1.950 µm mitigates the effect of TPA in As_2Se_3. Fig 4.2 (c) shows the calculated nonlinear absorption coefficient (β_{TPA}) of As_2Se_3 as a function of incident photon energy [126]. It is observed that β_{TPA} decreases by a factor of 13.6, from 0.14 cm/GW at a wavelength of 1.550 µm to 0.01 cm/GW at a wavelength of 1.950 µm. The use of As_2S_3 microwire instead of As_2Se_3 will provide advantage in terms of TPA as it has lower β_{TPA}, however increasing the required pump power levels for the subsequent wavelength conversion stage.

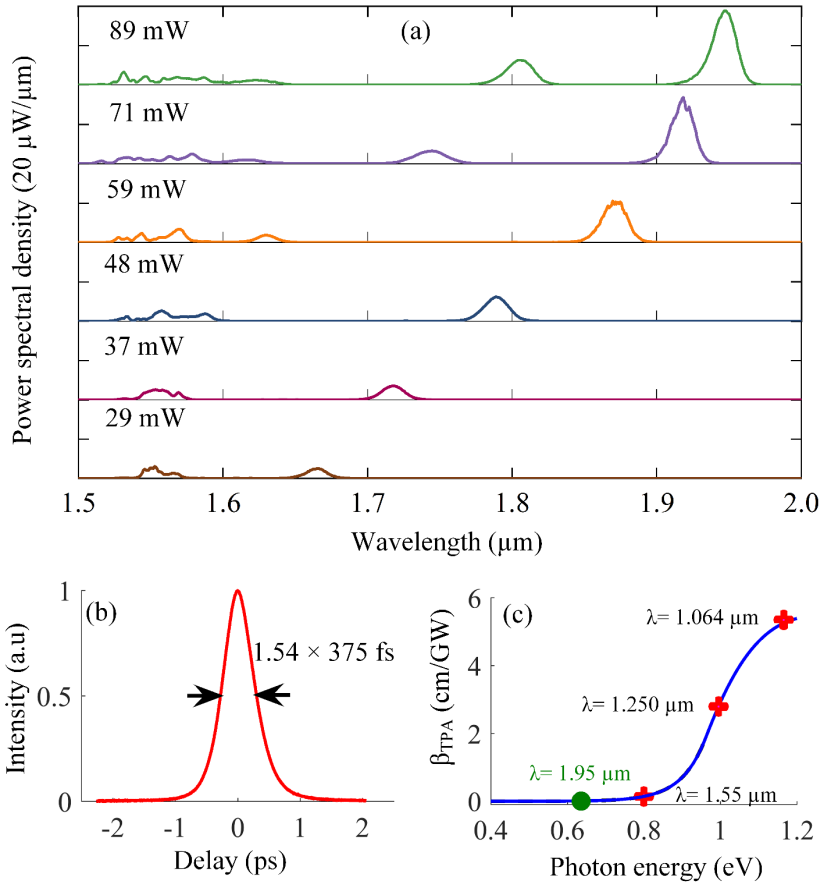

Figure 4.2. (a) Measured spectrum of the Raman-shifted soliton with increasing pump power. Seed pulse centered at 1.550 µm wavelength experiences a maximum shift to 1.95 µm. (b) Autocorrelation trace of the filtered soliton centered at 1.95 µm. (c) Calculated and experimental data [127], [128] *of β_{TPA} of As_2Se_3 glass*

4.2.2 Probe pulse generation by SPM

In the probe (upper) branch of fig. 4.1, seed pulses are initially amplified by an EDFA and spectrally broadened with a 200 meters-long silica-based highly nonlinear fiber (HNLF). The

second and third order dispersion coefficients (β_2 and β_3) of the nonlinear fiber are 5.1×10^{-2} ps^2/m and 3.2×10^{-5} ps^3/m, respectively, at a wavelength of 1.550 µm. Fig 4.3 (a) shows the spectral broadening in the HNLF as the average pump power increase from 1.2 mW to 9.5 mW. The spectrally broadened output is subsequently filtered with a tunable band-pass filter of FWHM of 4.5 nm. This results in probe pulses within the wavelength range of 1.550-1.660 µm. Time domain measurement of the probe pulses using Agilent 86100C digital communication analyzer shows that the FWHM duration varies between 14.7 ps to 15.9 ps, as shown in fig. 4.3 (b).

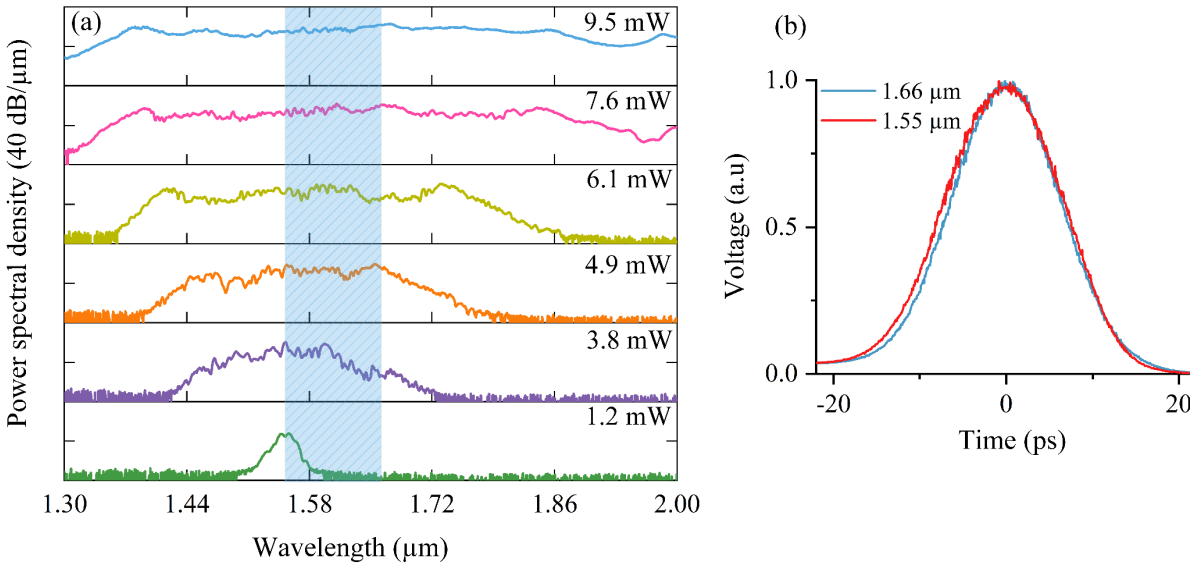

Figure 4.3. (a) Spectral broadening in the HNLF with increasing pump power. The shaded section indicates the total tuning range of the band pass filter. (b) Time domain measurement of the filtered probe pulses centered at 1.66 µm and 1.55 µm wavelength.

4.3 Microwire design

Both pump and probe pulses are recombined in one fiber using a WDM coupler. The temporal overlap between pump and probe pulses is ensured by using a motorized delay line in the probe arm with a range of 330 ps. Polarization states of pump and the probe pulses are co-aligned using a PC. The nonlinear medium used in this investigation is fabricated from an As_2Se_3 fiber with core/cladding diameters of 6 µm/167 µm and a numerical aperture of 0.2. A microwire section length of 1 cm is carved into the As_2Se_3 fiber by using a flame-brush tapering and real-time *in situ* monitoring technique, described in chapter 3. The length of the fiber section and

the transition section are 3 cm and 1.7 cm, respectively. β_2 of the microwire can be engineered into zero, anomalous or normal dispersion at the pump wavelength by choosing an appropriate microwire section diameter. Fig. 4.4 (a) shows the β_2 and β_4 of an As_2Se_3 microwire over a range of core diameters. The designed core diameter of the microwire section is 1.752 µm, which results in a positive $\beta_2 = 2.07 \times 10^{-2}$ ps^2/m and negative $\beta_4 = -9.28 \times 10^{-6}$ ps^4/m at the pump wavelength of 1.950 µm. The refractive index contrast between As_2Se_3 ($n_2 = 7.6 \times 10^{-18}$ m^2/W) and air leads to a waveguide nonlinearity of $\gamma = 17$ W^{-1}m^{-1} [117]. Parametric gain is generated under proper phase matching condition, where the frequency detuning from the pump frequency is given by, $\Delta\omega = \sqrt{\left(-\beta_2 \pm \sqrt{\beta_2^2 - 2\gamma P_0 \beta_4/3}\right)/(\beta_4/6)}$, where γ is the waveguide nonlinearity and P_p is the pump peak power [100]. Fig. 4.4 (b) shows the expected parametric gain as a function pump wavelength for a microwire with a core diameter of 1.752 µm, calculated by solving the coupled-wave equation provided by the nonlinear Schrödinger equation, described in section 2.5. Pumping under anomalous dispersion generates parametric gain relatively close to pump frequency and depends mainly on β_2. In contrast, pumping under normal dispersion with low negative fourth order dispersion leads to spectrally narrow parametric gain at frequency, $\Delta\omega = \sqrt{-12\beta_2/\beta_4}$, far-detuned from the pump frequency.

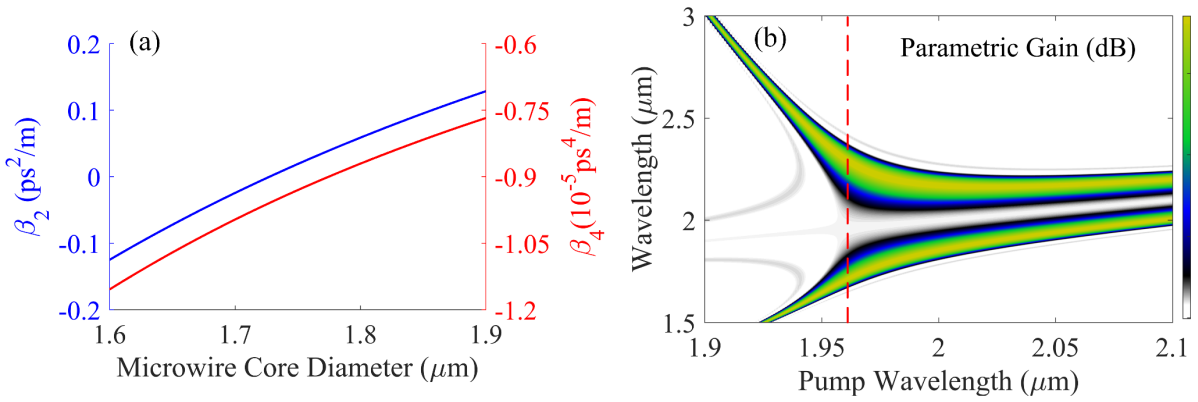

Figure 4.4. (a) Calculated β_2 and β_4 of a microwire as a function of the core diameter at a pump wavelength of 1.950 µm. (b) Calculated parametric gain spectrum of a microwire as function of pump wavelength. The core diameter, wire length and the pump power are 1.752 µm, 1 cm, and 11 W, respectively. A vertical dashed line indicates the ZDW.

The input facet of the device is polished and coupled to a standard G.652 fiber using UV epoxy. The output side of the device is coupled to a 20 cm long ZBLAN fiber to minimize the propagation losses in the MIR. The total insertion loss of the G.652- microwire-ZBLAN assembly at a wavelength of 1.950 µm is 5.5 dB. From this loss, 1 dB (0.5 dB/ interface) is due

to Fresnel reflection at the ChG-silica/ZBLAN interfaces, 1 dB from the mode-mismatch of the fibers, 2 dB from surface roughness loss of the microwire and non-adiabaticity in the transition regions, and 0.4 dB of propagation loss in the 10 cm long microtaper. Total insertion losses are typically reduced to < 3 dB with further optimization.

4.4 Results and analysis

Wavelength conversion results when pump and probe pulses temporally overlap in the ChG fiber microwire section. Initially, the pump wavelength is set at 1.950 μm. The average pump power coupled into the microwire section is 0.3 mW, corresponding to a peak power of 11 W. The average probe power is held constant at 0.08 mW, corresponding to a peak power of 2.6 W. Fig. 4.5 (a) shows the generated idler spectra recorded on an optical spectrum analyzer with a resolution bandwidth and sampling interval set to 2 nm and 0.04 nm, respectively. As the probe wavelength is tuned from 1.660 μm to 1.590 μm, the generated idler shifts in wavelength from 2.360 μm to 2.523 μm. The calculated walk-off length between the 1.950 μm pump and 2.523 μm idler is 1.2 cm, longer than the physical length of the microwire. Therefore, it is expected that walk-off has a negligible impact in the wavelength conversion process. The lower and upper wavelength limit of the generated idlers are set by the probe wavelength range and the parametric gain bandwidth, respectively. The maximum average MIR power measured 3 μW.

Additional tunability is achieved by shifting the location parametric gain spectrum towards longer wavelength by tuning the pump wavelength. The pump wavelength is shifted to 1.938 μm by decreasing the gain of the EDFA. In order to compensate for the reduced walk-off length caused by the increased detuning of the idlers, 40 m of G.652 fiber is spliced with SMF 2 to temporally increase the pump pulse duration to 2.7 ps. As a result, the peak pump power decreases to 5.5 W while the average probe power is unaffected, remaining at 0.08 mW. The walk-off length between the pump wavelength and the idler at a wavelength of 2.6 μm increases to 1.8 cm. The calculated β_2 and β_4 are 3.94×10^{-2} ps^2/m and $- 8.96 \times 10^{-6}$ ps^4/m, respectively. Fig. 4.5 (b) shows that the generated idlers shift in wavelength from 2.467 μm to 2.585 μm under the influence of tuning the probe from 1.596 μm to 1.550 μm. A total nonlinear spectral shift of 80 THz, including a pure parametric detuning of 41 THz is obtained.

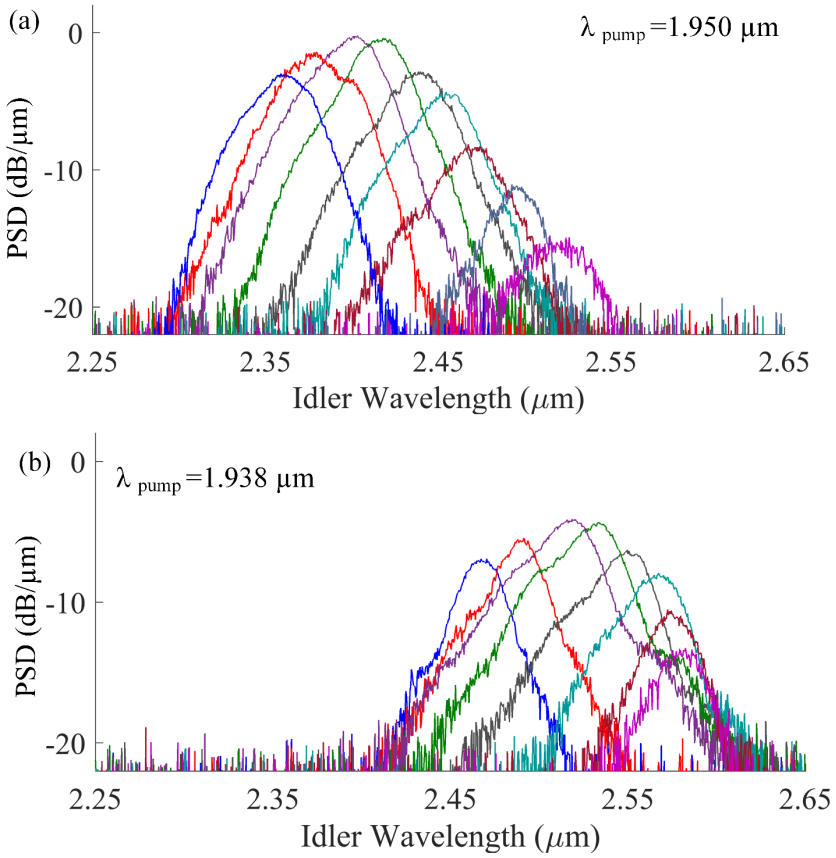

Figure 4.5. (a) Tunable MIR idlers generated from 2.300 µm to 2.640 µm for a range of probe wavelengths. (a) Pump wavelength, λ_{pump} = 1.950 µm and probe wavelength, λ_{probe} = 1.590-1.660 µm. (b) λ_{pump} = 1.938 µm and λ_{probe} = 1.550-1.596 µm.

In contrast to the conventional FWM techniques, this method allows additional advantages in terms of system compactness, cost-effectiveness and power scalability. Conventional wavelength conversion systems [95], [99] require separate pump and probe lasers to generate MIR idlers, whereas this method generates MIR light from a single laser input. Furthermore, in this method, FWM results from a probe and a pump that are both pulsed and synchronized, thereby generate a far more powerful idler for given pump and probe average powers, compared to the conventional FWM that results from a probe that is CW and a pump that is pulsed.

CE of the ChG waveguide is extracted by calculating the ratio between the output idler average powers over the input probe signal average power involved in the FWM process. The numerical aperture mismatch in between ZBLAN fiber and optical spectrum analyzer are also taken into consideration for CE calculation. Fig. 4.6 (a) shows the CE plotted as a function of idler wavelength for two different pump wavelengths along with the theoretical fit, evaluated by

solving the coupled wave equations. A maximum CE of -3 dB is achieved for wavelength combinations of 2.403 µm and 1.640 µm, corresponding to the maximum gain obtained from FWM. The maximum CE at a pump wavelength of 1.938 µm decreases to -6.5 dB with respect to the maximum CE at a pump wavelength of 1.950 µm due to the associated decrease in pump peak power. The error bars include the cumulative uncertainty on pump and probe pulse duration, power and wavelength.

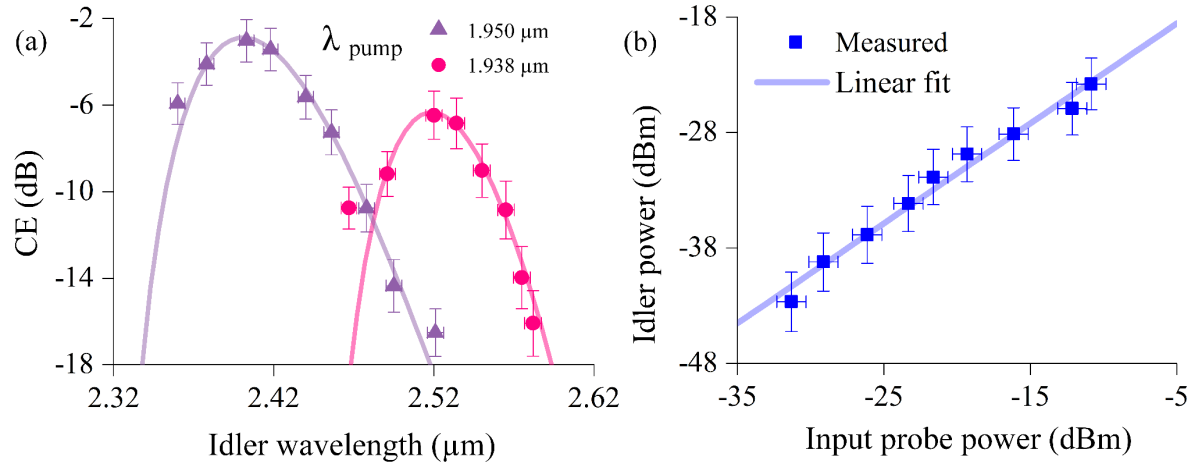

Figure 4.6. (a) CE of the ChG microwire at two different pump wavelengths. (b) Probe power at the microwire input versus the output idler power for pump and probe wavelength of 1.950 µm and 1.660 µm, respectively.

In order to understand the impact of probe-induced TPA on the wavelength conversion, the performance of the wavelength converter is characterized as a function of total probe power at the microwire input. The pump wavelength is fixed at a wavelength of 1.950 µm and peak power is maintained at 11 W. As observed in fig. 4.6 (b), the linear increase in the idler power (slope = 0.86) with increasing probe power corroborates with the theory [98]. The slope deviation from the ideal unity case is expected to occur from a polarization misalignment between pump and probe pulses. The maximum average idler power obtained is -23.8 dBm for an input average probe power of -9.7 dBm. This corresponds to a peak intensity of 14 MW/cm^2 at the probe wavelength of 1.66 µm. No signs of saturation is observed due to TPA or structural damage in the microwire. Hence, the idler power could be increased further by increasing the probe power. This clearly indicates that the strong MIR signals are generated by probing below the TPA threshold of the As_2Se_3 glass.

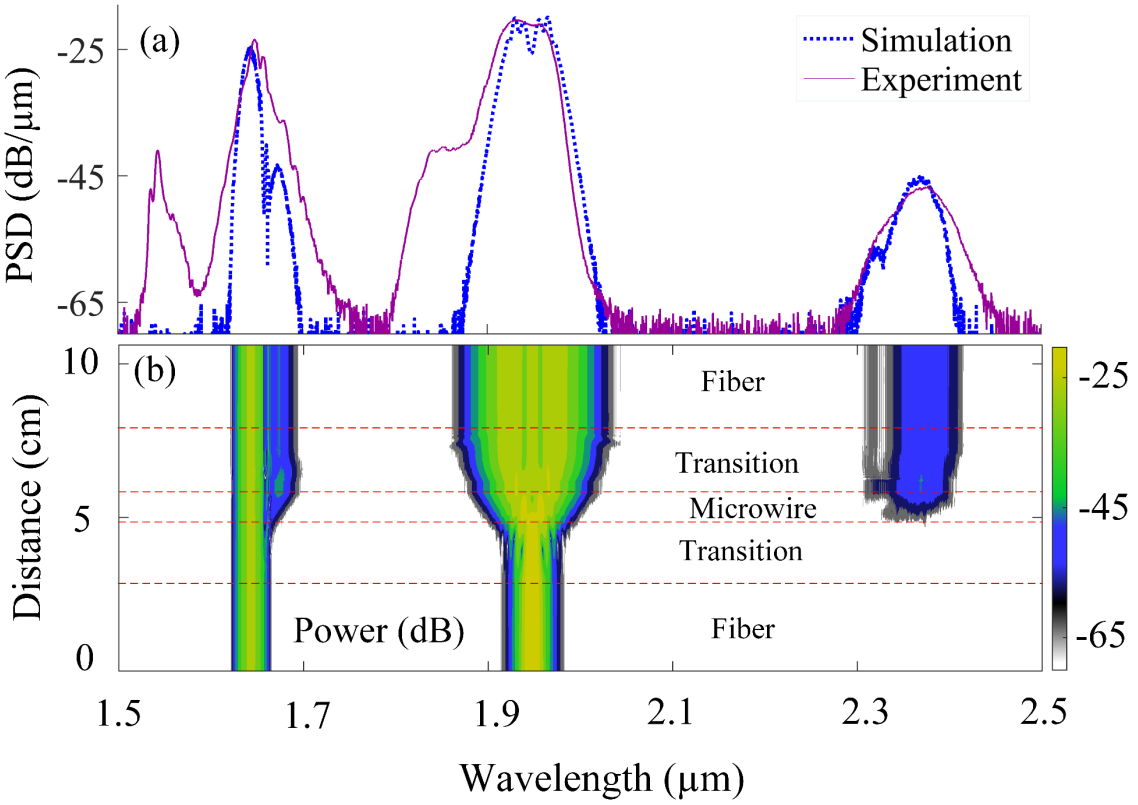

Figure 4.7. (a) Pump, probe and idler spectrum at the microwire output. Simulation (blue) and experiment (violet) for pump and probe wavelength of 1.950 µm and 1.650 µm, respectively. (b) Simulation of the spectral evolution along 10.4 cm long microtaper for a peak pump power of 11 W.

In order to interpret experimental result quantitatively, numerical simulation of the FWM mixing process is also performed by solving the GNLSE using the SSFM and stochastic noise model [45], [73], [100], described in section 2.3. All segments of the microwire including fiber, transition and microwire section are included in the simulation, considering also a random variation of the dispersion and nonlinear coefficient along the length of the waveguide that occurs inevitably during the microwire fabrication process. Fig. 4.7 (a) shows an excellent agreement found in between the experimental results and simulation. The probe pulses are considered to be negatively chirped due to the propagation in the 200 m of HNLF. The satellite peak at a wavelength of 1.544 µm occurs in the experiment due to a leakage from the TBPF. Fig. 4.7 (b) shows the dynamic evolution of the pump, probe and idler signals as they propagate along the microtaper. It is observed that the fiber section (γ=1.6 $W^{-1}m^{-1}$) and transition section have no significant contribution to the far-detuned parametric gain. It only builds up in the

microwire section, where the phase matching condition is satisfied and waveguide nonlinearity is highest.

4.5 Summary

In summary, an all-fiber C-band to MIR nonlinear wavelength conversion system has been demonstrated. Both the pump and probe pulses are generated from a single erbium-doped fiber laser. A tunable MIR idler within the spectral range of 2.300– 2.640 μm is efficiently generated while avoiding the effects of TPA present in As_2Se_3 in the C-band. The experimental results demonstrate that all-fiber wavelength conversion can be achieved from the widespread C-band fiber laser and simultaneous nonlinear conversion into silica and ChG fibers.

5 Mid-infrared soliton self-frequency shift in chalcogenide glass

This chapter describes the development of a highly efficient tunable soliton source based on SSFS in ChG glass. The demonstrated system is exceptionally compact, simple and fully fiberized. It generates continuously tunable Raman solitons over a broad spectral range of 2.047-2.667 μm, and consumes no more than 87 pJ per pulse. The spectral measurements suggest that the generated pulses are as short as 62 fs with a maximum power conversion efficiency of 43%. This result is realized thanks to an 8 cm long As_2S_3 microstructure optical fiber (MOF) tapered into a microwire. Thanks to their broad transparency, their high nonlinearity and their adjustable chromatic dispersion, ChG microwires are promising components for the development of compact, low power consumption and highly efficient MIR optical sources. The results of this chapter has been published in [129]–[132].

5.1 Introduction

As mentioned in section 2.4, if the pulse duration of a propagating soliton is significantly short (typically femtosecond), the pulse experiences Raman amplification at long wavelength range of the spectrum at the expense of the power at the shorter wavelength edge, thus resulting in a continuous red-shift of the input soliton. Adding to the different nonlinear approaches of pulse generation e.g FWM and SC generation, SSFS is also particularly interesting since it allows to obtain pulses in a spectral range that are otherwise inaccessible by traditional lasers. In contrast to the FWM described in chapter 3 and 4, the experimental approach of SSFS is relatively simple. It generates widely tunable, high quality ultrashort pulses from a simple, single pass system that contains only a precisely dispersion engineered nonlinear fiber paired with a pump source. It requires no additional probe laser or temporal synchronization, and the power spectral density of the generated pulses are solely concentrated towards a narrow, specific set of wavelengths.

The first experimental demonstration of SSFS were presented by Mitschke *et al.* in 1986 [133] in polarization maintaining SMF. Since then, SSFS has been extensively studied with a goal of maximizing the conversion efficiency and the wavelength shift per unit length. This includes investigation in HNLF [134], birefringent fiber [135], non-polarization maintaining SMF [136], PCF [137]–[141], tapered microstructure fiber [142], photonic bandgap fiber and higher order mode fiber [143]–[145]. Recently, Raman soliton generation in *Tm*-doped fiber amplifier system has been broadly investigated by several group with an aim to generate both high-energy soliton and extend the soliton wavelength above 2 μm [146], [147]. The highest soliton efficiency of 97 % was demonstrated by Luo *et al.* with a soliton tunability of 1.98-2.31 μm in wavelength [148]. Wang *et al.* showed the highest soliton energy of > 10 nJ with a continuous wavelength tunability of 1.98 μm to 2.29 μm [149]. However, the increasing material absorption of silica glass possess a challenge to extend the soliton wavelength beyond 2.2 μm wavelength. A larger SSFS beyond this wavelength results in the decrease of soliton energy [150], spectral distortion of the fundamental soliton and generation of new spectral features that leads to supercontinuum generation [151].

For SSFS applications at wavelengths longer than 2 μm, soft glass fibers such as ChG, fluoride and tellurite maintain low transmission losses thanks to their low phonon energies. For example, Tang *et al.* demonstrated Raman solitons that are tunable over the spectral range of 2-4.3 μm in a 2 m long InF_3 fiber from an input pump energy of 120 nJ [152]. Duval *et al.* generated solitons tunable from a wavelength of 2.8 μm to 3.6 μm from a maximum energy of 37 nJ injected into a 22 m long ZrF_4 fiber [153]. Nagl *et al.* showed SSFS up to 3.85 μm in 2 m long ZBLAN fiber at a pump energy of 5.5 nJ [154]. These hybrid fiber/free-space and fully free space systems generate solitons of nJ scale of energy that is not required for many low power applications. For example, in vivo applications in human tissue requires only picojoule level of energy for diagnostic purpose [155]. Therefore, to develop low power consuming wavelength converters that operate from low energy soliton, the use of highly nonlinear medium is desirable [45]. For example, Bi *et al.* have demonstrated 2.0-2.26 μm wavelength tunable SSFS in 0.41 m long suspended core tellurite fiber from a pump energy of 6.9 nJ [156]. Karpate *et al.* have also achieved a wavelength shift up to 2.4 μm in 0.05 m tellurite fiber from a pump wavelength and energy of 1.55 μm and 3 nJ, respectively [157]. Koptev *et al.* demonstrated SSFS in 0.5 m long microstructured tellurite fiber tunable within a wavelength range of 2.25-2.65 μm from an input energy of 3 nJ [158]. However, the development of more compact, low power consumption and portable systems requires a fully fiberized architecture capable to operate from pump energies

at the scale of pJ. These systems are desirable for spectroscopic and sensing applications such as breath analysis, environmental monitoring, food quality control and trace gas detection [7], [159]–[161].

ChG glasses are excellent candidates for the fabrication of SSFS-based wavelength converters that are compact and consume low power. Cheng *et al.* demonstrated SSFS in an As_2Se_2-As_2S_5 fiber from a solid-state pump source centered at a wavelength of 2.8 μm [162]. A frequency detuning of 620 nm (19.43 THz) was obtained for a pump power of 144 mW, or pulse energy of 1.8 nJ. Since this SSFS was observed in the context of supercontinuum generation, the generated fundamental soliton was not clearly distinguishable and the CE to this specific soliton remained negligible. To improve the CE and minimize the energy required to trigger SSFS, the enhanced nonlinear optical effect of ChG microwires are of great use [63]. The chromatic dispersion engineering of microwires enable an easy control of the soliton center wavelength [163]. Al-Kadry *et al.* performed theoretical investigation of SSFS in As_2Se_3 microwires where they predicted SSFS tunable from 2.10-2.75 μm with maximum PCE=95 % at a pump energy of 2.37 pJ [164]. However, to this date, there has been no experimental demonstration of a tunable soliton source realized via SSFS in ChG microwire.

In this chapter, the first experimental realization of high efficiency SSFS in ChG microwires are described. The wavelength converter is widely tunable within the spectral range of 2.047-2.667 μm, providing an SSFS detuning of up to 42.3 THz (729 nm) from a pump wavelength of 1.938 μm and an energy of <87 pJ per pulse. The core of the wavelength converter is an 8 cm long nonlinearity and dispersion engineered As_2S_3 microwire, tapered from a suspended core MOF. The CE in this experiment is exceptional, the largest ever demonstrated in ChG fiber, with a maximum of 43% and a value maintained above 20% over the whole tuning range. The proposed wavelength converter demonstrates the feasibility to develop light sources that are compact, with low power consumption, and broadly tunable in the MIR.

5.2 Device and experimental setup

The nonlinear medium used in this experiment is an As_2S_3 MOF with a diameter of 213 μm. Fig. 5.1 (a) shows the scanning electron microscope image of the MOF's cross-section. The suspended core has a diameter of 13.5 μm and is surrounded by six air holes. The fiber is multimode with a V-number of 47.7. Prior to fabrication, the MOF is coated with poly-methyl

methacrylate (PMMA) as an extra layer that brings robustness to the microwire while preserving the optical mode in the As_2S_3-air material. During fabrication, the central portion of the MOF is flame-brush tapered into a microwire section while simultaneously monitoring the chromatic dispersion up until a desired level of β_2 =- 1 ps^2/m, using the *in situ* method describe in chapter 3. After tapering, the microwire section reaches a length of 8 cm while the fiber section and the transition sections reach a length of 1 cm and 2 cm, respectively.

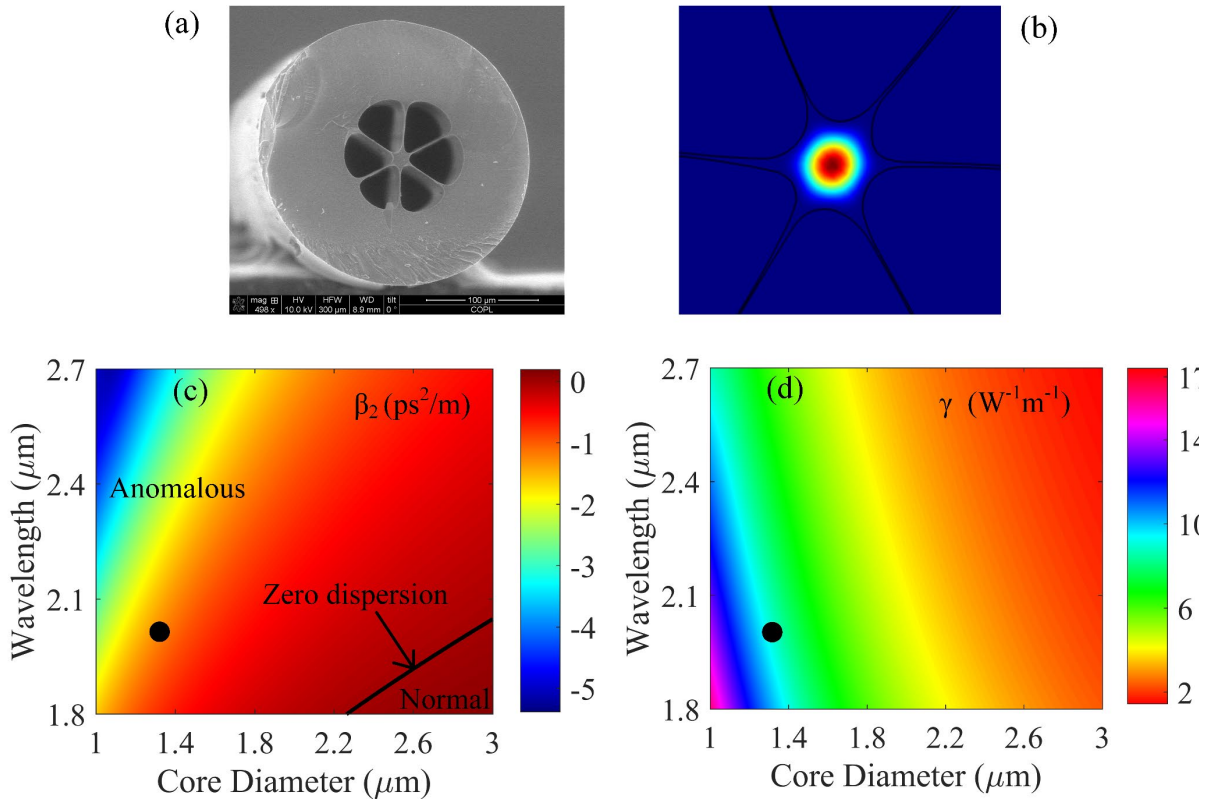

Figure 5.1. (a) Scanning electron microscope image of the As_2S_3 suspended core microstructured fiber (fiber diameter: 213 µm). (b) Electric field distribution of fundamental mode in the MOF at 1.94 µm wavelength. (c) β_2 of the microwire as a function of wavelength and core diameter. The zero-dispersion line separates the anomalous and normal dispersion regions. (d) Waveguide nonlinearity of the microwire. The black dot in both figures indicate parameters for the designed microwire.

Fig. 5.1 (b)-(d) shows the simulated fundamental mode profile of the MOF at 1.94 µm wavelength, β_2 and γ of the microwire, calculated by performing a full vectorial finite-element method analysis of the fiber geometry using COMSOL Multiphysics. For the designed β_2 at the pump wavelength of 1.94 µm, the core diameter of the MOF reduces to 1.34 µm. With this core diameter, strong modal confinement due to the large refractive index contrast between As_2S_3 (n_2 = 4.5 × 10^{-15} cm^2/W) [165] and air leads to a waveguide nonlinearity of γ = 9.14 W^{-1}m^{-1}.

The input facet of the taper is cleaved and aligned to a SMF-28. The output side of the taper is aligned to one end of a 20 cm-long single mode step index As_2Se_3 fiber (Coractive IRT-SE-6/170) with core/clad diameters of 6 µm/170 µm and NA=0.16. Both ends of the taper are then mechanically spliced using UV-cured epoxy. The total insertion loss of the SMF-taper-ChG fiber assembly at a wavelength of 1.938 µm is 3.4 dB. From this loss, 0.3 dB and 0.02 dB are due to Fresnel reflection at the As_2S_3 - silica and As_2S_3 - As_2Se_3 interfaces, respectively, 0.5 dB is due to propagation loss in the microtaper, 1 dB is due to mode-mismatch and the balance is attributed to fiber misalignment. For spectral analysis, the other end of the As_2S3_3 fiber is connected to a Yokogawa AQ6376 OSA. The short length of the As_2Se_3 fiber ensures that the low level of added chromatic dispersion is negligible for the sampled soliton.

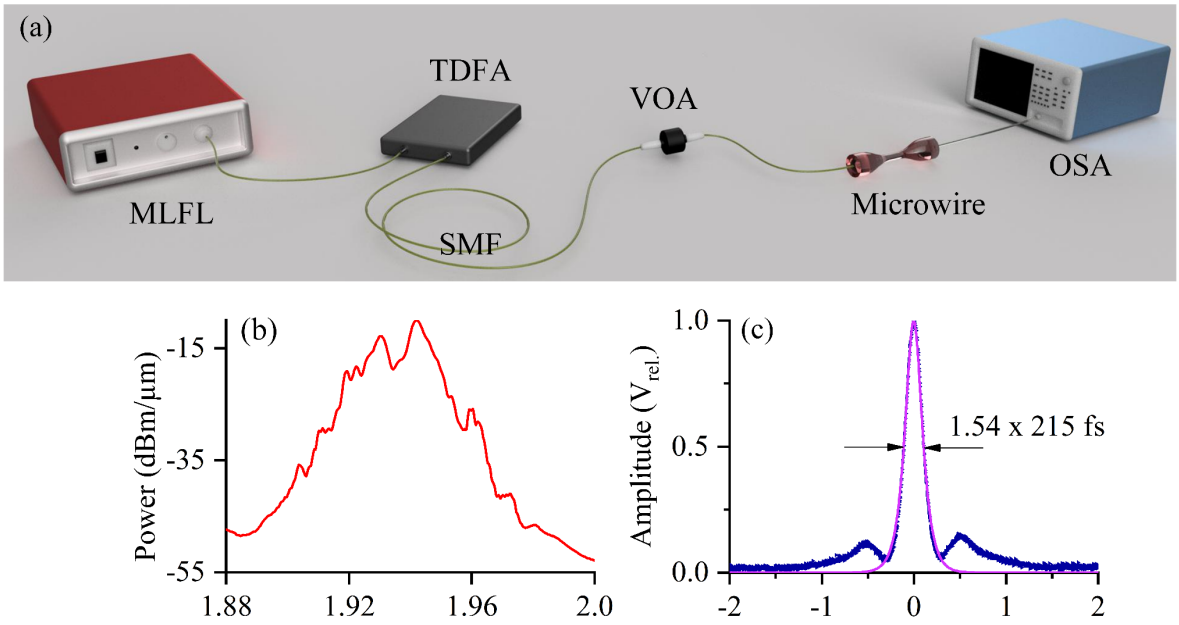

Figure 5.2. (a) Experimental setup (not drawn to scale). MLFL, mode- locked fiber laser; TDFA, thulium-doped fiber amplifier; SMF, single mode fiber; VOA, variable optical attenuator; OSA, optical spectrum analyzer. (b) The optical spectrum and (c) the autocorrelation trace of the compressed pump soliton at the input of the microwire.

Fig. 5.2 (a) shows the experimental setup of the wavelength converter. Mode locked seed pulses are launched from a fiber laser (AdValue AP-ML) at a repetition rate of 30 MHz, duration of 900 fs, central wavelength of 1.938 µm and average power of 7 mW. The pulses are amplified and compressed in a pulse formatting stage consisting of a TDFA followed by a 1.8 m long SMF-28. In the amplifier, the average power is increased to 40.5 mW. The pulses emerge

slightly chirped due to anomalous dispersion of the thulium-doped silica fiber. The pulses then propagate in the SMF-28 fiber and experience temporal compression. This compression can be understood as the higher-order soliton pulse compression, resulting from the interplay between the chirp induced by self-phase modulation and the anomalous GVD of the SMF [166]. The pump pulses are spectrally and temporally characterized right after the pulse formatting stage using an OSA and autocorrelator. Fig. 5.2 (b) and (c) show the optical spectrum of the pump pulse modulated by SPM and the corresponding autocorrelation trace. The obtained autocorrelation profile has characteristics of the peregrine soliton, i.e. a temporally localized peak sitting on an extended background [167]. The center part of the autocorrelation trace fits perfectly with a $sech^2$ shape with a pulse width of 215 fs. In a more practical assembly, both the mode locked fiber laser and the pulse formatting stage could be replaced with a pulsed laser of similar output pulse characteristics. After characterization, pump pulses from the formatting stage are delivered to a variable optical attenuator to control the pulse energy delivered to the microtaper. The frequency shifted output of the microwire is monitored using an OSA. It is worth mentioning that the whole system is entirely fiberized without using any free space optics. Furthermore, the low number of components adds to the simplicity and compactness of the setup.

5.3 Experimental results and discussion

Fig. 5.3 shows experimental output spectra as a function of input pump energy, considering the total insertion loss of the taper. The calculated soliton number increases from 2.91 to 6.13 as the pump energy increases from 19 pJ to 87 pJ. High-order solitons undergo temporal compression and break into multiple fundamental solitons due to higher order dispersion and Raman scattering. Raman scattering also leads to SSFS of the resulting solitons. Fig. 5.3 shows that with the increase of pump energy, a soliton is clearly identifiable and shifts towards long wavelengths, reaching a maximum central wavelength of 2.667 μm for a pump energy of 87 pJ and average pump power of 2.6 mW. This input energy can be further decreased by reducing the insertion loss of the SMF-taper-ChG fiber assembly by angle cleaving and applying anti-reflection coating at the fiber interfaces. With further increase in the pump energy, the main soliton shift slows down while the major fraction of the pump energy is transferred to secondary solitons and residual background.

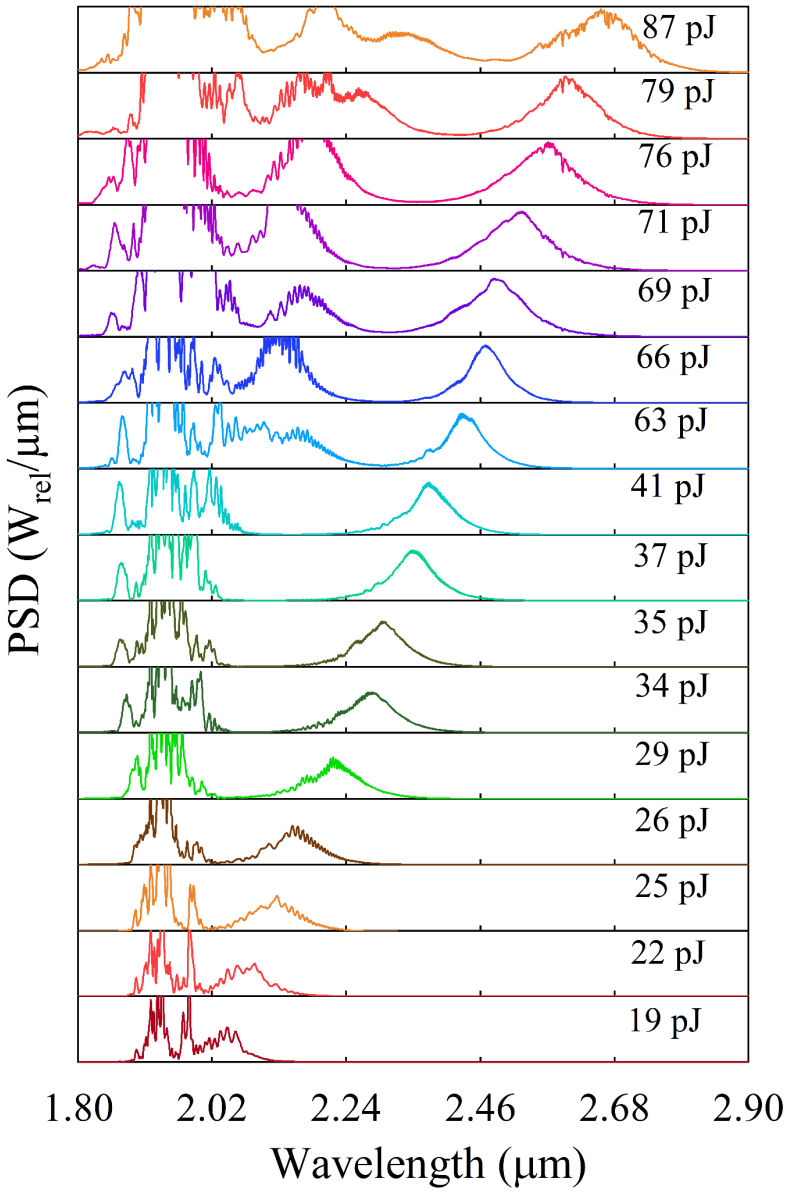

Figure 5.3. Measured output spectra of the SSFS with increasing input pump pulse energy. The input pump energy is indicated for each spectrum.

.

Fig. 5.4 (a) shows the CE and energy of the Raman soliton as a function of center wavelength. CE is defined as the ratio of the self-shifted soliton power to the total output power [148]. A maximum and minimum CE of 43 % and 20 % are obtained for a center wavelength of 2.127 µm and 2.667 µm, respectively. The high CE is ensured by the combination of the microwire specification and excitation conditions chosen to enhance Raman soliton formation, without the generation of broad supercontinuum. The initial increase in the CE with wavelength could be due to the incomplete shifting of the Raman soliton [149]. Any further increase in pump power leads to reduction in PCE, related to the generation of secondary solitons. A maximum pulse energy of 11.7 pJ is obtained for the soliton centered at a wavelength of 2.667 µm. The spectrum of the fundamental soliton fits well with a $sech^2$ spectrum (fig. 5.4 (b)),

which is suggestive of transform limited pulses. For pulses centered at 2.280 µm and 2.600 µm, the pulse durations are inferred to 62 fs and 69 fs, respectively. This results in peak powers of 125 W and 144 W, respectively.

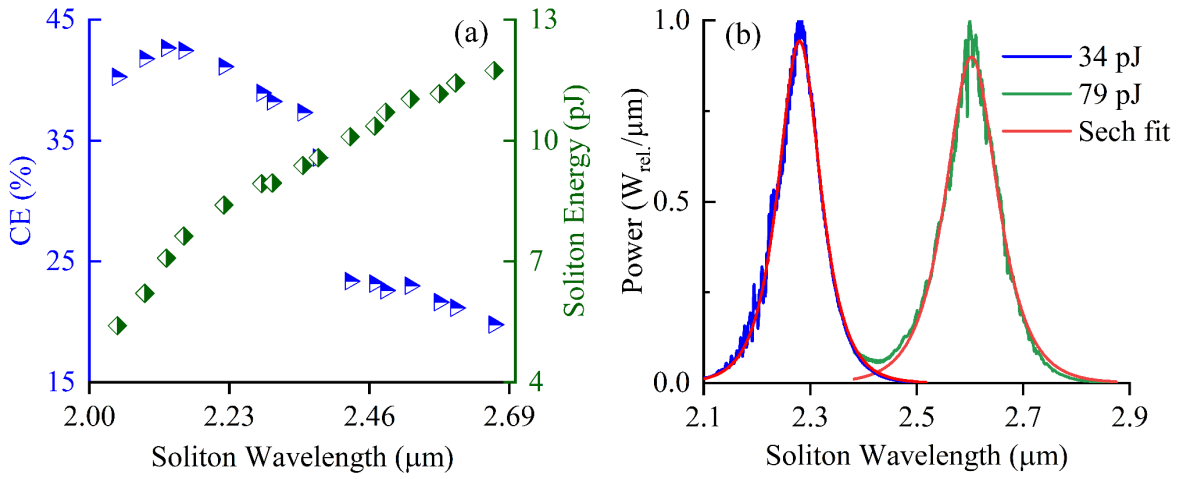

Figure 5.4. (a) CE and soliton energy as a function of soliton wavelength. (b) The spectrum of the fundamental soliton fitted with the spectrum of an ideal sech^2 shaped pulse, at two different pump energies.

The stability of the system is also evaluated by measuring the power and the center wavelength fluctuation. Fig. 5.5 shows the measured parameters of the soliton centered at 2.543 µm for duration of an hour at an acquisition rate of 33 mHz. The calculated coefficient of variation (standard deviation/mean) of the power and the center wavelength are 2.8 % and 0.57 % respectively. Such numbers indicate a reasonable stability of the system. A stability analysis of the pump laser shows that it remains stable within a variation of 0.02% in power, and 0.03% in central wavelength. Simulations suggest that such fluctuations have a negligible impact on the resulting Raman soliton. Since the pump laser seems stable, then we assume that fluctuations observed of the Raman soliton may occur from gradual drift of polarization with time. The Raman soliton stability could be improved by replacing the silica fiber in the system by polarization maintaining fiber.

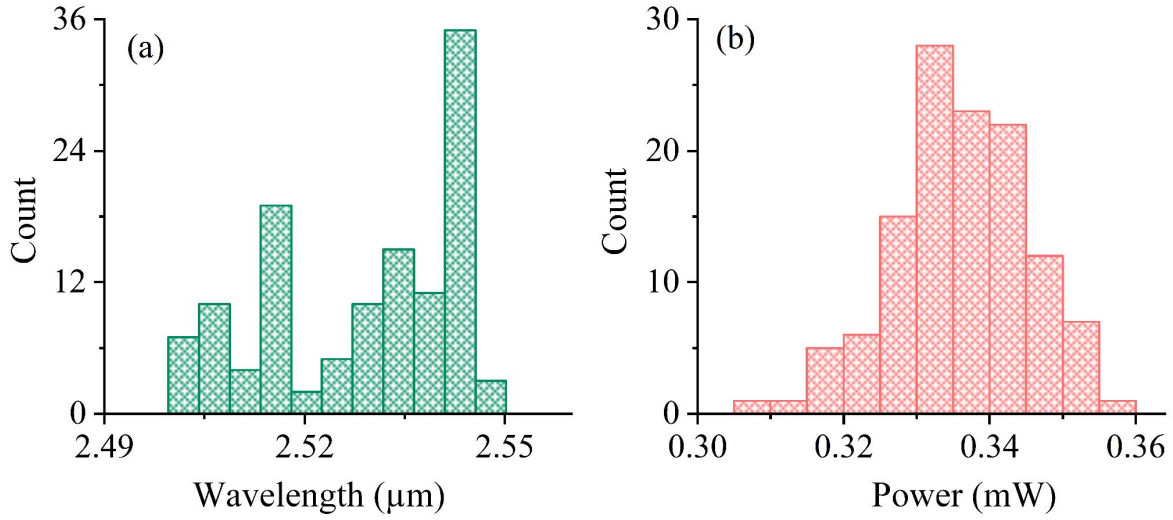

Figure 5.5. The stability measurement of the (a) center wavelength and (b) the power of the fundamental soliton.

5.4 Numerical analysis

This section presents a fully realistic simulation of the SSFS process in the ChG device that includes the fiber, transition and the microwire section. The nonlinear pulse propagation simulations are performed by solving the GNLSE with SSFM method [45], [73], combined with an adaptive step size [168]. As described in section 2.3.2, The GNLSE can be written in the following form.

$$\frac{\partial A(z,T)}{\partial z} + \frac{\alpha}{2}A - i\sum_{n=2}^{\infty}\frac{i^n\beta_n}{n!}\frac{\partial^n}{\partial T^n}A(z,T) = i\gamma\left(1 + i\tau_{shock}\frac{\partial}{\partial T}\right)\times\left(A(z,T)\int_{-\infty}^{\infty}R(T')\times|A(z,T-T')|^2dT'\right)$$

where, *A(z,T)* represents the complex pulse envelope propagating inside the microwire. The second term in the left models the linear propagation loss that is set to measured constant value of 0.04 dB/cm for the wavelength range under consideration. The third term models the dispersion with a Taylor expansion of the propagation constant *β(ω)*, where $\beta_n = \frac{\partial^n\beta(\omega)}{\partial\omega^n}$. Dispersion terms up to 8th order are considered, taking into account the wavelength dependence of the refractive index of As_2S_3 obtained from Sellmeier formula given in [169]. The first term in the right models the Kerr nonlinearity where waveguide nonlinearity (γ) is evaluated at the

pump frequency (ω_0) for a nonlinear refractive index value of n_2 = 5.44 × 10^{-18} m^2/W [127][170]. The wavelength dependence of the effective area (A_{eff}) is taken into account by introducing a first-order correction to the timescale τ_{shock} at the pump wavelength.

$$\tau_{shock} = \frac{1}{\omega_0} - \left[\frac{1}{A_{eff}(\omega)}\frac{dA_{eff}(\omega)}{d\omega}\right]_{\omega_0}$$

The nonlinear response function *R(T)* includes both instantaneous Kerr response and delayed Raman response. The Raman response function is modelled as a damped oscillation in the temporal domain using two characteristic time constants τ_1 and τ_2, related to the phonon dynamics of the material (see [45]). The fractional contribution and the Raman response function are taken to be f_r=0.1, τ_1=15.2 fs and τ_2=230.5 fs for As_2S_3 glass [171].

For the simulation, the 30 ps temporal window is discretized into 2^{12} samples for an input *sech* pulse of 215 fs duration. Quantum noise was added to the input pulse using one photon per mode model [172]. The best match with the experiment is obtained for ~30 % lower peak power in simulation. This is because the simulation considers perfectly polarized light and single mode propagation. However, the microwire is birefringent and although the coupling to the microwire is optimized for fundamental mode, due to the V number of 4.8, fraction of the pump energy is expected to remain in higher order modes. The simulation suggest that the fiber section and the transition section have a negligible effect on the pump pulse properties. Fig. 5.6 (a) and (b) show the temporal and spectral evolution of SSFS for a pump pulse of 145 W peak power. At the beginning of the microwire, the pulse has a soliton number of 7.03 and it undergoes soliton fission after propagating a length of 4 mm. From the multiple soliton resulting from fission process, the a fundamental soliton encounters continuous redshift in spectrum up to a wavelength of 2.58 μm (fig. 5.6 (b)), that corresponds to a 9.2 ps time delay in temporal domain (fig 5.6 (a)). Fig 5.6 (c) shows that an excellent agreement is found between the simulated spectrum and the measured spectrum for 145 W peak power. Fig. 5.6 (d) shows the simulated spectrum for the rest of the pump power levels as indicated in fig. 5.3.

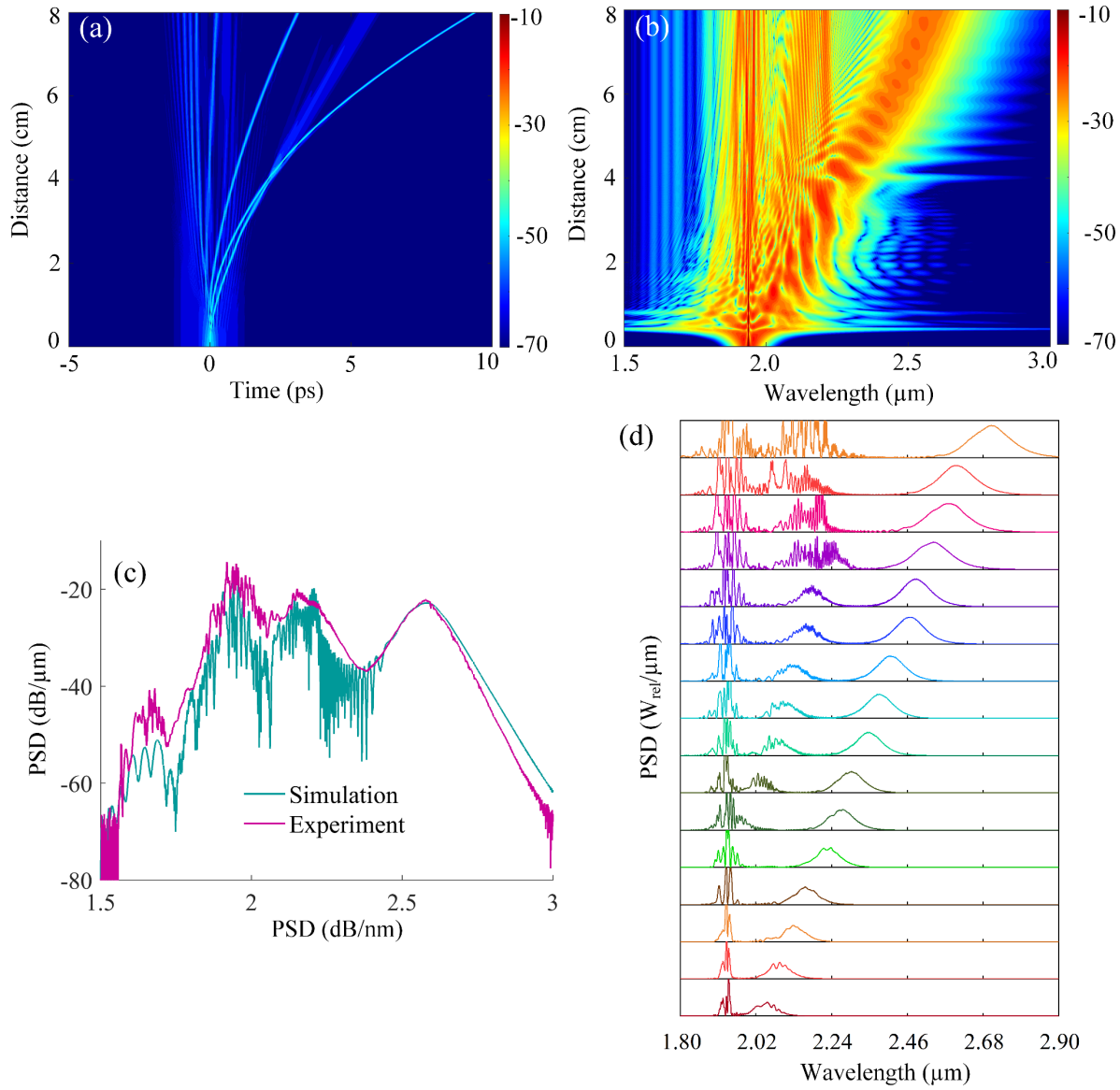

Figure 5.6. (a) Temporal and (b) spectral evolution in the microwire for a pump peak power of 145 W. Colormaps show power spectral density in dB. (c) Simulated and the measured spectrum for a simulated peak pump power of 145 W. Simulated spectra of SSFS for with increasing pump energy (from bottom to top).

Despite the generated SSFS up to a wavelength of 2.667 μm, it is possible to further improve the current performance of this system in terms of CE and shifted wavelength that are currently limited by the generation of multiple solitons. It is well know that efficiency of SSFS can be improved by reducing the soliton number, thereby generating as few solitons as possible [173]. A pump source generating shorter pulses will reduce the soliton number as well increase the

maximum frequency shift of the fundamental soliton since, $\Omega(z) \propto {}^{1}/_{T_0^4}$, where T_0, represents the pump pulse duration. Fig. 5.7 shows the simulation results for a pump duration of 90 fs and peak power 540 W. This results in N=3.64 and yield a wavelength shift of the fundamental soliton up to 3.4 µm for a propagation length of 8 cm.

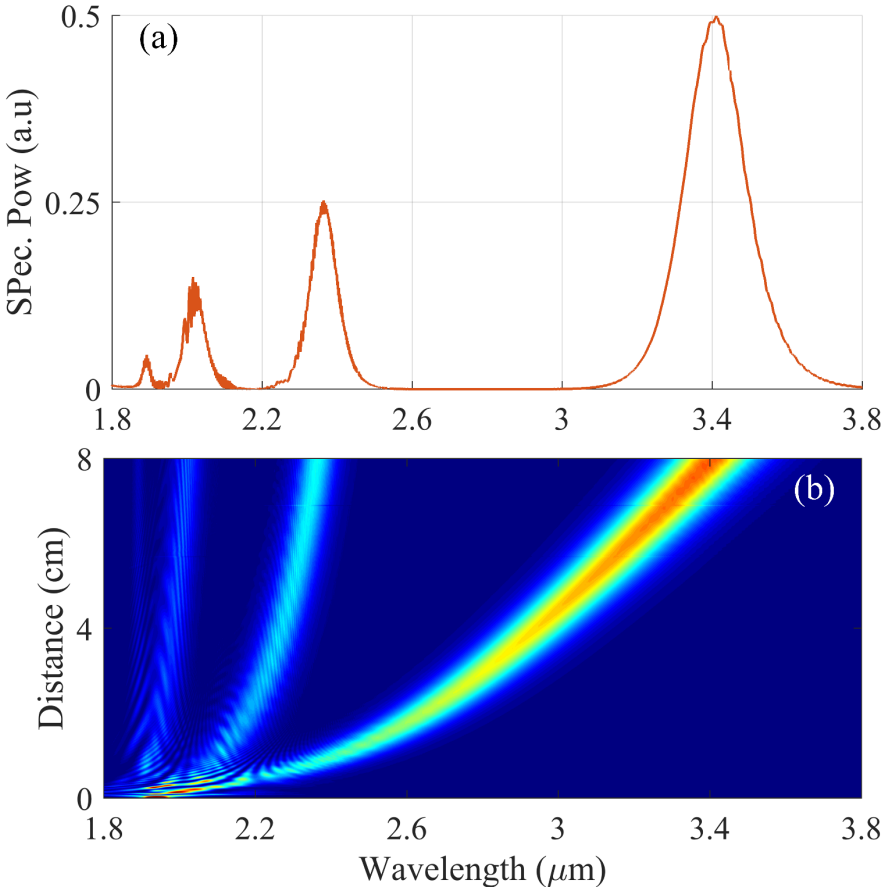

Figure 5.7. Simulated spectral evolution of the pulse propagating in an 8 cm long ChG microwire.

5.5 Summary

In conclusion, a wavelength converter tunable within the wavelength range of 2.047-2.667 µm in ChG microwire has been demonstrated with an ultralow pump power of 87 pJ. This energy level can be further reduced by using As_2Se_3 fiber, which possess a nonlinearity ~10 times higher than As_2S_3. The obtained CE of 43 % is also the highest number ever reported on ChG glass. Applications of this compact MIR source include spectroscopic analysis and pollution monitoring.

6 Supercontinuum generation in dispersion-varying Chalcogenide microwire

In this chapter, SC generation and its efficiency enhancement are experimentally demonstrated using dispersion-varying ChG microwire. The 0.85 cm long device is fabricated out of an As_2S_3 suspended core MOF, and includes a non-uniform segment with longitudinally varying core diameter. The non-uniform dispersion profile results in an enhanced energy transfer to the DWs in the shorter wavelength edge, as well as an increased SSFS towards the longer wavelength edge of the SC. The generated SC spans within the spectral range of 1.2-2.98 μm with an out-of-pump SC power enhancement of 4.5 dB towards shorter wavelength and a bandwidth extension of 262 nm, compared to the SC generated with the most optimal but constant dispersion profile. The results of this chapter has been published in [174]–[177].

6.1 Introduction

SC generation is a spectral broadening process that a narrowband pulse or a continuous wave undergoes as it propagates in a nonlinear medium [178], [179]. Since the first report of SC in bulk glass by Alfano *et al.* [180], there has been a continuous effort of generate MIR SC in various soft glass fibers e.g fluoride [181], tellurite [182] and ChG. MIR SC generation in ChG fiber was first demonstrated in As_2S_3 step-index fiber in 2005, where Wei *et al.* showed a spectral broadening of 310 nm wavelength from a pump wavelength of 1.5 μm [183]. In the following years, many researchers have attempted to develop all-fiber SC systems by the pumping ChG fibers with available fiber lasers centered at wavelengths between 1.0-2.0 μm [184], [185]. Since the ZDW of step-index ChG fiber is located at wavelength > 4.5 μm, these spectral extensions were produced in normal dispersion regime, by the combined effect of SPM, optical wave breaking and stimulated Raman scattering [44]. On the other hand, a more efficient and broadband SC can also be generated by pumping the waveguide in suitable anomalous

dispersion regime where, the SC broadening process is mainly dominated by soliton dynamics, including soliton fission, SSFS and DW generation [44], [186], as described in section 2.6. Such demonstration of ultra-broadband SC spanning from 1.4-13.3 µm wavelength was shown by Petersen *et al.* where, an 85 mm long As_2Se_3 fiber was pumped with an OPO centered at 6.3 µm wavelength [187]. Since then, towards an effort to enhance SC bandwidth and performance, various lengths and core diameters of ChG step-index fibers has been investigated at pump wavelength ranging form 3.1 µm to 4.5 µm [188]–[191]. However, these systems generally employed bulky and complex optical parametric amplifiers that require precision alignment and expensive high maintenance gas lasers.

To develop an all-fiber SC source, chromatic dispersion engineering of the ChG fiber is required in order to shift the ZDW at wavelengths at which compact fiber laser sources are available. Dispersion tailoring is generally performed by changing the structural parameters of the fibers including MOF [192], photonic crystal fibers [193] and/or tapering the fiber in form of a microwire [194]. Hudson *et al.* demonstrated SC generation within the spectral range of 1.8-9.5 µm by pumping an As_2S_3 core/As_2Se_3 cladding microwire at a wavelength of 2.9 µm [195]. Al-Kadry *et al.* generated supercontinuum extending from 1.1 µm to 4.4 µm in an As_2Se_3 microwire using a low pulse energy of 500 pJ [196] . These demonstrations are traditional SC generation techniques where the waveguide is characterized by a constant-dispersion (CD) profile. In contrast, dispersion-varying (DV) fibers with continuously shifting dispersion properties along propagation distance allow for a control of the spectral trajectory of Raman solitons, as well as continuous tailoring of the DW phase matching conditions [197]. Such a special design has the potential to simultaneously enhance the bandwidth and efficiency of the SC. Extensive experimental and numerical investigation have been performed in DV planar waveguide structures, where the dispersion management has led to flatter, more coherent, and spectrally broader SC compared to CD profile [198]–[201]. With fiber optics, a few numerical investigations [202], [203] and only two experimental [204], [205] demonstration of SC enhancement have been shown using DV profiles, limited in the visible or near-infrared spectral range. S. Pricking *et al.* generated SC from 0.4-1.2 µm in step index silica fiber and experimentally studied the effect of increasing and decreasing taper waist in soliton compression and fission dynamics [204]. A. Kudlinski *et al.* demonstrated a SC spanning 0.37-1.75 µm wavelength in a silica photonic crystal fiber, where the DV profile progressively modified parametric phase matching for the shorter anti-Stokes wavelength [205].

In this work, the first experimental demonstration of SC generation in DV ChG microwires are shown. The SC generation efficiency is enhanced simultaneously at longer and shorter wavelengths, with respect to an optimized CD fiber design. The microwire with DV profile generates a SC extending 1.20-2.98 µm from a low average pump power of 2.49 mW. The out-of-pump SC power is enhanced by 4.3 dB at shorter wavelengths, and 2.5 dB at longer wavelengths, resulting in an extension of the SC spectrum by 262 nm.

6.2 Device and experimental setup

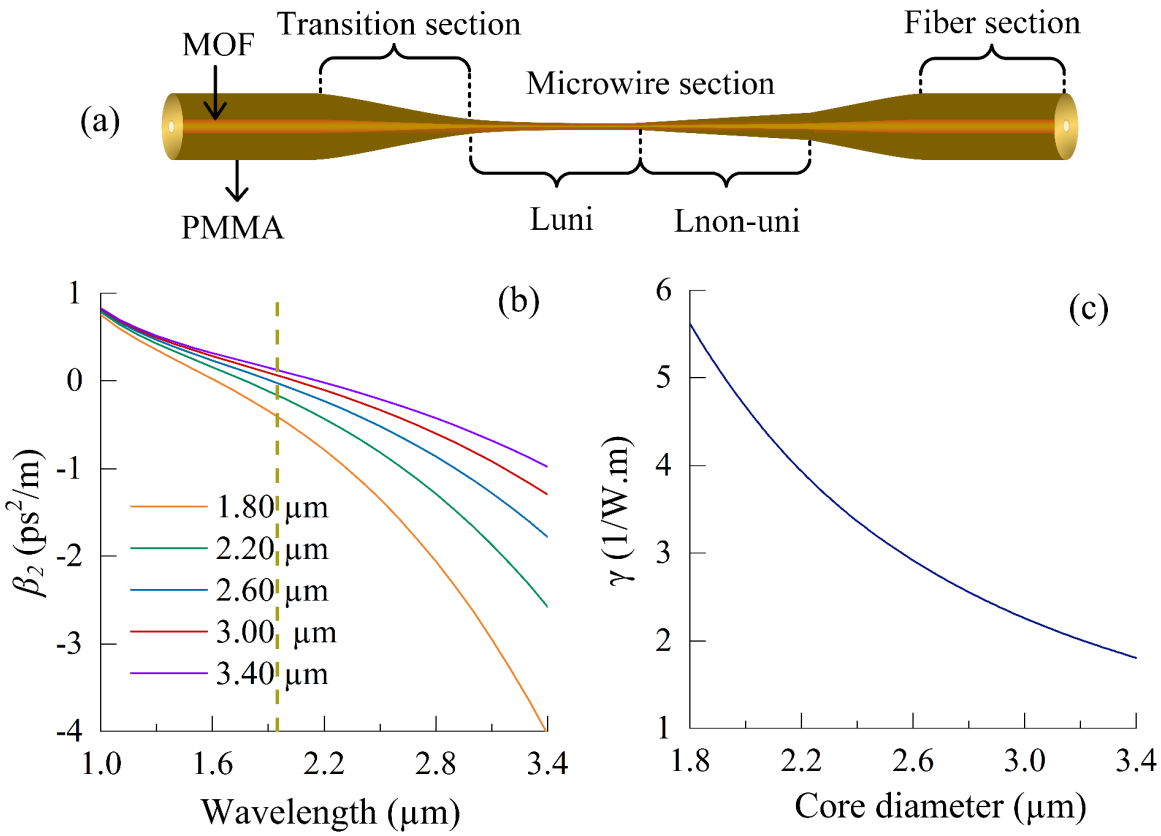

Figure 6.1. (a) Schematic of the PMMA coated DV fiber taper. (b) Calculated β_2 of the As_2S_3 microwire as a function of wavelength for a range of core diameters. (c) Calculated waveguide nonlinearity of the microwire as function of core diameter at a wavelength of 1.94 µm.

The nonlinear medium used in this experiment is an As_2S_3 suspended core MOF. The structural parameters including the SEM image of the fiber are described in section 5.2. Figure 6.1 (a) depicts a schematic of the DV microwire. It includes a microwire section where MOF core is reduced to a diameter of ~ 2 µm and where nonlinear process occurs. The microwire section consist of a uniform section of length L_{uni}, followed by a non-uniform section of length $L_{non\text{-}uni}$.

In the CD taper, there is only a uniform section and thus $L_{non\text{-}uni}$ =0. The fiber sections allow efficient coupling to external fibers, and the transition sections ensure an adiabatic modal conversion in between fiber and microwire section. Fig. 6.1 (b) show the calculated β_2 for a range of core diameters. From the fiber geometry, a vectorial finite-element method analysis was performed in COMSOL Multiphysics to calculate β_2. As the core diameter is decreased from 3.20 µm to 1.80 µm, the first ZDD is shifted from 2.17 µm to 1.62 µm in wavelength. A core diameter of 2.65 µm leads to zero dispersion at a wavelength of 1.94 µm, which corresponds to the wavelength of the pump laser used in this experiment. Fig. 6.1 (c) shows the waveguide nonlinearity parameter (γ) of the microwire. Strong confinement in a small modal area and a large nonlinear refractive index lead to waveguide nonlinearity as high as γ=5.5 $W^{-1}m^{-1}$, for a core diameter of 1.80 µm.

Fig. 6.2 shows the experimental setup for SC generation. Mode locked seed pulses are launched from a fiber laser (AdValue AP-ML) at a repetition rate of 30 MHz, duration of 900 fs, central wavelength of 1.94 µm and average power of 7 mW. In the TDFA, the pulses are amplified to an average power of 40.5 mW. The pulses emerge slightly chirped due to anomalous dispersion of the thulium-doped silica fiber. Afterwards, the pulses propagate in the 1.8 m SMF fiber and experience compression to a width of 215 fs due to higher-order soliton compression dynamics [166]. The VOA regulates the pulse energy and the PC controls polarization delivered to the taper.

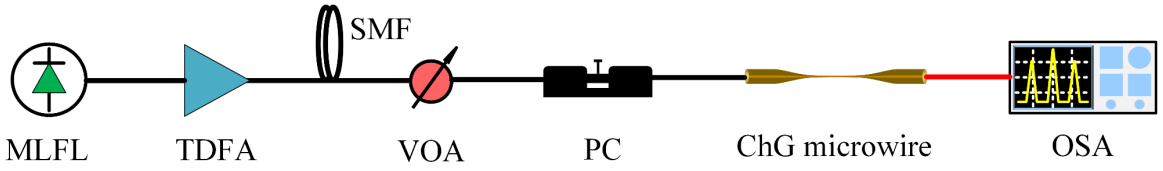

Figure 6.2. Schematics of the experimental setup. MLFL, mode- locked fiber laser; TDFA, thulium-doped fiber amplifier; SMF, single mode fiber; VOA, variable optical attenuator; PC, polarization controller; OSA.

6.3 Supercontinuum generation in constant dispersion microwire

At first, SC in generated in four different CD microwires with various dispersion profiles. These devices have microwire section core diameter of 2.25 µm, 2.10 µm, 2.00 µm and 1.90 µm, resulting in β_2= - 0.13 ps^2/m, -0.24 ps^2/m, - 0.28 ps^2/m and -0.35 ps^2/m, respectively. The

tapers have a uniform microwire section length of 0.85 cm. The lengths of the fiber section and the transition section are 1 cm and 2 cm. The input facet of the tapers is cleaved and mechanically spliced to SMF- 28 fibers. The output side of the tapers is coupled to 10 cm long single mode As_2Se_3 fiber with core/clad diameter of 6 µm/170 µm and NA=0.16 to minimize the propagation losses in the MIR. The total insertion loss of the samples varies from 3.1-3.6 dB at a wavelength of 1.94 µm. From this loss, 0.3 dB and 0.02 dB are due to Fresnel reflection at the As_2S_3-silica and As_2S_3- As_2Se_3 interfaces, respectively, 0.2 dB is due to the propagation loss in the taper, and the rest is attributed to mode-mismatch and alignment loss.

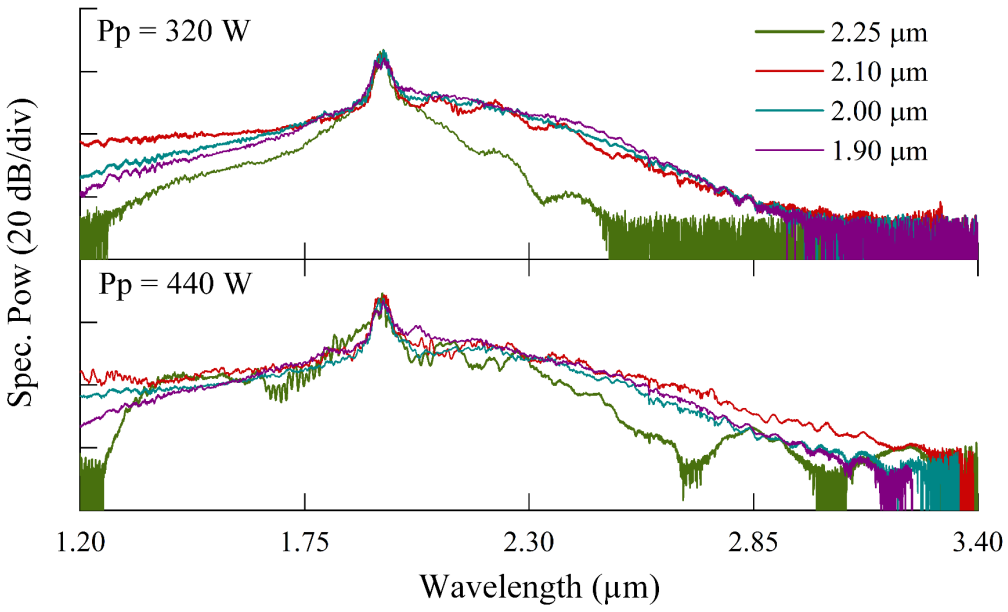

Figure 6.3. Measured SC spectra from CD tapers at two levels of pump power, 320 W and 440 W. The core diameter of the microwires ranges from 1.90-2.25 µm.

The input power conditions remain identical for all the devices under test, taking into account the different insertion loss of the samples. The SC spectra is measured at two different level of peak pump power (P_p) of 320 W and 440 W, corresponding to average power of 1.82 mW and 2.49 mW, respectively. Fig. 6.3 shows the generated SC in the CD microwires. Since the pump wavelength of 1.94 µm lies in anomalous dispersion regime for all the tapers, the SC generation process is dominated by soliton dynamics. As the $sech^2$ shaped pump pulse propagates in the microwire section, it initially undergo temporal compression and formation of higher order soliton, where the order is given by $N = \sqrt{\gamma P T_0/|\beta_2|}$, where P is the peak power and T_0 is the pulse width (FWHM=1.763 T_0). Due to the presence of high-order dispersion and Raman

effects, the higher order soliton deviates from its ideal periodic behavior and breaks into N fundamental solitons though soliton fission process. The fission length is defined by, $L_{fiss} = T_0^2/\beta_2 N$. For the pump power of 440 W, resulting fission lengths are 0.43 cm, 0.5 cm, 0.54 cm and 0.84 cm for microwire core diameters of 1.90 µm, 2.00 µm, 2.10 µm and 2.25 µm, respectively. The generated fundamental solitons experience SSFS and extend the longer wavelength edge of the SC.

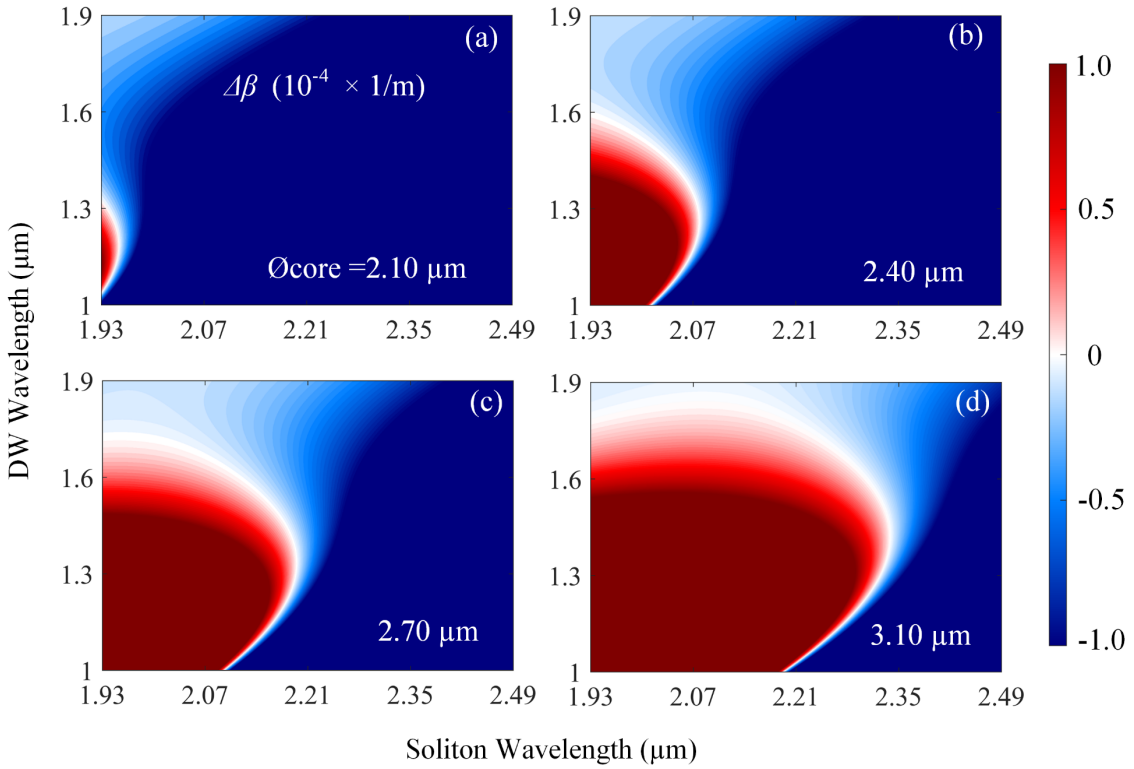

Figure 6.4. (a)-(d) Phase mismatch of the DWs as a function of DW generation wavelength and soliton wavelength for four different microwire section core diameter ranging from 2.10-3.10 µm.

Additionally, the fundamental solitons emits dispersive waves in the normal dispersion regime on the shorter wavelength side due to the presence of high-order dispersion. It is necessary to satisfy the phase matching condition for DW generation, which can written as, $\Delta\beta = \frac{\gamma P_{sol}}{2} - \sum_{k\geq 2} \frac{\beta_k \omega_{sol}}{k!}(\omega_{DW} - \omega_{sol})^k$ where, $\Delta\beta$ indicates the DW phase mismatch and P_{sol}, ω_{sol} and ω_{DW} are the peak power and angular frequency of the soliton and the DW respectively. The DW phase matching curves shown in fig. 6.4 indicate the wavelengths of DW generation ($\Delta\beta$=0) as a function of soliton wavelength across first ZDW. It is observed that for a fixed soliton wavelength, as the microwire core diameter decreases, the DW is emitted towards shorter

wavelength. Fig. 6.3 shows that the broadest SC is obtained for a microwire core diameter of 2.10 µm, and spans 1.20-2.45 µm (30 dB bandwidth) and 1.20-2.69 µm for pump powers of 320 W and 440 W, respectively. For microwire core diameter < 2.10 µm, the DW is further blue shifted to wavelengths < 1.10 µm whereas, for core diameter of 2.25 µm, the pump pulse encounters incomplete fission. Therefore, for both cases a reduction in spectral broadening is observed.

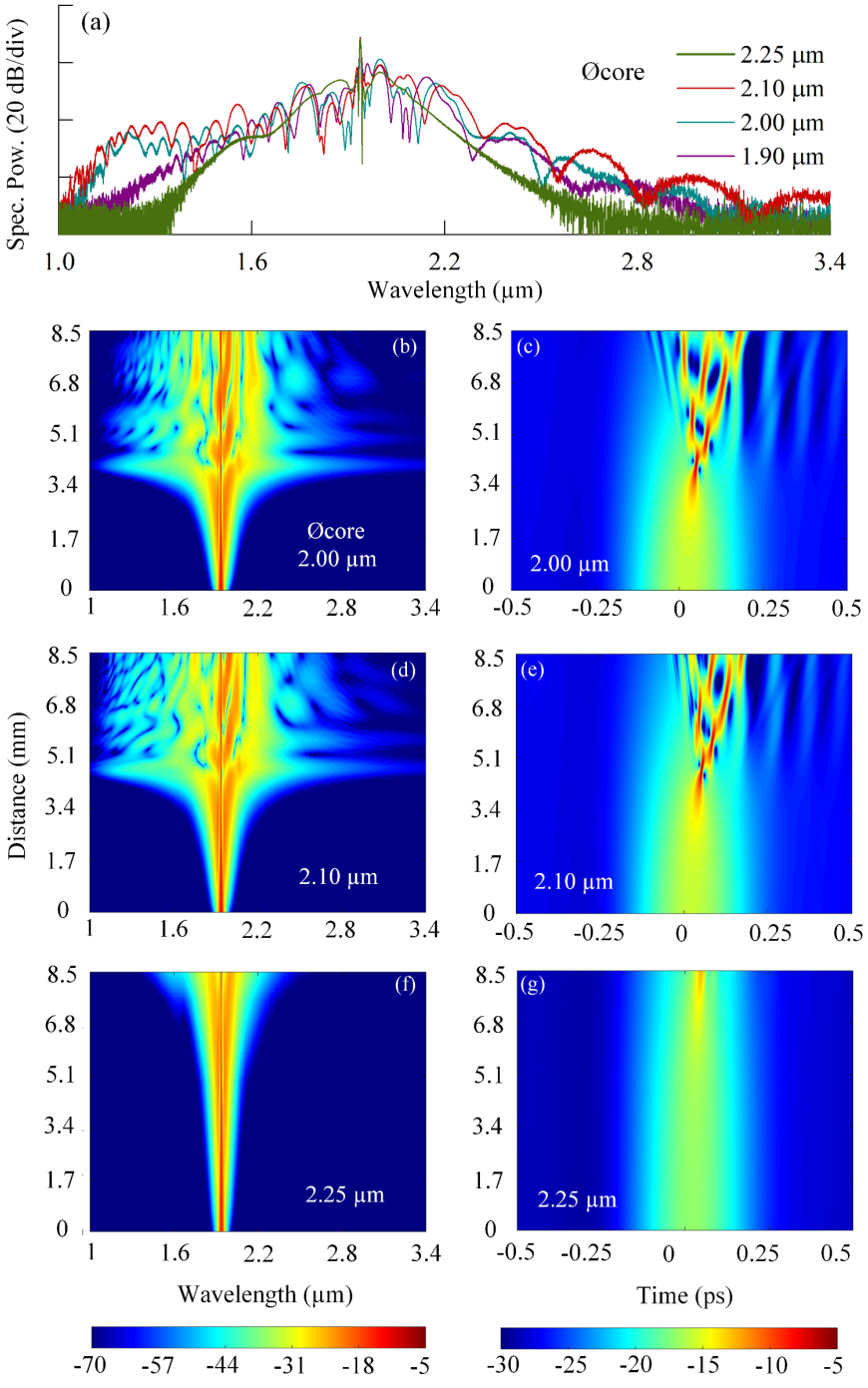

Figure 6.5. (a) Simulated SC spectra for CD microwires with core diameter ranging from 1.90-2.25 µm for a peak power of 300 W. The evolution of the simulated (b), (d), (f) spectral and (c), (e), (g) temporal pulse profiles for the CD taper with micowire core diameter of 2.00 µm, 2.10 µm and 2.25 µm, respectively. The color bars give the normalized power density in decibels.

To further understand the spectral broadening mechanism of the SC light, numerical simulations are performed by solving the GNLSE using SSFM, combined with adaptive step size. Dispersion order up to 8th order, Raman effect and self-steepening are taken into consideration. The wavelength dependence of waveguide nonlinearity is also included in the simulation. Fig. 6.5 (a) shows the simulated SC for a peak power 300 W. Fig 6.5 (b)-(e) illustrate the pulse evolution along the propagation length for the microwire core diameter of 2.0 µm, 2.10 µm and 2.25 µm respectively. As the microwire core diameter increases from 2.0 µm to 2.10 µm, fission length increases from 3.75 mm to 4.85 mm due to the increase of β_2. For the microwire of 2.10 µm core diameter, as the input pump pulse undergoes soliton fission, it generates DWs centered at 1.15 µm wavelength. As the resulting fundamental solitons experience frequency shift towards MIR, the phase matching condition is no longer satisfied and the energy transfer to DW ceases (see fig. 6.4 (a)). The initially generated DWs interact with the Raman solitons through cross-phase modulation and four-wave mixing with further propagation, thus flattening the blue portion of the SC [45], [206].

6.4 Supercontinuum generation in dispersion varying microwire

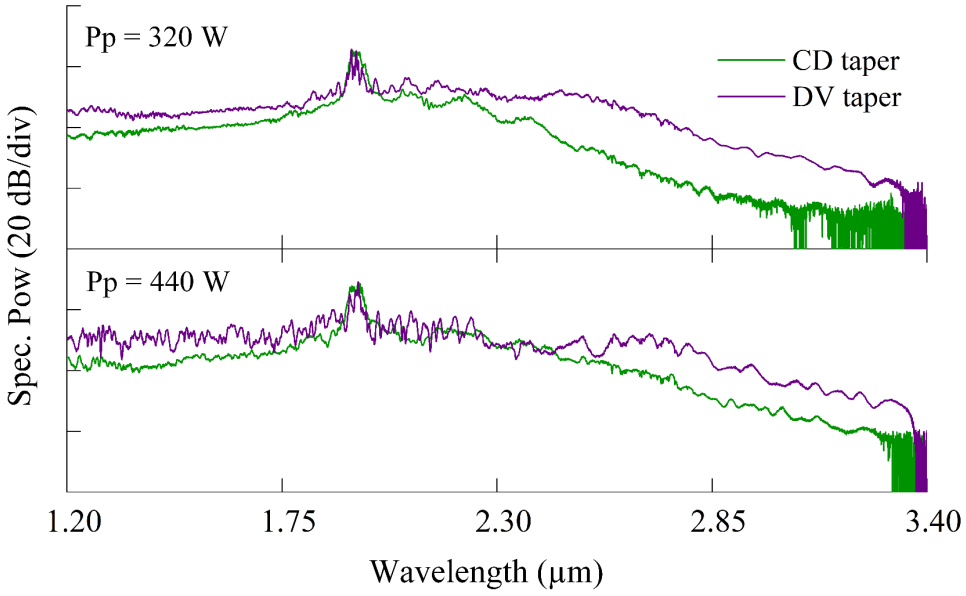

Figure 6.6. Measured SC for CD and DV taper at two levels of pump power, 320 W and 440 W. The CD taper has a microwire section core diameter of 2.10 µm.

Based on the characteristics of total dispersion, the DV taper is designed. The DV taper includes a uniform section with a core diameter of 2.10 µm and a length of 0.45 cm, followed by a non-uniform section with a core diameter that increases linearly from 2.10 µm to 3.20 µm within a length of 0.4 cm. Fig. 6.6 shows the generated SC spectrum for the DV taper at pump powers of 320 W and 440 W, respectively. It generates a SC with 30 dB bandwidth spanning from 1.20-2.85 µm and 1.20-2.98 µm for both power levels and clearly outperforms the broadest SC generated by the best CD taper. The signal power is enhanced by 4.3 dB and 2.5 dB in the shorter and longer wavelength side of the pump wavelength, respectively, resulting in an extension of SC bandwidth by 262 nm.

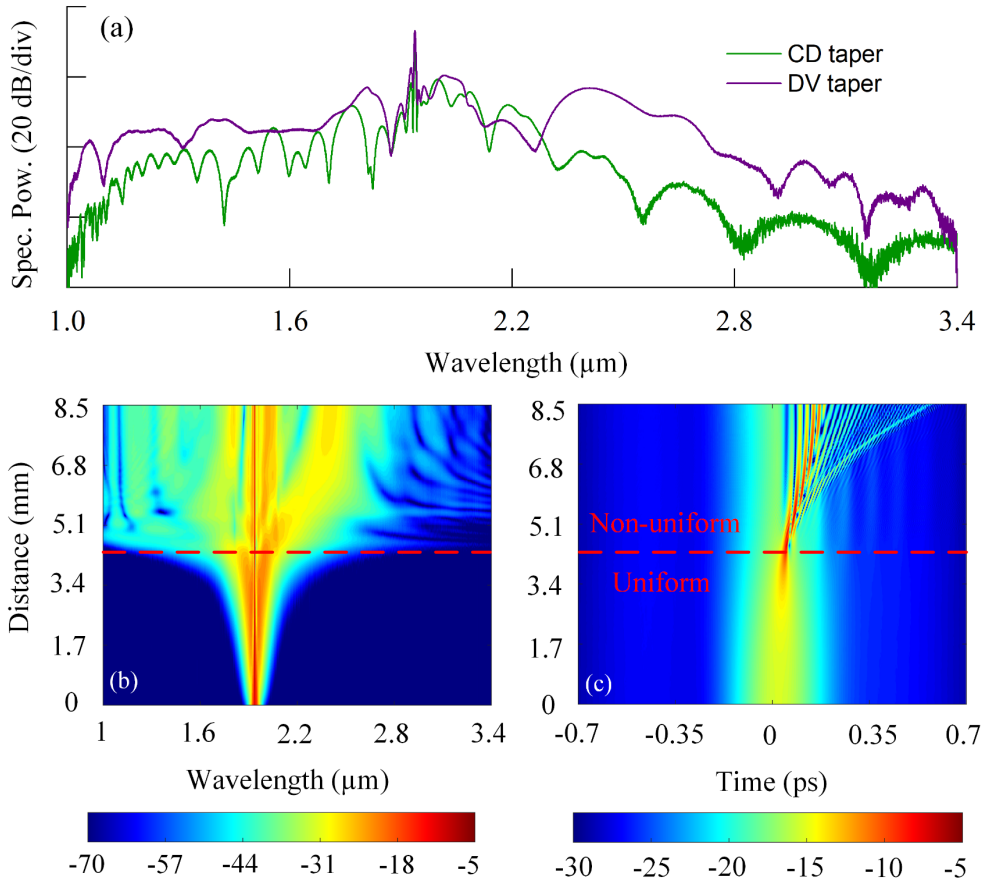

Figure 6.7. Simulated SC spectra for the DV and the CD taper for a peak power of 300 W. Pulse evolution in (a) spectral and (b) temporal domain along the length of the DV taper. The red dashed line separates the uniform and the non-uniform section of the DV taper. The color bars give the normalized power density in decibels.

The simulation of the SC generation in the DV taper shown in fig. 6.7 (a) agrees well with the experiment. Fig. 6.7 (b) and (c) shows the spectral and temporal evolution as the pulse

propagates through the both section of the microwire. It is seen that the higher order pump soliton breaks into multiple pulses through soliton fission at the end of the uniform section. In the non-uniform microwire section, the β_2 decreases along the propagation length (see fig. 6.2 (a)), resulting in an increase in the soliton number. Thus, to become fundamentals solitons again, these higher order solitons shifts to further into MIR, where the β_2 is higher and extends the longer edge of the SC [200][164]. At the same time, the non-uniform structure also causes a continuous modification of the DW phase matching conditions (see fig 6.4. (a)- (d)). This

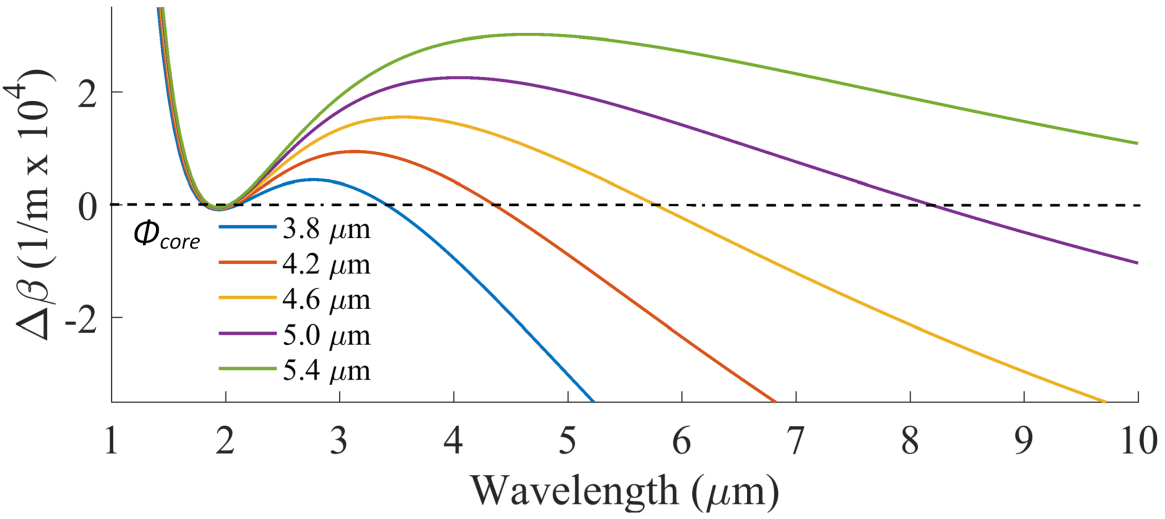

Figure 6.8: DW phase matching curves as a function of microwire core diameter. Zero crossings indicate the DW generation wavelength.

allows the solitons to remain phase matched with the DWs while being frequency shifted and transfer energy continuously towards the shorter wavelength edge. Fig. 6.7 (b) shows that the spectral power gradually grows within the wavelength range of 1.0-1.9 µm while propagation in the non-uniform section.

The DV microwire is designed to phase match the solitons only to the DW in the shorter wavelength side of the pump since our optical spectrum analyzer is limited within 1.2-3.4 μm wavelength. In figure 6.8, it is observed that the second zero dispersion wavelength of the wire shifts towards the longer wavelength with increasing diameter, hence can be used to phase match for DW generation continuously towards longer wavelength in a non-uniform section of increasing diameter.

6.5 Summary

In conclusion, SC generation in ChG DV microwire is presented. Both experiments and simulations have been performed to show the contribution of DV design in enhancing the efficiency of SC generation process. The optimized SCs are reproducible (appendix 10.5) and spans within the spectral range of 1.2-2.98 μm and outperforms the SC generated by the CD tapers. Applications of this compact MIR source include spectroscopic analysis and pollution monitoring.

7 Mode-locked laser based on nonlinear polarization rotation in a chalcogenide microwire

This chapter discusses the development of a fiber laser at a wavelength of 2 μm that is mode-locked thanks to nonlinear polarization rotation (NPR) in a ChG microwire. The high nonlinearity of the microwire leads to a combined reduction in mode-locking threshold power and cavity length compared to any all-silica NPR based mode-locked lasers. In the continuous wave mode-locking regime, the laser generates stable, tunable solitons pulses. In the Q-switched mode-locked regime, it allows single and multiwavelength pulses, tunable central wavelength and tunable multiwavelength separation. The result of this chapter has been published in [207]–[209].

7.1 Introduction

Mode-locked thulium-doped fiber lasers (TDFL) operating in 2 μm wavelength range find growing number of applications, including frequency conversion to further into MIR through either down conversion [210] or supercontinuum generation [113], [181], [211], sensing and spectroscopy [212], [213], medicine [214]–[216], material processing [217], particle acceleration [218] and attosecond physics [219]. In 1995, the first demonstration of TDFL was reported where, 500 fs and 13.7 pJ pulses were obtained using NPR mode-locking in a free space cavity design [220]. Soon after, an all-fiber semiconductor saturable absorber mirrors based mode-locked laser was presented that generated 190 fs and 8 pJ pulse train [221]. Since then, TDFL have been mode-locked using real saturable absorber such as carbon nanotube [222]–[225], graphene [226], [227], black phosphorus [228], MoS_2 [229], as well as artificial nonlinear saturable absorber, such as nonlinear amplifying loop mirror [230], [231], stretched-pulse operation [232] and NPR [233], [234], thus generating pulses from tens of femtoseconds

to a few picoseconds with energies up to ~100 nJ (A detailed review can be found in [235], [236]).

NPR effect, reported first time by Dahlstrom in 1972 [237], relies on the intensity dependent rotation of the polarization in a fiber. In a birefringent fiber, pulse components propagating in two orthogonal modes interact by applying an intensity dependent phase shift on each other by means of SPM and XPM. The addition of a polarizer after this interaction plays the role of saturable absorber, favoring the parts of the pulse which are best aligned with the polarizer, and attenuating the others [238], [239]. The NPR based mode-locking concept is demonstrated in fig 7.1. NPR effect is preferred mode-locking technique due to its fast saturable absorption that ensures efficient pulse formation and long-term stability [240]. NPR also allows several pulse generation regimes such as continuous wave mode locking (CWML) [241]–[243], Q-switched mode locking (QML) [244], [245] and multi-wavelength multi-pulse [246][247] regime, with each finding technological applications. The QML pulses exhibit higher peak power compared to CWML pulses while retaining ultrashort pulse width and have potential application in micromachining and medical surgery [248]. Multiwavelength lasers find applications in optical fiber sensing [249] and precision spectroscopy [250].

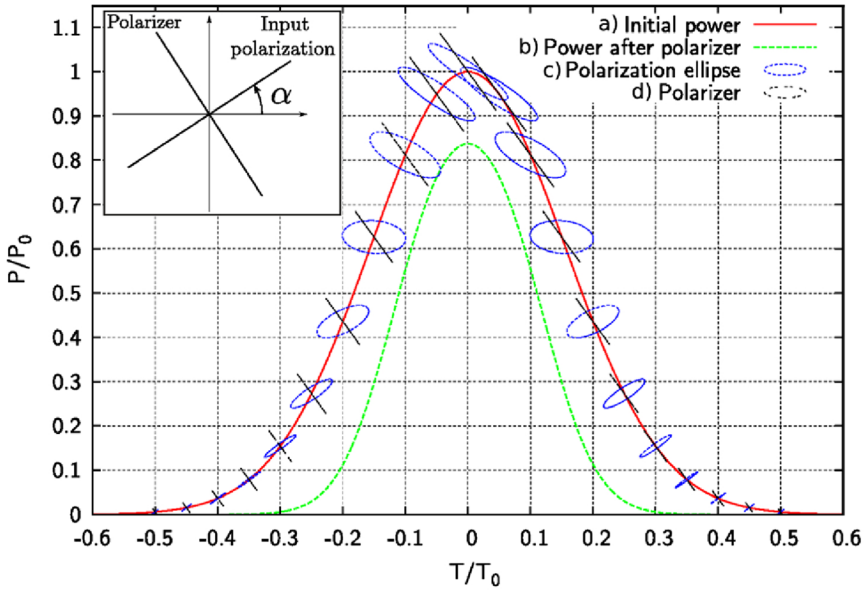

Figure 7.1: Illustration of NPR effect. Initial polarization angle is given by α. After propagation in the nonlinear medium, the polarization evolves spatially along the pulse due to XPM and SPM. Afterwards the pulse passes though polarizer aligned at an angle of α+90º, resulting in pulse shortened in time (green) (reproduced from [239]).

#	P_{th} (mW)	L_{Cav} (m)	L_{NLM} (m)	Refs.
1	240	22	17	[251]
2	330	80	70	[252]
3	800	67	50	[234]
4	1000	65	50	[243]
5	1140	17.6	8	[233]
6	230	9.5	0.1	This chapter

Table 7.1. Length and power values of mode-locked TDFL based on NPR. P_{th}: Pump threshold power, L_{Cav}: cavity length, L_{NLM}: nonlinear medium length.

In conventional all-silica TDFLs, tens of meters of silica fibers are paired with watt level of pump power to reach the nonlinearity threshold of silica glass and trigger NPR mode-locking [233], [234], [253]. A long cavity is usually associated with an increased sensitivity of the laser to environmental fluctuations as well as a relatively low repetition rate. Table 7.1 summarizes the specifications of NPR based all-silica TDFLs available in the literature, namely the power threshold, cavity length, and nonlinear medium length. Wang *et al.* demonstrated the lowest mode-locking threshold to this date, a value of 240 mW in a 22 m long fiber cavity, resulting in repetition rate of 9.78 MHz [251]. It can be observed that further reduction of the cavity length requires a significant increase of pump power. However, one method to develop a more compact and stable laser along with a simultaneous reduction in power consumption is to use a medium of increased nonlinearity with respect to silica, to locally trigger NPR. As_2S_3 glasses are perfect candidates for such applications due to their exceptionally high nonlinear refractive index that is more than two orders of magnitude beyond silica glass [165]. In addition, As_2S_3 microwire further enhances the γ by up to four orders of magnitude compared to single mode silica fiber [39], [60], [61]. Therefore, to obtain the same amount of nonlinear phase shift ($\Phi = \gamma PL$), the optical power (P) and propagation length (L) can both be reduced with an As_2S_3 microwire compared to a silica fiber. Additionally, the adjustable chromatic dispersion of the ChG taper [62], [63], [170] allows to balance the net cavity dispersion, a crucial parameter for versatile pulsed operation regimes [254][255]. Al Kadry *et al.* demonstrated NPR mode-locking

from an As_2S_3 microwire at a wavelength of 1.55 μm. The resulting fiber laser featured soliton and noise-like pulse emission, as well as multi-wavelength emission due to Lyot filtering effect [256]. For this purpose, the cavity and nonlinear medium lengths were 26.5 m and 10 cm, respectively, and the threshold signal power was 11 mW. The operation of such ChG based mode-locking technique in the wavelength band of 2 μm as well as the potential improvement in terms of P_{th}, L_{cav} and compatibility with multiple laser operation regimes remain to be investigated.

This chapter demonstrates a low power threshold and high repetition rate NPR mode-locking from a ChG microwire at a wavelength of 2 μm. The high nonlinearity of the device results in a reduced mode-locking threshold of 230 mW and a shortened cavity length of 9.45 m, compared to the all-silica based TDFLs mentioned in table 7.1. The laser can operate in both QML and CWML pulse generation regimes. The QML operation regime generates multiwavelength pulses by the combined effect of QML and intra-cavity optical parametric oscillation (OPO) showing tunable central wavelength, tunable wavelength separation and variable number of laser wavelengths. The CWML operation generates stable solitons with tunable central wavelength from 1.877 μm to 1.945 μm. This demonstration is a major step towards the development of compact and low threshold TDFLs operating in QML and CWML operation regimes.

7.2 Device and experimental setup

Fig. 7.2 (a) shows a schematic of the proposed fiber laser. It consists of a 20 cm long thulium-doped silica fiber (Coractive DCF-TM-6/128), core pumped by a C-band amplifier through a WDM coupler. An 80/20 fused fiber coupler serves to extract pulses from the laser cavity via the 20% output. The cavity also includes two polarization controllers and a polarizer-isolator that ensure a unidirectional operation of the laser. A microwire serves as a nonlinear medium that triggers and maintains self-pulsation through NPR. The extracted pulses from the laser cavity are characterized with Yokogawa- 6375 OSA and ET- 300A- 2 GHz photodetector and Agilent DSOX3034A- 350 MHz oscilloscope.

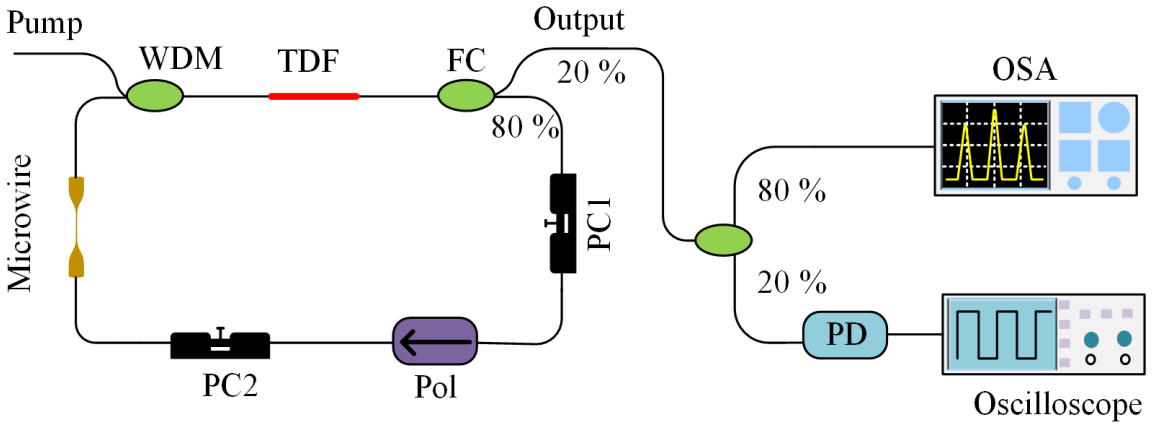

Figure 7.2. (a) Experimental setup of the proposed mode-locked laser. WDM, wavelength division multiplexer; TDF, thulium doped fiber; FC, fiber coupler; POL, polarizer; PC, polarization controller; PD, photodiode.

The nonlinear device is subdivided into a 10 cm long microwire section where nonlinear process occurs, two 2.5 cm long fiber section for efficient coupling to silica fiber, and two 3 cm long transition sections that ensure an adiabatic modal conversion in between fiber and microwire sections. The group GVD of the device is given by $\beta_{2,fiber}$=0.33 ps^2/m for the fiber and average $<\beta_{2,tran}>$=0.31 ps^2/m for the transition sections. The GVD of the microwire section can be engineered into zero, anomalous, or normal dispersion by choosing an appropriate core diameter. In this experiment, the microwire section is designed with a diameter of 2.0 µm, leading to an anomalous dispersion of $\beta_{2,wire}$=-0.07 ps^2/m at a wavelength of 1.95 µm (fig. 7.3 (a)). The cavity comprises of 9.23 m long SMF-28 fiber that are being essentially included due to the fiber optic components in the cavity and 20 cm long TDF. The GVD of the SMF-28 and the TDF are $\beta_{2,SMF}$ =- 0.07 ps^2/m and $\beta_{2,TDF}$ =- 0.09 ps^2/m, respectively. Therefore, the laser operates with net anomalous dispersion of 0.63 ps^2.

The waveguide nonlinearity parameter of the microwire is γ=3.4 W^{-1}m^{-1} at a wavelength of 1.95 µm (fig. 7.3 (a)), which is 9.68 × 10^3 times higher than that of silica fiber. The input and output facets of the microwire are polished and coupled to SMF-28 using UV epoxy. The total insertion loss of the ChG taper with two SMF-28 pigtails is 3.4 dB at a wavelength of 1.95 µm. From this loss, 0.5 dB per interface is due to Fresnel reflection and ~ 0.1 dB per interface is due to mode-mismatch in between ChG fiber and SMF-28, and ~ 4 dB of propagation loss in the microwire.

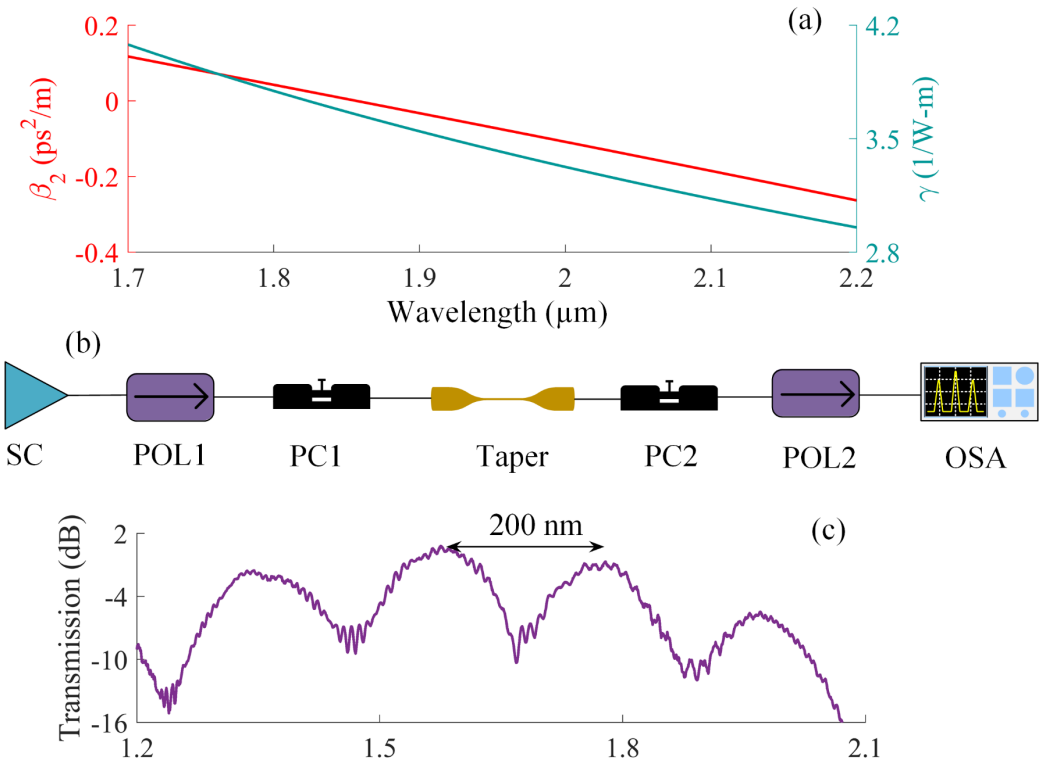

Figure 7.3. (a) Dispersion and waveguide nonlinearity parameter of As_2S_3-polycarbonate microwire; (b) Fixed analyzer setup for birefringence measurement; SC, supercontinuum source; POL, polarizer; PC, polarization controller; OSA, optical spectrum analyzer. (c) Wavelength dependent transmission spectrum.

The taper possesses linear birefringence due to residual stress applied by the polycarbonate cladding to the As_2S_3 glass during the microwire fabrication process. The magnitude of this birefringence is controllable over some extent by an adjustment of the fiber drawing temperature, and measured using the fixed analyzer method [257]. Fig. 7.3 (b) and (c) show the measurement setup and the wavelength dependent transmission through the fixed analyzer structure. Ripples observed in the transmission spectrum results from multimode interference due to the large refractive index contrast between the As_2S_3 core and polycarbonate cladding of the microwire. The main interference peaks are separated in wavelength by 200 nm, resulting in a modal birefringence, $B = \lambda^2/L\Delta\lambda$ =1.39 × 10^{-4}. Due to this birefringence, elliptically polarized light from polarization controller (PC2) in fig. 7.2 splits into two polarization components of unequal intensities along the slow and the fast axis of the microwire. Both components undergo different amount of nonlinear phase shift due to Kerr effect during their propagation inside the microwire section. As a result, there is a power-dependent rotation of the polarization state at the microwire output. Light passes through PC1 and reaches the

polarizer-isolator (POL), which only allows a linear polarization to pass though. Therefore, the combination of PC2-taper-PC1-POL acts as a fast saturable absorber for NPR mode-locking.

7.3 Q-Switched mode-locked laser

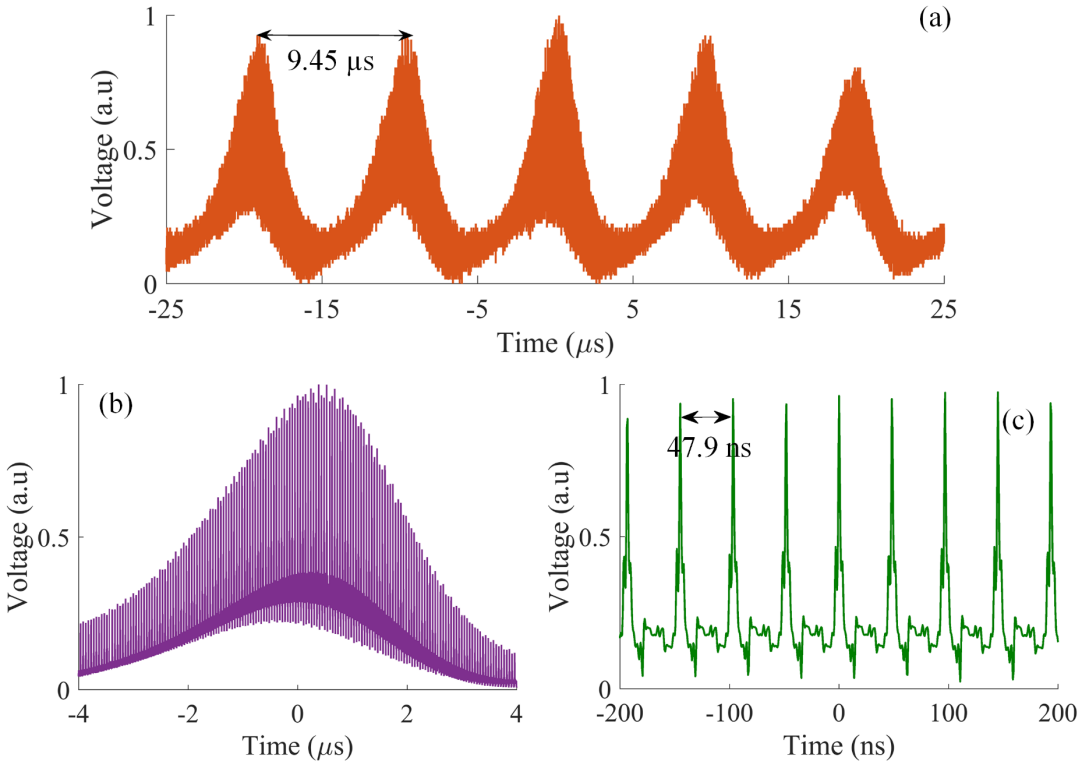

Figure 7.4. (a) Real-time oscilloscope trace of QML pulses in 50 µs timescale. (b) Envelope of the QML pulses. (c) Mode-locked pulse train under the Q-switched envelope.

As the pump power is increased from zero to 120 mW, the cavity starts lasing with CW emission. With an increase in pump power to 170 mW, the cavity switches to a QML regime. In this regime, mode locked pulses are modulated by long periodic Q-switched envelope [258], [259]. This results in an enhanced peak power of the central pulses in the mode-locked train with respect to pulses on the periphery [260]. Fig. 7.4 shows the power profile versus time in the QML regime. It is seen that that the Q-switched envelope repeats periodically every 9.45 µs, leading to a repetition rate of 105.8 kHz (fig. 7.4 (a)). Fig. 7.4 (b) shows a single Q-switched envelope with a FWHM of 4.12 µs. A close-up view of the ML pulses under the Q-switched envelope is shown in fig. 7.4 (c). The repetition rate of the ML pulses is 20.9 MHz, corresponding to the cavity round trip time of 47.9 ns, which is consistent with the total optical path length of 9.43 m (46.12 ns) of silica fiber and 21 cm (1.78 ns) of the As_2S_3 fiber.

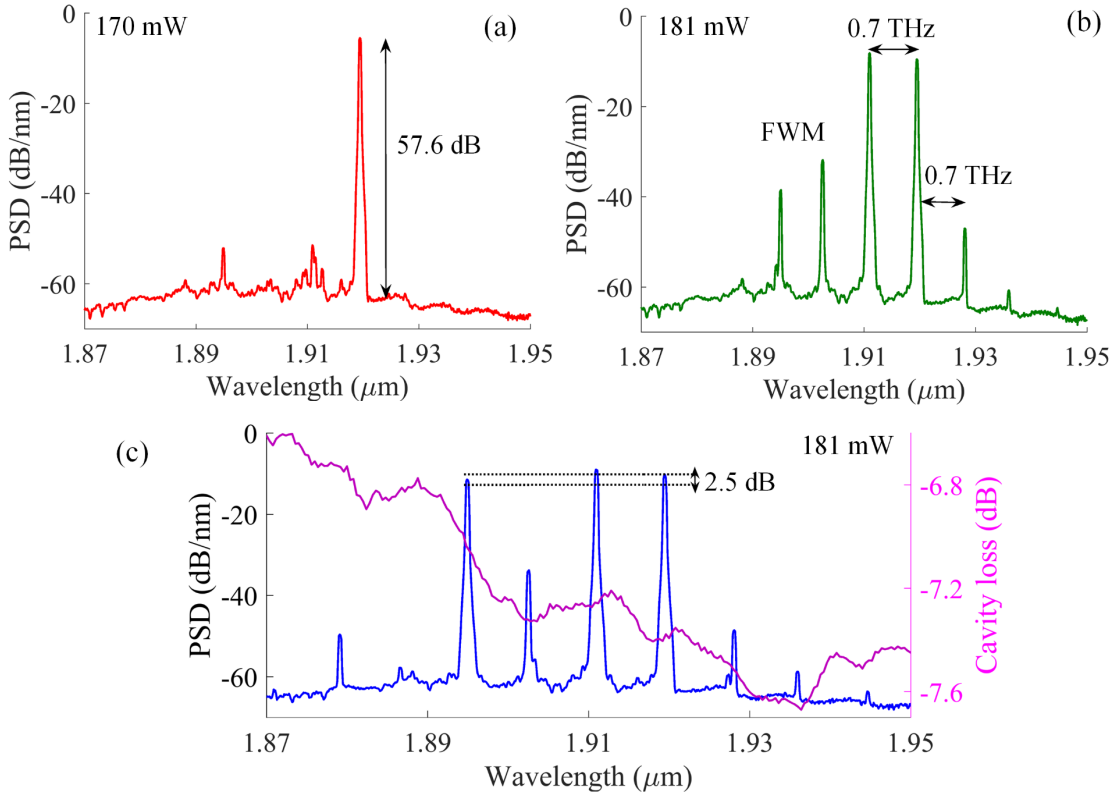

Figure 7.5. (a) Measured optical spectrum of the QML pulses at 170 mW pump power (b) Two lasing wavelength are generated due to combined effect of QML and OPO at 181 mW pump power. (c) Three wavelengths emission with identical pump power, however with different polarization state.

The optical spectrum corresponding to the QML signal of fig. 7.4 is shown in fig. 7.5 (a). The laser wavelength is centered at 1.919 µm with an optical signal to noise ratio of 57.6 dB, a level that is beneficial for sensitive spectroscopic applications. The anomalous GVD of the microwire also allows satisfying the phase matching condition for parametric side band generation [45]. As pump power increase, the burst of high power QML pulses serve as intra-cavity pump and generates parametric gain. For a pump power of 181 mW, the cavity shows lasing at a wavelength of 1.911 µm due to OPO (fig. 7.5 (b)). A wavelength converted signal due to stimulated FWM is also observed at 1.930 µm. Each of these central lasing wavelengths interact to generate cascaded FWM signals at 1.903 µm and 1.895 µm. Since parametric gain is polarization dependent, the PCs can be adjusted to properly align the emission line at 1.911 µm axis and generate a third emission line at 1.895 µm wavelength. The emission lines have equidistant spectral separation of 0.7 THz, which is clear indication of cascaded OPO operation. The emission lines are stable within a power difference of 2.5 dB among the lasing

wavelengths. Fig. 7.5 (c) shows that the total cavity loss is less on the shorter wavelength side due to the absorption loss pattern of the polycarbonate cladding [62]. For this reason, the cavity favors OPO mainly on the shorter wavelengths side of the QML pump centered at 1.919 µm wavelength. This result is the first demonstration of multi-wavelength laser operation due to the combined effect of QML and cascaded OPO. Take note that in the current cavity, although the PC1-taper-PC2-POL assembly also functions as a Lyot filter, as in [243], [256], [261] it plays no role in the manifestation of multiple wavelengths since birefringence is so low that it would lead to a free spectral range of 200 nm (fig 7.3 (c)).

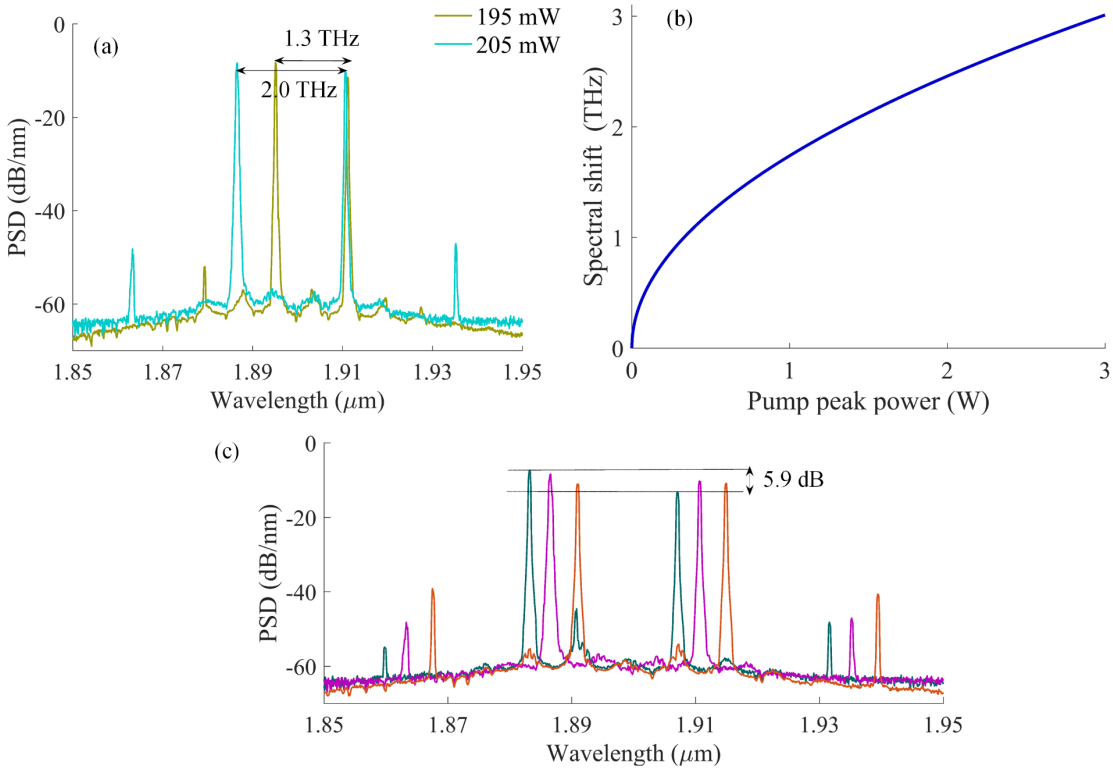

Figure 7.6. (a) Two wavelength emission measured with different polarization state and at pump powers of 195 mW and 205 mW. (b) Frequency detuning as a function of peak power in the As_2S_3 microwire (c) Tunable central wavelength measured with different polarization state at pump power of 205 mW.

Fig. 7.6 (a) shows that for two different pump powers of 195 mW and 205 mW, a frequency detuning of 1.3 THz and 2.0 THz are observed between emission lines, respectively. The adjustment of pump power results in the change of the phase matching condition, hence the OPO emission wavelengths [45], as shown in fig 7.6 (b). For a fixed pump power, the proper

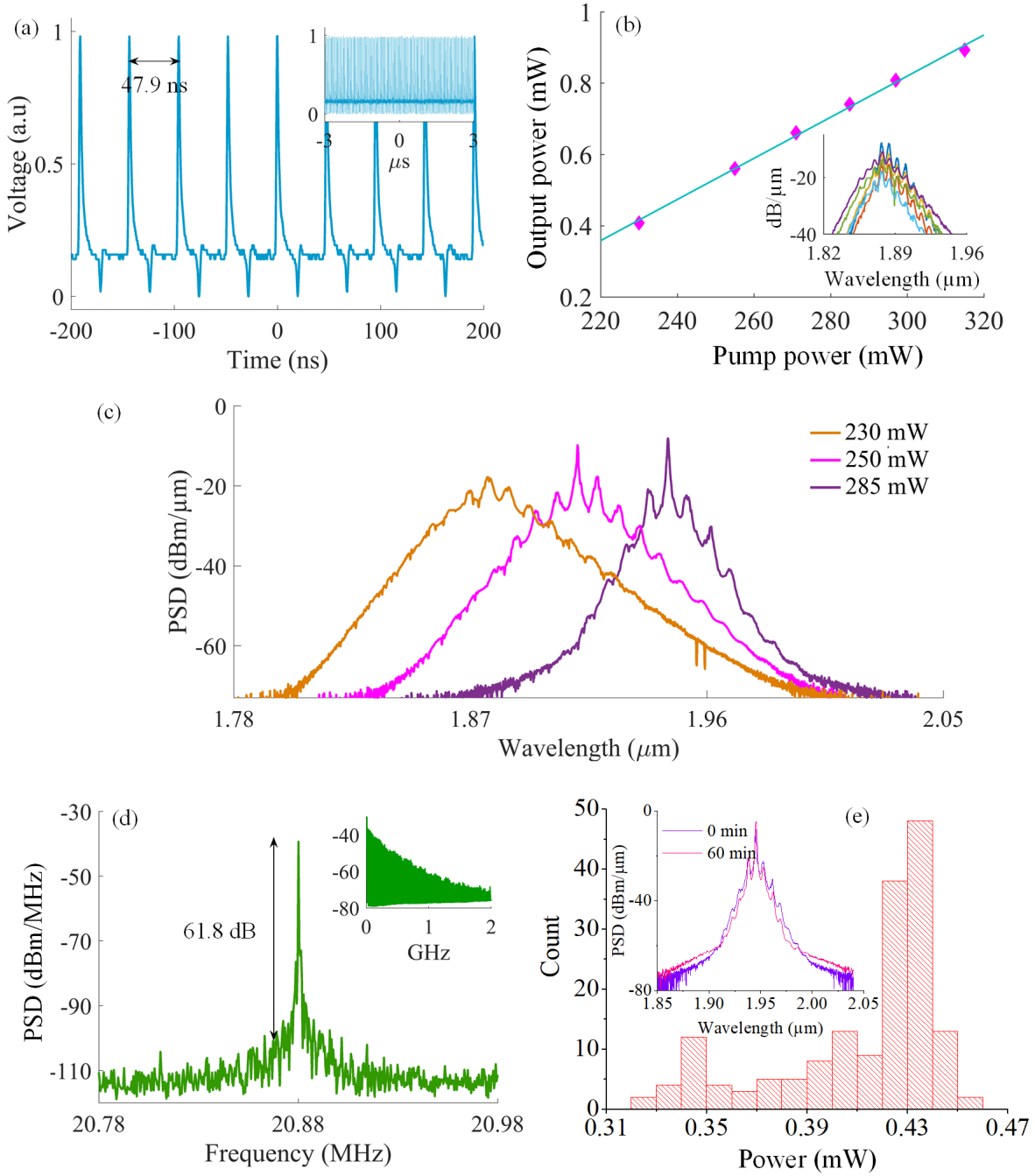

Figure 7.7. (a) Oscilloscope trace of CWML pulse train. Inset: Oscilloscope trace in 6 μs timescale. (b) Measured output power as a function of pump power. Inset: soliton spectral evolution with increasing pump power. (c) Tunable optical spectrum of the CWML pulses with increasing pump power. (d) RF spectrum in 0.2 MHz range. Inset: RF spectrum in a wide range of 2 GHz. (e) Power stability measurement. Inset: soliton spectrum at t=0 and t=60 min.

adjustment of the PCs allows the tuning of the wavelength dependent transmittivity function [262], therefore allowing the tuning of emission line central wavelength. Fig. 7.6 (c) shows that

for a pump power of 205 mW, the QML emission wavelength is tuned from 1.915 μm to 1.907 μm. As a result, the OPO center wavelength shifts from 1.891 μm to 1.883 μm.

7.4 Continuous wave mode-locked laser

CWML is obtained from increasing the pump power above the threshold of 230 mW and proper adjustment of the PCs. In CWML, pulses preserve constant properties i.e., peak power, duration, and energy, from one pulse to another. Fig. 7.7 (a) shows an oscilloscope trace of the train of solitons while the inset shows the same signal over an extended time window. The pulses are separated by 47.9 ns in the time domain, corresponding to the fundamental cavity repetition rate of 20.9 MHz. Wavelength tunability is obtained mainly by adjusting the polarization dependent loss in the cavity via adjustment of the PCs. Since the cavity loss is also wavelength dependent, the pump power needs to be controlled as well. Fig. 7.7 (c) shows the different soliton spectra for three different pump powers. By increasing the pump power from 230 mW to 285 mW and adjusting the PCs, center wavelength of the soliton can be switched from 1.877 μm to 1.945 μm, respectively. The laser operates with a total anomalous cavity dispersion. Kelly sidebands observed in the spectrum support the soliton behavior of these emission spectra. The soliton centered at a wavelength of 1.877 μm has an average power of 0.41 mW, a 3 dB spectral width of 4.67 nm and measured pulse duration of 2.4 ps. Fig. 7.7 (b) shows the output power as a function of input pump power, indicating a slope efficiency of 1.32 %. The inset shows the corresponding spectral evolution of the soliton as the pump power increases. The generated pulses are presumably chirped due to residual dispersion in the laser cavity. The laser stability is analyzed by sending the soliton pulses to a radio-frequency (RF) spectrum analyzer. Fig. 7.7 (b) shows the RF spectra measured with a resolution bandwidth of 100 Hz. The signal to noise ratio of 61.8 dB is obtained at the fundamental frequency. The inset shows of the same electrical spectrum within a 2 GHz span, measured with a resolution bandwidth of 5 MHz. The graph shows a smooth variation in the total envelope, certifying a stable mode-locking operation [8, 48]. Fig. 7.7 (e) shows the measured average power of the laser pulse centered at 1.945 μm wavelength for a duration of one hour at an acquisition rate of 33 mHz. The calculated coefficient of variation (standard deviation/mean) of the power is 7.8 %, which indicates a reasonable stability of the system. The slight optical power drift could occur from environmental temperature change.

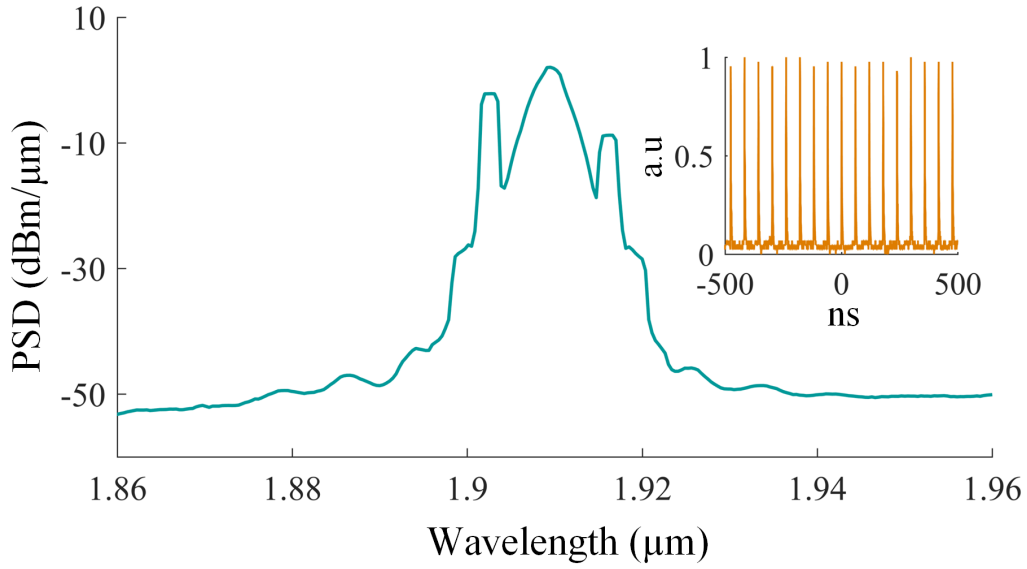

Figure 7.8: Optical spectrum of the CWML pulse in a all-silica cavity. Inset: oscilloscope time trace.

To understand the impact of ChG tapered fiber in the reduction the mode-locking threshold, the tapered fiber is replaced by a 3 m long silica fiber and increased pump power from C-band amplifiers. Mode-locking was achieved at a significantly high pump power of 1.35 W. Fig. 7.8 shows the soliton spectra centered at 1.910 µm while the inset shows the oscilloscope trace of the soliton train. The replacement of the tapered fiber with a silica fiber increases the pulse separation to 60.1 ns, resulting in a decrease of the cavity repetition rate to 16.6 MHz. This clearly indicates that the use of a ChG tapered fiber simultaneously shortens the nonlinear medium length by a factor of 30 and reduces the mode-locking threshold by a factor of 5.6, compared to an all-silica cavity.

7.5 Summary

In summary, the operation of a 2 µm mode-locked fiber laser based on NPR in ChG microwire has been demonstrated. The high nonlinearity of the taper results in a reduced threshold pump power of 230 W and a shorten cavity length of 9.45 m, compared to the all-silica based mode-locked laser. The laser generates multiwavelength emission with variable number of lasing lines (1-3), tunable central wavelength from 1.883 µm to 1.915 µm and tunable frequency separation from 0.7 THz to 2.0 THz. The multiwavelength operation has a threshold pump power of 179 mW and occurs from the combined effect of QLM and intra cavity OPO. The

CWML has a threshold pump power of 230 mW and generates stable tunable solitons from 1.887 μm to 1.911 μm. This technique can also be used to obtain mode-locking in ZBALN fiber laser system in the wavelength range of 2.7-3.5 μm. However, the As_2S_3/polycarbonate microwire is not transparent in that wavelength range due to the polymer cladding. It needs to be replaced by either a suspended core As_2S_3 or a bare As_2S_3 microwire.

8 All-fiber mid-infrared optical parametric oscillator

The wide range of applications in the MIR has intensified the research effort to develop novel optical sources. Optical parametric oscillators (OPO) based on glass fibers has shown great potential as an efficient and reliable approach towards this end. All-fiber OPO based on highly nonlinear silica fiber have shown record performance in the telecommunication wavelength band, however the strong material absorption of silica glass at wavelengths >2 μm limits its applicability in MIR. This chapter reports for the first time, a MIR OPO that overcomes this issue by designing the laser cavity entirely out of soft-glass fiber. The cavity consists of an As_2Se_3 low loss single-mode fiber coupler, an As_2Se_3 highly nonlinear and dispersion engineered microwire gain medium and commercially available ZBLAN delay fiber. From a compact fiber laser pump emitting at 1.95 μm wavelength, the OPO generates both Raman assisted and pure parametric gain and oscillates with tunable Stokes emission lines within 2.023-2.048 μm and 2.088-2.139 μm wavelength, respectively. This demonstration indicates the vast potential of ChG fibers in developing fully fiberized OPOs operating at MIR wavelengths. The results of this chapter include the publications [263]–[265].

8.1 Introduction

As mentioned in section 2.5, parametric gain builds up in a nonlinear medium from the phase matching between optical waves of different frequency. When a parametrically amplified signal circulates in laser cavity and experiences a gain that exceeds the total roundtrip cavity loss, the intensity of the signal grows exponentially with pump power, thus resulting in parametric oscillation. OPOs are one of the most efficient and reliable optical sources that allow access to broadly tunable and exceptional set of wavelength bands. Since its first demonstration 1965, OPOs have been realized in variety of configurations with nonlinear materials of second order $\chi^{(2)}$ and third order $\chi^{(3)}$ susceptibility. The OPOs that are based on second order nonlinear materials including orientation-patterned *GaAs* [266], $ZnGeP_2$ [267], periodically poled $LiNbO_3$

[268], *β-BaB_2O_4* [269], *LiB_3O_5* [270] and KTP [271] are capable of providing intense radiation across an extended spectral range, however these table-top free-space systems are generally bulky and susceptible to misalignment. In contrast, OPOs realized on $\chi^{(3)}$ material including HNLF [272], microstructured [273] and photonic crystal fibers [274] provide the additional advantage of compactness, robustness, high beam quality and flexible integration with external fiber systems, compared to the free space counterparts. All-fiber OPOs emitting in MIR wavelength find applications in in both fundamental science and engineering including precision spectroscopy, medical surgery, sensing, LIDAR, and free space communication [19], [275]. In the past, the major demonstrations of OPOs in near-infrared wavelength range has been enabled in systems that requires hundreds of meters long highly nonlinear silica fibers [276], [277]. However, such systems are incompatible in MIR wavelength due to the strong attenuation and low nonlinearity of the silica fiber.

In contrast to silica fibers, soft glass fibers e.g. ChG and fluoride fibers are more desirable for MIR applications, since their optical transmission spectrum extends to wavelengths up to 15 μm and 9 μm, respectively [33]. As demonstrated in chapter 3 and 4, ChG microwires in particular, are also excellent nonlinear engines for generating parametric gain due to their high nonlinearity and engineerable chromatic dispersion. Ahmad *et al.* developed the first Raman-assisted FOPO using an As_2Se_3 microwire as a gain medium and generated parametric sidebands detuned at 6.4 THz from the pump wavelength of 1.552 μm [278]. Abdukerim *et al.* made a FOPO based on pure parametric gain from the pump wavelength of 1.938 μm using an As_2Se_3 microwire as a gain medium, resulting into Stokes and anti-Stokes sidebands detuned by 5.2 THz from the pump [279]. The presence of silica-based optical fibers in the resonant cavity prevented the tunability of the above FOPOs to reach wavelengths >2 μm.

The gain and transmission of ChG microwires is however not limited to the transmission window of silica. Godin *et al.* demonstrated far-detuned modulation instability from pumping at a wavelength of 2.6 μm in an As_2Se_3 microwire, leading to gain at wavelengths up to 3.5 μm, or 30 THz of frequency detuning[100]. Li *et al.* demonstrated far-detuned wavelength conversion from pumping at a wavelength of 1.94 μm in an As_2Se_3 microwire, leading to gain at wavelengths up to 2.85 μm, or 49 THz of frequency detuning [99]. Alamgir *et al.* demonstrated a silica-As_2Se_3 hybrid wavelength conversion system and obtained a frequency detuning of 80 THz from a pump wavelength of 1.55 μm, including 41 THz of wavelength conversion from parametric gain [120]. From the all-fiber parametric gain provided by ChG,

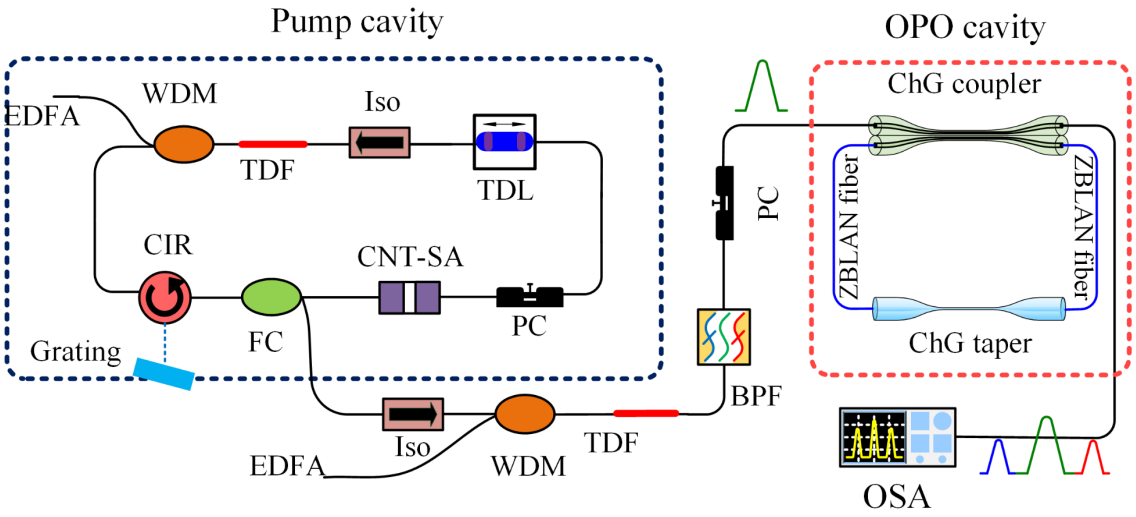

Figure 8.1. Schematics of the experimental setup. EDFA, erbium-doped fiber amplifier; WDM, wavelength division multiplexer; FC, fiber coupler; TDL, tunable delay line; TDF, thulium doped fiber; Iso, Isolator; CIR, Circulator; CNT-SA, Carbon nanotube saturable absorber; BPF, Band-pass filter; PC, polarization controller; OSA, optical spectrum analyzer

all that is missing to the fabrication of a MIR compatible FOPO is a resonant cavity. We recently demonstrated the fabrication of the first single-mode ChG fiber couplers, taking the form of power dividers/combiners, wavelength division multiplexers/demultiplexers, and polarization beamsplitters/combiners [280]–[282]. The coupler is an important building block of a resonant cavity, enabling the insertion of pump light and the extraction of the laser light.

In this chapter, the first demonstration of fully fiberized MIR OPO is shown, where the laser cavity is designed entirely out of soft-glass fibers. The cavity consists of ChG fiber coupler, ChG parametric gain medium, and ZBLAN delay fiber that provides MIR compatibility up to a wavelength of 5 µm, limited by the transmission of the ZBLAN fibers. Two separate experiments are conducted to demonstrate the design flexibility and the great potential of such cavity deign. In the first experiment, the OPO oscillates from Raman-assisted parametric gain with a 117.5 pJ of average threshold pump energy, 0.2 % of slope efficiency and 2.023-2.048 µm Stokes wavelength tunability. In the second experiment, the gain originates from a pure parametric process and generate signals tunable from 2.088-2.139 µm (Stokes) and 1.785-1.834 µm (anti-Stokes).

8.2 Device and Experimental setup

8.2.1 Carbon nanotube mode-locked fiber laser

Fig. 8.1 schematizes the experimental setup used to generate parametric oscillation at MIR. The pump pulses are generated from a mode-locked thulium fiber laser. The gain medium is a 20 cm long *Tm*-doped silica fiber (Coractive DCF-TM-6/128) with a GVD β_2 of - 0.09 ps^2/m at 1.95 µm wavelength. The gain fiber is core pumped by a commercial erbium-doped fiber amplifier (PriTel LNHPFA-33) through a 1.55 µm / 1.95 µm WDM coupler. Mode-locking is achieved by carbon nanotube (CNT) saturable absorber [223], [225], [283], [284]. The CNTs used in this investigation are semiconducting single walled tubes, purchased commercially from Nanointegris. The material were synthesized using high pressure carbon monoxide method and dissolved in 90 % aqueous solution. The CNTs were polymer coated, with diameter and length distribution ranging from 1-1.7 nm and 0.3-4 µm respectively. The CNT dispersion was initially diluted with deionized water and sonicated for 1 hour to obtain well separated tubes. Afterwards 12 µL of solution was directly deposited on FC/PC fiber pigtail and dried in vacuum oven at 70° C temperature for 30 minutes. Upon drying, the CNTs were permanently deposited across the fiber facet. The power dependent absorption of the saturable absorber at 1.94 µm wavelength is measured with a commercial mode-locked fiber laser (AdValue AP-ML) and plotted in fig 8.2. The modulation depth and the pump saturation intensity are 8.8 % 7.3 MW/cm^2, respectively.

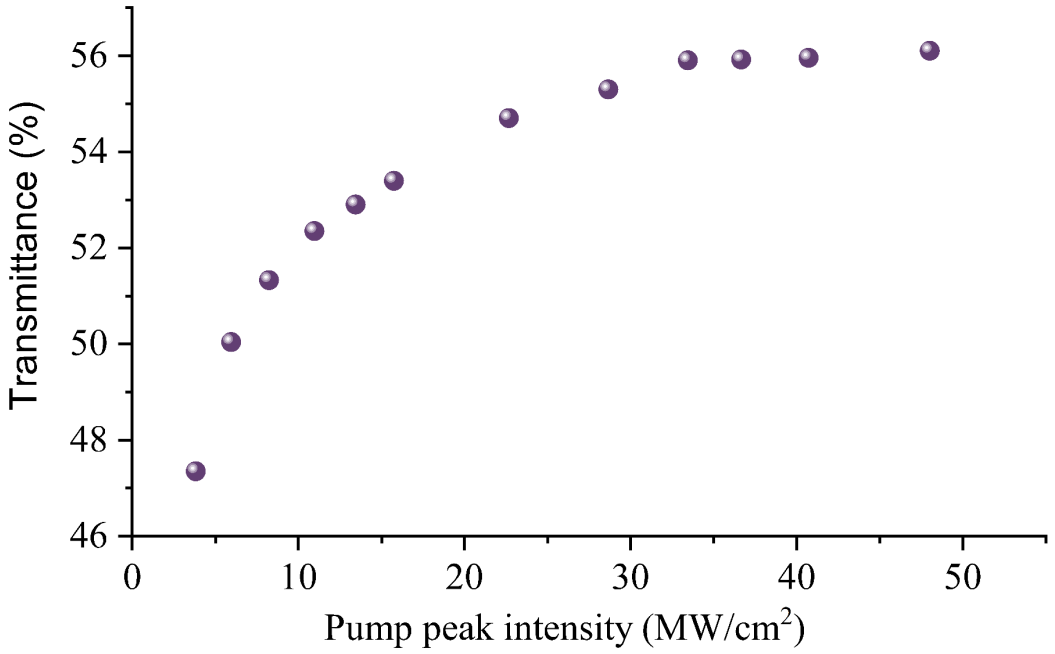

Figure 8.2. Measured power-dependent transmittance of the fabricated CNT saturable absorber.

A polarization independent isolator is spliced after the gain fiber that ensures the unidirectional operation of the laser. The tunable delay line allows a delay up to 330 ps which is used to precisely adjust the repetition rate of the pump laser according to the OPO cavity length. An in-line PC is employed to optimize the polarization state inside the cavity. The Gaussian BPF is designed using Littrow configuration and provides a wavelength tunability of 65 nm (1.888-1.953 μm) with a FWHM of 5 nm, as shown in fig 8.3 (a). A 80/20 coupler is used in the cavity to couple out 20 % of the intracavity light. Fig. 8.3 (b) shows the oscilloscope trace of the pulse train while the inset shows the same signal over an extended time window. The pulses are separated by 35.08 ns in the time domain. This corresponds to the fundamental cavity repetition rate of 28.5 MHz, which is consistent with the total optical path length of 7.18 m. Fig. 8.3 (c) shows the autocorrelation trace for the pulse centered at a wavelength of 1.936 μm. The strong anomalous dispersion of the cavity results in a relatively broad pulse width of 1.8 ps [224]. Fig. 8.3 (d) and (e) shows the measured parameters of the soliton centered at 1.936 μm for duration of an hour at an acquisition rate of 33 mHz. The stability of the system is indicated by the calculated coefficient of variation (standard deviation/mean) of the power and the center wavelength, that are 8.6 % and 0.0031 %, respectively.

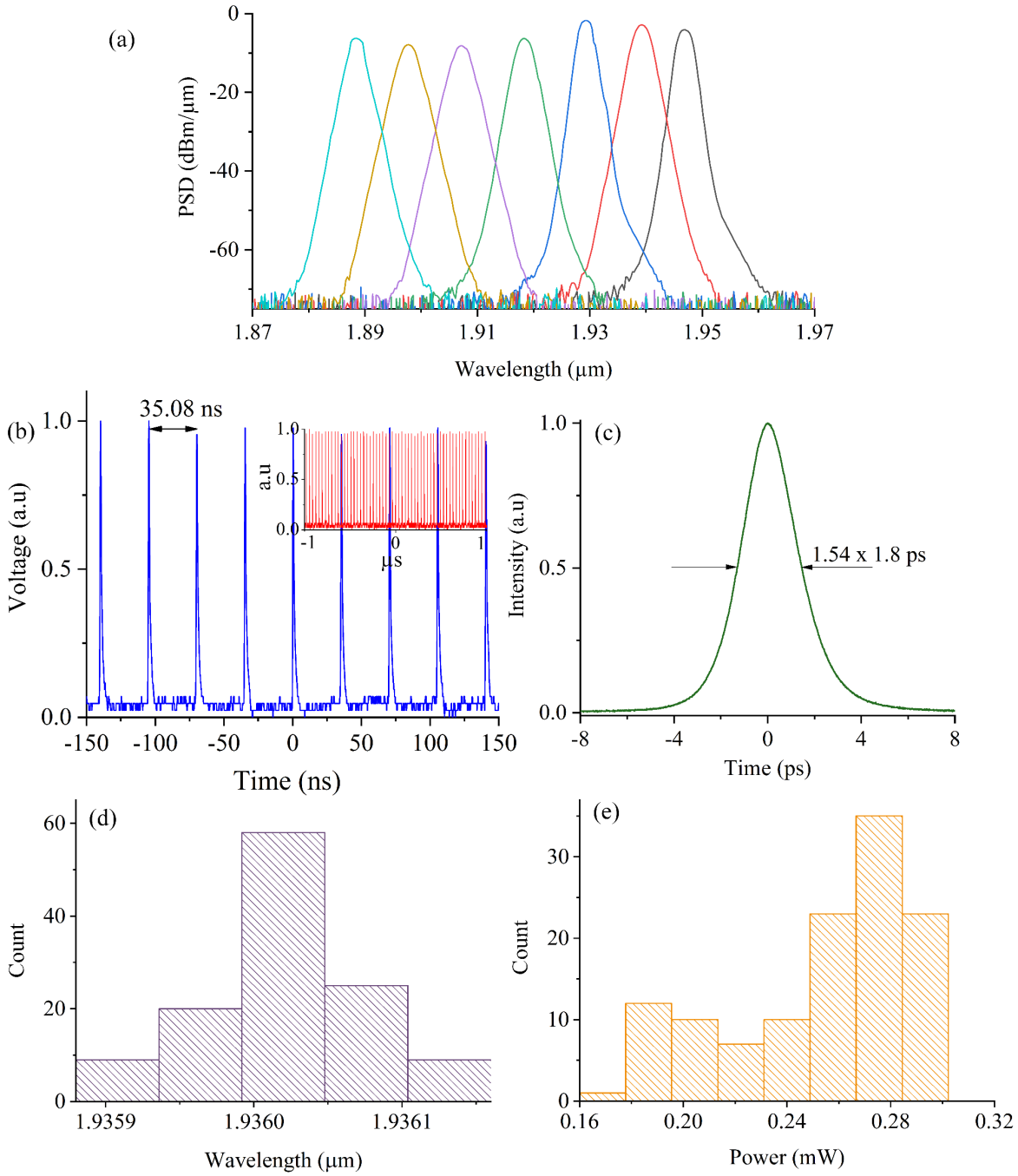

Figure 8.3. (a) Center wavelength tunability of the mode-locked laser. (b) Oscilloscope and (c) autocorrelation trace of the mode-locked pulse centered at a wavelength of 1.936 µm. (d) The stability measurement of the (d) center wavelength and (e) power of the laser.

The pulses are then amplified with a TDFA and filtered using a 2 nm FWHM tunable band-pass filter to eliminate the amplified spontaneous emission of the fiber amplifier. Due to spectral filtering, the final pump pulses are further broadened to a duration of 3 ps, measured using a femtorchrome FR-103XL autocorrelator. Since the parametric processes are polarization

dependent, a final PC is required to control the PC state of the pump pulses that are coupled into the OPO cavity. The OPO cavity consists of three passive fiber components, As_2Se_3 fiber coupler for in and out-coupling of the pump and the generated signals, respectively. The dispersion engineered As_2Se_3 tapered microwire that functions as the nonlinear medium to generate parametric gain. The ZBLAN fiber that serves as a delay fiber to match the OPO cavity to the repetition rate of the pump laser.

8.2.2 As_2Se_3 fiber coupler design

Fig. 8.4 (a) shows the schematics of the As_2Se_3 fiber coupler. The coupler consists of two long fiber section for efficient coupling to external fibers, two long transition region that ensures the adiabatic criteria and avoid the excitation of higher order modes and one waist region, where the coupling takes place between two fibers. The As_2Se_3 fiber used for coupler fabrication has a core/clad diameter of 6 µm/170 µm with 0.12 NA. The fiber is single-mode fiber at a wavelength of 1.55 µm. Initially, one facet of the 11 cm long fiber is mechanically spliced to 1.55 m long ZBLAN (Le Verre Fluoré ZFG SM) fiber using UV cured epoxy. The other facet of the fiber is spliced to SMF28 fiber. The insertion loss of the two ZBLAN-ChG-SMF28 assembly vary between 3-4 dB, which includes 1 dB Fresnel reflection loss at the ChG-Silica/ZBLAN interface, 0.4 dB propagation loss, 1 dB for the mode mismatch loss and the rest is attributed to the misalignment loss. Afterwards, the coupler is fabricated using the heat-brush tapering technique [280]. During fabrication, continuous wave light at 1.55 µm wavelength is injected in one of the coupler input and the evolution of transmitted power is monitored in both output ports. Fig. 8.4 (b) shows the recorded power in both through-port and cross-port of coupler during fabrication. The tapering process is terminated at an extension of 11.1 cm, resulting in a waist diameter of 6.2 µm. The final tapering loss is 4 dB and the resulting transition region and waist length is 4.5 cm and 3 cm, respectively. The GVD of the fiber, the <transition> and the waist section 0.76 ps^2/m, 0.72 ps^2/m and 0.68 ps^2/m, respectively Fig. 8.4 (c) shows the transmission spectrum of the through- and cross-port of the coupler measured using thulium amplifier spontaneous emission and Yokogawa 6375B OSA. The coupler broadband with 3 dB coupling ratio at 1.865 µm. The coupler shows negligible polarization dependence and slight multimodal characteristics, as indicated by the 1.1 dB peak to peak power variation in spectrum.

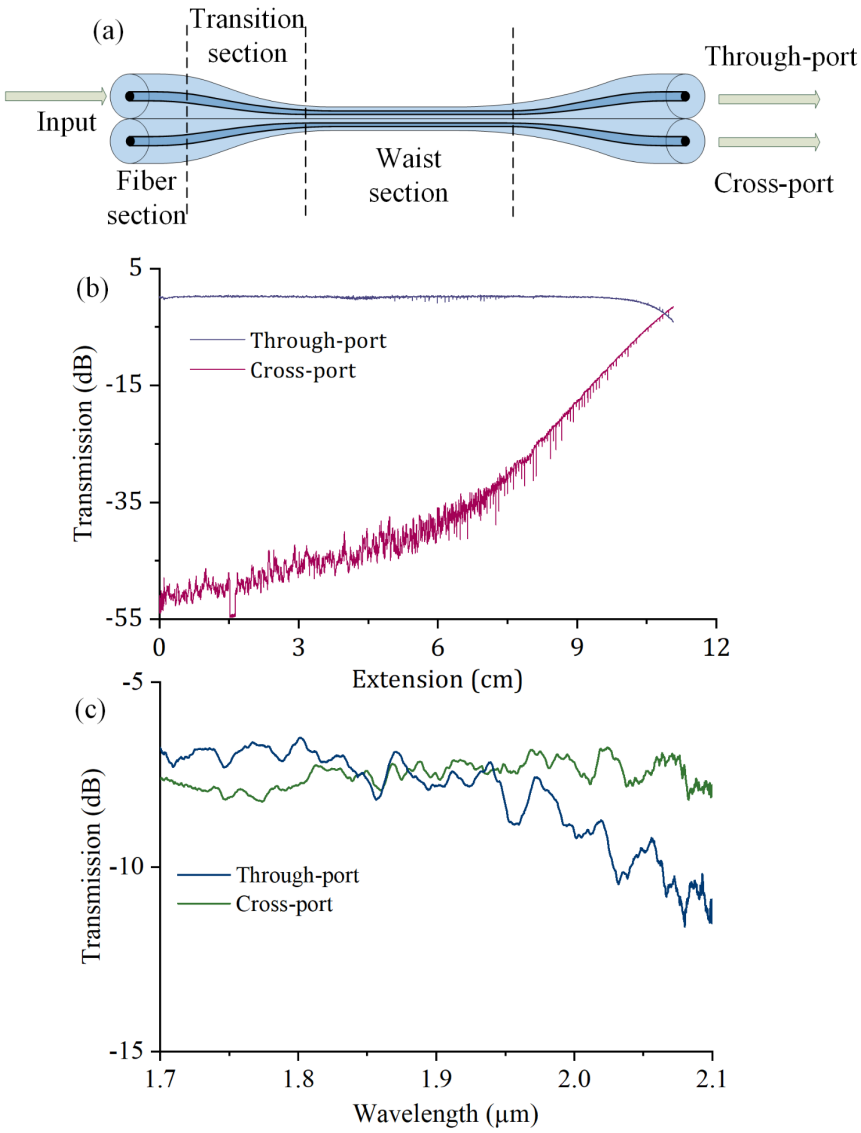

Figure 8.4. (a) Schematics of As_2Se_3 fiber coupler. (b) In situ transmission of the through-port and the cross-port of the fiber coupler with tapering extension. (c) Through-port and cross-port transmission spectra of the coupler.

8.2.3 As_2Se_3 parametric gain medium design

Two microwires are fabricated with identical As_2Se_3 fiber, using a flame-brush tapering and real-time *in situ* monitoring technique [25]. Both devices have two 5 cm long fiber section, two 4 cm long transition section and an 8 cm long microwire section. The microwire core diameter can be adequately engineered to obtain a suitable group velocity dispersion and the

corresponding parametric gain wavelength. Fig. 8.5 (a) shows the calculated β_2 of an As_2Se_3 core surrounded by air for a range of microwire core diameters, determined by solving the characteristic equation of an infinite cladding cylindrical waveguide. Parametric gain is generated in the microwire section under proper phase matching condition, given by $\Delta k = 2\gamma P_p + \beta_2 \Delta\omega^2 + (\beta_4/12)\Delta\omega^4$, where γ, $\Delta\omega$ and P_p are waveguide nonlinearity, frequency detuning and peak pump power, respectively.

Fig. 8.5 (b) shows the expected parametric gain as a function of microwire for a pump wavelength of 1.95 µm, calculated by solving the coupled-wave equation provided by the NLSE. The dashed lines indicate the designed microwire section core diameter of 1.32 µm and 1.57 µm for device 1 and device 2. These selections result into β_2 of -0.55 ps^2/m and - 0.16 ps^2/m, and β_4 of -0.19×10^4 ps^4/m and -0.12×10^4 ps^4/m, respectively. Fig. 8.5 (b) also shows that the Raman scattering wavelength of 2.046 µm coincides with the peak of the parametric gain spectrum of microwire 1 whereas; they are separated by 66 nm for microwire 2. The high nonlinear index and strong modal confinement between As_2Se_3 and air leads to a waveguide nonlinearity as high as 21.5 W^{-1} m^{-1}. The microwires are mechanically spliced to 1.55 m long ZBLAN fiber using UV cured epoxy. The insertion loss of the assemblies are ~5- 6 dB, of which 1 dB is due to the Fresnel reflection at the ChG /ZBLAN interfaces, 1 dB from the mode-mismatch of the fibers, 0.3 dB due to the propagation loss, 2.5 dB from the tapering loss, and the rest is attributed to misalignment loss. The microwires are then characterized by measuring the modulation instability (MI) gain spectrum. Fig. 8.5 (c) and (d) shows the MI gain bands for a pump wavelength and power of 1.94 µm and 3.3 mW respectively, along with the microwire insertion loss. The two MI sidebands observed on both sides of the pump indicate the anomalous dispersion of the devices. For microwire 1, the overlap of the parametric and the Raman gain results in 2.5 dB of higher Stokes signal power compared to the anti-Stokes signal (fig 8.5 (c)). On the other hand, microwire 2 shows clearly distinguishable Raman and parametric sidebands, separated by an amount of 6.3 THz (fig 8.5 (d)). The feature at 1.864 µm wavelength results from the FWM between the pump and the Raman signal as a consequence of the broad parametric gain (see fig 8.5 (a)).

Finally, the coupler and the taper assembly are mechanically spliced together to construct the OPO cavity. The total splice loss between the ZBALN fibers are approximated to be between 1-2 dB for the two OPOs. The total length of the ZBALN fiber in the cavity is 6.2 m with a total normal dispersion of 0.002 ps^2/m at 1.95 µm.

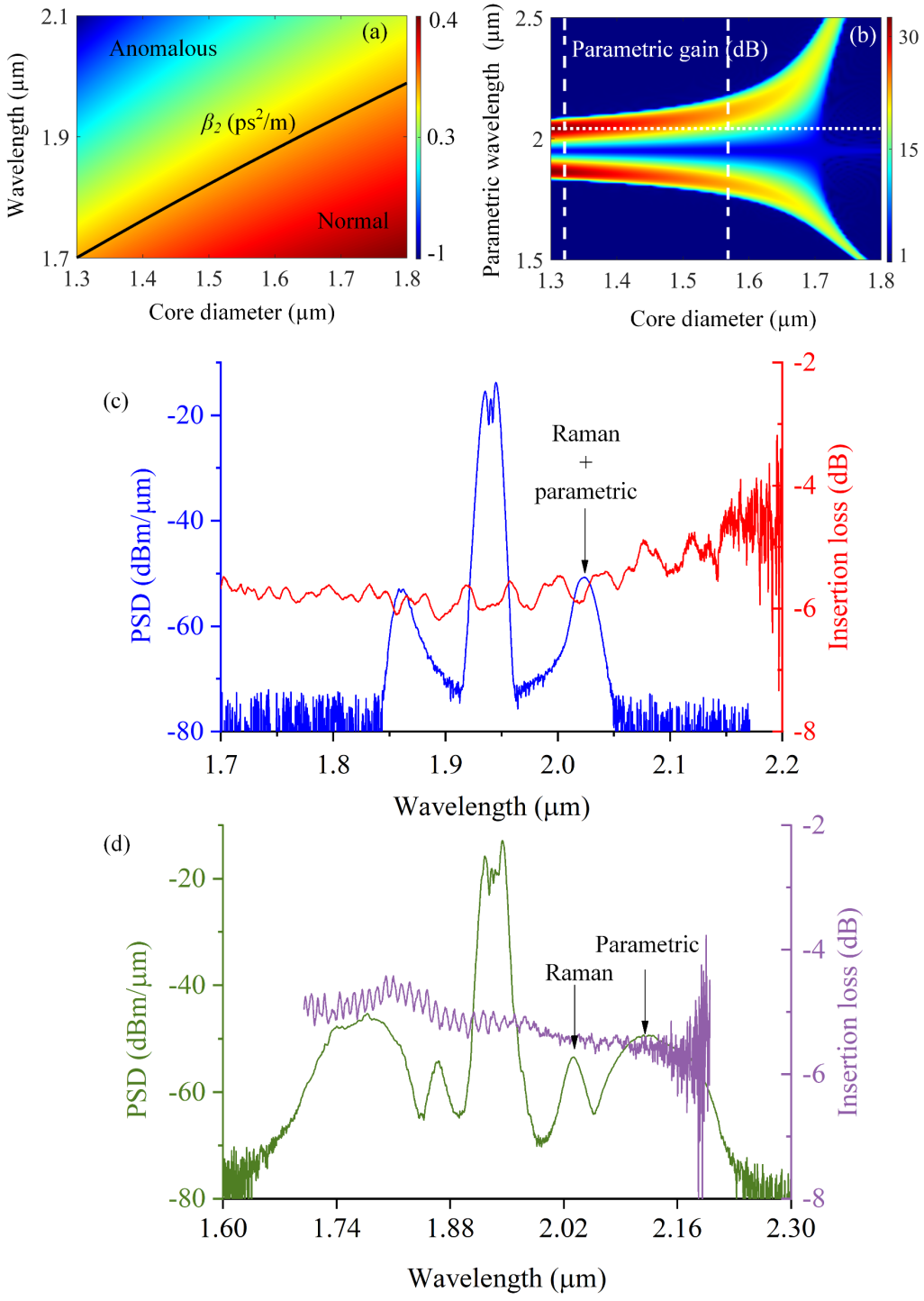

Figure 8.5. (a) β_2 of the As_2Se_3-Air microwire as a function core diameter and wavelength. The zero-dispersion line separates anomalous and normal dispersion region. (b) Calculated parametric gain of an 8 cm long microwire with core diameter for a pump power of 10 W. The horizontal line shows the Raman wavelength detuning from a pump wavelength of 1.95 µm. The vertical lines show the designed microwire core diameter of the two microwires used in the experiments. MI sideband generation and insertion loss for (c) microwire 1 and (d) microwire 2.

8.3 Raman-assisted parametric oscillation

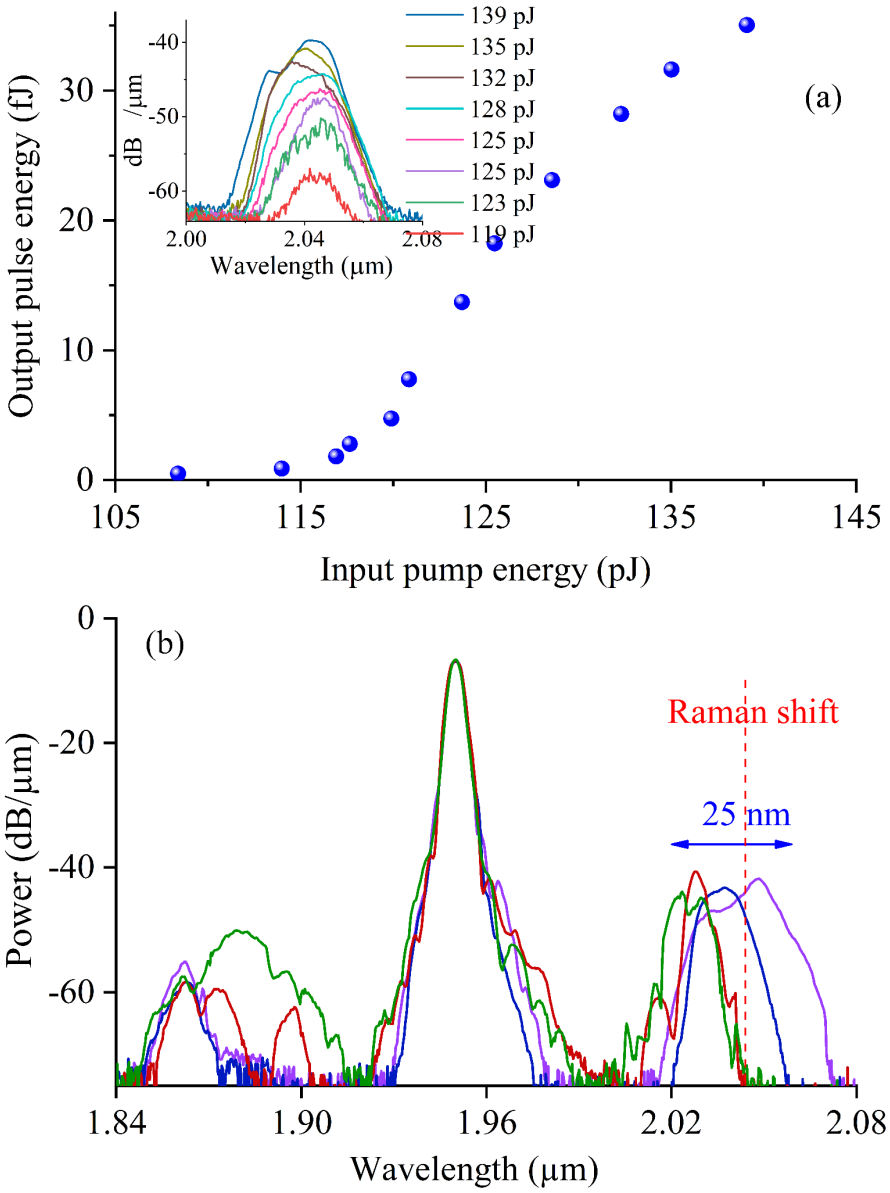

Figure 8.6. (a) Output Stokes signal pulse energy versus input pump pulse energy. Inset. Evolution of signal spectrum with increasing input pump power. (b) Output spectra of the OPO1 with various delay settings in the pump cavity.

In the first set of experiment, we demonstrate Raman assisted parametric oscillation with microwire 1. The OPO cavity has a total roundtrip cavity loss of ~21 dB and a net normal cavity dispersion of 0.15 ps^2. The oscillation begins as the nonlinear gain of the microwire reaches this roundtrip cavity loss and the oscillating pulses are synchronized with the pump pulses by adjusting the pump laser repetition rate. Fig. 8.6 (a) shows the generated Stokes signal energy

at 2.044 μm wavelength as a function of pump pulse energy. The OPO has a threshold energy of 117.5 pJ that corresponds to a peak pump power of 34.5 W. The measured slope efficiency is 0.2 %. The inset shows the evolution of the signal spectrum with increasing pump energy. The slight saturation tendency of the signal energy could occur due to the effect of pump depletion. The wavelength tunability is obtained by the means of dispersion tuning where the repetition rate of the pump laser is adjusted via the optical delay line. Fig. 8.6 (b) shows the wavelength tunability of the oscillator for multiple delay settings for a peak pump power of 38.1 W. For this design, it is observed that the center wavelength of the parametric gain overlaps with the Raman frequency shift, detuned by the amount of 7.07 THz from the pump wavelength [29]. Due to the overlap of gains in the longer wavelength side, the Stokes wavelengths reach lasing threshold at lower pump power, compared to the anti-Stokes signal. The Stokes oscillation shows a wavelength tunability of 25 nm within 2.023-2.048 μm, resulting wavelength converted anti-Stokes signal from 1.861-1.880 μm wavelength. The calculated shortest walk-off length between the pump and oscillating signal is 5.4 cm for taper 1. This length is shorter than the physical length of the microwire, indicating that the temporal walk-off effects the performance of the OPO. The obtained CE is -36 dB, which is ~ 9 dB less than the CE obtained by Abdukerim *et al*. in their 2 μm wavelength ChG-silica hybrid OPO [279]. The CE can be further improved by reducing the total cavity loss and the increasing the walk-off length. Cavity loss can be improved by fusion splicing the ChG-ZBLAN and ZBLAN-ZBALN interfaces. Thapa *et al.* demonstrated fusion splicing between silica and single mode ChG fiber with a splice loss of 0.5 dB with splice strength of 12 kpsi by using Vytran glass processing system [285]. Yang *et al.* demonstrated silica-ZBLAN fusion splicing, with a splice loss of less than 0.1 dB [286]. Recently, the splicing between soft glasses i.e. fluorotellurite and ChG fibers were also demonstrated with a low loss of 0.55 dB [287]. These demonstrations indicate the possibility of splicing of ChG-ZBLAN and ZBLAN-ZBALN interfaces in this OPO cavity, thereby potentially reducing the cavity loss by more than 6-8 dB.

Additional wavelength tunability can also be obtained by tuning the pump wavelength. Fig. 8.7 (a) shows the tunable Stokes lines that are generated between 1.995-2.037 μm wavelengths due to pump wavelength tuning between 1.919-1.951 μm. Furthermore, the stability of the system is evaluated by measuring the power fluctuation of the lasing signal. Fig. 8.7 (b) shows the measured parameter of the Stokes oscillation centered at 2.044 μm for duration of an hour at an acquisition rate of 66 mHz. The calculated coefficient of variation (standard deviation/mean) of the power is 10.36 %, which indicates a reasonable stability of the

system. The stability could be further improved by using increasing the pump stability and controlling the polarization state of the circulating fields in the cavity by incorporating a PC.

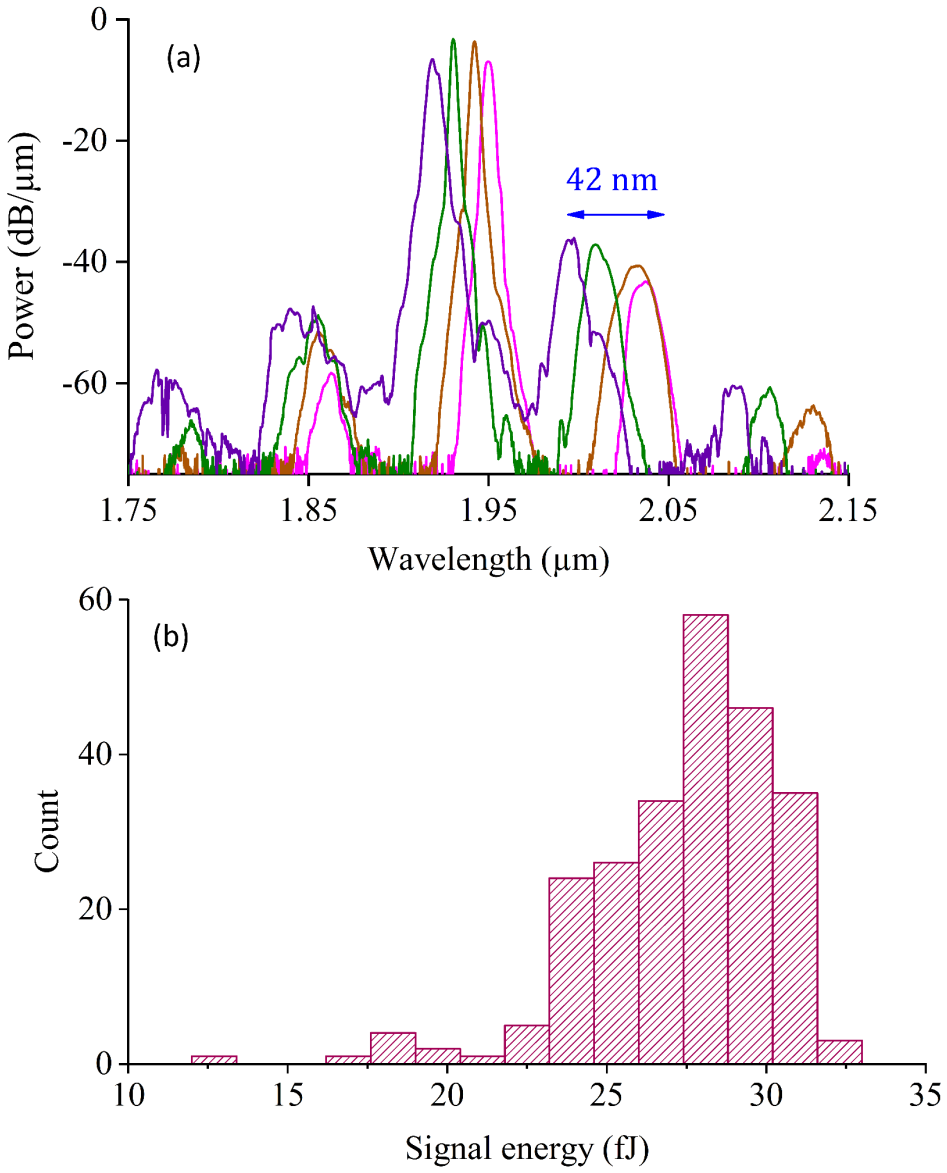

Figure 8.7. (a) Output spectra of the OPO with tunable pump wavelength. (b) Power stability measurement of the Stokes emission line at 2.044 μm wavelength.

8.4 Pure parametric oscillation

In the second set of experiments with microwire 2, the oscillation is maintained solely by the parametric gain. The OPO has a net dispersion and roundtrip cavity loss of 0.18 ps^2 and ~21 dB,

respectively. Inset of fig. 8.8 shows the pulse energy of the Stokes signal at 2.103 µm wavelength as a function of pump energy. The threshold energy/peak power and slope efficiency is 150.1 pJ/44 W and 0.1 % respectively. Fig 8.8 shows the spectra of the OPO obtained using dispersion tuning at a pump energy of 185 pJ. On the longer wavelength side, the OPO is continuously tuned from 2.088-2.139 µm, resulting to a total tuning range of 51 nm. The longest oscillation wavelength is expected to limited by the temporal walk-off since, the shortest walk-off length is 4.6 cm. It is clearly observed that these emission lines exceeds the Raman scattering wavelength and oscillates purely from parametric gain. On the shorter wavelength side, the OPO is wavelength tuned from 1.785-1.834 µm.

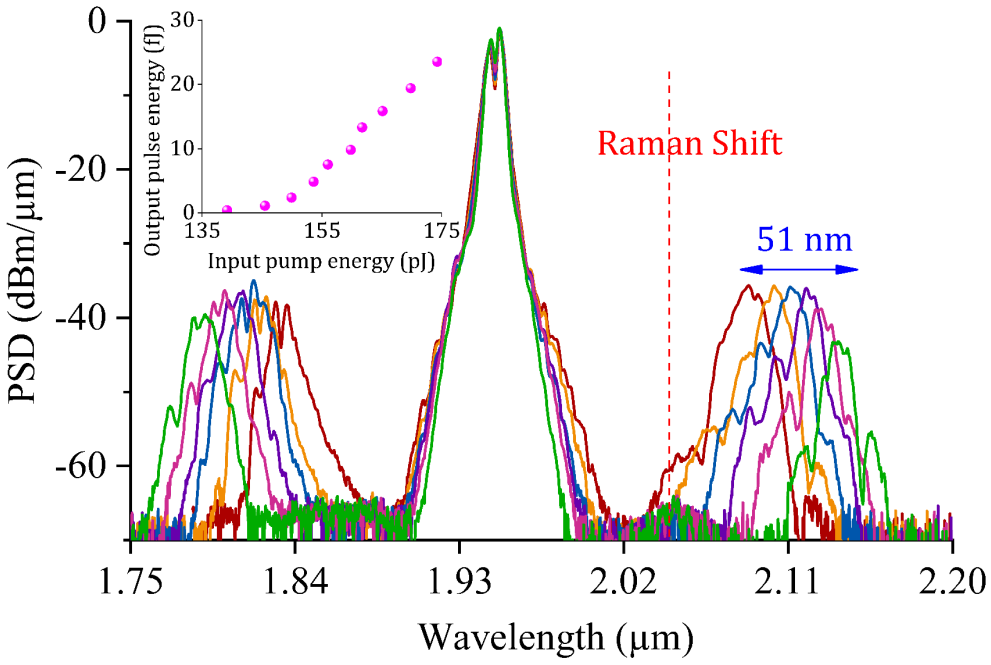

Figure 8.8. Output spectra of the OPO2 with various delay settings in the pump cavity.

8.5 Summary

This chapter describes for the first time, an all-fiber MIR OPO where the laser cavity entirely out of soft-glass fiber. The cavity consists of an As_2Se_3 low loss single-mode fiber coupler, an As_2Se_3 highly nonlinear and dispersion engineered microwire gain medium and commercially available ZBLAN delay fiber. The OPO generates both Raman assisted and pure parametric gain and oscillates with tunable Stokes emission lines within 2.023-2.048 µm and 2.088-

2.139 μm wavelength, respectively. This demonstration indicates the vast underlying potential soft-glass fiber systems in the future development of MIR transmittable fiber lasers.

9 Conclusion and future work

This dissertation summarizes the research work conducted over the last five year, towards the realization of ChG based MIR fiber sources. The high nonlinearity of the microwire, combined with the flexible dispersion engineering, allow the development of compact, low power consuming, and hand portable nonlinear systems that generate ultrafast MIR pulses. In this thesis, first, a novel microwire fabrication technique is presented that allows the *in situ* optimization of far-detuned parametric gain in wavelength converters. A GVD resolution of ~0.0071 ps^2/m is obtained that corresponds to a wavelength offset precision of 3.1 THz. This high precision fabrication technique paved the way for the second research project where, an all-fiber C-band to MIR wavelength conversion system is demonstrated. Combined with a pulse formatting stage that is developed from the widely surrounding telecommunication structure, the far-detuned FWM in ChG microwire generate picosecond pulses within the wavelength range of 2.30-2.64 μm. Third, the development of a highly efficient tunable soliton source based on SSFS in ChG glass is presented. This fiber optic MIR source is exceptionally simple and generates continuously tunable Raman solitons over a broad spectral range of 2.047-2.667 μm, using ultralow pump pulse energy of < 87 pJ. The generated pulses are as short as 62 fs with a maximum power conversion efficiency of 43%. Subsequently, the fourth project demonstrates a SC efficiency enhancement method in As_2S_3 suspended core microwire using a DV structure. The specially designed dispersion profile of the microwire allows an enhanced energy transfer to the DWs in the shorter wavelength edge, as well as an increased SSFS towards the longer wavelength edge of the SC. The generated SC spans within the spectral range of 1.2-2.98 μm with an out-of-pump SC power enhancement of 4.5 dB towards shorter wavelength and a bandwidth extension of 262 nm, compared to the SC generated with the tradition dispersion profile. Afterwards, a mode-locking technique based on NPR effect in ChG microwire is presented as the fifth project. The use of ChG microwire leads to a combined reduction in mode-locking threshold power and cavity length, compared to any all-silica NPR based mode-locked lasers. Finally, the development of a MIR OPO entirely based on soft-glass fiber cavity is demonstrated. This novel cavity design consists of an As_2Se_3 low loss single-mode fiber coupler, an As_2Se_3 highly nonlinear and dispersion engineered microwire gain medium and commercially available ZBLAN delay fiber. The OPO generates both Raman assisted and pure

parametric gain and oscillates with tunable Stokes emission lines within 2.023-2.048 µm and 2.088-2.139 µm wavelength, respectively.

The spectral coverage of these developed sources lie within the range of 1.9-3.0 μm and have variable power levels between microwatt to a few milliwatt. Numerous spectroscopic applications including breath analysis, environmental monitoring and remote sensing would benefit from these sources due to their low power requirement [43], [159], [161], [288], [289]. For example, D. Grassani *et al.* developed a Si_3N_4 based MIR optical source and demonstrated gas absorption spectroscopy of C_2H_2 molecules at 3 µm wavelength with only <50 pJ of pulse energy, corresponding to <1 mW of average power [43]. Moreover, take into account that in case of important losses in between the source and the detection system, the detection could be synchronized with the repetition rate of the source, and that then that the peak power of watts is to be taken into account rather than the average power. In any case, these systems offers the potential improvement in average power as well by replacing the As_2Se_3 based systems with As_2S_3. A demonstration of such system is provided in appendix 10.6.

The ultrafast pulse generation techniques described in this thesis generate light within 1.9-3.0 µm wavelength band. Meanwhile, the remaining mid-IR spectral range up to 12 µm is yet to be explored, which is entirely covered by transmission windows of ChG glass. Currently the MIR frequency detuning of wavelength conversion systems presented chapter 4 is limited by the wavelength of the generated probe signal. By replacing the C-band component in the probe branch with O-band and 1.0 µm band components and amplifiers, a wavelength converted signal up to 4.0 µm can be achieved. A preliminary demonstration is provided in appendix 10.3. Furthermore, the *Tm* fiber laser pump can also be replaced with 3.0 µm Er: ZBLAN fiber laser and the *in situ* fabrication method can be used to optimize the far-detuned gain towards a wavelength > 5 µm. The Er: ZBLAN laser can also be used to generate Raman solitons further into MIR. As described in chapter 5, the simulation suggest that a pump pulse of <100 fs centered at 3.0 µm wavelength has the potential to generate femtosecond Raman solitons within the spectral range of 4-7 µm. Furthermore, the dispersion varying microwire structure will add to the wavelength shift of the Raman solitons [126]. Finally, the soft-glass cavity demonstrated in chapter 8 represents an enormous potential toward the development of all-fiber lasers operating throughout the entire MIR range. Currently, the cavity is characterized by high loss due to the mechanical splicing of the components. This loss can be significantly reduced to obtain higher signal power by using fusion splicing. Finally, by combining microwires of far-

detuned parametric gain with wavelength selective couplers, and 3 μm wavelength pump laser, oscillations can be obtained at practically any wavelengths deep inside the MIR. Preliminary results for the far-detuned MIR OPO is presented in appendix 10.6.

10 Appendix

10.1 Microwire fabrication

Prior to fabrication, the As_2Se_3/As_2Se_3 (core/clad) fiber and (As_2S_3/Polycarbonate) fibers are polished using a Krell Radian bare fiber polisher (see [290] for details). For suspended core As_2S_3 fiber, polishing damages inner structure of the fiber. For this case a razor blade is used to cleave the fiber. First the fiber is placed on the index finger and a small scratch is made. Afterwards, the fiber end is hit firmly that breaks the fiber into two pieces originating from the scratch.

ChG microwires are fabricated by using heat-brush tapering model described in [291]. In this technique, the tapering is performed in alternating steps of heat, stretch and translate. Fig. 10.1 shows the schematics of the fabrication setup [281]. The fabrication is performed in normal atmospheric condition without using any inert gas environment. First, the fiber is heat-softened by HE and extended by a small distance called the extension step, through stretching by the PS. The new fiber radius is then estimated by calculating the average diameter in the region softened by the HE and using the mass conservation law. Then, the HE is translated by TR over a small distance, called the hot ring step. This process repeated throughout the entire tapering process.

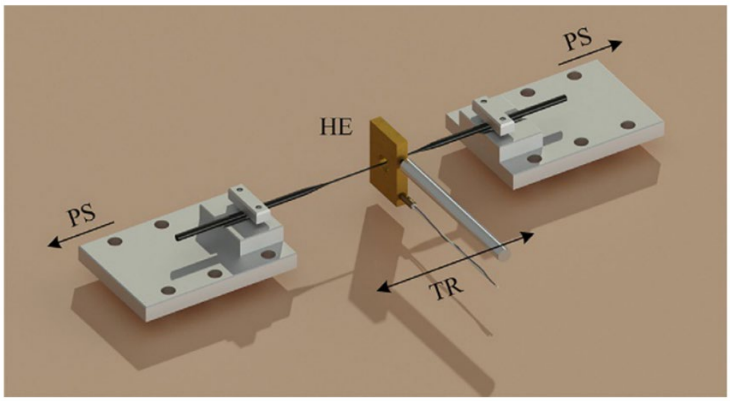

Figure 10.1: Schematics of heat-brush tapering setup. PS: Pulling stage, HE: Heating element, TR: Translating rod (reproduced from [281]).

Fig. 10.2 (a) shows the transmitted power versus elongation of an air cladded As_2Se_3 microwire with 6 cm microwire section length. The oscillation at the primary stages of fabrication occurs

due to the coupling between the fundamental and the higher order modes. Afterwards, the tapering loss gradually recovers and adiabatic guiding is obtained, as the cladding changes from As_2Se_3 to air. Fig 10. 2(b) shows the transmission of the fabricated device in Thulium wavelength band. The slightly multimodal characteristic of the microwire occurs due to the high refractive index contrast between the As_2Se_3 core and air cladding. This procedure is used for fabricate microwires of different material and structure, including air cladded As_2Se_3, As_2S_3, large diameter As_2Se_3, polymer cladded As_2S_3, As_2Se_3 cladded *TeAsSe* and suspended core As_2S_3 and As_2Se_3.

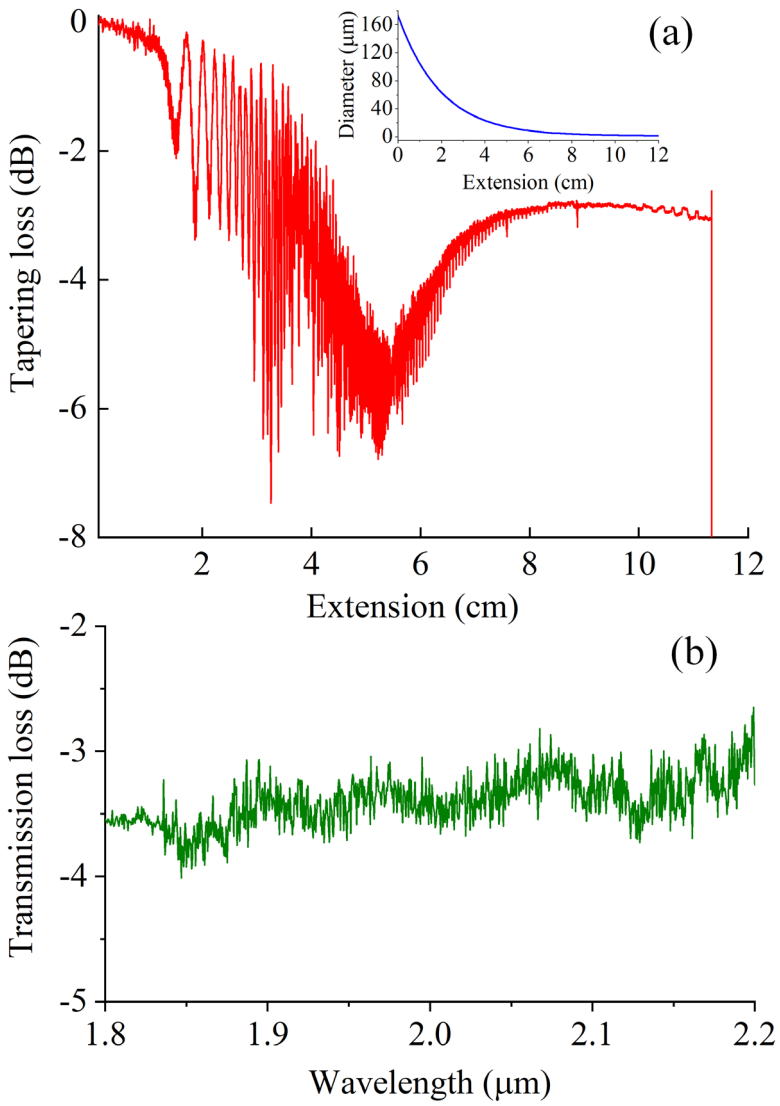

Figure 10.2 (a) Transmitted power versus extension during microwire fabrication process. (b) Wavelength dependent transmission of the fabricated microwire.

Table 10.1 shows the fabrication temperature, glass transition temperatures and minimum obtainable core diameter of different ChG fibers. The minimum diameters are listed considering a microwire section length of 1 cm. For longer microwires, these minimum diameters will change. The fabrication temperatures for the Coractive fiber remains constant, whereas for fibers from the Laval university, the stochastic composition varies from batch to batch, resulting in a varying fabrication temperature.

Table 10.1: Fabrication parameters.

Fiber type (core/clad)	*Fabrication temperature (^oC)*	*Glass transition temperature (^oC)*	*Minimum diameter (μm)*
As_2Se3/As_2Se_3 (Coractive)	173	175	1.2
As_2S_3/As_2S_3(Coractive)	212	187	1.0
As_2S_3/As_2S_3 (Laval)	205-220	187-195	
As_2S_3/polycarbonate (Coractive)	208	187/150	0.5
As_2Se_3/COP (Coractive)	173	167/138	0.5
As_2S_3 MOF (Laval)	210-220	187-195	1.1

Table 10.1: Fabrication parameters.

After the fabrication, polymer cladded microwires can be handled with bare hands as the polymer provides robustness and mechanical strength. The air cladded microwires on the other hand, are handled by a specially designed setup that allows to remove and move the microwire as it remains secure to the fabrication stage plates.

After the experiment, the fiber and microwires are stored in desiccator box and purged with nitrogen to remove moisture. The amber box is then placed in a dark environment. It was observed that with these storage condition, the polymer cladded microwires remain healthy for years, however the air cladded microwires degrades at a faster rate i.e. within a few months.

10.2 Effect of dispersion fluctuation on far-detuned parametric gain

This section briefly presents the impact of dispersion fluctuation on far-detuned parametric gain of a ChG microwire. Such an effect occurs due to the random fluctuation in diameter during microwire fabrication process. Every fabricated microwire has unique diameter non-uniformity, resulting in different parametric gain profile from one microwire to another, although the designed parameters remain identical. Fig 10.3 (a)-(c) show simulated spectra for 30 realizations for 6 cm long As_2Se_3/air microwires designed with core diameters of 1.655 µm, 1.705 µm and 1.755 µm, respectively with 20 nm of diameter fluctuation. Parametric gain is calculated using propagation matrix model [292]. For anomalous dispersion, the dispersion fluctuation has shown to have negligible impact on the parametric gain, whereas it deteriorates and severely degrades the gain in zero and normal dispersion region, respectively.

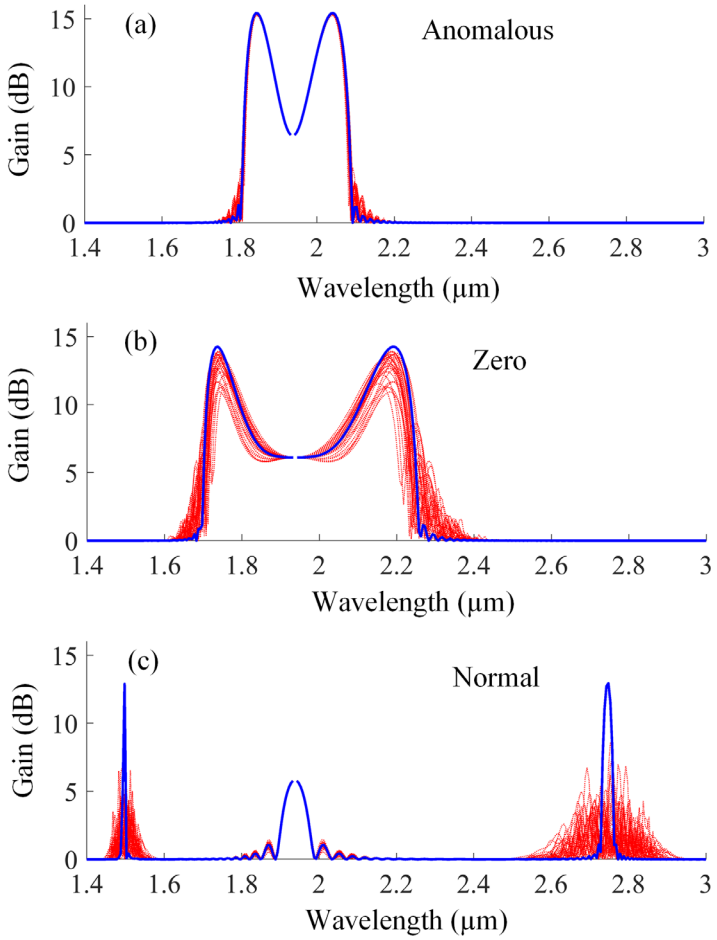

Figure 10.3: Parametric gain fluctuation due to the by random diameter fluctuation along the length of the microwire (red). Blue curves denote the ideal parametric gain spectrum.

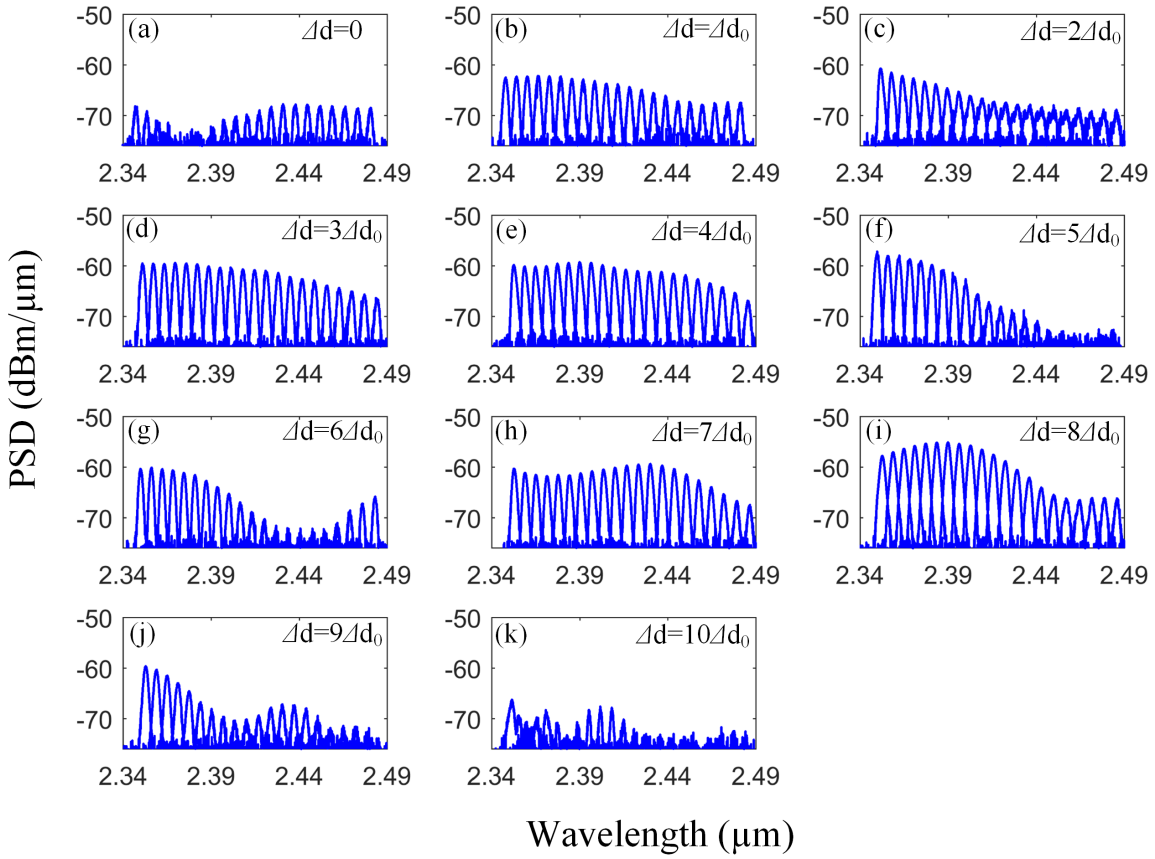

Figure 10.4: Measured idler spectra at different times of the tapering process for a microwire length of 2 cm. the microwire diameter decreases by steps of Δd0 =8 nm.

In general, in a microwire of 1 cm or smaller length the effect of diameter fluctuation remains negligible and shows sample to sample reproducibility. However, for longer microwire section length, the effect of such dispersion fluctuation on parametric gain shape and repeatability is observed during the experiment. Fig 10.4 (a) and (b) show the different steps of *in situ* parametric gain characterization for two identically designed 2 cm long microwires. Compared with the microwire demonstrated in chapter 3, it can be observed that an increase in the microwire length by 1 cm results in a deviation of the parametric gain from the theoretical gain. Since this of effect of diameter fluctuation is random, the repeatability of the samples are also effected. These results further corroborate the advantage of this *in situ* fabrication approach in optimizing the parametric gain at a desired wavelength.

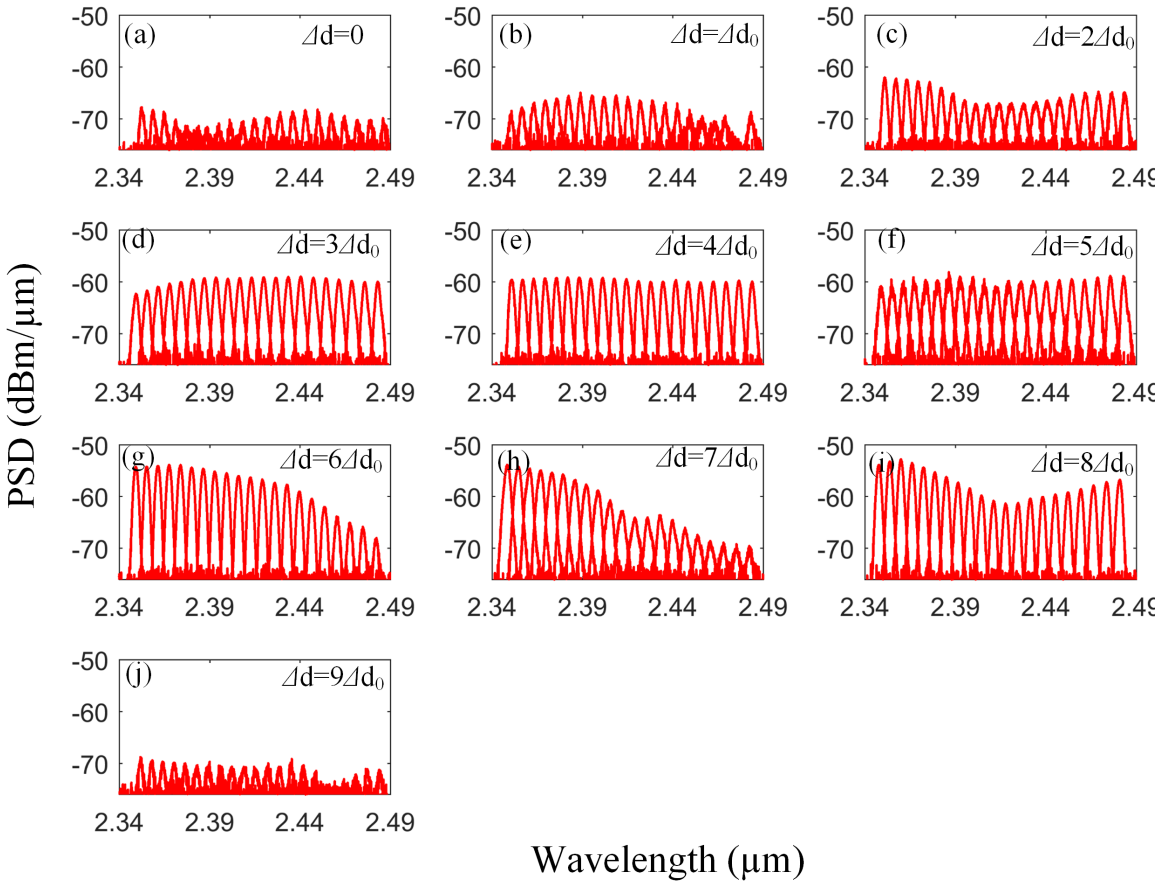

Figure 10.5: Measured idler spectra of a second microwire fabricated with identical designed parameters of microwire shown in fig. 10.4.

10.3 E-band to MIR wavelength conversion system

This section shows the improvement in frequency detuning obtained from the nonlinear wavelength conversion system described in chapter 4. In this experiment, the probe signal is generated by filtering the SC output at a wavelength of 1.422 μm. This probe signal is injected in the microwire along with the pump signal centered at 1.93 μm. Fig. 10.5 shows the generated wavelength converted idler centered at a wavelength of 3.0 μm. The low idler power results from the combined effect of low probe power and small walk-off length. Both the idler power and wavelength can be improved by using an O-band probe signal that is amplified using a commercially available semiconductor optical amplifier.

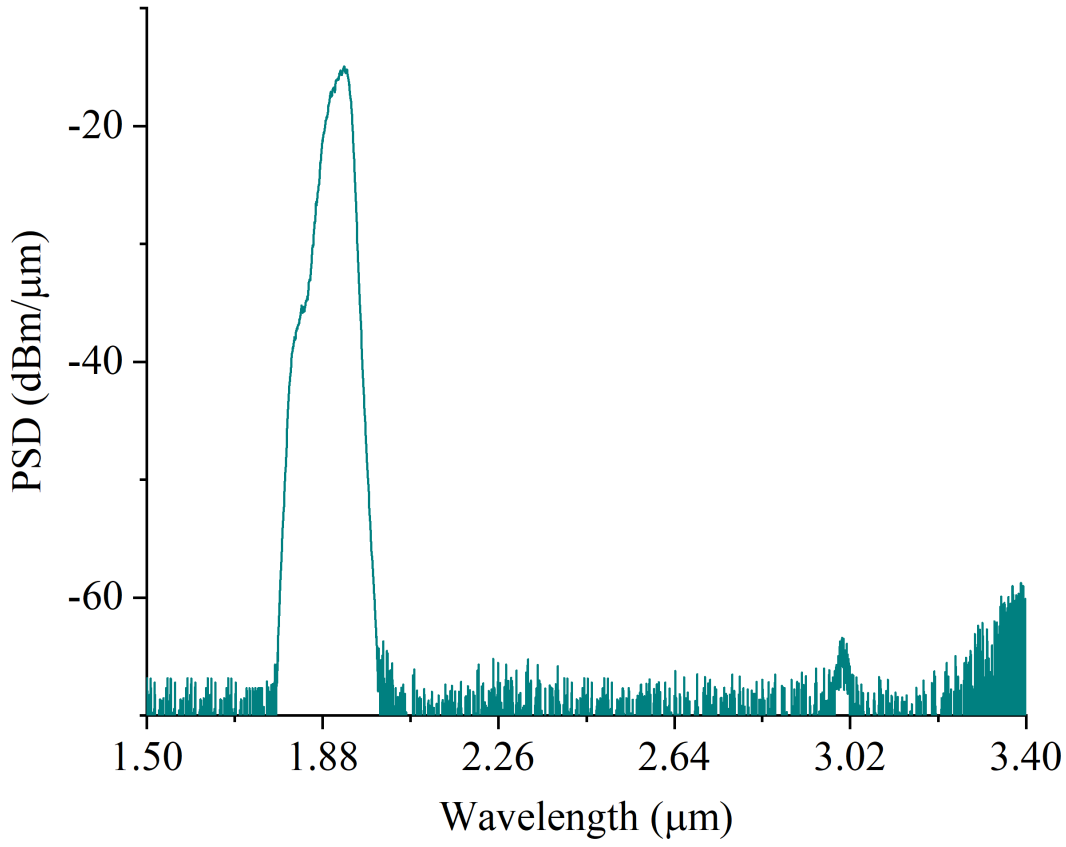

Figure 10.6: E-band to 3μm wavelength conversion.

10.4 SSFS at MIR wavelength: Additional spectra

This section shows the additional spectra of the generated SSFS at MIR. Fig 10.7 (a) and (b) shows spectra of the generated Raman solitons for microwire core diameter of 1.50 μm and 1.75 μm, respectively. These microwires are characterized by higher soliton number, resulting is a noisier Raman soliton and stronger residual background, compared to the device described in chapter 5.

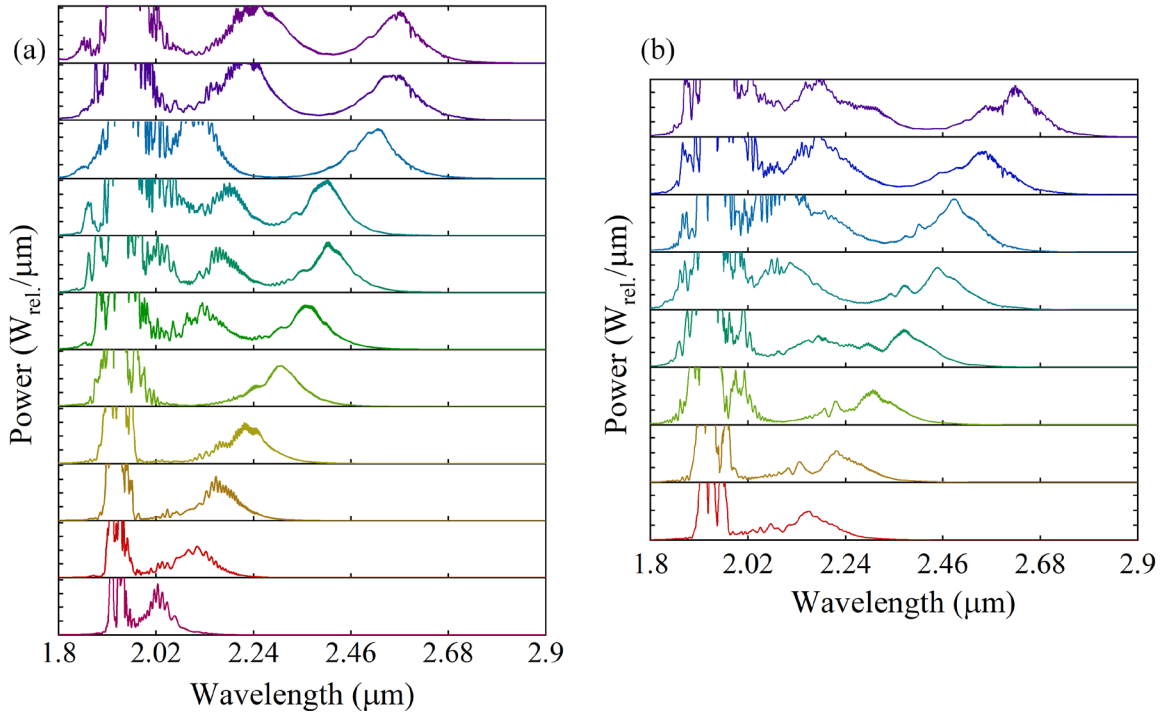

Figure 10.7: Measured output spectra of the SSFS with increasing input pump pulse.

10.5 SC repeatability is DV microwires

This section shows the SC repeatability in DV microwires. Three DV microwires are fabricated with identical parameters. All the fabricated samples showed SC improvement compared to SC generated in CD microwire, as shown in fig 10.7.

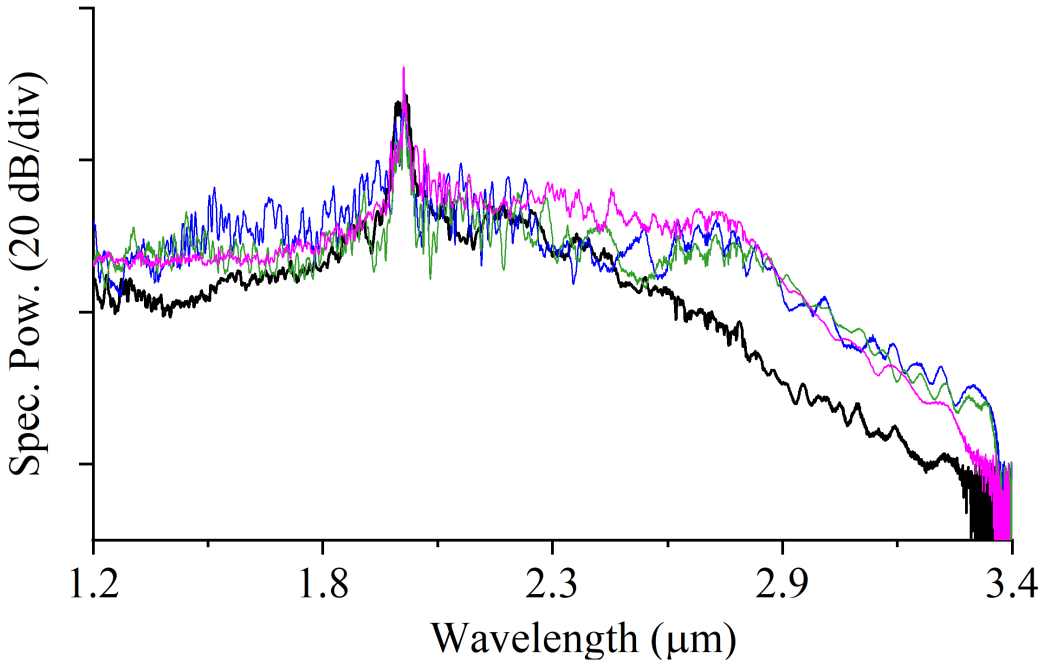

Figure 10.8: Generated SCs in CD (black) and DV (colors) microwires.

10.6 Power and frequency detuning improvement of the MIR OPO

The OPOs demonstrated in chapter 8 are developed using As_2Se_3 based fiber coupler and microwire, which are generally unsuitable for high power applications. However, the laser power can be improved by replacing the As_2Se_3 material with As_2S_3 fiber components, which are characterized by their large power handling capacity. Fig 10.9 shows the output spectrum of such OPO. Maximum MIR laser power obtained is 126 pJ which is more than four orders of magnitude improvement from the As_2Se_3 based OPOs.

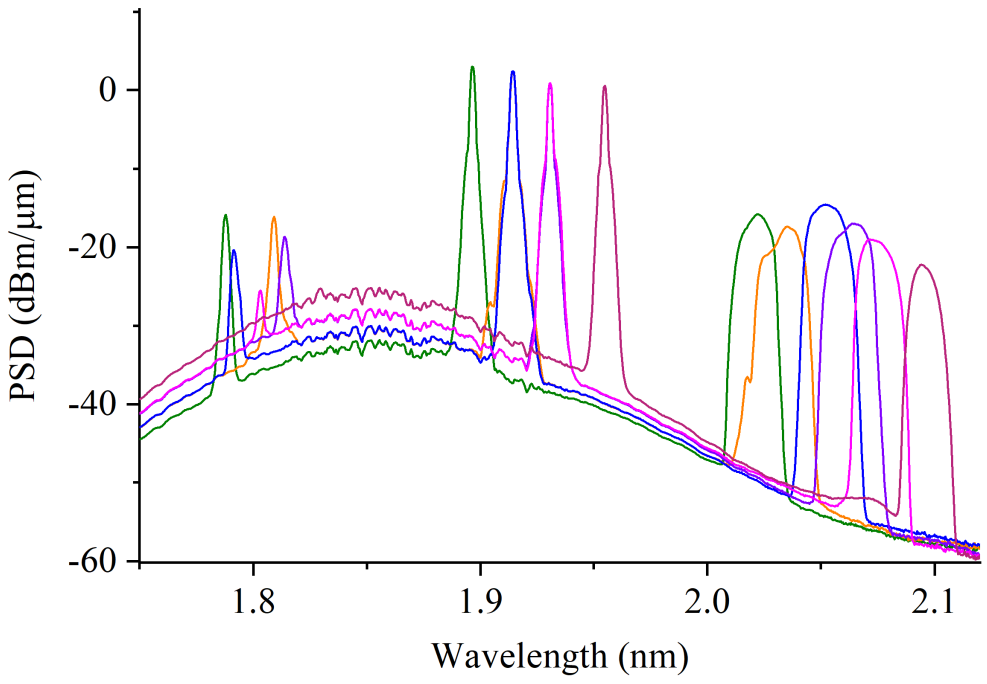

Figure 10.9: Parametric oscillation of the As_2S_3 based OPO. In order to obtain high power operation, pump pulses are injected using filtering beforehand.

At present, the frequency detuning of the OPO towards MIR are limited due to the high cavity loss at longer wavelength. However, with proper dispersion tuning and temporal walk-off compensation, far-detuned wavelength conversion up to 2.24 μm and parametric oscillation near infrared wavelength are observed, as shown in fig. 10.10. In the future, use of WDM coupler can be used to improve the cavity loss at MIR to obtain parametric oscillation deep inside the MIR.

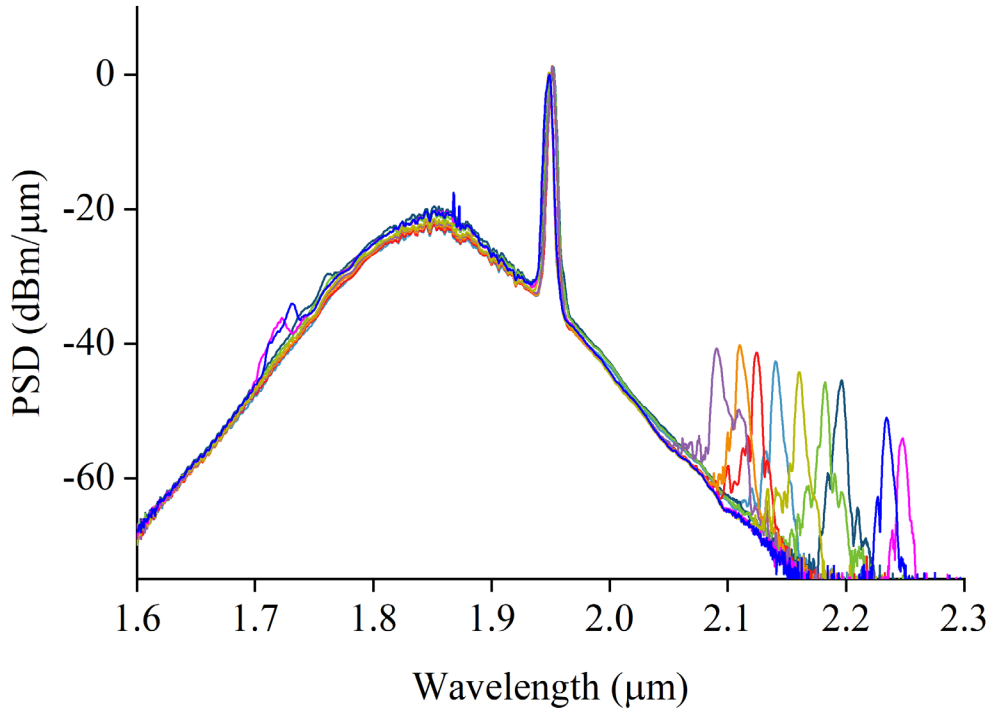

Figure 10.10: Far-detuned operation of the OPO.

10.7 Matlab codes for solving GNLSE

```
%% GNLSE with adaptive step size code for far detuned pulsed FWM
clear all
close all
L = 0.01;                       % length of microwire section
randn('state',1);               % state of random number generator
c = 2.99792458e8;               % Speed of light (m/s)
npts = 2^17;                    % Number of time-frequency points
taxis =  2e-10;                 % t-axis span (s)
toff = 7.5e-12;     %+2         % t-axis offset (s)
toffPrb = 0e-12;                % t-axis offset (s)
h_ratio = 100;                  % L_LN/h_ratio = h
nplots = 51;                    % Number of Intermediate plots per iteration
ploton = 1;                     % Plot intermediate runs (a bit slower)
tdisp = 1e12;                   % Display unit for time axis (1e12 or 1e15)
dtau = 0.6e-12;                 % Input Pulse Temporal FWHM (s) 300fs-1.2ps
lambda0 = 1945e-9;              % Input Pulse Wavelength (m)1950-1960nm
T0 = dtau/1.7627;
f0 = c/lambda0;                 % Input pulse frequency (s^-1)
w0 = 2*pi*f0;                   % Input pulse ang. frequency (rad s^-1)
pulsetype = 1;                  % 0 for sech, 1 for gaussian,
noisefrac = 0/100;              % Intensity noise fraction on input pulse
fR = 0.1;                       % Raman fraction - usually 0.18 for SiO2
n2=1.1e-17;                     % nonlinear R.I in m^2/W
A_eff=61.52e-12;                % Effective mode area at 1550 nm from LVF
nonlintype = 1;                 % 1 to include shock / self-steepening
taushock = nonlintype/w0 ;      % shock timescale / nonlinear dispersion with Aeff
correction
dispersiontype = 0;             % 0 for Taylor expansion, 1 for file
maxorder = 4;                   % max beta_i order for Taylor series
h = 6.62e-34;                   % constante de planck

%    ---------------- 2  Make time and frequency arrays ------------------
t = (-npts/2:npts/2-1)/npts*taxis;
dt = t(2)-t(1);
fmax=0.5/dt;
f = linspace(-fmax+0*fmax,fmax+0*fmax,npts);
df = f(2)-f(1);
shift = -round(npts*0/2);
wrel = 2*pi*f;                          % relative angular frequency
wabs = 2*pi*(f+f0);                     % absolute angular frequency
lambda = 2*pi*c./wabs;                  % wavelength array
lambdanm = lambda*1e9;                  % wavelength array in nm
lambdanm(lambdanm<0) = nan;             % if neg. freqs => neg. lambdas
[min(lambdanm)*1e-9 max(lambda)]
% filter
filtret = exp(-(t./(0.483*taxis)).^50);
%% Fiber section
%    ---------------- 3 Dispersion Data ---------------------------------
beta2 = 7.21121053874896e-25;
beta3 = 9.75926096358903e-40;
beta4=3.35038387438685e-56;
beta = 0;
    for ii = 2:maxorder
        eval(['beta = beta + beta' num2str(ii) '*wrel.^' num2str(ii) ...
            '/factorial(' num2str(ii) ');']);
    end
 gamma0=0.363658611919977;   % Nonlinearity coefficient in (/W/m)
%    ---------------- 4 Raman Response ----------------------------------
% normalisation such that sum(hR)*dt = 1
T1 = 23.2e-15;
T2 = 195e-15;
hR = zeros(1,npts);
hR(t>0) = (T1^2+T2^2)/(T1*T2^2)*exp(-t(t>0)/T2).*sin(t(t>0)/T1);
Ramansum = sum(hR)*dt;
```

```
chi = fft(fftshift(hR))*dt;
%    ---------------- 5 Input Pulse ---------------------------------------
C=0;                    % Pump has neglegible chirp
C2 =-20;                % Probe chirp was calculated seperatey due to HLNF
P0 =12;                 % Pump power
P0_pb = 0.35;           % Probe power with average reprtition rate 20 MHz
lam_pb = 1584e-9;       % Probe wavelength
T0_pb = 7e-12/1.661;    %Probe duration
c=299792458;            % Speed of light [m/s]
w0=2*pi*c/lambda0;      % Central ang. frequency
ww=wrel+w0;
w_pb = 2*pi*c/lam_pb;
lam=2.*pi.*c./ww;
delw = w_pb-w0;
A0_pump=sqrt(P0).*sech((t-toff)./T0).*exp(-1i.*C.*(t-toff).^2./(2.*T0.^2));    %
Define pump
A0_pb = sqrt(P0_pb).*exp(-(t-toffPrb).^2./(2.*T0_pb.^2)).*exp(1i.*delw.*t).*exp(-
1i.*C2.*t.^2./(2.*T0_pb.^2)); % define probe
E = A0_pump+0.95*A0_pb; % Total field
%% Wire parameters and propagation
L=0.01;    % Microwire lengtth in meters
WireDia=1.7690e-06;    % Microwire diameter
%Import diameter, dispersion and nonliearity curve
A_Dia_Beta_Gamma=xlsread ('Dia_Dispersion_Gamma_1950nmPump');
fR = 0.1;                           % Raman fraction
gamma0=interp1(A_Dia_Beta_Gamma(:,1),A_Dia_Beta_Gamma(:,5),WireDia,'spline')
%    ---------------- 3 Dispersion Data ---------------------------------
 beta2 = interp1(A_Dia_Beta_Gamma(:,1),A_Dia_Beta_Gamma(:,2),WireDia,'spline')
 beta3 = interp1(A_Dia_Beta_Gamma(:,1),A_Dia_Beta_Gamma(:,3),WireDia,'spline');
 beta4=interp1(A_Dia_Beta_Gamma(:,1),A_Dia_Beta_Gamma(:,4),WireDia,'spline');
 beta = 0;
 for ii = 2:maxorder
 eval(['beta = beta + beta' num2str(ii) '*wrel.^' num2str(ii) ...
            '/factorial(' num2str(ii) ');']);
 end
z = 0;
h_mon = zeros(1,500000);
beta = fftshift(beta);
betaop = exp(-1i*h*beta);
ind1 = [(2:npts) 1];
ind2 = [npts (1:npts-1)];
sel = (L/(nplots-1));
plotsel = sel;
plotn = 1;
zsel = linspace(0,L,nplots)';
Ap = zeros(nplots,npts);
ApFT = zeros(nplots,npts);
% Initial fields at z = 0
E = fftshift(E);
EFT = fft(E);
Ap(1,:) = fftshift(E);
ApFT(1,:) = fftshift(circshift((EFT),shift));
lossw = 0;
tic
k = 0;
while z<L
   k = k+1;
  % Nonlinear step
   A0 = E;
   peakP = max(abs(E).^2);
   h = (1./(gamma0.*peakP))./h_ratio;
   IFT = fft(abs(A0).^2);
   Iz = (1-fR)*(abs(A0).^2)+fR*ifft(chi.*IFT);
   NLfn = A0.*Iz;
   A1 = A0-h/2*1/(2*dt).*gamma0.*taushock.*(NLfn(ind1)-NLfn(ind2));
   IFT = fft(abs(A1).^2);
   Izh = (1-fR)*(abs(A1).^2)+fR*ifft(chi.*IFT);
```

```
   NLfn = A1.*Izh;
   A1 = A0-h.*1i.*gamma0.*A1.*(Izh-Iz)-
h.*1./(2.*dt).*gamma0.*taushock.*(NLfn(ind1)-NLfn(ind2));
   E  = A1.*exp(-1i.*gamma0.*h.*Iz);
   % Dispersion + birefringence step
   betaop = exp(-1i*h*beta);
   EFT = circshift(fft(E),shift);
   EFT = EFT.*betaop;
    %   Include loss
   EFT= EFT.*(fftshift(exp(-lossw.*h)));%.*fftshift(filtret);
   E  = ifft(circshift(EFT,-shift));%.*fftshift(filtret);
   % Plot selection step
if (z > plotsel)
       plotsel = plotsel+sel;
       plotn = plotn+1;
       disp(['Curve No. ' num2str(plotn) ' of ' num2str(nplots)])
       Ap(plotn,:) =  fftshift(E);
       ApFT(plotn,:) = fftshift(EFT);
       EFiledPhase=angle( Ap(plotn,:));
       Chirp=-diff(EFiledPhase);
       figure(5),subplot(211),yyaxis left,plot(t*tdisp,abs(Ap(plotn,:)).^2,'b')
       xlabel('Time (ps)')
       ylabel('Power (W)')
       title(['Wire Section   ''z = ' num2str(z) 'm'])
       axis([-2+(toff/1e-12) 2+(toff/1e-12) 0 max(abs(Ap(plotn,:)).^2)])
       yyaxis right,plot(t*tdisp,[Chirp,0],'r')
       ylabel('Frequency Chirp')
       axis([-2+(toff/1e-12) 2+(toff/1e-12) -0.1 0.1])
       figure(5),subplot(212),plot(lambdanm,10*log10(abs(ApFT(plotn,:)).^2),'b'),
       xlabel('\lambda (nm)')
       ylabel('Spectrum (dB)')
       axis([1400 2900 0 100])
       drawnow
end
    z = z+h
    h_mon(k) = h;
end
Ap(end,:) =  fftshift(E);
ApFT(end,:) = fftshift(EFT);
Especout = ApFT(end,:);
Especoutt7=10*log10(abs(Especout).^2);
figure(11)
plot(lambdanm,Especoutt7,'linewidth',1)
xlim([1500 2900])
ylim([0 100])
%This code is adapted from the MEng thesis of F. St-Hilaire, McGill University
```

11 References

[1] G. R. Hunt and J. W. Salisbury, "Lunar Surface Features: Mid-Infrared Spectral Observations," *Science,* vol. 146, p. 614, 1964.

[2] M. Harwit, B. T. Soifer, J. R. Houck, and Ju. L. Pipher, "Why Many Infrared Astronomical Sources emit at 100 μm," *Nature Phyical. Science*, vol. 236, p. 103, 1972.

[3] R. A. Minzne, W. E. Shen, R. D. Teagle, and J. Steranka, "Stereographic cloud heights from imagery of SMS/GOES satellites," *Geophysical Research Letlers.*, vol. 5, p. 21, 1978.

[4] R. Legeckis, "A survey of worldwide sea surface temperature fronts detected by environmental satellites," *Journal of Geophysical Research*, vol. 83, p. 4501, 1978.

[5] "Laserfocus.com." .

[6] "Extending opportunities," *Nature Photonics*, vol. 6, p. 407, 2012.

[7] P. Werle, F. Slemr, K. Maurer, R. Kormann, M. Robert, and J. Bernd, "Near- and mid-infrared laser-optical sensors for gas analysis," *Optics and Lasers in Engineering*, vol. 37, p. 101, 2002.

[8] S. W. Sharpe, T. J. Johnson, R. L. Sams, P. M. Chu, G. C. Rhoderick, and P. A. Johnson, "Gas-phase databases for quantitative infrared spectroscopy," *Applied Spectroscopy.*, vol. 58, p. 1452, 2004.

[9] U. Willer, M. Saraji, A. Khorsandi, P. Geiser, and W. Schade, "Near- and mid-infrared laser monitoring of industrial processes, environment and security applications," *Optics and Lasers in Engineering.*, vol. 44, p. 699, 2006.

[10] L. Jun, T. Qiulin, Z. Wendong, X. Chenyang, G. Tao, and X. Jijun, "Miniature low-power IR monitor for methane detection," *Measurement*, vol. 44, p. 823, 2011.

[11] H. Waechter and M. Sigrist, "Trace gas analysis with isotopic selectivity using DFG-sources," *NATO Science for Peace and Security Series B - Physics and Biophysics*, pp. 495–510, 2008.

[12] D. Richter, M. Erdelyia, R. F. Curla, F. K. Tittela, C. Oppenheimerb, H. J. Duffellb, M. Burton, "Field measurements of volcanic gases using tunable diode laser based mid-

infrared and Fourier transform infrared spectrometers," *Optics and Lasers in Engineering*, vol. 37, p. 171, 2002.

[13] T. Arusi-Parpar, D. Heflinger, and R. Lavi, "Photodissociation followed by laser-induced fluorescence at atmospheric pressure and 24 °C: a unique scheme for remote detection of explosives," *Applied Optics*, vol. 40, p. 6677, 2001.

[14] E. Mendes and N. Duarte, "Mid-infrared spectroscopy as a valuable tool to tackle food analysis: A literature review on coffee, dairies, honey, olive oil and wine," *Foods*, vol. 10, p. 1–32, 2021.

[15] J. Haas and B. Mizaikoff, "Advances in Mid-Infrared Spectroscopy for Chemical Analysis," *Annual Review in Analytical Chemisty*, vol. 9, p. 45–68, 2016.

[16] M. L. Brandil, V. Monbet, B. Bureau, C. Boussard-Plédel, O. Loréal, Jean-Luc Adam. O. Sire., "Identification of foodborne pathogens within food matrices by IR spectroscopy," *Sensors and Actuators B: Chemical*, vol. 160, p. 202–206, 2011.

[17] E. Domingo, A. A. Tirelli, C. A. Nunes, M. C. Guerreiro, and S. M. Pinto, "Melamine detection in milk using vibrational spectroscopy and chemometrics analysis: A review," *Food Research International*, vol. 60, p. 131–139, 2014.

[18] C. Heuer, C. Heuer, H. J. Luinge, E.T.G. Lutz, Y. H. Schukken, J. H. van der Maas, H. Wilmink, and J.P.T.M. Noordhuizen, "Determination of acetone in cow milk by Fourier transform infrared spectroscopy for the detection of subclinical ketosis," *Journal of Dairy Science.*, vol. 84, pp. 575–582, 2001.

[19] Ebrahim-Zadeh M, *Mid-Infrared Optical Parametric Oscillators and Applications*. Springer, Dordrech, 2005.

[20] O. B. Crofford, R. E. Mallard, and R. E. Winton, "Acetone in breath and blood," *Transaction of the American Clinical and Climatological Association.*, vol. 88, p. 128–139, 1977.

[21] C. Roller, K. Namjou, J. Jeffers, W. Potter, P. J. McCann, and J. Grego, "Simultaneous NO and CO_2 measurement in human breath with a single IV–VI mid-infrared laser," *Optics Letters.*, vol. 27, p. 107, 2002.

[22] Z. Movasaghi, S. Rehman, and I. U. Rehman, "Fourier transform infrared (FTIR)

spectroscopy of biological tissues," *Applied Spectroscopu Review.*, vol. 43, pp. 134–179, 2008.

[23] S. Vasilyev, I. Moskalev, M. Mirov, S. Mirov, and V. Gapontsev, "Three optical cycle mid-IR Kerr-lens mode-locked polycrystalline Cr^{2+}:ZnS laser," *Optics Letters*, vol. 40, p. 5054, 2015.

[24] I. T. Sorokina, E. Sorokin, S. Mirov, V. Fedorov, V. Badikov, V. Panyutin, and K. I. Schaffers, "Broadly tunable compact continuous-wave Cr^2+:ZnS laser," *Optics Letters*, vol. 27, p. 1040, 2002.

[25] S. Mirov, V. Fedorov, I. Moskalev, D. Martyshkin, and C. Kim, "Progress in Cr2+ and Fe2+ doped mid-IR laser materials," *Laser and Photonics Review*, vol. 4, pp. 21–41, 2010.

[26] A. V. Okishev and J. D. Zuegel, "Intracavity-pumped Raman laser action in a Mid-IR, continuous-wave (cw) MgO: PPLN optical parametric oscillator," *Optics Express*, vol. 14, pp. 12169–12173, 2007.

[27] R. K. Feaver, R. D. Peterson, and P. E. Powers, "Longwave-IR optical parametric oscillator in orientation-patterned GaAs pumped by a 2 μm Tm,Ho:YLF laser," *Optics Express*, vol. 21, p. 16104, 2013.

[28] Z. Zhang*, D. T. Reid, S. C. Kumar, M. Ebrahim-Zadeh, P. G. Schunemann, K. T. Zawilski, and C. R. Howle*, "Femtosecond CdSiP2 optical parametric oscillator producing 100-MHz pulses centered at 6.2 μm," *Advanced Solid-State Lasers Congress.*, Paris, 2013.

[29] S. Ghimire and D. A. Reis, "High-harmonic generation from solids," *Nature Physics*, vol. 15, pp. 10–16, 2019.

[30] T. M. Monro and H. Ebendorff-Heidepriem, "Progress in microstructured optical fibers," *Annual Review in Material Research.*, vol. 36, pp. 467–495, 2006.

[31] P. Russell, "Photonic crystal fibers," *Science.*, vol. 299, pp. 358–362, 2003.

[32] G. Brambilla, "Optical fibre nanowires and microwires: A review," *Journal of Optics*, vol. 12, 2010.

[33] L. Calvez, "Chalcogenide glasses and glass-ceramics: Transparent materials in the

infrared for dual applications," *Comptes Rendus Physics.*, vol. 18, pp. 314–322, 2017.

[34] X. Feng, F. Poletti, A. Camerlingo, F. Parmigiani, P. Petropoulos, P. Horak, G. M. Ponzo, M. Petrovich, J. Shi, W. H. Loh, D. J. Richardson ., "Dispersion controlled highly nonlinear fibers for all-optical processing at telecoms wavelengths," *Optical Fiber Technology*, pp. 378–391, 2010.

[35] R. E. Slusher, G. Lenz, J. Hodelin, J. Sanghera, L. B. Shaw, and I. D. Aggarwal, "Large Raman gain and nonlinear phase shifts in high-purity As2Se3 chalcogenide fibers," *Journal of Optical sociaty of America B*, vol. 21, p. 1146, 2004.

[36] J. M. Harbold, F. Ö. Ilday, F. W. Wise, J. S. Sanghera, V. Q. Nguyen, L. B. Shaw, and I. D. Aggarwal., "Highly nonlinear As–S–Se glasses for all-optical switching," *Optics Letters*, vol. 27, p. 119, 2002.

[37] V. G. Ta'eed *et al.*, "Ultrafast all-optical chalcogenide glass photonic circuits," *Opt. Express*, vol. 15, no. 15, pp. 9205–9221, 2007.

[38] A. Al-kadry, C. Baker, M. El Amraoui, Y. Messaddeq, and M. Rochette, "Broadband supercontinuum generation in As2Se3 chalcogenide wires by avoiding the two-photon absorption effects," *Optics Letters*, vol. 38, p. 1185, 2013.

[39] C. Baker and M. Rochette, "High nonlinearity and single-mode transmission in tapered multimode As2Se3-PMMA fibers," *IEEE Photonics Jorunal*, vol. 4, pp. 960–969, 2012.

[40] D. Mazzotti, P. De Natale, G. Giusfredi, C. Fort, J. A. Mitchell, and L. Hollberg, "Saturated-absorption spectroscopy with low-power difference-frequency radiation,", *Optics Letters*, vol. 25, pp. 350–352, 2000.

[41] B. Urgner, V. I. J. Ayaraman, and R. A. J. R. Am, "Low-power swept-source Raman spectroscopy", *Optics Express*, vol. 29, pp. 24723–24734, 2021.

[42] M. Yu, Y. Okawachi, A. G. Griffith, N. Picqué, M. Lipson, and A. L. Gaeta, "Silicon-chip-based mid-infrared dual-comb spectroscopy," *Naure. Communication*, vol. 9, pp. 6–11, 2018.

[43] D. Grassani, E. Tagkoud, H. Guo, C. Herkommer, F. Yang, T. J. Kippenberg, Camille-Sophie Brès, "Mid infrared gas spectroscopy using efficient fiber laser driven photonic chip-based supercontinuum," *Nature Communication,* vol. 10, p. 1553, 2019.

[44] J. M. Dudley and J. R. Taylor, *Supercontinuum Generation in Optical Fibers*. Cambridge University Press, 2010.

[45] G. P. Agrawal, *Nonlinear fiber optics*. Academic Press, 2019.

[46] R. Zallen, R. E. Drews, R. L. Emerald, and M. L. Slade, "Electronic structure of crystalline and amorphous As2S3 and As2Se3," *Physical Review Letters*, vol. 26, pp. 1564–1567, 1971.

[47] T. Katsuyama and H. Matsumura, *Infrared optical fibres*. 1989.

[48] J. S. Sanghera, V. Q. Nguyen, P. C. Pureza, R. E. Miklos, F. H. Kung, and I. D. Aggarwal, "Fabrication of long lengths of low-loss IR transmitting As40S(60-x) glass fibers," *Journal of Lightwave Technology.*, vol. 14, pp. 743–748, 1996.

[49] G. E. Snopatin, V. S. Shiryaev, V. G. Plotnichenko, E. M. Dianov, and M. F. Churbanov, "High-purity chalcogenide glasses for fiber optics," *Inorganic Materials*, vol. 45, pp. 1439–1460, 2009.

[50] Y. Wu, M. Meneghetti, J. Troles, and J. L. Adam, "Chalcogenide microstructured optical fibers for mid-infrared supercontinuum generation: Interest, fabrication, and applications," *Applied Sciences*, vol. 8, 2018.

[51] R. W. Boyd, *Nonlinear Optics*, Academic Press 2020.

[52] S. Shibata, M. Horiguchi, K. Jinguji, S. Mitachi, T. Kanamori, and T. Manabe, "Prediction of loss minima in infra-red optical fibres," *Electronics. Letters.*, vol. 17, pp. 775–777, 1981.

[53] M. F. Churbanov, "High-purity chalcogenide glasses as materials for fiber optics," *J. Non-Crystalline Solidournal Non-Crystalline Solid*, vol. 184, pp. 25–29, 1995.

[54] F. Wooten, *Optical Properties of Solids,* Academic Press, 1972.

[55] A. I. Konyukhov, E. A. Romanova, and V. S. Shiryaev, "Chalcogenide glasses as a medium for controlling ultrashort IR pulses: Part I," *Optics and Spectroscopy.*, vol. 110, pp. 442–448, 2011.

[56] C. Lafond, J.-F. Couillard, J.-L. Delarosbil, F. Sylvain, and P. de Sandro, "Recent improvements on mid-IR chalcogenide optical fibers," *Infrared Technology and*

Applications XL, 90701C, 2014.

[57] T. A. Birks, W. J. Wadsworth, and P. S. J. Russell, "Supercontinuum generation in tapered fibers," *Optics Letters*, vol. 25, pp. 1415–1417, 2000.

[58] R. P. Kenny, T. A. Birks, and K. P. Oakley, "Control of optical fibre taper shape," *Electronics Letters.*, vol. 27, pp. 1654–1656, 1991.

[59] P. Dumais, F. Gonthier, S. Lacroix, J. Bures, A. Villeneuve, P. G. J. Wigley, and G. I. Stegeman, "Enhanced self-phase modulation in tapered fibers," *Optics Letters*, vol. 18, pp. 1996–1998, 1993.

[60] E. C. Mägi, D. Il Yeom, H. C. Nguyen, L. Fu, and B. J. Eggleton, "Enhanced kerr nonlinearity in sub-wavelength diameter As2Se3 chalcogenide fibre tapers," *Optics Express*, vol. 15, pp. 10324–10329, 2007.

[61] C. Baker and M. Rochette, "Highly nonlinear hybrid AsSe-PMMA microtapers," *Optics Express*, vol. 18, pp. 12391–12398, 2010.

[62] L. Li, A. Al-Kadry, N. Abdukerim, and M. Rochette, "Design, fabrication and characterization of PC, COP and PMMA-cladded As2Se3 microwires," *Optical Material Express*, vol. 6, p. 912, 2016.

[63] L. Li, N. Abdukerim, and M. Rochette, "Chalcogenide optical microwires cladded with fluorine-based CYTOP," vol. 24, pp. 18931–18937, 2016.

[64] L. Li, "Chalcogenide microwires cladded with hydrogen- and fluorine-based polymers and their applications," PhD Thesis, 2017.

[65] A. Zakery and S. R. Elliott, *Optical Nonlinearities in Chalcogenide Glasses and their Applications*, Springer, 2007.

[66] J. S. Sanghera, L. B. Shaw, P. Pureza, V. Q. Nguyen, D. Gibson, L. Busse, I. D. Aggarwal, C. M. Florea, F. H. Kung, "Nonlinear Properties of Chalcogenide Glass Fibers," *International Journal of Applied Glass Science*, vol. 1, pp. 296–308, 2010.

[67] K.J. Blow and D. Wood, "Theoretical description of transient stimulated Raman scattering in optical fibers," *IEEE Journal of Quantum Electronics.*, vol. 25, p. 2665, 1989.

[68] S. Venck, F. St-Hilaire, L. Brilland, A. N. Ghosh, R. Chahal, C. Caillaud, M. Meneghetti, J. Troles, F. Joulain, S. Cozic, S. Poulain, G. Huss, M. Rochette, J. M. Dudley, T. Sylvestre., "2–10 μm Mid-Infrared Fiber-Based Supercontinuum Laser Source: Experiment and Simulation," *Laser and Photonics Reviews*, vol. 14, pp. 1–10, 2020.

[69] J. S. Sanghera, I. D. Aggarwal, L. B. Shaw, C. M. Florea, P. Pureza, V. Q Nguyen, F. Kung, I. D. Aggarwal, "Nonlinear properties of chalcogenide glass fibers," *Journal of Optoelectronics and Advanced Material*, vol. 8, pp. 2148–2155, 2006.

[70] J. W. Choi, Z. Han, B. Uk Sohn, G. F. R. Chen, C. Smith, L. C. Kimerling, K. A. Richardson, A. M. Agarwal and D. T. H. Tan, "Nonlinear characterization of GeSbS chalcogenide glass waveguides," *Scientific Reports*, vol. 6, pp. 1–8, 2016.

[71] A. Hasegawa and F. Tappert, "Transmission of stationary nonlinear optical pulses in dispersive dielectric fibers. I. Anomalous dispersion," *Applied Physics Letters*, vol. 23, pp. 171–172, 1973.

[72] L. F. Mollenauer, R. H. Stolen, and J. P. Gordon, "Experimental observation of picosecond pulse narrowing and solitons in optical fibers," *Physical Review Letters*, vol. 45, pp. 1095–1098, 1980.

[73] J. M. Dudley, G. Genty, and S. Coen, "Supercontinuum generation in photonic crystal fiber," *Reviews of Modern Physics*, vol. 78, pp. 1135–1184, 2006.

[74] E. E. Serebryannikov and A. M. Zheltikov, "Supercontinuum generation through cascaded four-wave mixing in photonic-crystal fibers: When picoseconds do it better," *Optics Communication*, vol. 274, pp. 433–440, 2007.

[75] V. Tombelaine, A. Labruyère, J. Kobelke, K. Schuster, V. Reichel, P. Leproux, V. Couderc, R. Jamier, and H. Bartelt, "Nonlinear photonic crystal fiber with a structured multi-component glass core for four-wave mixing and supercontinuum generation," *Optics Express*, vol. 17, p. 15392, 2009.

[76] R. A. Martinez, G. Plant, K. Guo, B. Janiszewski, M. J. Freeman, R. L. Maynard, M. N. Islam, F. L. Terry, O. Alvarez, F. Chenard, R. Bedford, R. Gibson, and A. I. Ifarraguerri, "Mid-infrared supercontinuum generation from 1.6 to > 11 μm using concatenated step-index fluoride and chalcogenide fibers," *Optics Letters*, vol. 43, p. 296, 2018.

[77] A. M. Heidt, J. S. Feehan, J. H. V. Price, and T. Feurer, "Limits of coherent

supercontinuum generation in normal dispersion fibers," *Journal of Optical Sociaty of. America B*, vol. 34, p. 764, 2017.

[78] I. Alamgir, N. Abdukerim, and M. Rochette, "In situ fabrication of far-detuned optical fiber wavelength converters," *Optics Letters*, vol. 44, p. 4467, 2019.

[79] I. Alamgir, N. Abdukerim, and M. Rochette, "Far-Detuned parametric gain optimization in Wavelength Converters," in *IEEE Photonics Conference*, 2018.

[80] I. Alamgir, N. Abdukerim, and M. Rochette, "In situ fabrication of far-detuned mid-infrared optical fiber wavelength converters," *CLEO/Europe EQEC Conference*, 2019.

[81] I. Alamgir, N. Abdukerim, and M. Rochette, "In Situ Fabrication of Far-Detuned Wavelength Converters," in *21st International Symposium on Non-Oxide and New Optical Glasses*, 2018.

[82] J. E. Sharping, "Microstructure fiber based optical parametric oscillators," *Journal of Lightwave Technology*, vol. 26, pp. 2184–2191, 2008.

[83] S. Duval, M. Bernier, V. Fortin, J. Genest, M. Piché, and R. Vallée, "Femtosecond fiber lasers reach the mid-infrared," *Optica*, vol. 2, pp. 623, 2015.

[84] M. R. Majewski, R. I. Woodward, and S. D. Jackson, "Dysprosium-doped ZBLAN fiber laser tunable from 28 μm to 34 μm, pumped at 17 μm," *Optics Letters*, vol. 43, p. 971, 2018.

[85] J. W. Nicholson, M. F. Yan, P. Wisk, J. Fleming, F. DiMarcello, E. Monberg, A. Yablon, C. Jørgensen, and T. Veng, "All-fiber , octave-spanning supercontinuum,", *Optics Letters*, vol. 28, pp. 643–645, 2003.

[86] F. Parmigiani, P. Horak, Y. Jung, L. Grüner-Nielsen, T. Geisler, P. Petropoulos, and D. J. Richardson, "All-optical mode and wavelength converter based on parametric processes in a three-mode fiber," *Optics Express*, vol. 25, p. 33602, 2017.

[87] R. H. Stolen, J. E. Bjorkholm, and A. Ashkin, "Phase-matched three-wave mixing in silica fiber optical waveguides," *Applied Physics Letters*, vol. 24, pp. 308–310, 1974.

[88] C. Finot, J. Fatome, A. Sysoliatin, A. Kosolapov, and S. Wabnitz, "Competing four-wave mixing processes in dispersion oscillating telecom fiber," *Optics Letters*, vol. 38, p. 5361, 2013.

[89] K. S. Abedin, J. T. Gopinath, E. P. Ippen, C. E. Kerbage, R. S. Windeler, and B. J. Eggleton, "Highly nondegenerate femtosecond four-wave mixing in tapered microstructure fiber," *Applied Physics Letters*, vol. 81, pp. 1384–1386, 2002.

[90] J. E. Sharping, A. Coker, M. Fiorentino, P. Kumar, and R. S. Windeler, "Four-wave mixing in microstructure fiber," *Optics Letters*, vol. 26, p. 1048, 2001.

[91] J. Liu, T. H. Cheng, and L. Xue, "Broad-band tunable wavelength converter based on degenerate four-wave mixing in a highly nonlinear photonic crystal fiber," *Optics Letters*, vol. 30, pp. 2375–2377, 2008.

[92] W. Petrich, "Mid-infrared and Raman spectroscopy for medical diagnostics," *Applied Spectroscopic Reviews*, vol. 36, pp. 181–237, 2001.

[93] F. Toor, S. Jackson, X. Shang, S. Arafin, and H. Yang, "Mid-infrared Lasers for Medical Applications: introduction to the feature issue," *Biomedical Optics. Express*, vol. 9, p. 6255, 2018.

[94] A. Soibel, Malcolm W. Wright, William H. Farr, Sam A. Keo, Cory J. Hill, Rui Q. Yang, and H. C. Liu., "Midinfrared Interband Cascade Laser for Free Space Optical Communication," *IEEE Photonics Technology Letters*, vol. 22, pp. 121–123, 2010.

[95] A. Billat, S. Cordette, and C.-S. Brès, "Broadly tunable source around 2050 nm based on wideband parametric conversion and thulium–holmium amplification cascade," *Optics Express*, vol. 22, p. 26635, 2014.

[96] J. S. Sanghera, "Nonlinear Properties of Chalcogenide Glass Fibers," *International Journal of Applied Glass Science*, vol. 1, pp. 296–308, 2010.

[97] R. Ahmad and M. Rochette, "All chalcogenide Raman-parametric laser , wavelength converter and broadband source in a single microwire," *IEEE Journal of Seclected. Topics in Quantum Electronics*, vol. 1, pp. 3–4, 2014.

[98] R. Ahmad and M. Rochette, "High Efficiency and ultra broadband optical parametric four-wave mixing in chalcogenide- PMMA hybrid microwires," *Optics Express*, vol. 20, pp. 4629–4637, 2011.

[99] L. Li, N. Abdukerim, and M. Rochette, "Mid-infrared wavelength conversion from As_2Se_3 microwires," *Optics Letters*, vol. 42, p. 639, 2017.

[100] T. Godin, Y. Combes, R. Ahmad, M. Rochette, T. Sylvestre, and J. M. Dudley, "Far-detuned mid-infrared frequency conversion via normal dispersion modulation instability in chalcogenide microwires.," *Optics Letters*, vol. 39, pp. 1885–8, 2014.

[101] T. Singh Saini, T. Hoang Tuan, M. Matsumoto, G. Sakai, T. Suzuki, and Y. Ohishi, " Mid-infrared wavelength conversion using dispersion-engineered As2S5 microstructured optical fiber pumped with an ultrafast laser at 2 μm ," *Optics Letters*, vol. 45, p. 2736, 2020.

[102] K. Nagasaka, H. T. Tong, H. P. Trung, T. Suzuki, and Y. Ohishi, "Far-detuned four-wave mixing for mid-infrared wavelength conversion in chalcogenide As2S5 suspended core," Proc. SPIE 10528, Optical Components and Materials XV, 105281M, 2018.

[103] D. M. Nguyen, S. D. Le, K. Lengle, D. Méchin, M. Thual, T. Chartier, Q. Coulombier, J. Troles, L. Bramerie, and . Brilland, "Demonstration of nonlinear effects in an ultra-highly nonlinear AsSe suspended-core chalcogenide fiber," *IEEE Photonics Technology Letters*, vol. 22, pp. 1844–1846, 2010.

[104] S. D. Le, M. Gay, L. Bramerie, M. C. e Silva, K.Lenglé, T. Chartier, M. Thual, J.-C. Simon, L. Brilland, D. Méchin, P. Toupin, and J. Troles , "Wavelength conversion in a highly nonlinear chalcogenide microstructured fiber," *Optics Letters*, vol. 37, p. 4576, 2012.

[105] C.-S. Brès, S. Zlatanovic, A. O. J. Wiberg, and S. Radic, "Continuous-wave four-wave mixing in cm-long Chalcogenide microstructured fiber.," *Optics Express*, vol. 19, pp. B621, 2011.

[106] S. Xing, D. Grassani, S. Kharitonov, A. Billat, and C.-S. Brès, "Characterization and modeling of microstructured chalcogenide fibers for efficient mid-infrared wavelength conversion," *Optics Express*, vol. 24, p. 9741, 2016.

[107] S. Xing, D. Grassani, S. Kharitonov, L. Brilland, C. Caillaud, J. Trolès, and C.-S. Brès, "Mid-infrared continuous-wave parametric amplification in chalcogenide microstructured fibers," *Optica*, vol. 4, p. 643, 2017.

[108] D. Chow, J. C. Tchahame, A. Denisov, J.-C. Beugnot, T. Sylvestre, L. Li, R. Ahmad, M. Rochette, K. Hey Tow, M. A. Soto, and L. Thévenaz, "Mapping the Uniformity of Optical Microwires Using Phase-Correlation Brillouin Distributed Measurements,"

Frontiers in Optics, 2015.

[109] F. Yaman, Q. Lin, S. Radic, and G. P. Agrawal, "Impact of dispersion fluctuations on dual-pump fiber-optic parametric amplifiers," *IEEE Photonics Technology Letters*, vol. 16, pp. 1292–1294, 2004.

[110] J. S. Y. Chen, S. G. Murdoch, R. Leonhardt, and J. D. Harvey, "Effect of dispersion fluctuations on widely tunable optical parametric amplification in photonic crystal fibers," *Optics Express*, vol. 14, p. 9491, 2006.

[111] N. Abdukerim, "Ultrafast mid-infrared pulse generation and characterization in chalcogenide microwires," *PhD thesis*, 2018.

[112] C. W. Rudy, A. Marandi, Konstantin L. Vodopyanov, and R. L. Byer, "Octave-spanning supercontinuum generation in in situ tapered As2S3 fiberpumped by a thulium-doped fiber laser," *Optics Letters*, vol. 38, p. 2865, 2021.

[113] A. Marandi, C. W. Rudy, V. G. Plotnichenko, E. M. Dianov, K. L. Vodopyanov, and R. L. Byer, "Mid-infrared supercontinuum generation in tapered chalcogenide fiber for producing octave-spanning frequency comb around 3 μm," *Optics Express*, vol. 20, p. 24218, 2012.

[114] A. W. Snyder and J. D. Love, *Optical Waveguide Theory*, Chapman & Hall, 1983.

[115] Q. Lin, O. J. Painter, and G. P. Agrawal, "Nonlinear optical phenomena in silicon waveguides: modeling and applications," *Optics Express*, vol. 15, p. 16604, 2007.

[116] C. Baker and M. Rochette, "A generalized heat-brush approach for precise control of the waist profile in fiber tapers," *Optical Material. Express*, vol. 1, pp. 3426–3437, 2011.

[117] G. Lenz, J. Zimmermann, T. Katsufuji, M. E. Lines, H. Y. Hwang, S. Spälter, R. E. Slusher, S.-W. Cheong, J. S. Sanghera, and I. D. Aggarwal, "Large Kerr effect in bulk Se-based chalcogenide glasses.," *Optics Letters*, vol. 25, pp. 254–256, 2000.

[118] Schott Infrared Chalcogenide Glass IRG 26, "https://www.us.schott.com," 2000. .

[119] J. Hansryd, P. A. Andrekson, M. Westlund, J. Li, and P. O. Hedekvist, "Fiber-based optical parametric amplifiers and their applications," *IEEE Journal of Seclected Topics in Quantum Electronics*, vol. 8, pp. 506–520, 2002.

[120] I. Alamgir, F. St-Hilaire, and M. Rochette, “All-fiber nonlinear optical wavelength conversion system from the C-band to the mid-infrared,” *Optics Letters*, vol. 45, p. 857, 2020.

[121] I. Alamgir, F. St-Hilaire, and M. Rochette, “Nonlinear optical wavelength conversion system from the c-band to the mid-infrared,” *Conference on Lasers and Electro-Optics*, 2020.

[122] C. R. Petersen, R. D. Engelsholm, C. Markos, L. Brilland, C. Caillaud, J. Trolès, and O. Bang, “Increased mid-infrared supercontinuum bandwidth and average power by tapering large-mode-area chalcogenide photonic crystal fibers,” *Optics Express*, vol. 25, p. 15336, 2017.

[123] N. Abdukerim, L. Li, M. El Amraoui, Y. Messaddeq, and M. Rochette, “2 μ m Raman fiber laser based on a multimaterial chalcogenide microwire,” *Applied Physics Letters*, vol. 110, p. 161103, 2017.

[124] S. Zlatanovic, J. S. Park, S. Moro, J. M. Chavez Boggio, I. B. Divliansky, N. Alic, S. Mookherjea & S. Radic, “Mid-infrared wavelength conversion in silicon waveguides using ultracompact telecom-band-derived pump source,” *Nature Photonics*, vol. 4, pp. 561–564, 2010.

[125] A. Kowligy, D. D. Hickstein, A. Lind, D. R. Carlson, H. Timmers, N. Nader, D. L. Maser, D. Westly, K. Srinivasan, S. B. Papp, and S. A. Diddams, “Tunable mid-infrared generation via wide-band four wave mixing in silicon nitride waveguides,” *Optics Letters*, vol. 43, pp. 4220–4223, 2018.

[126] A. Al-Kadry, “Mid-infrared soliton self-frequency shift and supercontinuum sources based on As2Se3 chalcogenide microwires,” *PhD thesis*, 2014.

[127] J. M. Harbold, F. Ö. Ilday, F. W. Wise, J. S. Sanghera, V. Q. Nguyen, L. B. Shaw, and I. D. Aggarwal., “Highly nonlinear As-S-Se glasses for all-optical switching.,” *Optics Letters*, vol. 27, pp. 119–121, 2002.

[128] J. Troles, F. Smektala, G. Boudebs, and A. Monteil, “Third order nonlinear optical characterization of new chalcohalogenide glasses containing lead iodine,” *Optical Materials*, vol. 22, pp. 335–343, 2003.

[129] I. Alamgir, M. H. M. Shamim, W. Correr, Y. Messaddeq, and M. Rochette,

"GLISSEMENT DE FRÉQUENCE DE SOLITONS DANS L'INFRAROUGE MOYEN À PARTIR D'IMPULSIONS DE FAIBLE ÉNERGIE," in *Optique Dijon*, 2021.

[130] I. Alamgir, M. Hosne Mobarok Shamim, W. Correr, Y. Messaddeq, and M. Rochette, "Mid-infrared soliton self-frequency shift using ultra-low pump pulse energy," in *Conference on Lasers and Electro-Optics*, 2021.

[131] I. Alamgir, M. Hosne Mobarok Shamim, W. Correr, Y. Messaddeq, and M. Rochette, "Mid-infrared soliton self-frequency shift using ultra-low pump pulse energy," in *CLEO/Europe EQEC Conference*, 2021.

[132] I. Alamgir, M. H. M. Shamim, W. Correr, Y. Messaddeq, and M. Rochette, "Mid-infrared soliton self-frequency shift in chalcogenide glass," *Optics Letters,* vol. 46, p. 5513, 2021.

[133] F. M. Mitschke and L. F. Mollenauer, "Discovery of the soliton self-frequency shift," *Optics Letters*, vol. 11, p. 659, 1986.

[134] D. A. Chestnut and J. R. Taylor, "Soliton self-frequency shift in highly nonlinear fiber with extension by external Raman pumping," *Optics Letters*, vol. 28, p. 2512, 2003.

[135] N. Nishizawa and T. Goto, "Compact System of Wavelength-Tunable Femtosecond Soliton Pulse Generation Using Optical Fibers," *IEEE Photonics Technology Letters*, vol. 11, pp. 325–327, 1999.

[136] A. E. Korolev, D. V. Kuksenkov, and V. N. Nazarov, "Controllable self-frequency shift of subpicosecond soliton light pulses in a nonlinear optical fiber," *Optical Spectroscopy* vol. 102, pp. 86–89, 2007.

[137] K. S. Abedin and F. Kubota, "Widely tunable femtosecond soliton pulse generation at a 10-GHz repetition rate by use of the soliton self-frequency shift in photonic crystal fiber," *Optics Letters*, vol. 28, p. 1760, 2003.

[138] E. G. Turitsyna and S. Webb, "Observation of soliton self-frequency shift in photonic crystal fibr," *Electronics Letters*, vol. 41, pp. 40–41, 2005.

[139] N. Nishizawa, Y. Ito, and T. Goto, "0.78-0.90-Mm Wavelength-Tunable Femtosecond Soliton Pulse Generation Using Photonic Crystal Fiber," *IEEE Photonics Technology*

Letters, vol. 14, pp. 986–988, 2002.

[140] N. Ishii, C. Y. Teisset, S. Köhler, E. E. Serebryannikov, T. Fuji, T. Metzger, F. Krausz, A. Baltuška, and A. M. Zheltikov, "Widely tunable soliton frequency shifting of few-cycle laser pulses," *Physical Review E,* vol. 74, pp. 1–10, 2006.

[141] J. Takayanagi, T. Sugiura, M. Yoshida, and N. Nishizawa, "1.0-1.7-μm wavelength-tunable ultrashort-pulse generation using femtosecond Yb-doped fiber laser and photonic crystal fiber," *IEEE Photonics Technology Letters*, vol. 18, pp. 2284–2286, 2006.

[142] X. Liu, C. Xu, W. H. Knox, J. K. Chandalia, B. J. Eggleton, S. G. Kosinski, and R. S. Windeler, "Soliton self-frequency shift in a short tapered air-silica microstructure fiber," *Optics Letters*, vol. 26, pp. 358–360, 2001.

[143] D. G. Ouzounov, F. R. Ahmad, D.Muller, N. Venkataraman, M. T. Gallagher, M. G. Thomas, J. Silcox, K. W. Koch, A. L. Gaeta, "Generation of megawatt optical solitons in hollow-core photonic band-gap fibers," *Science*, vol. 301, pp. 1702–1704, 2003.

[144] J. van Howe, J. H. Lee, S. Zhou, F. Wise, C. Xu, S. Ramachandran, S. Ghalmi, and M. F. Yan, "Demonstration of soliton self-frequency shift below 1300nm in higher-order mode, solid silica-based fiber," *Optics Letters*, vol. 32, p. 340, 2007.

[145] J. H. Lee, J. Van Howe, C. Xu, S. Ramachandran, S. Ghalmi, and M. F. Yan, "Generation of femtosecond pulses at 1350 nm by cherenkov radiation in higher-order-mode fiber," *Optics Letters*, vol. 32, pp. 1053–1055, 2007.

[146] M. Y. Koptev, E. A. Anashkina, A. V. Andrianov, S. V. Muravyev, and A. V. Kim, "Two-color optically synchronized ultrashort pulses from a Tm/Yb-co-doped fiber amplifier," *Optics Letters*, vol. 39, p. 2008, 2014.

[147] S. Kivistó, T. Hakulinen, M. Guina, and O. G. Okhotnikov, "Tunable Raman soliton source using mode-locked Tm/Ho fiber system," in *CLEO/Europe and IQEC*, 2007.

[148] J. Luo, B. Sun, J. Ji, E. L. Tan, Y. Zhang, and X. Yu, "High-efficiency femtosecond Raman soliton generation with a tunable wavelength beyond 2 μm," *Optics Letters*, vol. 42, p. 1568, 2017.

[149] J. Wang, S. Lin, X. Liang, M. Wang, P. Yan, G. Hu, T. Albrow-Owen, S. Ruan, Zhipei Sun, and T. Hasan, "High-energy and efficient Raman soliton generation tunable from

198 to 229 μm in an all-silica-fiber thulium laser system," *Optics Letters*, vol. 42, p. 3518, 2017.

[150] H. Hoogland, S. Wittek, W. Hänsel, S. Stark, and R. Holzwarth, "Fiber chirped pulse amplifier at 208 μm emitting 383-fs pulses at 10 nJ and 7 MHz," *Optics Letters*, vol. 39, p. 6735, 2014.

[151] D. Klimentov, N. Tolstik, V. V. Dvoyrin, R. Richter, and I. T. Sorokina, "Flat-Top Supercontinuum and Tunable Femtosecond Fiber Laser Sources at 1.9-2.5 μm," *Journal of Lightwave Technology*, vol. 34, pp. 4847–4855, 2016.

[152] Y. Tang, L. G. Wright, K. Charan, T. Wang, C. Xu, and F. W. Wise, "Generation of intense 100 fs solitons tunable from 2 to 43 μm in fluoride fiber," *Optica*, vol. 3, p. 948, 2016.

[153] S. Duval, J.-C. Gauthier, L.-R. Robichaud, P. Paradis, M. Olivier, V. Fortin, M. Bernier, M. Piché, and R. Vallée., "Watt-level fiber-based femtosecond laser source tunable from 2.8 to 3.6 μm," *Optics Letters*, vol. 41, p. 5294, 2016.

[154] N. Nagl, K. F. Mak, Q. Wang, V. Pervak, F. Krausz, and O. Pronin, "Efficient femtosecond mid-infrared generation based on a Cr :ZnS oscillator and step-index fluoride fibers," *Optics Letters*, vol. 44, pp. 2390–2393, 2019.

[155] K. König, A. Ehlers, F. Stracke, and I. Riemann, "In vivo drug screening in human skin using femtosecond laser multiphoton tomography," *Skin Pharmacology and Physiology.*, vol. 19, pp. 78–88, 2006.

[156] W. Bi, X. Li, Z. Xing, Q. Zhou, Y. Fang, W. Gao, L. Xiong, L. Hu, and M. Liao, "Wavelength conversion through soliton self-frequency shift in tellurite microstructured fiber with picosecond pump pulse," *Journal of Applied Physics.*, vol. 119, 2016.

[157] T. Karpate, G. Stepniewski, D. Pysz, A. Rampur, Y. Stepanenko, R. Buczynski, and M. Klimczak, "Soliton detuning of 685 THz in the near-infrared in a highly nonlinear suspended core tellurite fiber," *Journal of Optical Society of America B*, vol. 37, p. 1502, 2020.

[158] M. Y. Koptev, E. A. Anashkina, A. V. Andrianov, V. V. Dorofeev, A. F. Kosolapov, S. V. Muravyev, and A. V Kim, "Widely tunable mid-infrared fiber laser source based on soliton self-frequency shift in microstructured tellurite fiber," *Optics Letters*, vol. 40, p.

4094, 2015.

[159] T. P. J. Blaikie, J. Couper, G. Hancock, P. L. Hurst, R. Peverall, G. Richmond, G. A. D. Ritchie, D. Taylor, and K. Valentine, "Portable device for measuring breath acetone based on sample preconcentration and cavity enhanced spectroscopy," *Analytical Chemistry*, vol. 88,pp. 11016–11021, 2016.

[160] L. M. F. Barreira, Y. Xue, G. Duporté, J. Parshintsev, K. Hartonen, M. Jussila, M. Kulmala, and M.-L. Riekkola, "Potential of needle trap microextraction-portable gas chromatography-mass spectrometry for measurement of atmospheric volatile compounds," *Atmospheric Measurement Technique*, vol. 9, pp. 3661–3671, 2016.

[161] P. M. Santos, E. R. Pereira-Filho, and L. E. Rodriguez-Saona, "Application of hand-held and portable infrared spectrometers in bovine milk analysis," *Journal of Agricultural and Food Chemistry*, vol. 61, pp. 1205–1211, 2013.

[162] T. Cheng, Y. Kanou, K. Asano, D. Deng, M. Liao, M. Matsumoto, T. Misumi, Takenobu Suzuki, and Y. Ohishi1, "Soliton self-frequency shift and dispersive wave in a hybrid four-hole AsSe2-As2S5 microstructured optical fiber," *Applied Physics Letters*, vol. 104, 2014.

[163] A. Al-Kadry and M. Rochette, "Maximized soliton self-frequency shift in non-uniform microwires by the control of third-order dispersion perturbation," *Journal of Lightwave Technology*, vol. 31, pp. 1462–1467, 2013.

[164] A. M. Al-kadry and M. Rochette, "Mid-infrared sources based on the soliton self-frequency shift," *Journal of Optical Society of Americal B*, vol. 29, pp. 1347–1355, 2012.

[165] A. Zakery and S. R. Elliott, "Optical properties and applications of chalcogenide glasses: A review," *Journal of Non-Crystalline Solids*, vol. 330, pp. 1–12, 2003.

[166] L. F. Mollenauer, W. J. Tomlinson, R. H. Stolen, and J. P. Gordon, "Extreme Picosecond Pulse Narrowing Via the Soliton Effect in Single-Mode Optical Fibers", *Optics Letters* vol. 8, p. 204, 1983.

[167] A. Tikan, C. Billet, G. El, A. Tovbis, M. Bertola, T. Sylvestre, F. Gustave, S. Randoux, G. Genty, P. Suret, and J. M. Dudley, "Universal peregrine soliton structure in nonlinear pulse compression in optical fiber," *Physical Review Letters*, vol. 119, pp. 033901, 2017.

[168] O. V. Sinkin, R. Holzlöhner, J. Zweck, and C. R. Menyuk, "Optimization of the split-step Fourier method in modeling optical-fiber communications systems," *Journal of Lightwave Technology.*, vol. 21, pp. 61–68, 2003.

[169] William S. Rodney, Irving H. Malitson, and Thomas A. King, "Refractive index of arsenic trisulphide," *Journal of Optical Society of America*, vol. 48, pp. 633–636, 1958.

[170] A. Al-Kadry, L. Li, T. North, M. Rochette, M. El-Amraoui, and Y. Messaddeq, "Broadband supercontinuum generation in all-normal dispersion chalcogenide microwires," *Optics Letters*, vol. 40, pp. 4687–4690, 2015.

[171] C. Xiong, E. Magi, F. Luan, A. Tuniz, S. Dekker, J. S. Sanghera, L. B. Shaw, I. D. Aggarwal, and B. J. Eggleton, "Characterization of picosecond pulse nonlinear propagation in chalcogenide As2S3 fiber," *Applied Optics*, vol. 48, pp. 5467–5474, 2009.

[172] E. Genier, P. Bowen, T. Sylvestre, J. M. Dudley, P. Moselund, and O. Bang, "Amplitude noise and coherence degradation of femtosecond supercontinuum generation in all-normal-dispersion fibers," *Journal of Optical Society of America B*, vol. 36, p. A161, 2019.

[173] S. A. Dekker, A. C. Judge, R. Pant, I. Gris-Sánchez, J. C. Knight, C. M. de Sterke, and B. J. Eggleton, "Highly-efficient, octave spanning soliton self-frequency shift using a photonic crystal fiber with low OH loss," *Optics Express*, vol. 19, pp. 17766–17773, 2011.

[174] I. Alamgir, M. H. M. Shamim, M. El Amraoui, Y. Messaddeq, and M. Rochette, "Supercontinuum Generation in Suspended Core As2S3Tapered Fiber," in *IEEE Photonics Conference*, 2020.

[175] I. Alamgir, M. H. Mobarok Shamim, W. Correr, Y. Messaddeq, and M. Rochette, "Enhanced supercontinuum from a dispersion-varying fiber," in *Conference on Lasers and Electro-Optics*, 2021.

[176] I. Alamgir, M. H. M. Shamim, W. Correr, Y. Messaddeq, and M. Rochette, "Supercontinuum enhancement in dispersion-varying chalcogenide taper," in *Photonics North Conference*, 2021.

[177] I. Alamgir, H. M. Shamim, W. Correr, and Y. Messaddeq, "Supercontinuum bandwidth

enhancement in a dispersion- varying chalcogenide fiber," *To be submitted to Applied Physics Letters.*

[178] S. Venck, F. St-Hilaire, L. Brilland, A. N. Ghosh, R. Chahal, C. Caillaud, M. Meneghetti, J. Troles, F. Joulain, S. Cozic, S. Poulain, G. Huss, M. Rochette, J. M. Dudley,T. Sylvestre, "2–10 μm Mid-Infrared Fiber-Based Supercontinuum Laser Source: Experiment and Simulation," *Laser Photonics Reviews*, vol. 14, pp. 2000011, 2020.

[179] R. Kormokar, M. H. M. Shamim, and M. Rochette, "High-order analytical formulation of soliton self-frequency shift," *Journal of Optical Society of America B*, vol. 38, p. 466, 2021.

[180] R. R. Alfano and S. L. Shapiro, "Observation of self-phase modulation and small-scale filaments in crystals and glasses," *Physical Review Letters*, vol. 24, pp. 592–594, 1970.

[181] J. Swiderski, M. Michalska, and G. Maze, "Mid-IR supercontinuum generation in a ZBLAN fiber pumped by a gain-switched mode-locked Tm-doped fiber laser and amplifier system," *Optics Express*, vol. 21, p. 7851, 2013.

[182] J. Picot-Clemente, C.Strutynskia, F.Amrania, F.Désévédavya, J-C. Jules, G.Gadret, D.Deng, T.Cheng, K.Nagasaka, Y.Ohishi, B.Kibler, F.Smektalaa, "Enhanced supercontinuum generation in tapered tellurite suspended core fiber," *Optics Communication*, vol. 354, pp. 374–379, 2015.

[183] D.-P. Wei, T. V. Galstian, I. V. Smolnikov, V. G. Plotnichenko, and A. Zohrabyan, "Spectral broadening of femtosecond pulses in a single-mode As-S glass fiber," *Optics Express*, vol. 13, p. 2439, 2005.

[184] R. R. Gattass, L. Brandon Shaw, V. Q. Nguyen, P. C. Pureza, I. D. Aggarwal, and J. S. Sanghera, "All-fiber chalcogenide-based mid-infrared supercontinuum source," *Optical Fiber Technology*, vol. 18, pp. 345–348, 2012.

[185] J. Geng, Q. Wang, and S. Jiang, "High-spectral-flatness mid-infrared supercontinuum generated from a Tm-doped fiber amplifier," *Applied Optics*, vol. 51, pp. 834–840, 2012.

[186] K. Sakamaki, M. Nakao, M. Naganuma, and M. Izutsu, "Soliton induced supercontinuum generation in photonic crystal fiber," *IEEE J. Sel. Top. Quantum Electron.*, vol. 10, no. 5, pp. 876–884, 2004.

[187] C. R. Petersen, U. Møller, I. Kubat, B. Zhou, S. Dupont, J. Ramsay, T. Benson, S. Sujecki, N. Abdel-Moneim, Z. Tang, D. Furniss, A. Seddon and O. Bang, "Mid-IR supercontinuum covering the 1.4 μm to 13.3 μm molecular fingerprint region using ultra-high NA chalcogenide step-index fibre," *Nature Photonics*, vol. 8, pp. 1–6, 2014.

[188] I. Kubat, C. S. Agger, U. Møller, A. B. Seddon, Z. Tang, S. Sujecki, T. M. Benson, D. Furniss, S. Lamrini, K. Scholle, P. Fuhrberg, B. Napier, M. Farries, J. Ward, P. M. Moselund, and O. Bang., "Mid-infrared supercontinuum generation to 12.5μm in large NA chalcogenide step-index fibres pumped at 45μm," *Optics Express*, vol. 22, p. 19169, 2014.

[189] B. Zhang, W. Guo,Y. Yu,C. Zhai, S. Qi, A. Yang, L. Li, Z. Yang, R. Wang, D. Tang, G. Tao, B. Luther-Davies, "Low loss, high Na chalcogenide glass fibers for broadband mid-infrared supercontinuum generation," *Journal of American Ceramic Society.*, vol. 98, pp. 1389–1392, 2015.

[190] Y. Yu, B. Zhang, X. Gai, C. Zhai, Sisheng Qi, W. Guo, Z. Yang, R. Wang, D.-Y Choi, S. Madden, and B. Luther-Davies, "1.8-10 μm Mid-Infrared Supercontinuum Generated in a Step-Index Chalcogenide Fiber Using Low Peak Pump Power," *Optics Letters*, vol. 40, p. 1081, 2015.

[191] D. D. Hudson, M. Baudisch, D. Werdehausen, B. J. Eggleton, and J. Biegert, "1.9 octave supercontinuum generation in a As2S3 step-index fiber driven by mid-IR OPCPA," *Optics Letters*, vol. 39, pp. 5752–5755, 2014.

[192] M. El-Amraoui, G. Gadret, J. C. Jules, J. Fatome, C. Fortier, F. Désévédavy, I. Skripatchev, Y. Messaddeq, J. Troles, L. Brilland, W. Gao, T. Suzuki, Y. Ohishi, and F. Smektala, "Microstructured chalcogenide optical fibers from As2S3 glass: towards new IR broadband sources," *Optics Express*, vol. 18, pp. 26655–26665, 2010.

[193] S. Xing, S. Kharitonov, J. Hu, and C.-S. Brès, "Linearly chirped mid-infrared supercontinuum in all-normal-dispersion chalcogenide photonic crystal fibers," *Optics Express*, vol. 26, p. 19627, 2018.

[194] C. R. Petersen, R. D. Engelsholm, C. Markos, L. Brilland, C. Caillaud, J. Trolès, and O. Bang., "Increased mid-infrared supercontinuum bandwidth and average power by tapering large-mode-area chalcogenide photonic crystal fibers," *Optics Express*, vol. 25,

p. 15336, 2017.

[195] D. D. Hudson, S. Antipov, L. Li, I. Alamgir, T. Hu, M. El Amraoui, Y. Messaddeq, M. Rochette, S. D. Jackson, and A. Fuerbach, "Toward all-fiber supercontinuum spanning the mid-infrared," *Optica*, vol. 4, p. 1163, 2017.

[196] A. Al-Kadry, M. El Amraoui, Y. Messaddeq, and M. Rochette, "Two octaves mid-infrared supercontinuum generation in As_2Se_3 microwires.," *Optics Express*, vol. 22, pp. 31131–7, 2014.

[197] A. C. Judge, O. Bang, B. J. Eggleton, B. T. Kuhlmey, E. C. Mägi, R. Pant, and C. Martijn de Sterke, "Optimization of the soliton self-frequency shift in a tapered photonic crystal fiber," *Journal of Optical Society of America B*, vol. 26, p. 2064, 2009.

[198] H. Hu, X. Zhang, W. Li, and N. K. Dutta, "Simulation of octave spanning mid-infrared supercontinuum generation in dispersion-varying planar waveguides," *Applied Optics*, vol. 54, p. 3448, 2015.

[199] C. Ciret and S.-P. Gorza, "Generation of ultra-broadband coherent supercontinua in tapered and dispersion-managed silicon nanophotonic waveguides," *Journal of Optical. Society of America B*, vol. 34, p. 1156, 2017.

[200] N. Singh, D. Vermulen, A. Ruocco, N. Li, E. Ippen, F. X. Kärtner, and M. R. Watts, "Supercontinuum generation in varying dispersion and birefringent silicon waveguide," *Optics Express*, vol. 27, p. 31698, 2019.

[201] J. Wei, C. Ciret, M. Billet, F. Leo, B. Kuyken, and S. P. Gorza, "Supercontinuum generation assisted by dispersive waves trapping in dispersion-managed integrated silicon waveguides," *Physical Review Applied.*, vol. 14, p. 054045, 2020.

[202] Z. Chen, S. Ma, and N. K. Dutta, "An efficient method for supercontinuum generation in dispersion-tailored lead-silicate fiber taper," *Optics Communication*, vol. 283, pp. 3076–3080, 2010.

[203] Z. Chen, A. J. Taylor, and A. Efimov, "Coherent mid-infrared broadband generation in non-uniform ZBLAN fiber taper," *Optics Express*, vol. 17, pp. 2880–2887, 2009.

[204] S. Pricking and H. Giessen, "Tailoring the soliton and supercontinuum dynamics by engineering the profile of tapered fibers," *Optics Express*, vol. 18, p. 20151, 2010.

[205] A. Kudlinski, A. K. George, J. C. Knight, J. C. Travers, A. B. Rulkov, S. V. Popov, and J. R. Taylor, "Zero-dispersion wavelength decreasing photonic crystal fibers for ultraviolet-extended supercontinuum generation," *Optics Express*, vol. 14, p. 5715, 2006.

[206] A. V. Gorbach, D. V. Skryabin, J. M. Stone, and J. C. Knight, "Four-wave mixing of solitons with radiation and quasi-nondispersive wave packets at the short-wavelength edge of a supercontinuum," *Optics Express*, vol. 14, p. 9854, 2006.

[207] I. Alamgir and M. Rochette, "2 μm mode-locked fiber laser enabled by NPR in a chalcogenide taper," in *CLEO/Europe EQEC Conference*, 2021.

[208] I. Alamgir and M. Rochette, "Q-switched mode-locking by NPR in As2S3 tapers Imtiaz," in *Conference on Lasers and Electro-Optics*, 2022.

[209] I. Alamgir and M. Rochette, "Thulium-doped fiber laser mode-locked by nonlinear polarization rotation in a chalcogenide tapered fiber," Accepted in *Optics Express*, 2022.

[210] N. Leindecker, A. Marandi, R. L. Byer, K. L. Vodopyanov, J. Jiang, I. Hartl, M. Fermann, and P. G. Schunemann, "Octave-spanning ultrafast OPO with 26-61μm instantaneous bandwidth pumped by femtosecond Tm-fiber laser," *Optics Express*, vol. 20, p. 7046, 2012.

[211] C. R. Phillips, C. Langrock, J. S. Pelc, M. M. Fejer, J. Jiang, M. E. Fermann, and I. Hartl, "Supercontinuum generation in quasi-phase-matched LiNbO_3 waveguide pumped by a Tm-doped fiber laser system," *Optics Letters*, vol. 36, p. 3912, 2011.

[212] N. P. Barnes, B. M. Walsh, D. J. Reichle, and R. J. DeYoung, "Tm:fiber lasers for remote sensing," *Optical Materical.*, vol. 31, pp. 1061–1064, 2009.

[213] M. I. Kayes, N. Abdukerim, A. Rekik, and M. Rochette, "Free-running mode-locked laser based dual-comb spectroscopy," *Optics Letters*, vol. 43, pp. 1–4, 2018.

[214] N. M. Fried and K. E. Murray, "New technologies in endourology: High-power thulium fiber laser ablation of urinary tissues at 1.94 μm," *Journal of Endourology*, vol. 19, pp. 25–31, 2005.

[215] K. D. Polder and S. Bruce, "Treatment of Melasma Using a Novel 1,927-nm Fractional Thulium Fiber Laser: A Pilot Study," *Dermatologic Surgury.*, vol. 38, pp. 199–206,

2012.

[216] N. J. Scott, C. M. Cilip, and N. M. Fried, “Thulium fiber laser ablation of urinary Stones through small-core Optical fibers,” *IEEE Journal of Seclected Topics of Quantum Electronics*, vol. 15, pp. 435–440, 2009.

[217] H. Kalaycioglu, P. Elahi, O. Akcaalan, and F. O. Ilday, “High-Repetition-Rate Ultrafast Fiber Lasers for Material Processing,” *IEEE Jounral of Seclected Topics of Quantum Electronics*, vol. 24, 2018.

[218] B. E. Carlsten, E .R .Colby, E.H.Esarey, M.Hogan, F.X.Kärtner, W.S.Graves, W.P.Leemans, T.Rao, J.B.Rosenzweig, C.B.Schroeder, D.Sutter, W.E.White “New source technologies and their impact on future light sources,” Nuclear Instruments and Methods in Physics Research Section A: Accelerators, Spectrometers, Detectors and Associated Equipment, vol. 622, pp. 657–668, 2010.

[219] T. Popmintchev, M. C. Chen, P. Arpin, M. M. Murnane, and H. C. Kapteyn, “The attosecond nonlinear optics of bright coherent X-ray generation,” *Nature Photonics*, vol. 4, pp. 822–832, 2010.

[220] L. E. Nelson, E. P. Ippen, and H. A. Haus, “Broadly tunable sub-500 fs pulses from an additive-pulse mode-locked thulium-doped fiber ring laser,” *Applied Physics Letters*, vol. 67, p. 19, 1995.

[221] R. C. Sharp, D. E. Spock, N. Pan, and J. Elliot, “190 Fs Passively Mode-Locked Thulium Fiber Laser With Low Threshold,” *Conferce on Lasers and Electro-Optics*, vol. 21, p. 31, 1996.

[222] G. Sobon, A. Duzynska, M. Świniarski, J. Judek, J. Sotor, and M. Zdrojek, “CNT-based saturable absorbers with scalable modulation depth for Thulium-doped fiber lasers operating at 1.9 μm,” *Scientific Reports*, vol. 7, pp. 1–9, 2017.

[223] Y. Meng, Y. Li, Y. Xu, and F. Wang, “Carbon nanotube mode-locked thulium fiber laser with 200 nm tuning range,” *Scientific Reports*, vol. 7, pp. 1–7, 2017.

[224] M. A. Solodyankin, E. D. Obraztsova, A. S. Lobach, A. I. Chernov, A. V. Tausenev, V. I. Konov, and E. M. Dianov, “Mode-locked 193 μm thulium fiber laser with a carbon nanotube absorber,” *Optics Letters*, vol. 33, p. 1336, 2008.

[225] R. Dai, Y. Meng, Y. Li, J. Qin, S. Zhu, and F. Wang, "Nanotube mode-locked, wavelength and pulsewidth tunable thulium fiber laser," *Optics Express*, vol. 27, p. 3518, 2019.

[226] J. Lee, J. Koo, P. Debnath, Y. W. Song, and J. H. Lee, "A Q-switched, mode-locked fiber laser using a graphene oxide-based polarization sensitive saturable absorber," *Laser Physics Letters*, vol. 10, 2013.

[227] M. Zhang, E. J. R. Kelleher, F. Torrisi, Z. Sun, T. Hasan, D. Popa, F. Wang, A. C. Ferrari, S. V. Popov, and J. R. Taylor, "Tm-doped fiber laser mode-locked by graphene-polymer composite," *Optics Express*, vol. 20, pp. 25077–25084, 2012.

[228] J. Sotor, G. Sobon, M. Kowalczyk, W. Macherzynski, P. Paletko, and K. M. Abramski, "Ultrafast thulium-doped fiber laser mode locked with black phosphorus," *Optics Letters*, vol. 40, p. 3885, 2015.

[229] Z. Tian, K. Wu, L. Kong, N. Yang, Y. Wang, R. Chen, W. Hu, J. Xu and Y. Tang, "Mode-locked thulium fiber laser with MoS2," *Laser Physics Letters*, vol. 12, pp. 2–7, 2015.

[230] M. A. Chernysheva, A. A. Krylov, P. G. Kryukov, and E. M. Dianov, "Nonlinear amplifying loop-mirror-based mode-locked thulium-doped fiber laser," *IEEE Photonics Technology Letters*, vol. 24, pp. 1254–1256, 2012.

[231] C. W. Rudy, K. E. Urbanek, M. J. F. Digonnet, and R. L. Byer, "Amplified 2-μm thulium-doped all-fiber mode-locked figure-eight laser," *Journal of Lightwave Technology*, vol. 31, pp. 1809–1812, 2013.

[232] F. Haxsen, A. Ruehl, M. Engelbrecht, D. Wandt, U. Morgner, and D. Kracht, "Stretched-pulse operation of a thulium-doped fiber laser," *Optics Express*, vol. 16, p. 20471, 2008.

[233] C. Gao, Z. Wang, H. Luo, and L. Zhan, "High Energy All-Fiber Tm-Doped Femtosecond Soliton Laser Mode-Locked by Nonlinear Polarization Rotation," *Journal of Lightwave Technology*, vol. 35, pp. 2988–2993, 2017.

[234] T. Wang, W. Ma, Q. Jia, Q. Su, P. Liu, and P. Zhang, "Passively Mode-Locked Fiber Lasers Based on Nonlinearity at 2-μm Band," *IEEE Journal of Seclected Topics on Quantum Electronics*, vol. 24, 2018.

[235] A. Sincore, J. Bradford, J. Cook, L. Shah, and M. Richardson, "High Average Power Thulium-doped Silica Fiber Lasers: Review of Systems and Concepts," *IEEE Journal of Seclected Topics on Quantum Electronics*, vol. 24, pp. 1–8, 2017.

[236] C. W. Rudy, M. J. F. Digonnet, and R. L. Byer, "Advances in 2-μm Tm-doped mode-locked fiber lasers," *Optical Fiber Technology*, vol. 20, pp. 642–649, 2014.

[237] L. Dahlström, "Passive mode-locking and Q-switching of high power lasers by means of the optical Kerr effect," *Optics Communicaiton*, vol. 5, pp. 157–162, 1972.

[238] T. North and M. Rochette, "Fabrication and characterization of a pulsed fiber ring laser based on As2S3.," *Optics Letters*, vol. 37, pp. 716, 2012.

[239] T. North, "Broadband self-pulsating sources based on nonlinear effects," *PhD thesis*, 2014.

[240] J. Li, Z. Yan, Z. Sun, H. Luo, Y. He, Z. Li, Y. Liu, and L. Zhang, "Thulium-doped all-fiber mode-locked laser based on NPR and 45°-tilted fiber grating," *Optics Express*, vol. 22, p. 31020, 2014.

[241] C. Li, X. Wei, C. Kong, S. Tan, N. Chen, J. Kang, and K. K. Y. Won, "Fiber chirped pulse amplification of a short wavelength mode-locked thulium-doped fiber laser," *APL Photonics*, vol. 2, pp. 0–5, 2017.

[242] J. Li, Y. Wang, H. Luo, Y. Liu, Z. Yan, Z. Sun, and Lin Zhang, "Kelly sideband suppression and wavelength tuning of a conventional soliton in a Tm-doped hybrid mode-locked fiber laser with an all-fiber Lyot filter," *Photonics Research*, vol. 7, p. 103, 2019.

[243] W. Ma, T. Wang, Y. Zhang, P. Liu, Y. Su, Q. Jia, M. Bi, P. Zhang, and H. Jiang, "Widely tunable 2 μm continuous-wave and mode-locked fiber laser," *Applied Optics*, vol. 56, p. 3342, 2017.

[244] X. Yang and C. X. Yang, "Q-switched mode-locking in an erbium-doped femtosecond fiber laser based on nonlinear polarization rotation," *Laser Physics*, vol. 19, pp. 2106–2109, 2009.

[245] Y. Gan, W. H. Xiang, and G. Z. Zhang, "Studies on CW and Q-switched mode-locked in passive mode-locked ytterbium-doped fibre laser," *Laser Physics*, vol. 19, pp. 445–

449, 2009.

[246] X. Wang, Y. Zhu, P. Zhou, X. Wang, H. Xiao, and L. Si, "Tunable, multiwavelength Tm-doped fiber laser based on polarization rotation and four-wave-mixing effect," *Optics Express*, vol. 21, p. 25977, 2013.

[247] Y. Wang, J. Li, B. Zhai, Y. Hu, K. Mo, R. Lu, and Y. Liu, "Tunable and switchable dual-wavelength mode-locked Tm^3+-doped fiber laser based on a fiber taper," *Optics Express*, vol. 24, p. 15299, 2016.

[248] U. Keller, "Recent developments in compact ultrafast lasers," *Nature*, vol. 424, pp. 831–838, 2003.

[249] L. Talaverano, S. Abad, S. Jarabo, and M. López-Amo, "Multiwavelength fiber laser sources with Bragg-grating sensor multiplexing capability," *Journal of Lightwave Technology*, vol. 19, pp. 553–558, 2001.

[250] J. Marshall, G. Stewart, and G. Whitenett, "Design of a tunable L-band multi-wavelength laser system for application to gas spectroscopy," *Measurement Science Technology*, vol. 17, pp. 1023–1031, 2006.

[251] Q. Wang, T. Chen, B. Zhang, A. P. Heberle, and K. P. Chen, "All-fiber passively mode-locked thulium-doped fiber ring oscillator operated at solitary and noiselike modes," *Optics Letters*, vol. 36, p. 3750, 2011.

[252] Z. Yan, B. Sun, X. Li, J. Luo, P. P. Shum, X. Yu, Y. Zhang & Q. J. Wang, "Widely tunable Tm-doped mode-locked all-fiber laser," *Scientific Reports*, vol. 6, pp. 1–7, 2016.

[253] S. Liu, F. Yan, Y. Li, L. Zhang, Z. Bai, H. Zhou, and Y. Hou, "Noise-like pulse generation from a thulium-doped fiber laser using nonlinear polarization rotation with different net anomalous dispersion," *Photonics Research*, vol. 4, p. 318, 2016.

[254] S. Kobtsev, S. Smirnov, S. Kukarin, and S. Turitsyn, "Mode-locked fiber lasers with significant variability of generation regimes," *Optical Fiber Technology*, vol. 20, pp. 615–620, 2014.

[255] Z. Shao, X. Qiao, Q. Rong, and D. Su, "Observation of the evolution of mode-locked solitons in different dispersion regimes of fiber lasers," *Optics Communications*, vol. 345. pp. 105–110, 2015.

[256] A. Kadry, M. El Amraoui, and Y. Messaddeq, "Mode-locked fiber laser based on chalcogenide microwires," *Optics Letters*, vol. 40, pp. 4309–4312, 2015.

[257] R. Motuz, P. Munster, and M. Filka, "PMD study & measurement - Fixed analyzer method," *Journal of Communiations Software and Systems*, vol. 11, pp. 199–203, 2015.

[258] C. Cuadrado-Laborde, A. Díez, J. L. Cruz, and M. V. Andrés, "Doubly active Q switching and mode locking of an all-fiber laser," *Optics Letters*, vol. 34, p. 2709, 2009.

[259] L. C. Kong, G. Q. Xie, P. Yuan, L. J. Qian, S. X. Wang, H. H. Yu, and H. J. Zhang, "Passive Q-switching and Q-switched mode-locking operations of 2 μm Tm:CLNGG laser with MoS2 saturable absorber mirror," *Photonics Research*, vol. 3, p. A47, 2015.

[260] J. Lin, H. Chen, H. Hsu, M. Wei, K. Lin, and W. Hsieh, "Stable Q-switched mode-locked Nd3+:LuVO4 laser by Cr4+:YAG crystal," *Optics Express*, vol. 16, no. 21, pp. 16538–16545, 2008.

[261] S. Liu, F. Yan, F. Ting, L. Zhang, Z. Bai, W. Han, and H. Zhou, "Multi-Wavelength Thulium-Doped Fiber Laser Using a Fiber-Based Lyot Filter," *IEEE Photonics Technology Letters*, vol. 28, pp. 864–867, 2016.

[262] X. Feng, H. Tam, and P. K. A. Wai, "Stable and uniform multiwavelength erbium-doped fiber laser using nonlinear polarization rotation," *Optics Express*, vol. 14,, p. 8205, 2006.

[263] I. Alamgir, M. Rezaei, and M. Rochette, "Optical parametric oscillator based on all-chalcogenide fiber components," in *OSA Advanced Photonics Congress*, 2020.

[264] I. Alamgir, M. Rezaei, and M. Rochette, "Optical parametric oscillation from soft-glass fiber cavity," in *Conference on Lasers and Electro-Optics*, 2022.

[265] I. Alamgir, M. Rezaei, and M. Rochette, "Fiber Optical Parametric Oscillator Made of Soft Glass," Under review in *Optics Letters.*

[266] Q. Clément, J.-M. Melkonian, J.-B. Dherbecourt, M. Raybaut, A. Grisard, E. Lallier, B. Gérard, B. Faure, G. Souhaité, and A. Godard, "Longwave infrared, single-frequency, tunable, pulsed optical parametric oscillator based on orientation-patterned GaAs for gas sensing," *Optics Letters*, vol. 40, p. 2676, 2015.

[267] E. Lippert, G. Rustad, and K. Stenersen, "High power and efficient long wave IR ZnGeP2 optical parametric oscillator," *Optics Express*, vol. 16, pp. 13878–13884, 2008.

[268] K. Finsterbusch, R. Urschel, and H. Zacharias, “Fourier-transform-limited, high-power picosecond optical parametric oscillator based on periodically poled lithium niobate,” *Optics Letters*, vol. 27, p. 1543, 2000.

[269] R. C. Bapna, C. S. Rao, and K. Dasgupta, “Low-threshold operation of a 355-nm pumped nanosecond β-BaB2O4 optical parametric oscillator,” *Optics and Laser Technology*, vol. 40, pp. 832–837, 2008.

[270] H. Q. Li, H. B. Zhang, Z.Bao, J.Zhang, Z.P.Sun, Y.P.Kong, Y.Bi, X.C.Lin, A.Y.Yao, G.L.Wang, W.Hou, R.N.Li, D.F.Cui, Z.Y.Xu, “High-power nanosecond optical parametric oscillator based on a long LiB3O5 crystal,” *Optics Communication*, vol. 232, pp. 411–415, 2004.

[271] M. H. Wu, W. C. Tsai, Y. C. Chiu, and Y. C. Huang, “Generation of ∼100 kW narrow-line far-infrared radiation from a KTP off-axis THz parametric oscillator,” *Optica*, vol. 6, p. 723, 2019.

[272] Y. Yamamoto, Y. Tamura, and T. Hasegawa, “Silica-based highly nonlinear fibers and their applications,” *IEEE Journal of Seclected Topics of Quantum Electronics*, vol. 15, p. 103, 2009.

[273] L. Zhang, T. H. Tuan, H. Kawamura, T. Suzuki, and Y. Ohishi, “Optical parametric oscillator based on degenerate four-wave mixing in suspended core tellurite microstructured optical fiber,” *Optics Express*, vol. 23, pp. 26299–26304, 2015.

[274] L. Zhang, S. Yang, X. Wang, D. Gou, X. Li, H. Chen, M. Chen, and S. Xie, “Widely tunable all-fiber optical parametric oscillator based on a photonic crystal fiber pumped by a picosecond ytterbium-doped fiber laser,” *Optics Lett*ers vol. 38, p. 4534, 2013.

[275] M. Henriksson, “Mid-infrared optical parametric oscillators,” *Handbook of Solid State Lasers*, pp. 463–492, 2013.

[276] Y. Zhou, K. K. Y. Cheung, Q. Li, S. Yang, P. C. Chui, and K. K. Y. Wong, “Fast and wide wavelength-swept fiber optical parametric oscillator based on dispersion-tuning,” *Frontiers in Optics.*, vol. 35, pp. 2427–2429, 2010.

[277] A. Gershikov, E. Shumakher, A. Willinger, and G. Eisenstein, “Fiber parametric oscillator for the 2 μm wavelength range based on narrowband optical parametric amplification.,” *Optics Letters*, vol. 35, pp. 3198–3200, 2010.

[278] R. Ahmad and M. Rochette, "Chalcogenide optical parametric oscillator," *Optics Express*, vol. 20, p. 10095, 2012.

[279] N. Abdukerim, L. Li, and M. Rochette, "Chalcogenide-Based Optical Parametric Oscillator," *Optics Letters*, vol. 1, pp. 25–26, 2016.

[280] M. Rezaei and M. Rochette, "All-chalcogenide single-mode optical fiber couplers," *Optics Letters*, vol. 44, p. 5266, 2019.

[281] Stuart Jackson, M. Bernier, and R. Vallée, *Mid-Infrared Fiber Photonics: Glass Materials, Fiber Fabrication and Processing, Laser and Nonlinear Sources, Woodhead Publishing,* 2021.

[282] F. Tavakoli, A. Rekik, and M. Rochette, "Broadband and Wavelength-Dependent Chalcogenide Optical Fiber Couplers," *IEEE Photonic Technology Letters*, vol. 29, pp. 735–738, 2017.

[283] J. Wang, X. Liang, G. Hu, Z. Zheng, S. Lin, D. Ouyang, X. Wu, P. Yan, S. Ruan, Z. Sun & T. Hasan, "152 Fs Nanotube-Mode-Locked Thulium-Doped All-Fiber Laser," *Scientific. Reports*, vol. 6, pp. 4–10, 2016.

[284] K. Kieu and F. W. Wise, "Soliton thulium-doped fiber laser with carbon nanotube saturable absorber," *IEEE Photonics Technology Letters*, vol. 21, pp. 128–130, 2009.

[285] R. Thapa, R. R. Gattass, V. Nguyen, G. Chin, D. Gibson, W. Kim, L. B. Shaw, and J. S. Sanghera, "Low-loss, robust fusion splicing of silica to chalcogenide fiber for integrated mid-infrared laser technology development," *Optics Letters*, vol. 40, p. 5074, 2015.

[286] L. Yang, B. Yan, R. Zhao, D. Wu, T. Xu, P.Yang, Q.Nie, S. Dai., "Ultra-low fusion splicing loss between silica and ZBLAN fiber for all-fiber structured high-power mid-infrared supercontinuum generation," *Infrared Physics and Technology*, vol. 113, p. 103576, 2021.

[287] L. Yang, Y. Wang, K. Jiao, S. Dai, R. Zhao, Q. Nie, X. Wang, Z. Jia, G. Qin., "High-coupling efficiency and robust fusion splicing between fluorotellurite and chalcogenide fibers," *Infrared Physics and Technology*, vol. 122, p. 104075, 2022.

[288] L. M. F. Barreira, Y. Xue, G. Duporté, J. Parshintsev, K. Hartonen, M. Jussila, M. Kulmala, and M.-L. Riekkola, "Potential of needle trap microextraction-portable gas

chromatography-mass spectrometry for measurement of atmospheric volatile compounds," *Atmospheric Measurement Techniques*, vol. 9, pp. 3661–3671, 2016.

[289] P. Werle, F. Slemr, K. Maurer, R. Kormann, R. M. Ucke C, and B. J. Anker, "Near-and mid-infrared laser-optical sensors for gas analysis," O*ptics and Lasers in Engineering*, vol. 37, pp.101, 2002.

[290] L. Li, "Chalcogenide microwires cladded with hydrogen-and fluorine-based polymers and their applications," *PhD thesis*, 2017.

[291] C. Baker, "Hybrid As2Se3-PMMA Microtapers and Applications," *PhD thesis*, 2013.

[292] M. Farahmand and M. de Sterke, "Parametric amplification in presence of dispersion fluctuations.," *Optics Express*, vol. 12, pp. 136–142, 2004.